

Interindividual differences in the brain during aging and Alzheimer's disease

Frédéric St-Onge

Integrated Program in Neuroscience

McGill University, Montreal

October 2023

A thesis submitted to McGill University in partial fulfillment of the requirements of
the degree of Doctor of Philosophy in Neuroscience



© Frédéric St-Onge, 2023

Table of Contents

I - ABSTRACT (ENGLISH)	7
II - RÉSUMÉ (FRANÇAIS)	8
III – ACKNOWLEDGEMENTS	10
III.I – PERSONAL ACKNOWLEDGEMENTS	10
III.II – FUNDING SOURCES	13
IV – CONTRIBUTION TO ORIGINAL KNOWLEDGE	15
V – PUBLICATIONS AND CONTRIBUTIONS OF AUTHORS	17
VI – OTHER CONTRIBUTIONS	18
A. – PUBLICATIONS	18
<i>A.1 – Villeneuve Lab publications</i>	18
A.2 – PAPERS FROM COLLABORATORS	20
B. – SCIENTIFIC CONSULTING	21
<i>B.1 – Academia</i>	21
<i>B.2 – Industry</i>	22
VII – LIST OF FIGURES AND TABLES	24
VIII – LIST OF ABBREVIATIONS	29
CHAPTER 1 – INTRODUCTION	31
1.1 – OBJECTIVES AND HYPOTHESES	31
1.2 – ALZHEIMER’S DISEASE DEMENTIA	33
1.3 – HETEROGENEITY IN ALZHEIMER’S DISEASE	38
1.4 – INTERINDIVIDUAL DIFFERENCES IN NEUROIMAGING	41
<i>1.4.1 – Brain fingerprints and their properties</i>	42
<i>1.4.2 – Aging and interindividual differences</i>	44

1.5 – INTERINDIVIDUAL DIFFERENCES AND IMPACT ON AD CLINICAL RESEARCH	48
1.6 – MEASURING INTERINDIVIDUAL DIFFERENCES	50
1.7 – INTERINDIVIDUAL DIFFERENCES BEYOND ACADEMIC ENVIRONMENTS	53
CHAPTER 2 – FUNCTIONAL CONNECTOME FINGERPRINTING ACROSS THE LIFESPAN.....	55
2.1 – PREFACE	56
2.2 – ABSTRACT	57
2.3 – INTRODUCTION	58
2.4 – RESULTS	60
2.4.1 - Fingerprint identification accuracy in a lifespan cohort	60
2.4.2 - Both self-identifiability and others-identifiability change non-linearly and in parallel across the lifespan	65
2.4.3 - Regions contributing to self-identifiability across the lifespan.....	67
2.4.4 - Variability in FC, but not variability in BOLD features, differ over the lifespan	70
2.4.5 - Self-identifiability is associated with grey matter volume	72
2.5 – DISCUSSION.....	75
2.5.1 – Strengths and limitations	80
2.5.2 – Conclusion	80
2.6 – MATERIAL AND METHODS	82
2.6.1 – Participants	82
2.6.2 – Magnetic resonance imaging	82
2.6.3 – Sliding-window analysis	84
2.6.4 – Fingerprinting	84
2.6.5 - Predicting self-identifiability using combinations of edges	86
2.6.6 – Age-related outcome: Structural aging morphometric network	87
2.6.7 – Supplementary analyses on FC variability	88
2.6.8 – Software	89

2.6.9 – <i>Statistical analyses</i>	90
2.7 – ACKNOWLEDGEMENTS.....	93
2.9 – REFERENCES OF CHAPTER 2	94
2.10 – SUPPLEMENTARY MATERIAL OF CHAPTER 2.....	107
2.10.1 – <i>Methods</i>	107
2.10.2 – <i>Results</i>	112
2.10.3 – <i>Supplementary Figures</i>	117
2.10.4 – <i>Supplementary references</i>	154
CHAPTER 3 - TAU ACCUMULATION AND ITS SPATIAL PROGRESSION IN THE LATE ONSET ALZHEIMER’S DISEASE	
SPECTRUM	155
3.1 – PREFACE	156
3.2 – ABSTRACT	158
3.3 – INTRODUCTION	160
3.4 – METHODS.....	163
3.4.1 – <i>Participants</i>	163
3.4.2 – <i>PET acquisition and processing</i>	163
3.4.3 – <i>Regional tau-PET and other measures of interest</i>	164
3.4.4 – <i>Neuropsychological measures</i>	167
3.4.5 – <i>Statistical analyses</i>	167
3.4.6 – <i>Data availability</i>	171
3.5 – RESULTS	173
3.5.1 – <i>Participants</i>	173
3.5.2 – <i>Cross-sectional tau-PET patterns</i>	173
3.5.3 – <i>Longitudinal tau-PET patterns</i>	176
3.5.4 – <i>Heterogeneity of regional tau-PET abnormality</i>	181
3.5.5 – <i>Associations with demographic information, cognitive profiles and cognitive decline</i>	182

3.6 – DISCUSSION.....	189
3.6.1 – <i>Strengths and limitations</i>	192
3.6.2 – <i>Conclusion</i>	194
3.7 – ACKNOWLEDGEMENTS.....	196
3.8 – <i>Funding</i>	197
3.9 – <i>Competing interests</i>	198
3.10 – <i>References of Chapter 3</i>	199
3.11 – SUPPLEMENTARY RESULTS	209
CHAPTER 4 – GENERAL DISCUSSION	239
4.1 – SUMMARY OF THESIS CONCLUSIONS	239
4.2 – THE BRAIN IS MADE OF SHARED AND IDIOSYNCRATIC PATTERNS	240
4.3 – INTERINDIVIDUAL DIFFERENCES IMPACT OUR UNDERSTANDING OF THE BRAIN.....	242
4.4 – CREATING TOOLS TO ASSESS AND LEVERAGE INTERINDIVIDUAL DIFFERENCES	246
4.5 – STRENGTHS AND LIMITATIONS	247
4.6 – FUTURE DIRECTIONS.....	250
4.7 – GENERAL CONCLUSIONS.....	251
IX - REFERENCE LIST	252
X – ANNEX: <i>SIHNPY</i> DOCUMENTATION.....	287
X.I – INTRODUCTION TO <i>SIHNPY</i>	288
X.II – DESCRIPTION OF <i>SIHNPY</i> 'S MODULES	292
<i>X.II.I – Software development and general philosophy</i>	292
<i>X.II.II – Datasets module</i>	293
<i>X.II.III. – Fingerprinting module</i>	295
<i>X.II.IV. – Spatial extent module</i>	299
<i>X.II.V. – Sliding-window module</i>	302

<i>X.II.VI. – Imbalance mapping module</i>	304
<i>X.II.VII. – Data preprocessing</i>	306
X.III. – DISCUSSION	314
XI – ANNEX: OPTINA DIAGNOSTICS – DATA SCIENCE REPORT	315
SECTION 1 – SUMMARY AND RECOMMENDATIONS	318
SECTION 2 – INTRODUCTION AND OBJECTIVES.....	319
SECTION 3 – METHODOLOGY	320
<i>Section 3.1 – Participants</i>	320
<i>Section 3.2 – Data gathering and preprocessing</i>	320
<i>Section 3.3 – Variables</i>	321
SECTION 4 – RESULTS	323
<i>Section 4.1 – Describe demographics, neuroradiological visual reads and quantitative PET SUVR positivity.</i>	323
<i>Section 4.3 - Exploring discordant cases between visual read and PET SUVR</i>	327
SECTION 5 – CONCLUSIONS AND RECOMMENDATIONS	334
XII – COPYRIGHT	336

I - Abstract (English)

Traditional brain imaging research designs typically include either a contrast of brain features between two groups of interest, or an average of brain features within a single group. In either case, this relies on the assumption that participants are homogenous enough that any differences can be considered negligible. This contrasts with more recent research indicating that brain features can vary widely between very demographically similar individuals. Particularly in disorders like Alzheimer's, many studies are now demonstrating the diversity in clinical and molecular presentations, stressing the need to understand interindividual differences in the brain better.

We sought to first understand the extent of these interindividual differences in the brain using functional brain imaging in a healthy population spanning the lifespan. We found that individuals have a unique signature of brain activity across all ages, with no single brain regions commonly contributing to it across individuals. Furthermore, this signature was related to atrophy in age-sensitive regions, suggesting clinical relevance. Next, we sought to understand the extent of these differences in a clinical population using molecular imaging. We found significant heterogeneity in patterns of tau across the Alzheimer's disease spectrum and demonstrated that measures accounting for this variability could improve association with clinical outcomes at different stages of the disease. Finally, we provide the scientific community with practical software-based tools to assess interindividual differences in their research and provide a concrete data science industry example where these tools are applied. Overall, this thesis emphasizes the importance of accounting for interindividual differences in brain imaging research, be it in structural, functional, or molecular imaging, in healthy and clinical populations.

II - Résumé (Français)

Les devis d'études traditionnels en neuroimagerie incluent soit un contraste de caractéristiques cérébrales entre deux groupes d'intérêt ou étudient la moyenne d'un seul groupe. Dans les deux cas, ces devis se basent sur l'assomption que les cerveaux des participants sont assez homogènes pour que toute différence puisse être considérée comme négligeable. Cela contraste avec des études récentes indiquant que les caractéristiques du cerveau peuvent varier drastiquement entre des individus démographiquement similaires. Particulièrement dans des maladies comme la maladie d'Alzheimer, plusieurs études illustrent désormais une vaste diversité de présentations cliniques et moléculaires, urgeant le besoin de mieux comprendre les différences interindividuelles du cerveau.

Nous avons cherché à comprendre l'étendue des différences interindividuelles du cerveau en utilisant l'imagerie fonctionnelle du cerveau dans une population en santé de tout âge. Nous avons trouvé que les individus ont une signature d'activité cérébrale unique à tout âge, avec aucune région cérébrale contribuant à la signature chez tous les individus uniformément. De plus, cette signature était associée à de l'atrophie dans des régions sensibles à l'effet de l'âge, suggérant une utilité clinique. Ensuite, nous avons cherché à comprendre l'impact des différences interindividuelles dans une population clinique en utilisant de l'imagerie moléculaire. Nous avons trouvé beaucoup d'hétérogénéité dans les patrons d'accumulation de la pathologie tau dans le spectre de la maladie d'Alzheimer, et démontré que des mesures prenant compte de cette variabilité peuvent améliorer les associations entre la pathologie et les mesures cliniques à différents stages de la maladie. Finalement, nous donnons accès à la communauté

scientifique les outils développés durant cette thèse et donnons un exemple concret de leurs applications dans un contexte de science des données en industrie. Cette thèse met l'emphase sur l'importance de prendre en compte les différences interindividuelles dans la recherche en neuroimagerie, que ce soit de l'imagerie structurelle, fonctionnelle ou moléculaire, dans une population en santé ou clinique.

III – Acknowledgements

III.I – Personal acknowledgements

While I was the one sitting behind this keyboard writing this thesis, it is not possible to see all the support I received that helped support this work. This journey would not have been possible without the continuous support from everyone around me, and although it is ending, the support I received during my PhD will be forever engraved in my memory.

I want first to acknowledge my biggest supporters, my family, who have been unwavering throughout this whole endeavour. Paul and Kevin, thank you for being my rocks, my anchors, and a continued daily source of support in the highs and the lows of this adventure. It is difficult to imagine my Ph.D. without your input, be it on a statistical model to implement, a funny adventure at the lab or how to best arrange my outfit before a conference. Your infallible support allows me to stand tall and push forward in all of my endeavours. Destiny, Hope and Alysha, thank you for bringing all of your adventures—big or small—into my life. Not only were they good distractions to have outside of work, but I have learned a lot as a human and a parent and that is truly invaluable. It is a blessing to have all five of you in my life. Maman, papa et Gab, merci pour tout votre support durant cette longue aventure. Toutes nos conversations et votre support inconditionnel m'ont permis d'avancer et de réfléchir, de questionner et parfois, simplement, de prendre une pause. Gab, un merci tout particulier pour ton aide technique de programmation. Je suis un grand frère très inspiré par ton expertise et ta facilité d'apprendre.

Outside the home, I was also well supported and I am truly grateful for their support during my journey. First, I want to thank Emma, Callie and Amanda. Your support has

made it possible for me to focus on my studies and become a better human, and for that, I will always be grateful. Deuxièmement, Karyna et Pascal, un grand merci pour votre support durant ce processus. Vos conseils, votre écoute et simplement votre présence ont toujours été une grande source de motivation pour moi.

I became a well-rounded scientist in part due to all the people in my lab and they need to be properly acknowledged. Sylvia, thank you for guiding me to be an independent scientist with the ability to tackle any challenges thrown at me and thank you for providing me with the opportunity to network and gain many different skills, both within and outside the lab. Alexa, thank you for your mentoring during my PhD, particularly during my second paper. I also want to extend a heartfelt thanks to all the lab members I have had the pleasure to work with over the years; I will try to keep this section short. I want to thank everyone I worked with over the years for your enthusiastic help with all the projects I was involved with, including all the help, mentorship, feedback and fun conversations: Hazal, Julie G., Pierre-François, Theresa, Jordana, Jonathan, Cherie, Ting, Ali, Bery, Yara, Bery, Sophie, Julien, Alfonso, Valentin, Julie B., Christine, Louise and Jen. This thesis, and my personal growth, would not have been possible without all of you. I want to give a special mention to Jordana, Bery and Yara. Jordana, your computational and linguistic support over the years has made many new things possible for me. I will also be eternally grateful for your relentless attention to detail; you have inspired me to do the same, and I will do my best to carry this skill with me as I move forward. Bery, as one of your mentors in the lab, thank you for your confidence in letting me teach you. The skills I learned teaching you—and your eternal good mood—made my Ph.D. experience more complete. Yara, thank you for all the fun conversations and for your relentless determination; it is inspiring

to see and always inspires me to aim higher. Thank you to Danilo and Alain, my committee members, for your thoughtful feedback over the years, and to Nathan Spreng, Golia Shafiei, Bratislav Misic, Etienne Vachon-Pressseau, Marianne Chapleau and John Breitner for your support, feedback, and critical revisions on my manuscripts.

Last but not least, I want to thank Marie-Christine Ouellet and Simon Beaulieu-Bonneau, my first scientific supervisors. Marie-Christine, as a young undergrad with no research experience, you took a chance on me. You trained me, gave me responsibilities, and always took the time to mentor me whenever I needed it. You made me feel important and competent as a young student and inspired me to reach as high as I could. Simon, your patience in teaching me, your thoroughness in your attention to detail and your trust in making me participate in your projects were always so appreciated. Together, you have both fostered the budding scientist I was and gave me a solid foundation for the scientist I became. You ignited my undying passion for research, and for that, I will be ever thankful.

III.II – Funding sources

The science done in this thesis was also made possible through the generous support of multiple organizations that awarded me with scholarships, travel, or merit awards throughout the years. I am very thankful for their support in these endeavours.

Scholarships

Sep 2019 – Aug 2020	Mitacs Accelerate program (Industry internship)
Aug 2020	McGill Faculty of Medicine – Internal studentship (Declined)
Sep 2020 – Aug 2021	Healthy Brain for Healthy Lives
Nov 2020 – May 2021	Mitacs Accelerate program (Industry internship)
Sep 2021 – Aug 2022	Healthy Brain for Healthy Lives
Jun 2022 – Dec 2023	Fonds de Recherche du Québec – Santé

Merit and Travel awards

Feb 2020	University of Gothenburg (Sweden) – Travel award
Mar 2021	Quebec Bio-Imaging Network – Best presentation
May 2021	University of Gothenburg (Sweden) – Best research design
July 2023	Douglas Research Center – Roger J. Paiement Outreach Award
July 2023	Organization for Human Brain Mapping – Merit Award
July 2023	Alzheimer’s Association – Travel Fellowship
Nov 2023	Human Amyloid Imaging 2024 – Young Investigator Award (Declined)

Data sources and organizational support

Cambridge Center for Aging and Neuroscience – First project

Alzheimer's Disease Neuroimaging Initiative – Second project

Pre-symptomatic Evaluation of Experimental or Novel Treatments for Alzheimer
Disease (PREVENT-AD) – SIHNPY development

Digital Research Alliance of Canada – Software and hardware support

IV – Contribution to original knowledge

The main goal of this thesis was to understand the importance of multimodal interindividual heterogeneity in brain features across healthy and clinical populations. To do so, we used two cohorts: the Cam-CAN cohort comprising healthy participants aged from 18 to 88 years of age and the Alzheimer’s Disease Neuroimaging Initiative comprising participants on the spectrum of Alzheimer’s disease. We studied these differences in multiple modalities including structural, functional and molecular imaging and provided a comprehensive theoretical and practical overview of interindividual differences across these two populations. The thesis’s contributions can be summarized in two main points:

1. We found that interindividual differences on functional magnetic resonance imaging are preserved across the lifespan in healthy participants, confirming previous results from younger populations. We also suggest that these differences are associated with other age-related variables, suggesting a potential utility beyond the simple identification of participants.
2. We confirmed that, while broad group-level patterns of tau positron emission tomography are followed, there are important differences between individuals on where tau accumulates. This impacts associations between tau and cognition—particularly outside of memory—and suggests that interindividual differences must be accounted for.

However, throughout my training, I have also developed other skills that resulted in significant contributions both within and outside of academia.

1. I developed an all-in-one compendium of open-access Python-based tools for other researchers to study interindividual differences (fingerprinting, spatial extent, sliding window and imbalance mapping) in the brain, hopefully encouraging researchers to measure and leverage these differences in their data. A formal version of the package documentation is available in Annex X.
2. Acting as a data science consultant for Optina Diagnostics, I conducted research in an industry setting and reported results with a clear impact on the methods used at the company. Part of the results incorporated the tools I developed in Annex X. The report is available in Annex XI.

V – Publications and contributions of authors

Below are the publications resulting from my scientific work during my PhD. The publications are, respectively, Chapters 2 and 3 of this thesis. My contribution and the contribution of each of the coauthor is listed for each publication.

St-Onge F, Javanray M, Pichet Binette A, Strikwerda-Brown C, Remz J, Spreng RN, Shafiei G, Mistic B, Vachon-Preseau E, Villeneuve S. (2023) **Functional connectome fingerprinting across the lifespan**. *Network Neuroscience*. doi: https://doi.org/10.1162/netn_a_00320

St-Onge: Study design, code writing, statistical analyses, interpretation of results, drafting of manuscript, critical revision of the manuscript.

Javanray, Pichet Binette, Strikwerda-Brown, Spreng, Shafiei, Mistic, Vachon-Preseau: Statistical analyses, critical revision of the manuscript.

Remz: Critical revision of the manuscript.

Villeneuve: Study design, statistical analyses, interpretation of results, critical revision of the manuscript.

St-Onge F, Chapleau M, Breitner JCS, Villeneuve S, Pichet Binette A, for the Alzheimer's Disease Neuroimaging Initiative. (2024) **Tau accumulation and its spatial progression across the Alzheimer's disease spectrum**. *medRxiv*. 2023.06.02.23290880; doi: <https://doi.org/10.1101/2023.06.02.23290880> (Preprint accepted to Brain Communications)

St-Onge, Pichet Binette: Study design, code writing, statistical analyses, interpretation of results, drafting of manuscript, critical revision of the manuscript.

Chapleau: Statistical analyses, critical revision of the manuscript.

Breitner: Critical revision of the manuscript.

Villeneuve: Study design, interpretation of results, drafting of manuscript, critical revision of the manuscript.

VI – Other contributions

During my studies, I contributed to various scientific projects both within and outside of my laboratory. Below is a list of past and ongoing projects in which I contributed, as well as a detailed summary of my implication.

A. – Publications

Below is a list of scientific publications to which I contributed.

A.1 – Villeneuve Lab publications

1. Strikwerda-Brown C, Hobbs DA, Gonneaud J, **St-Onge F**, Binette AP, Ozlen H, Provost K, Soucy JP, Buckley RF, Benzinger TLS, Morris JC, Villemagne VL, Doré V, Sperling RA, Johnson KA, Rowe CC, Gordon BA, Poirier J, Breitner JCS, Villeneuve S; PREVENT-AD, HABS, and AIBL Research Groups. (2022) **Association of Elevated Amyloid and Tau Positron Emission Tomography Signal With Near-Term Development of Alzheimer Disease Symptoms in Older Adults Without Cognitive Impairment.** *JAMA Neurology*, 79(10), 975-985. doi: 10.1001/jamaneurol.2022.2379

In this paper, I created a figure illustrating both amyloid- and tau-PET uptake for a few of our participants. I also critically revised the manuscript's initial draft and after the scientific revisions.

2. Ozlen H, Pichet Binette A, Köbe T, Meyer PF, Gonneaud J, **St-Onge F**, Provost K, Soucy JP, Rosa-Neto P, Breitner J, Poirier J, Villeneuve S; for the Alzheimer's Disease Neuroimaging Initiative, the Harvard Aging Brain Study and the Presymptomatic Evaluation of Experimental or Novel Treatments for Alzheimer Disease Research Groups. (2022) **Spatial Extent of Amyloid- β Levels and Associations With Tau-PET and Cognition.** *JAMA Neurology*, 79(10), 1025-1035. doi: 10.1001/jamaneurol.2022.2442.

In this publication, I created a figure illustrating the amyloid-PET uptake for a few of the included participants. I also contributed statistical advice during the project conception. Finally, I critically and editorially revised the manuscript.

3. Yakoub Y, Ashton NJ, Strikwerda-Brown C, Montoliu-Gaya L, Karikari TK, Kac PR, Gonzalez-Ortiz F, Gallego-Rudolf J, Meyer PF, **St-Onge F**, Schöll M, Soucy JP, Breitner JCS, Zetterberg H, Blennow K, Poirier J, Villeneuve S; PREVENT-AD Research Group. (2023) **Longitudinal blood biomarker trajectories in preclinical Alzheimer's disease.** *Alzheimer's & Dementia*. doi: 10.1002/alz.13318.

In this paper, I contributed statistical advice and code on multiple analyses. I also collected some of the cognitive data. Finally, I critically revised the manuscript.

4. Ourry V, Pichet Binette A, **St-Onge F**, Strikwerda-Brown C, Chagnot A, Poirier J, Breitner J, Arenaza-Urquijo Eider, Rabin JS, Buckley R, Gonneaud J, Marchant NL, Villeneuve S. (2023) **How do modifiable risk factors affect Alzheimer's disease pathology or mitigate its effect on clinical symptom expression?** *Biological Psychiatry*. doi: 10.1016/j.biopsych.2023.09.003.

In this review, I created the main figure summarizing the link between lifestyle factors during the lifespan and biological mechanisms explaining their functions. I also contributed editorial and critical advice on the manuscript's initial draft and revisions.

5. Qiu T, Liu ZQ, Strikwerda-Brown C, **St-Onge F**, Pichet Binette A, Descoteaux M, for the PREVENT-AD Research Group. (In revision) **Diffusion MRI subnetwork efficiency is associated with cognitive resilience to AD pathology in cognitively unimpaired older adults at risk of AD dementia.** *Alzheimer's & Dementia*.

I participated in the design of the study, critically revised the abstract and will critically revise the article.

6. Mohammedyan B, Baril AA, **St-Onge F**, Ourry V, Carrier J, Breitner J, Poirier J, Villeneuve S, PREVENT-AD Research Group. (In preparation) **Sleep Quality and Day-to-Day Variability: Relation to Alzheimer's pathology in Cognitively Unimpaired Older Adults At-Risk of AD Dementia.**

In this paper in preparation, I contributed study design and statistical advice. I will also critically revise the manuscript.

7. Strikwerda-Brown C, **St-Onge F**, Yakoub Y, Ozlen H, Pichet Binette A, Breitner J, Villeneuve S, PREVENT-AD Research Group. (In preparation) **Associations between psychological factors, grey matter volume, and resistance and resilience to tau pathology in cognitively unimpaired older adults.** *Alzheimer's & Dementia*. 2022 Dec. (Project presented at AAIC 2022)

This project was initially presented at the Alzheimer's Association International Conference in 2022 and the article is in preparation. I was involved in the study design and statistical methods. I also critically revised the published abstract and will critically revise the article once completed.

8. Pichet Binette A, Gonneaud J, Tremblay-Mercier J, Ozlen H, **St-Onge F**, McSweeney M, Köbe T, Meyer PF, Gallego J, Strikwerda-Brown C, Remz J, Bedetti C, Madjar C, Das S, Vachon-Preseu E, Marchant N, Collins L, Rajah MN, Tardif C, Baillet S, Poline JB, Evans MAC, Chakravarty MM, Spreng RN, Breitner J, Poirier J, Villeneuve S, for the PREVENT-AD Research Group. (In preparation) **PREVENT-AD Stage 2 data repository: neuroimaging, behavioral and follow-up cognitive data in older adults at risk of Alzheimer's disease.**

Article in preparation. I participated in the data collection for the PREVENT-AD. This included recruiting participants, coordinating positron emission tomography visits, (lifestyle, positron emission tomography, magnetic resonance imaging and the cognition data), data preprocessing workflow (positron emission tomography), data organization and critical revision of the manuscript. I also set up tutorials for future students on how to use the preprocessing workflow.

A.2 – Papers from collaborators

I am actively collaborating on two projects outside the laboratory which resulted in scientific publications. Below are the details of the articles as well as a description of my implication in each.

9. Savignac C, **St-Onge F**, Villeneuve S, Badhwar A, Gagliano Taliun SA, Farhan S, Geddes M, Iturria Medina Y, Poirier J, Spreng RN, Bzdok D, for the PREVENT-AD Research Group. (In revision) **Parent-of-origin effects in Alzheimer's liability dissociate neurocognitive and cardiovascular traits in at-risk individuals.**

In this project, I was responsible for providing advice on the data structure of the PREVENT-AD dataset, as well as providing general advice on clinical interpretation of the results in the context of Alzheimer's disease. I also critically revised the manuscript.

10. Tremblay C, Rahayel S, Pastor-Bernier A, **St-Onge F**, Vo A, Rheault F, Daneault V, Morys F, Rajah N, Villeneuve S, Dagher A, the PREVENT-AD Research Group & the Alzheimer's Disease Neuroimaging Initiative. **Pattern and Mechanisms of Atrophy Progression in Individuals with a Family History of Alzheimer's Disease: A Comparative Study** (Manuscript in preparation)

In this project, I was responsible for preprocessing positron emission tomography data from the Alzheimer Disease Neuroimaging Initiative and doing quality control on the resulting images. I also drafted a part of the methods section on the collection and processing of positron emission tomography data, and I revised the final manuscript.

B. – Scientific consulting

During my program, I also provided scientific counsel to different research teams for projects that have not resulted in publications at this time.

B.1 – Academia

- *Judes Poirier's laboratory (McGill University)*

I provided scientific advice to two students from the laboratory, mostly related to the data structure organization of the PREVENT-AD and Alzheimer's Disease Neuroimaging Initiative. I also cleaned Alzheimer's Disease Neuroimaging Initiative cerebrospinal fluid data for analyses and provided statistical analysis advice.

- *Simon Ducharme's laboratory (McGill University)*

I preprocessed tau positron emission tomography data for 5 participants. I also provided training and supervision on how to preprocess magnetic resonance imaging and

positron emission tomography data. Finally, I advised them on interpreting tau positron emission data.

B.2 – Industry

- *Optina Diagnostics Inc. (Montreal, Canada)*

During my PhD, I worked as a data science consultant for Optina Diagnostics Inc. The goal of the company is to create diagnostic tools for Alzheimer's Disease using retinal scan biomarkers based on artificial intelligence. During this time, I took on multiple projects.

First, I undertook a literature review on the prevalence of amyloid pathology (measured with positron emission tomography) in cognitively unimpaired older adults, individuals with mild cognitive impairment and individuals with Alzheimer's disease. The review was included as part of a diagnostic tool application presented to the U.S. Food and Drugs Administration.

Second, I managed a research project on comparing amyloid positivity determined by a visual read from a neuroradiologist to a quantitative assessment of amyloid pathology in data collected by the company. The visual read assessment was used to train and test their diagnostic tool—an artificial intelligence algorithm—but the company wanted to verify whether a quantitative assessment (standardized uptake value ratios) could provide additional information on discrepant cases. This project was done in two distinct phases: First, they sent over 150 magnetic resonance imaging and 150 amyloid positron emission tomography scans from a multi-site study, which I preprocessed. Then, I created and proposed a statistical analysis plan for the comparisons. After incorporating feedback from the company, I did the analyses, which I presented in a report. Second, I

repeated this process with data collected from 128 participants from the PREVENT-AD cohort, which is presented in Annex XI of this thesis. Overall, the results guided the company by indicating that quantitative assessment of amyloid load would miss participants who are starting to accumulate amyloid but which isn't yet widespread through the brain.

Third, I participated in the set-up and recruitment of a clinical project to validate their tool. The goal was to recruit participants from the PREVENT-AD cohort to undergo a retinal scan and an amyloid positron emission tomography scan. I was responsible for creating the recruitment protocol, presenting the consent form to participants, coordinating the visits for the retinal and positron emission tomography scans, managing the financial aspects of the project, sending the clinical data to the company, and preprocessing the positron emission tomography data. A total of 146 participants who underwent both procedures were recruited over a one-year period; I participated in the recruitment and coordination of approximately 50 participants over 6 months and preprocessed the positron emission tomography data for all participants.

VII – List of Figures and Tables

Chapter 2

Table 2.1 – Demographics information	p.61
Figure 2.1 – Illustration of the methodology	p.62
Figure 2.2 – Unique connectomes across the lifespan, networks, and tasks	p.64
Figure 2.3 – Differences in self- and others-identifiability across the lifespan	p.66
Figure 2.4 – Distribution of nodes predicting self-identifiability across the brain	p.69
Figure 2.5 – Association between grey matter volume and self-identifiability	p.73
Supplementary Figure 2.1 – Fingerprint identification accuracy across the lifespan using different window parameters	p.117
Supplementary Figure 2.2 – Fingerprint identification accuracy, and self- and others-identifiability using a randomized subset of nodes	p.118
Supplementary Figure 2.3 – Fingerprint identification accuracy, and self- and others-identifiability using the Power atlas	p.119
Supplementary Figure 2.4 – Differences in self- and others-identifiability across the lifespan, excluding the last decade	p.121
Supplementary Figure 2.5 – Association between self- and others-identifiability and age across the lifespan using product–moment-calculated functional connectivity	p.123
Supplementary Figure 2.6 – Model performance of elastic net models predicting self-identifiability from FC edges	p.125
Supplementary Figure 2.7 – Illustration of the connectome predictive modelling	p.126
Supplementary Figure 2.8 – Connectome predictive modelling performance and predictive edges of self-identifiability (Rest modality)	p.128

Supplementary Figure 2.9 – Connectome predictive modelling performance and predictive edges of self-identifiability (Task modality)	p.130
Supplementary Figure 2.10 – Illustration of the edge-wise intra-class correlation (ICC) methodology adapted from Amico & Goñi (2018)	p.132
Supplementary Figure 2.11 – Edge-wise contribution to self- and others-identifiability (window size = 100, step size = 40)	p.133
Supplementary Figure 2.12 – Nodal density of edges highly contributing to self-identifiability	p.135
Supplementary Figure 2.13 – Nodal density of edges highly contributing to others-identifiability	p.137
Supplementary Figure 2.14 – Average overlap between group-level and individual-level clustering of functional connectivity edges	p.139
Supplementary Figure 2.15 – Change in within- and between-individual variability in functional connectivity across the lifespan and across tasks	p.140
Supplementary Figure 2.16 – Association between BOLD signal amplitude and age across the lifespan	p.142
Supplementary Figure 2.17 – Association between BOLD signal amplitude and self-identifiability across the lifespan	p.144
Supplementary Figure 2.18 – Association between grey matter volume and others-identifiability	p.146
Supplementary Figure 2.19 – FC variability and grey matter associations	p.147
Supplementary Table 2.1 – McNemar tests comparing fingerprint identification accuracy obtained from within-network edges and between-network edges	p.149

Supplementary Table 2.2 – McNemar tests comparing the fingerprint identification accuracy between networks (within-network edges)	p.150
Supplementary Table 2.3 – McNemar tests comparing fingerprint identification accuracy from product-moment-derived FC and from partial correlation derived FC (within-network edges)	p.152
Supplementary Table 2.4 – McNemar tests comparing fingerprint identification accuracy from product-moment-derived FC and from partial correlation derived FC (between-network edges)	p.153
Chapter 3	
Figure 3.1 – Spatial extent methodology	p.165
Figure 3.2 – Amyloid and tau status in the cohort	p.171
Table 3.1 – Demographics information	p.175
Figure 3.3 – Spatial extent of abnormal tau deposition in amyloid positive participants of the ADNI cohort	p.177
Figure 3.4 – Spatial localization of abnormal tau accumulation over time in amyloid-positive participants of the ADNI cohort	p.180
Figure 3.5 – Association between tau-PET measures, and memory performance and decline	p.183
Figure 3.6 – Region-wise associations between regional tau-PET SUVR and cognitive performance and decline in participants with MCI and Alzheimer’s disease	p.187
Supplementary Figure 3.1 – Spatial extent of abnormal tau deposition and accumulation in amyloid negative participants of the ADNI cohort	p.211
Supplementary Figure 3.2 – Tau measures by amyloid and clinical status	p.213

Supplementary Figure 3.3 – Annual change in tau-PET measures	p.215
Supplementary Figure 3.4 – Heterogeneity in tau-PET spatial extent at baseline and longitudinally	p.216
Supplementary Figure 3.5 – Association between tau-PET measures, and executive functioning performance and decline	p.218
Supplementary Figure 3.6 – Association between tau-PET measures, and language performance and decline	p.220
Supplementary Figure 3.7 – Association between tau-PET measures, and visuospatial performance and decline	p.222
Supplementary Figure 3.8 – Association between tau measures and age	p.224
Supplementary Figure 3.9 – Amyloid and tau status in the cohort using thresholds from cognitively unimpaired A β - participants	p.225
Supplementary Figure 3.10 – Spatial extent using CU-based thresholds for abnormal tau deposition in amyloid-positive participants of the ADNI cohort	p.226
Supplementary Figure 3.11 – Association between spatial extent index derived from CU A β - thresholds, and cognitive performance	p.227
Supplementary Figure 3.12 – Association between spatial extent index derived from CU A β - thresholds, and cognitive decline	p.229
Supplementary Figure 3.13 – Comparison of spatial extent approaches	p.231
Supplementary Figure 3.14 – Spatial extent of tau abnormality in CU A β + participants at baseline	p.233
Supplementary Table 3.1 – Regional thresholds of tau positivity	p.234

Supplementary Table 3.2 – Regional thresholds of tau positivity based on 2 standard deviation from cognitively unimpaired A β - participants	p.235
Supplementary Table 3.3 – Regional tau abnormality across regions of interest	p.236
Supplementary Table 3.4 – Regional tau abnormality progression across regions of interest	p.237
Supplementary Table 3.5 – Braak stages thresholds	p.238

Annexes

Figure X.I – Illustration of sihnpy’s modules	p.290
Figure 1 - Presentation of the method used to derive SUVR-based measures	p.322
Table 1 – Demographic information	p.323
Figure 2 – Comparison of SUVR methods and visual readings	p.325
Table 2 – Optimal amyloid thresholds	p.326
Table 3 – False positive and false negative participants’ characteristics	p.327
Figure 3 – Reader agreement by the amount of amyloid	p.328
Figure 4 – Localization of amyloid by agreement	p.330
Figure 5 – Longitudinal change in visual reading status	p.332

VIII – List of Abbreviations

A β : Amyloid beta

AD: Alzheimer's disease

ADNI: Alzheimer's Disease Neuroimaging Initiative

AIC: Akaike Information Criterion

AV-1451: Flortaucipir

BOLD: Blood-oxygen-level-dependent

Cam-CAN: Cambridge Center for Aging and Neuroscience

CU: Cognitively unimpaired

FC: Functional connectivity

FDR: False discovery rate

fMRI: Functional magnetic resonance imaging

GMM: Gaussian Mixture Modelling

ICC: Intraclass correlation

MCI: Mild cognitive impairment

MNI: Montreal Neurological Institute

MRI: Magnetic resonance imaging

PET: Positron emission tomography

ROI: Region of interest

RMSE: Root mean square error

SUVr: Standardized uptake value ratio

TDP-43: TAR DNA-binding protein 43

Chapter 1 – Introduction

1.1 – Objectives and hypotheses

The main objective of this thesis was to study multimodal interindividual differences in the brain across the lifespan in a cognitively unimpaired population and in the context of Alzheimer's disease. To do so, we conducted two studies.

Chapter 2 – Functional connectome fingerprinting across the lifespan

In this study, we aimed to describe interindividual differences in the brain across the lifespan of cognitively unimpaired individuals. Specifically, we aimed to:

2.A – Characterize fingerprint stability across the lifespan

- Our main hypothesis for this objective was that, as functional brain fingerprints are stable over years in the literature, we expected that fingerprints would remain relatively stable across the lifespan.

2.B – Determine which regions contribute to fingerprints across the lifespan

- Previous literature consistently identified the frontoparietal and default-mode networks as being the main drivers of accurate fingerprints. As such, we expect these networks to be driving identifiability in our analyses as well.

2.C – Study the association between fingerprints and other age-related markers

- As brain anatomy varies with increasing age, we expected fingerprint measures to be associated with age-related brain volume.

Chapter 3 - Tau accumulation and its spatial progression in the late onset

Alzheimer's disease spectrum

Next, we investigated whether and to which extent interindividual differences influenced our understanding of the accumulation of tau pathology in Alzheimer's disease, and whether accounting for these differences could have a clinical impact. Specifically, we aimed to:

3.A – Characterize global tau-PET heterogeneity cross-sectionally and longitudinally

- As the literature highlights different patterns of tau spreading subtypes, we expected heterogeneity at the individual level in tau-PET patterns.

3.B – Compare group- to individual-level tau-PET in its association with cognition

- Individualized measures of tau-PET would improve association with cognition as they account for different affected regions in each individual

3.C – Study in which region tau-PET signal is associated with cognition

- As different clinical variants of AD would show different patterns of tau-PET, regional tau-PET associated with cognition would differ across cognitive domains

1.2 – Alzheimer’s disease dementia

1.2.1 – Epidemiology

Alzheimer’s disease (AD) dementia is a highly prevalent neurodegenerative disorder, with 10% of older adults over 65 years of age currently diagnosed with AD dementia in Canada. This prevalence is estimated to triple by 2040 as the population continues to age (Alzheimer’s Society of Canada, 2022). Worldwide, about 44 million people suffer from AD dementia, and it is currently the fifth leading cause of death (Nichols et al., 2019). The disease doesn’t only affect patients but also imposes an enormous burden on healthcare systems and families. In Canada alone, a total of 472 million hours are dedicated to informal caregiving for patients with dementia, the equivalent of 227,211 full-time jobs (Alzheimer’s Society of Canada, 2022). This added burden on families means less contribution to the workforce but also increased physical and psychological burden to families (Alzheimer’s Association, 2023). These estimates emphasize the importance of better understanding AD dementia and its progression to help curb this massive public health burden.

1.2.2 – Clinical and neuropsychological profile

Most patients with AD dementia will present with episodic memory impairments, i.e., recalling information related to their everyday life (McKhann et al., 2011; Weintraub et al., 2012). This impairment will progress to multiple cognitive domains as the disease develops, affecting nearly all cognitive functions (Scheltens et al., 2021; Weintraub et al., 2012) and, consequently, impairing daily living activities (McKhann et al., 2011). Progression of AD dementia is usually considered to be slow; one of the primary diagnostic criteria is that symptoms progress over years, not weeks or months (McKhann

et al., 2011). On average, patients will usually spend ten years with the diagnosis, seven of which with moderate to severe disability (Arrighi et al., 2010).

1.2.3 – Pathological presentation

A diagnosis of AD dementia cannot be made based on clinical presentation alone as different disorders can present with similar symptoms: only a neuropathological diagnosis can confirm whether the disease is definitely AD dementia (McKhann et al., 2011; Scheltens et al., 2021).

The main pathological hallmarks of AD are extracellular amyloid-beta ($A\beta$) plaques and intracellular tau neurofibrillary tangles (Bloom, 2014; Hardy & Selkoe, 2002). $A\beta$ plaques tend to aggregate extracellularly over a long period of time before symptoms occur (Bateman et al., 2013; Jack et al., 2013). As plaques accumulate, they subtly affect synapses and transmission of information, causing injury to neurons—and more specifically synapses—over time. These injuries, in turn, alter kinase and phosphatase activities within the neuron, causing the formation of hyperphosphorylated tau tangles intracellularly. Over time, the accumulation of tau causes neuronal death and, ultimately, cognitive symptoms as neurons die (Bloom, 2014; Hardy & Selkoe, 2002).

Both pathologies accumulate in their specific stereotypical patterns. $A\beta$ plaques accumulate mostly following the Thal phases: plaques start in the neocortex before spreading to the diencephalic nuclei, striatum and other subcortical structures, and finally progressing to the cerebellum and brainstem (Braak & Braak, 1991; Montine et al., 2012; Thal et al., 2002). Tau tangles follow the Braak stages: they accumulate more focally at first within small structures of the middle temporal lobe—specifically the rhinal and

entorhinal cortices—before progressing to other temporal and frontal lobe structures, and finally, to the rest of the associative cortex (Braak & Braak, 1991; Montine et al., 2012).

1.2.4 – Measuring AD pathology in vivo

Neuropathological assessment requires a brain biopsy, which can only be performed upon a patient's death. In the past few decades, several methods have been developed to find a solution to this problem, including measuring the pathology from cerebrospinal fluid, plasma or through molecular imaging such as positron emission tomography (PET).

Using a lumbar puncture, we can collect cerebrospinal fluid from participants which contains information on the level of amyloid (e.g., $A\beta_{40}$, $A\beta_{42}$) and tau (e.g., p-tau) in the brain with high accuracy matching autopsy-confirmed diagnoses (Mattsson-Carlgrén et al., 2022). Cerebrospinal fluid markers also show good predictive power to identify future clinical progression to MCI or AD (Salvadó et al., 2023), making them key markers for diagnosing AD already a decade ago (McKhann et al., 2011). However, in a few cases, participants can experience side effects including headaches, hematoma and pain at the puncture site, and in very rare cases, infection or subdural hematoma (Engelborghs et al., 2017). Partly for these reasons and for the invasiveness of the procedure, many participants are resistant to undergoing lumbar puncture (Tsvetkova et al., 2017).

In more recent years, plasma markers have been developed to measure $A\beta$ and tau pathology in-vivo using a simple blood draw, negating most of the potentially negative effects of lumbar puncture and at a lower cost. While they are still being validated for the clinic, promising use include ruling out AD in symptomatic participants with low $A\beta$ pathology, identifying participants with elevated plasma markers without cognitive

symptoms for inclusion in clinical trials and, potentially, diagnosing AD by replacing cerebrospinal fluid or PET (Blennow et al., 2023). However, evidence is still lacking on these potential uses, particularly for the diagnosis of AD (Hansson et al., 2022). Still, evidence is mounting on the utility of these markers at the preclinical stage. For instance, recent work from our group showed that the plasma marker ptau181 is altered in individuals with high levels of cerebral amyloid and tau but with no cognitive symptoms (Yakoub et al., 2023).

However, a key information missing from cerebrospinal fluid or plasma markers is the spatial localization of the pathology. Positron emission tomography (PET) allows us to bridge this gap. By tagging pathological proteins in the brain with a radioactive tracer, both A β and tau can be imaged in vivo using PET. A β was first imaged using the Pittsburgh Compound-B (Klunk et al., 2004) almost two decades ago. Since then, many different tracers have been developed to tag A β in vivo and many studies have replicated the Thal stages of A β neuropathology deposition with initial deposits seen in the neocortex followed by subcortical structures (Fantoni et al., 2020; Jagust, 2018; Thal et al., 2018). More recently, tau pathology can be imaged in-vivo using the AV-1451 tracer (Lowe et al., 2016; Marquié et al., 2015) and largely replicates the Braak stages observed in neuropathological assessments (Lowe et al., 2016; Schöll et al., 2016; Therriault, Pascoal, Lussier, et al., 2022). There is also in vivo evidence of both A β and tau following the A β cascade hypothesis, with initial deposits of A β , followed by tau and neurodegeneration. (Guo et al., 2021).

In addition to replicating neuropathological observations relatively well, measuring pathology using PET has many other advantages. First, PET can measure accumulation

in real-time during life in individuals rather than only once upon death (Bollack et al., 2023; Fantoni et al., 2020). Second, PET has a higher spatial resolution compared to neuropathology assessments, leading to a more precise spatial and temporal ordering of the pathology progression (Grothe et al., 2017; Villeneuve et al., 2015). Third, PET imaging can be combined with other brain imaging modalities to better understand different aspects of the disease. For example, functional and structural connectivity has been used to explain the spread of pathology in the brain (Vogel et al., 2020). Structural imaging can also allow tracking neurodegeneration—i.e., atrophy—concurrently as pathology accumulates (Jagust, 2018). In fact, these advantages have slowly pushed PET biomarkers to be an integral part of the research field toward a primarily biological definition of AD (Jack et al., 2018), though clinical measures in combination with PET are still recommended to properly assess the disease (Dubois et al., 2021). PET A β biomarkers are also making slow headway in the clinic as a tool to help clinicians distinguish AD dementia from other disorders (Rabinovici et al., 2019).

However, PET is not a perfect tool, and some limitations need to be acknowledged. First, off-target binding—i.e., the binding of PET tracers to brain regions with no pathology—is relatively common, particularly for the tau tracer AV-1451 (Marquié et al., 2015). This forces the exclusion of some important regions from the analyses (e.g., hippocampus). Second, there are differences between different commercial scanners and PET tracers making comparisons more difficult across studies, though some efforts to harmonize PET results across sites have been pushed forward in recent years (Klunk et al., 2015; Villemagne et al., 2023). Third, while the match between neuropathology and PET is concordant, there is some mismatch between the two, making comparisons

sometimes difficult (Fantoni et al., 2020; Lowe et al., 2016). Finally, access to PET imaging is unequal. Many countries do not have access to PET scanners, and even fewer have access to cyclotron facilities to produce the tracers necessary for A β and tau imaging (Gallach et al., 2020).

1.3 – Heterogeneity in Alzheimer’s disease

Up to now, most of the description of AD included generalized observations across individuals: patients usually present with episodic memory impairment, caused by specific patterns of A β and tau accumulation, which can be measured in vivo using PET. However, in recent years, more evidence has emerged that AD dementia is heterogenous, with many different presentations and potential causes.

1.3.1 – Clinical heterogeneity

While participants with AD will present with episodic memory impairment, up to 30% of patients with AD will present with a different cognitive impairment as their primary complaint (Qiu et al., 2019). In fact, it is now well established that AD dementia can present under four different clinical phenotypes: classical amnesic type, logopenic primary progressive aphasia variant, behavioural/dysexecutive and posterior cortical atrophy. (Graff-Radford et al., 2021; Ossenkoppele et al., 2015) In the logopenic primary progressive aphasia variant, patients present with single-word aphasia and/or sentence repetition impairment. Their symptoms frequently overlap with other forms of primary progressive aphasia traditionally associated with frontotemporal dementia (Gorno-Tempini et al., 2011) or symptoms associated with stroke (Graff-Radford et al., 2021). In the behavioural/dysexecutive variant, participants will often present with apathy, loss of

social convention, disinhibition, and various executive functioning impairments. Their symptoms frequently overlap with the behavioural variant of frontotemporal dementia (Ossenkoppele et al., 2021; Rascovsky et al., 2011). In posterior cortical atrophy, patients will mostly present with visuospatial complaints, such as spatial or object perception issues, dyscalculia, dysgraphia, or difficulties reading. These patients are often diagnosed with functional issues such as visual impairment rather than neurological issues. Overall, clinical diagnosis of AD dementia is complicated by the frequent symptoms outside of classical memory impairment.

1.3.2 – Pathological heterogeneity

While A β and tau are the main culprits behind AD, only about a third of patients with clinical AD dementia symptoms will exclusively have pathological A β and tau in their brain (Robinson et al., 2018): many other pathologies, such as vascular injuries (Attems & Jellinger, 2014; Mehta & Schneider, 2021), TDP-43 (Bejanin et al., 2019) and alpha-synuclein (Boyle et al., 2019) frequently co-occur and play a role in the cognitive profile (Boyle et al., 2019) and the atrophy pattern (Boyle et al., 2019) occurring in AD. Unfortunately, most of these co-pathologies cannot be measured in vivo yet, complicating the understanding of their impact during disease progression. For now, it is important to consider these pathologies as potential sources explaining the variability observed in AD.

However, even in patients who only present with “pure” pathological profiles (i.e., only A β and tau at death), only 60% present memory impairment as the predominant symptom (Bertoux et al., 2020). As such, even with “homogenous” pathological profiles, cognitive profiles may strongly differ across participants.

1.3.3 – *Spatial heterogeneity in imaging*

One possible explanation for “pure” pathological profiles at death presenting different cognitive profiles is that neurodegeneration accrues in spatially distinct regions across participants. Multiple data-driven studies have demonstrated different subtypes of atrophy patterns in AD patients (Sintini et al., 2019; Young et al., 2018) leading to different clinical AD variants (Lehmann et al., 2013) and different cognitive profiles (Ferreira et al., 2020; Ossenkoppele et al., 2020; N. Sun et al., 2019). However, neurodegeneration occurs quite late in the classical A β cascade hypothesis. Logically, patterns of A β and tau accumulation, occurring before atrophy, should also be heterogeneous across individuals.

A β has long been considered to accumulate in a homogeneous, widespread manner throughout the brain (Grothe et al., 2017; Mattsson et al., 2019; Villeneuve et al., 2015), even in other clinical variants of AD (La Joie et al., 2020). Yet, recent evidence points to different A β spreading subtypes across individuals (Collij et al., 2022; Y. Sun et al., 2023). However, higher A β accumulation does not consistently reflect subsequent cognitive decline (Parent et al., 2023), and associations between A β and cognition remain weak, even in patients with advanced AD (Jagust, 2018; Ossenkoppele et al., 2018). Measuring tau pathology tends to be more discriminative than measuring A β or atrophy (Ossenkoppele et al., 2018). In fact, it is once A β and tau pathology both become abnormal that the risk for subsequent cognitive decline increases the most (Ossenkoppele et al., 2022; Strikwerda-Brown et al., 2022).

As described before, tau pathology was also originally thought to follow relatively homogenous patterns measured with PET, following the Braak stages (Lowe et al., 2016;

Schöll et al., 2016; Therriault, Pascoal, Lussier, et al., 2022). Yet, persuasive evidence is emerging that tau-PET patterns are not uniform across individuals. For instance, the different clinical variants of AD show distinct tau-PET patterns, with logopenic primary progressive aphasia variant showing strong left lateralization, tau-PET uptake being the highest in the left temporal lobe (La Joie et al., 2020), posterior cortical atrophy showing highest uptake in the occipital and posterior parietal lobe (La Joie et al., 2020) and the behavioural/dysexecutive variant showing a widely heterogeneous pattern, mostly affecting the frontal lobe (Singleton et al., 2021). Multiple studies have also derived disease subtypes from tau-PET uptake, revealing different trajectories of tau accumulation not necessarily dependent on the clinical phenotype (Ossenkoppele et al., 2019; Therriault, Pascoal, Savard, et al., 2022; Vogel et al., 2021).

1.4 – Interindividual differences in neuroimaging

These observations of heterogeneity in AD echo growing evidence of heterogeneity measured in the brain from cohorts of cognitively unimpaired participants, suggesting that the heterogeneity observed in AD could originate from fundamental anatomical or functional differences. Anatomically, the brain shows substantial differences between individuals during development (T. T. Brown, 2017) and across the lifespan (Bethlehem et al., 2022), measured with grey matter volume or cortical thickness. These differences can be observed across the entire cortical mantle (Nadig et al., 2021).

Consequently, it is perhaps not surprising that the functional organization of the brain also differs substantially across individuals. Functional connectivity—measured with functional magnetic resonance imaging (fMRI)—is often used to infer the functional

organization of the brain in different networks that each have specific roles and functions (Sporns & Betzel, 2016). This is measured at the group level where brain organization is inferred to be shared across individuals and a label for a brain network is assigned to each of the brain's voxels to infer the brain organization (Schaefer et al., 2018).

Multiple studies demonstrated that the connectivity within these networks varies significantly between individuals in a gradient where higher associative cortex regions show the most variability and sensorimotor regions show the least (Gratton et al., 2018; Ma et al., 2021; Mueller et al., 2013). These patterns of variability are not static: they are influenced by the task undergone by an individual in the scanner, suggesting that brain activation in the face of the same task can be different between people (Geerligs et al., 2015; Gratton et al., 2018). Finally, despite similar networks being identified across studies, the voxels belonging to these networks vary between individuals (Betzel et al., 2019; Bijsterbosch et al., 2018; Xu et al., 2016). Even within a single imaging session, voxels show a remarkable degree of dynamic interindividual differences in terms of which brain network they are assigned to (Liao et al., 2017; Van De Ville et al., 2021).

1.4.1 – Brain fingerprints and their properties

These differences in the functional organization of the brain are of such magnitude that they can be leveraged to capture unique brain signatures that accurately distinguish an individual's brain from a larger cohort of participants. This concept is called “brain fingerprinting” (Airan et al., 2016; Amico & Goñi, 2018; Finn et al., 2015, 2017; Peña-Gómez et al., 2018; Tavor et al., 2016). A brain fingerprint is usually derived by correlating the functional connectivity—within a given network or across the brain—of an individual during a task or at rest to the functional connectivity pattern of the same individual during

a different task or at a different time (self-identifiability). Then, the functional connectivity of that individual is correlated to the functional connectivity pattern of all other individuals included in the study (others-identifiability). If the self-identifiability of a participant is higher than their average others-identifiability, it means that the functional connectivity pattern is unique enough to accurately identify a participant, i.e., fingerprint identifiability (Amico & Goñi, 2018; Finn et al., 2015).

Brain fingerprints possess many interesting properties. They can be identified across different fMRI tasks (Amico & Goñi, 2018; Finn et al., 2015, 2017; Vanderwal et al., 2017), though some tasks yield more reliable fingerprints than others (Finn et al., 2017), suggesting that individual responses to tasks may increase the ability to fingerprint. Brain fingerprints are also remarkably stable over time, whether scans are days (Finn et al., 2015; Jalbrzikowski et al., 2020), weeks (Horien et al., 2019; Hu et al., 2022; Menon & Krishnamurthy, 2019) or years apart (Horien et al., 2019; Jalbrzikowski et al., 2020; Miranda-Dominguez et al., 2017; Ousdal et al., 2020). They can also be reliably measured with scans taken across different imaging sites (Bari et al., 2019). Fingerprints also seem to be, at least in part, genetically determined; increased genetic similarity leads to similar fingerprint identifiability (Demeter et al., 2020) and brain fingerprints of monozygotic twins correlate with one another (Xu et al., 2016). They also seem to be restricted to specific areas of the brain, many studies indicate that the best identifiability stems from the frontoparietal (Airan et al., 2016; Demeter et al., 2020; Finn et al., 2015; Horien et al., 2019; Jalbrzikowski et al., 2020; Kaufmann et al., 2017; Waller et al., 2017) or default-mode (Airan et al., 2016; Demeter et al., 2020; Finn et al., 2015; Jalbrzikowski et al., 2020) networks. Opposingly, the sensorimotor areas have shown the worst identifiability

(Airan et al., 2016; Finn et al., 2015). This matches the areas with the most (frontoparietal) and the least (sensorimotor) interindividual differences in functional connectivity (Mueller et al., 2013). While most of the research focused on fMRI features, brain fingerprints have been shown to be remarkably stable across imaging modalities. Fingerprint identifiability has been demonstrated using many different structural measures, including cortical folding (Duan et al., 2020; Mansour et al., 2020), cortical thickness (Mansour et al., 2020; Valizadeh et al., 2018), grey matter volume (Valizadeh et al., 2018), grey matter surface area (Valizadeh et al., 2018) and structural connectivity (Mansour et al., 2020). More recently, fingerprint identifiability was also demonstrated with electrophysiological activity as measured with magnetoencephalography (da Silva Castanheira et al., 2021) and by using both structural and functional modalities at once (Griffa et al., 2022).

While fingerprints are reliably demonstrated across many studies, they can be strongly affected by several methodological choices. Poor scanner resolution (Horien et al., 2018), lower parcellation resolution (Airan et al., 2016; Finn et al., 2015), less acquisition time (Airan et al., 2016; Finn et al., 2017; Horien et al., 2018) and bigger sample sizes can also lead to less identifiability (Waller et al., 2017), though that last factor has not been reliably shown in the literature. Concurrently, methods increasing noise removal from brain imaging due to motion or other factors reliably increase the identifiability (Airan et al., 2016; Amico & Goñi, 2018; Horien et al., 2018). Overall, this suggests that more quality data on the brain tends to increase fingerprint identifiability.

1.4.2 – Aging and interindividual differences

The previous section presented brain fingerprints, which are unique, individual-specific, genetically determined signatures of brain anatomy or function that are stable

across tasks, over time and imaging modalities. This emphasizes just how much interindividual differences exist. Yet, there are still major research gaps in our understanding of brain fingerprints.

For instance, most studies presented until this point stem from a single homogenous population: young, healthy, educated, North American, white adults. (Airan et al., 2016; Horien et al., 2019; Jalbrzikowski et al., 2020; Peña-Gómez et al., 2018). In fact, much of the research on brain fingerprints stems from a single cohort: the Human Connectome Project (Amico & Goñi, 2018; Demeter et al., 2020; Finn et al., 2015, 2017; Griffa et al., 2022; Horien et al., 2018; Mansour et al., 2020; Menon & Krishnamurthy, 2019; Miranda-Dominguez et al., 2017; Tavor et al., 2016; Waller et al., 2017; Xu et al., 2016). The Human Connectome Project recruited approximately 1,200 young adults, including twins, aged between 22 and 35 years for a thorough imaging data collection with the explicit reasoning that these participants were at their most stable: they had reached the maximum brain development milestones and were not yet at risk of potential neurodegenerative processes. Furthermore, extensive screening was conducted to remove participants with major physical or mental health diagnoses (Van Essen et al., 2012, 2013). These studies reinforce the importance of interindividual differences as, even in this demographically homogenous population, important differences are found, but they also leave important gaps, such as what happens to these signatures when the brain undergoes important transformations.

The brain undergoes massive changes from birth until adulthood. Brain volume grows to nearly 80% of its adult size two to three weeks after birth, mostly due to grey matter change, with white matter developing more slowly throughout childhood (Gilmore

et al., 2018). The development of brain networks and structures also change during childhood and teenage before stabilizing in young adults (Váša et al., 2018), following relatively well-coordinated and shared patterns across individuals (Bethlehem et al., 2022; T. T. Brown, 2017; Raznahan et al., 2011). Yet, significant heterogeneity in brain structure and function is observed throughout the human development (T. T. Brown, 2017; Vanderwal et al., 2021). In fact, both cortical folding (Duan et al., 2020) and functional connectivity (Vanderwal et al., 2021) have been used to successfully identify brain fingerprints in children, even as young as two weeks from birth (Hu et al., 2022). However, research on the developing brain indicated that the components of fingerprints (e.g., self-identifiability) change during childhood, increasing until early adulthood before stabilizing (Kaufmann et al., 2017). As such, interindividual differences in the brain exist since birth, but their properties change during brain development (Bethlehem et al., 2022).

At the opposite end of the lifespan, the brain also massively changes during aging. The brain accrues significant atrophy with age, but most distinctly in the frontal lobe (Binette et al., 2020). Structural covariance (DuPre & Spreng, 2017) and structural connectivity (Betz et al., 2014) also tend to decrease with increasing age across the brain during the lifespan. Similarly, the brain exhibits numerous changes in functional organization in older adults. Many studies displayed a generalized decrease in within-network and increase in between-network connectivity in older adults (Betz et al., 2014; Chan et al., 2014; Chen et al., 2016; Chong et al., 2019; Setton et al., 2022).

However, little is known about interindividual differences in the brain in older adults. Studies on the topic indicate that, despite the widespread convergent brain changes observed across older adults, interindividual differences in the cortical thickness (Nadig

et al., 2021) and functional connectivity (Geerligs et al., 2015) increase during life. However, whether and how this affects brain fingerprints is unknown. Brain fingerprints represent an interesting measure as a proxy capturing interindividual differences in the brain. To use them in an aging population, however, we first must gain a better understanding of brain fingerprints across the entire lifespan in healthy populations. **As such, this thesis will first study the interindividual differences—measured through brain fingerprints—and verify whether they are preserved, or whether their properties change during the lifespan.**

1.5 – Interindividual differences and impact on AD clinical research

Despite the consistent demonstration of interindividual differences in the brain, their impact is unclear. If behaviours and disease patterns truly are shared across individuals, differences in brain structure and function observed across individuals may only represent measurement error or other idiosyncratic factors with negligible impact on measuring neurological phenomena (Mantwill et al., 2022).

Already, in cognitively unimpaired samples of younger adults, interindividual differences in the brain have been shown to be associated with cognitive performance including fluid intelligence (Bijsterbosch et al., 2018; Finn et al., 2015; Greene et al., 2018; Mansour et al., 2020), information integration (Liao et al., 2017) and motor capability (Ma et al., 2021). Interindividual differences in brain structure and function have also been linked to clinical measures such as drug and alcohol use (Bijsterbosch et al., 2018; Mansour et al., 2020) and mental health diagnoses (Kaufmann et al., 2017, 2018; Mansour et al., 2020). Specifically, less interindividual differences was associated with increased drug and alcohol use, and with increased severity of mental health diagnoses.

This preliminary evidence seems to point to interindividual differences being meaningful in explaining differences in behavioural measures and clinical diagnoses. This suggests that incorporating these differences in clinical measures could help better account for differences between participants, and consequently, offer more precise tools capturing the reality of individual patients.

Specifically in AD, a constellation of studies has consistently laid out common cognitive and pathological patterns for the disease. Yet, new robust evidence pushes the idea that participants actually present a myriad of cognitive and pathological patterns.

Most of the research on AD heterogeneity, however, focused on large group subtypes rather than on differences between individuals. Considering the high degree of interindividual differences even in the brain of cognitively unimpaired participants, we wanted to verify whether interindividual differences could help explain discrepancies between classical and newer conceptions of the disease, as an example of how measuring interindividual differences can help us better understand neurological disorders.

For example, a major conception of AD pathology progression in the brain involves the spread of the pathology along structural or, and particularly, functional brain networks (Franzmeier et al., 2020; Vogel et al., 2020). This idea gained a lot of traction due to convincing evidence of prediction of future pathology accumulation along these networks. However, there is still significant variability in these models which remains unexplained. One possible explanation is that these models discount interindividual differences and generated predictions from group-level networks, and neither did they account for differences in the patterns of tau pathology across individuals.

In the face of this evidence and with the evidence of interindividual differences on fMRI in the first objective, **as a second objective, this thesis aimed to verify whether accounting for interindividual differences can help better explain the accumulation of tau pathology in AD dementia across individuals and lead to stronger associations with cognition.**

1.6 – Measuring interindividual differences

A common theme in the literature presented so far is that research on the brain initially identifies broad universal patterns in brain imaging, with subsequent research indicating that these patterns show remarkable heterogeneity across individuals. For instance, many studies suggested that functional connectivity decreased in specific brain networks in older adults (Betzel et al., 2014), while subsequent research indicated that there is a lot of variability in the functional connectivity of older adults (Geerligs et al., 2015). Similarly, in the patterns of tau pathology in the brain during Alzheimer’s disease, research pointed to the Braak staging scheme as a universally shared pattern of tau spreading (Braak & Braak, 1991; Schöll et al., 2016) but recent research indicated that this patterns differs between individuals (Vogel et al., 2021).

From a theoretical point of view, studies directly accounting for interindividual differences from their inception could help understand both global and group-level neuroimaging patterns shared across individuals as well as understand how idiosyncratic (i.e., individual-level) differences play a role in explaining observed differences in the brain (Gratton et al., 2018). From a practical—and clinical—point of view, accounting for interindividual differences when studying diseases could also help develop personalized diagnoses and treatments adapted to the reality of each patient.

This is not a new idea, but rather the concept of personalized medicine (Schork, 2015; Whitcomb, 2012). The concept of personalized medicine was developed on many observations that traditional treatments developed in clinical trials show poor efficacy in their target population. For instance, only between 7 and 20% of patients using the highest-selling drugs in the United States for neurological disorders will experience

benefits using these medications (Schork, 2015). One reason for this is the reliance on the idea that, in patients sharing a clinical diagnosis, on average, at least some of them will respond to the drug as expected (Iturria-Medina et al., 2018). Yet, we know from the Alzheimer's disease literature that while patients can present the same clinical symptoms, they may have different underlying pathology patterns (Bertoux et al., 2020; Ferreira et al., 2020) and opposingly, different pathology patterns can lead to similar clinical symptoms (Robinson et al., 2018).

The widespread study of interindividual differences and personalized medicine hits multiple obstacles. Systemically, interindividual differences in neuroimaging are not included in study designs. Systematic review of brain imaging findings in the last decade pointed to less than 14% of studies reporting ethnicity and race information, and nearly 30% not reporting sex and gender information (Sterling et al., 2022). Furthermore, predictions of symptoms based on brain imaging variables are highly dependent on the diversity of the clinical sample included (Benkarim et al., 2022), highlighting that the lack of consideration for interindividual differences can be detrimental to the generalizability of clinical predictions. This issue is not limited to the reporting of these variables, but also to the inclusion of participants in clinical trials. For instance, older African Americans and Hispanics represent nearly 20% of the population in the United States—a proportion set to reach 30% by 2060 (Shaw et al., 2021). They are also 1.5 times more likely to develop dementia than non-Hispanic Whites (Alzheimer's Association, 2023). Yet, they only represent about 5% of the population recruited in neurology clinical trials (George et al., 2014). This lack of representation of diverse populations in trials could explain in part why treatments have so little efficacy in the general population (Schork, 2015). Similarly, this

could explain why fundamental associations between the brain and behaviours are difficult to replicate across studies unless a very large sample size is reached (Marek et al., 2022).

Some of the systemic issues mentioned above stem from a relatively practical issue: there is a lack of tools to study and account for interindividual differences. Many of the traditional and well-adopted methods in brain imaging assume that interindividual differences are noise rather than biologically meaningful (Ashburner, 2007; Brett et al., 2011; Poldrack et al., 2008). In response, many studies have developed resourceful methods to account for interindividual differences in recent years, including devising individual-specific predictors and measures, which treat individual differences as a main interest instead of noise. However, these methods are not easily accessible by the scientific community. The code to reproduce these methods is often not shared (e.g., (Franzmeier et al., 2020; Leuzy et al., 2023; Tijms et al., 2013)), or may lack explanations to fully reproduce (Nadig et al., 2021). Others may require advanced computing skills and extensive data on hand to run the analysis (Iturria-Medina et al., 2018). In all cases, there is often a lack of data to test the analysis and ensure comparability between teams. These practical issues were kept in mind during the conception and execution of both of this thesis' projects, and led to the creation of a Python package—study of interindividual heterogeneity of neuroimaging in Python (sihnp)—which is presented in the annex of this thesis and referred to by the following chapters.

1.7 – Interindividual differences beyond academic environments

Interindividual differences do not only exist in research study participants, but extend to the entire population. As such, interindividual differences should also be considered in industry research studying the brain. Through my work outside of academia during my thesis, I have used the tools I developed (specifically the spatial extent index) during my PhD to study and offer recommendations to a private company—Optina Diagnostics—doing private research on a medical device aimed at diagnosing Alzheimer’s disease. Results and recommendations from this study are presented in Annex of this thesis.

Chapter 2 – Functional connectome fingerprinting across the lifespan

Frédéric St-Onge^{1,2}, Mohammadali Javanray^{1,2}, Alexa Pichet Binette³, Cherie Strikwerda-Brown², Jordana Remz², R. Nathan Spreng^{2,4,5}, Golia Shafiei⁵, Bratislav Misic⁵, Étienne Vachon-Pressseau^{6,7,8}, Sylvia Villeneuve^{1,2,5}

1. Integrated Program in Neuroscience, Faculty of medicine, McGill University, Montreal, Canada
2. Research Center of the Douglas Mental Health University Institute, Montreal, Canada
3. Clinical Memory Research Unit, Faculty of Medicine, Lund University, Lund, Sweden
4. Department of Neurology and Neurosurgery, Montreal Neurological Institute, McGill University, Montreal, Canada
5. McConnell Brain Imaging Centre, Montreal Neurological Institute, McGill University, Montreal, Canada
6. Faculty of Dental Medicine and Oral Health Sciences, McGill University, Montreal, Canada
7. Department of anesthesia, Faculty of medicine, McGill University, Montreal, Canada
8. Alan Edwards Centre for Research on Pain (AECRP), McGill University, Montreal, Canada

2.1 – Preface

Individual differences in the brain are commonly reported across studies in functional connectivity (Mueller et al., 2013), so much so that functional connectivity patterns can be uniquely identified at the individual level to form functional connectome fingerprints (Finn et al., 2015). These fingerprints were extensively studied in younger adults, but less is known about their properties across the lifespan. The overall goal of this thesis is to study interindividual differences in the brain during the lifespan and Alzheimer’s disease. As the brains of individuals undergo massive group-level changes both during aging (Binette et al., 2020; Zonneveld et al., 2019) and Alzheimer’s disease (Binette et al., 2020), it is important to consider whether interindividual differences change during these processes and whether they impact other variables we associate with the brain. In this first project, we first assess interindividual differences using functional connectivity across the entire lifespan in 483 cognitively unimpaired individuals, spanning 18 to 87 years of age from the Cam-CAN cohort (Taylor et al., 2017). These findings were published in *Network Neuroscience* in the October 2023 issue.

2.2 – Abstract

Systematic changes have been observed in the functional architecture of the human brain with advancing age. However, functional connectivity (FC) is also a powerful feature to detect unique “connectome fingerprints”, allowing identification of individuals among their peers. Although fingerprinting has been robustly observed in samples of young adults, the reliability of this approach has not been demonstrated across the lifespan. We applied the fingerprinting framework to the Cambridge Centre for Aging and Neuroscience cohort (n=483 aged 18 to 89 years). We found that individuals are “fingerprintable” (i.e., identifiable) across independent functional MRI scans throughout the lifespan. We observed a U-shape distribution in the strength of “self-identifiability” (within-individual correlation across modalities), and “others-identifiability” (between-individual correlation across modalities), with a decrease from early adulthood into middle-age, before improving in older age. FC edges contributing to self-identifiability were not restricted to specific brain networks and were different between individuals across the lifespan sample. Self-identifiability was additionally associated with regional brain volume. These findings indicate that individual participant-level identification is preserved across the lifespan despite the fact that its components are changing non-linearly.

2.3 – Introduction

The structural and functional organization of the brain is reliably consistent within species due to strong genetic control of this biological system (Gómez-Robles et al., 2015). In humans, however, substantial intra-individual variability has been found at a fine-grained level (Amico & Goñi, 2018; Finn et al., 2015; Mansour et al., 2020; Mueller et al., 2013). An emerging body of evidence suggests that inter-individual differences in brain connectomes are sufficient to match brain scans and effectively identify individuals among large datasets of brain images. These “signatures” or “fingerprints” (Finn et al., 2015, 2017) are stable over years (Guo et al., 2012; Horien et al., 2019; Jalbrzikowski et al., 2020; Ousdal et al., 2020), between scan conditions (Finn et al., 2015, 2017; Vanderwal et al., 2017) and are found using other brain scanning modalities such as magnetoencephalography (da Silva Castanheira et al., 2021). Individual participant identifiability is observable in homogeneous samples of young adults (Finn et al., 2015; Mueller et al., 2013), yet older adults have been relatively neglected in the literature.

Cross-sectional studies comparing older and younger adult groups have revealed substantial differences in FC (Chen et al., 2016; Setton et al., 2022; Zonneveld et al., 2019), raising questions about the reliability of FC fingerprinting in older adults. Our aims were to (i) test the stability of fingerprint identification accuracy (i.e., uniqueness of the connectomes, which facilitates individual participant identification), (Finn et al., 2015) (ii) determine self-identifiability (i.e., a continuous variable measuring within-individual similarity across independent observations) (Amico & Goñi, 2018) and (iii) characterize others-identifiability (i.e., a continuous variable measuring how similar an individual is relative to others). (Amico & Goñi, 2018) These aims were examined across the lifespan,

spanning the full connectome, as well as within and between large-scale networks, using functional magnetic resonance imaging (fMRI). We then determined which functional connections between regions (i.e., edges) reliably contributed to identification and how these patterns varied across the lifespan. Finally, we explored the association between identifiability and brain volume, a significant predictor of participant age (Gonneaud et al., 2021). We derived fingerprint metrics using a pair of fMRI conditions (resting-state and sensorimotor task) from cognitively healthy adults across the lifespan in the Cambridge Centre for Aging and Neuroscience (Cam-CAN) cohort (n = 483; ages 18-89y) (Shafto et al., 2014; Taylor et al., 2017). Our results indicate that fingerprint identifiability is a reliable metric across the lifespan. We also show that self- and others-identifiability measures had non-linear distributions across the lifespan. Self- and others-identifiability was high in young adults, decreased into middle-age, then increased again into older adulthood. Elastic net models revealed that the fingerprinting methodology identifies dominant individual-specific features of FC, reliably demarcating unique patterns for each healthy adult at each decade of life. Finally, self-identifiability, but not others-identifiability, was associated with brain volume in regions known to atrophy in the context of normative aging. Overall, the results suggest that intra-individual variability in the organization of the human brain, particularly in older adults, warrants consideration in parallel with normative trajectories of age-related brain change.

2.4 – Results

Analyses were performed on 483 individuals of the Cam-CAN cohort (Shafiq et al., 2014; Taylor et al., 2017) aged 18 to 89 years. Participants were included if they had at least two fMRI scans (Rest and Sensorimotor Task modalities) passing quality control. Demographic information is presented in Table 2.1. About half of our sample was composed of females. Most participants were right-handed. The final sample comprised at least 50 individuals in each decade of life, except individuals between 80-89 years of age, with only 34 included participants.

2.4.1 - Fingerprint identification accuracy in a lifespan cohort

To test the stability of the fingerprint metrics of interest (fingerprint identification accuracy, self-identifiability and others-identifiability; Finn et al., 2015), we correlated the FC pattern of a given individual to their own FC pattern across Rest and Task conditions (self-identifiability) and to the FC pattern of all other individuals (others-identifiability; Amico & Goñi, 2018). If the self-identifiability correlation coefficient was stronger than any of the others-identifiability correlation coefficient, then the participant was identified as having a unique signature (fingerprint identification accuracy). This method is illustrated in Figure 2.1A. Edges used in the identification paradigm and the rest of the analyses comprised the whole brain connectome, edges within a given network (within-network edges), and edges between a given network and all other network nodes (between-network edges). We used the Schaefer parcellation with 400 nodes (Schaefer et al., 2018) and Yeo's 7-network solution (Yeo et al., 2011) to derive the FC and to compute the fingerprint metrics. Results were also replicated using the Power parcellation (264 nodes; Supp Fig 2.3A) (Power et al., 2011).

Table 2.1 – Demographics information

Decades of age	18-29 (n = 71)	30-39 (n = 88)	40-49 (n = 95)	50-59 (n = 68)	60-69 (n = 71)	70-79 (n = 56)	80-89 (n = 34)	Overall (n = 483)
Variables								
Sex (F)	40	43	50	34	30	27	15	239
Sex (M)	31	45	45	34	41	29	19	244
	Mean (SD)							
Age	25.00 (3.50)	34.83 (2.64)	44.54 (3.06)	54.51 (2.89)	64.45 (2.84)	75.16 (2.97)	83.06 (2.39)	50.49 (18.24)
Handedness	75.01 (49.57)	78.08 (48.75)	74.22 (55.35)	75.91 (54.06)	77.15 (52.92)	85.09 (42.77)	86.53 (36.06)	77.82 (50.12)
Motion (mm) (Rest)	0.175 (0.048)	0.173 (0.047)	0.196 (0.057)	0.203 (0.050)	0.221 (0.041)	0.235 (0.047)	0.238 (0.046)	0.201 (0.054)
Motion (mm) (Task)	0.153 (0.044)	0.147 (0.042)	0.170 (0.051)	0.182 (0.049)	0.198 (0.046)	0.209 (0.047)	0.230 (0.052)	0.178 (0.053)
Number of frames (Rest)	238.06 (31.14)	246.08 (26.66)	230.31 (34.58)	227.62 (32.12)	223.28 (41.48)	211.82 (38.74)	205.88 (38.79)	229.05 (36.23)
Number of frames (Task)	242.18 (29.75)	247.85 (20.68)	237.46 (28.61)	234.29 (26.11)	233.41 (32.38)	215.39 (39.24)	200.44 (43.10)	233.84 (32.90)

Handedness was measured as a continuous variable from -100 (fully left-handed) to 100 (full right-handed). Motion is reported as the average frame displacement for each modality. The number of frames is the number of fMRI frames remaining after removing frames with excessive motion. Counts are presented for categorical data while average and standard deviation are presented for continuous data.

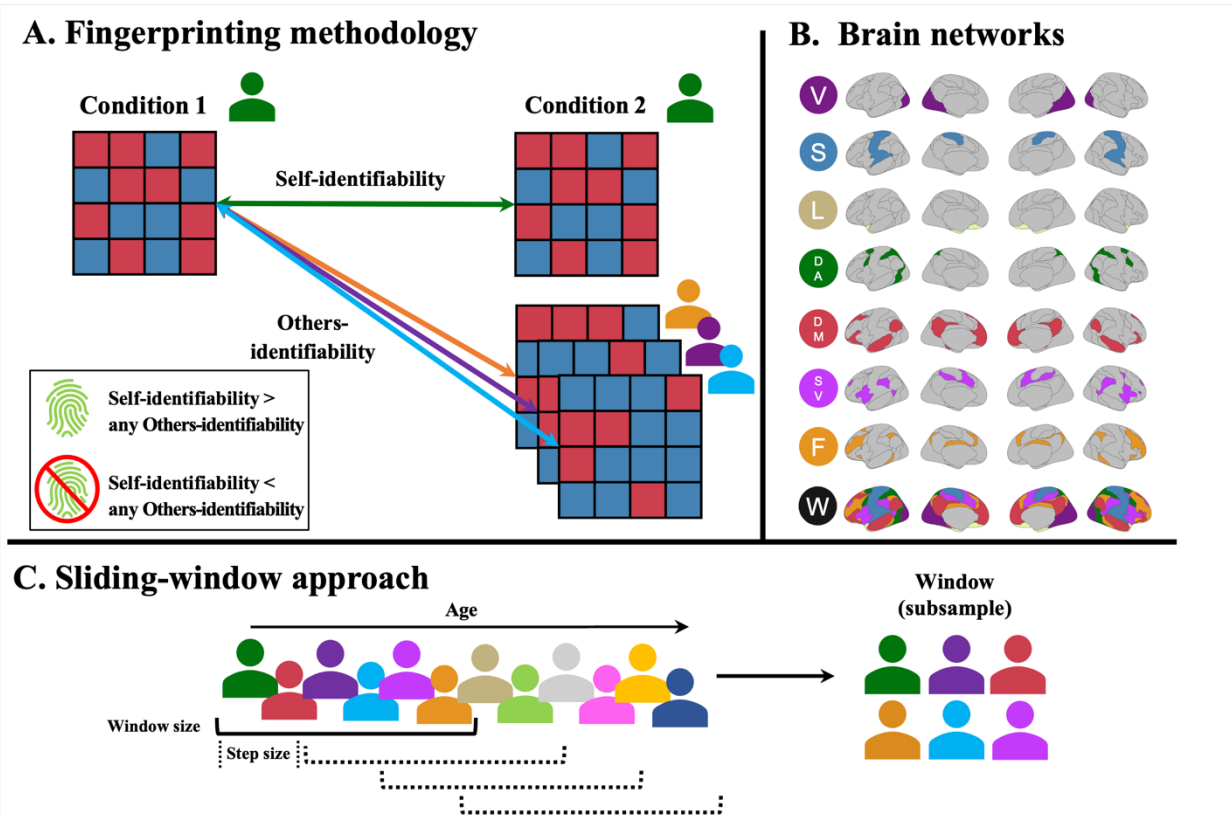


Figure 2.1 – Illustration of the methodology

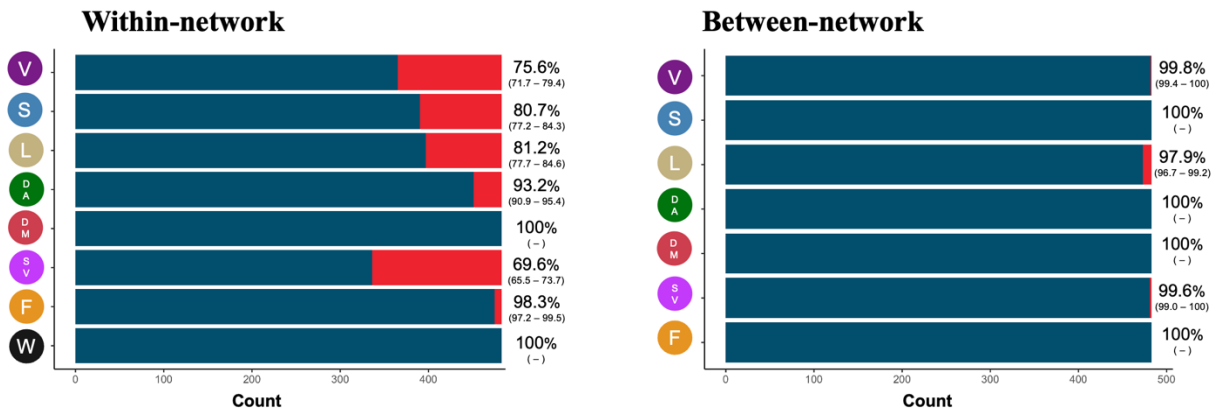
A. Illustration of the fingerprinting framework described in the methods section. Fingerprints are established by the correlation of the functional connectivity of participants between conditions. The correlation within the same individual constitutes self-identifiability while the correlation between individuals constitutes others-identifiability. (Amico & Goñi, 2018) If the self-identifiability is higher than any other others-identifiability for a given participant, they are successfully identified. (Finn et al., 2015) **B.** Yeo functional networks used in the analyses of the paper. V = Visual, S = Somatomotor, L = Limbic, DA = Dorsal attention, DM = Default mode, SV = Salience/Ventral attention, F = Frontoparietal, W = Whole brain. **C.** Illustration of the sliding-window approach to select sub-groups of participants. Subsamples of participants (window size) were chosen iteratively by taking the participants from the cohort, ordered by age, and slowly moving

along (step size) the lifespan. This method yields subsets of overlapping participants across the lifespan, offering a cross-sectional, semi-continuous overview of changes during aging. Window size and step size were varied to obtain different combinations of subsamples.

Across the full sample, we found high rates—up to 100% in some networks—of fingerprint identification (Figure 2.2A). McNemar tests indicated that identification was increased when using between-network edges (compared to within-network edges; Supplementary Table 2.1) and using higher associative cortices (default, frontoparietal and dorsal attention compared to visual, sensorimotor and limbic; Supplementary Table 2.2). Using between-network edges, we were able to achieve 100% fingerprint identification accuracy in the somatomotor, dorsal attention, default and frontoparietal networks. Using whole brain connectome and within-network edges in the default network, we achieved 100% fingerprint identification accuracy.

To determine how stable identifiability was throughout the lifespan, we adapted a between-participant sliding-window approach (Figure 2.1C) (Váša et al., 2018). Briefly, participants were ordered by age and slices of overlapping participants were selected to create groups of participants across different ages of the lifespan. Using this approach, identifiability was stable throughout the lifespan across networks (Figure 2.2B, Supp Fig 2.1; approach described in Figure 2.1C). Finally, employing McNemar tests, identification rates using within-network edges were similar for partial correlation-derived FC compared to product–moment correlation-derived FC, but were superior when using between-network edges (Supplementary Table 2.3&2.4).

A. Identification accuracy across the sample (n = 483)



B. Identification accuracy across aging windows

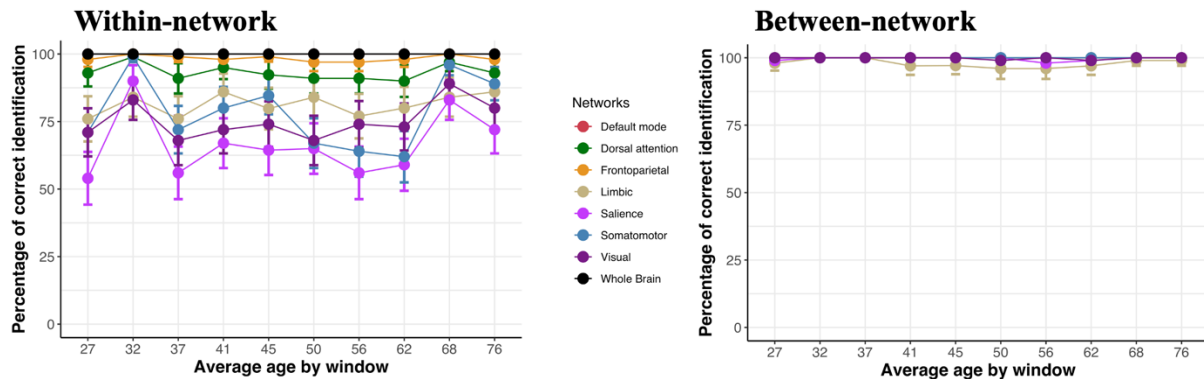


Figure 2.2 – Unique connectomes across the lifespan, networks, and tasks

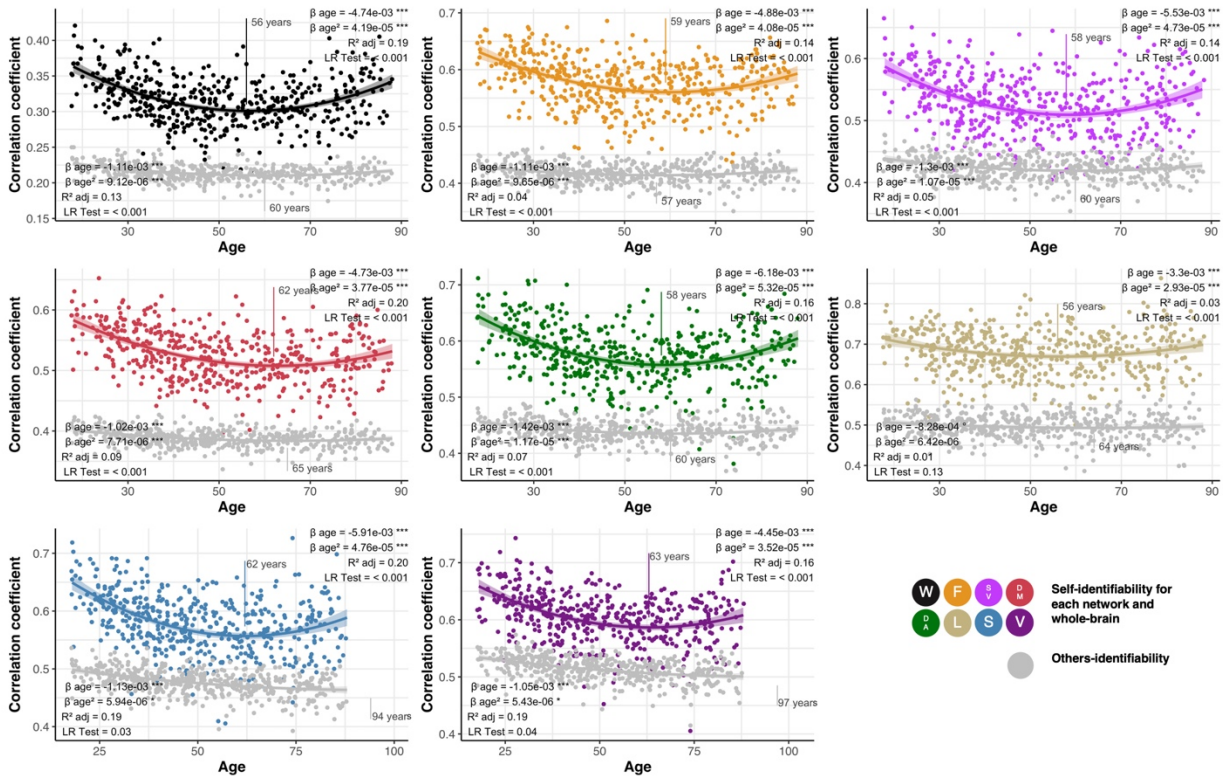
Fingerprint identifiability in the pair of Rest and Task conditions. Panel A. illustrates the fingerprint identification accuracy across the entire sample using within- and between-network edges. The blue color in the bar graphs and the percentages (with confidence intervals; $\alpha = 0.05$) to the right of the graphs indicate the proportion of individuals correctly identified. Network acronyms on the y-axis match graphics in Figure 1B and represent the specific functional network used for identification. In panel B., we used a between-individual, age-group sliding-window approach to plot how stable the fingerprint identification accuracy was across the lifespan for each network.

We also tested whether using a random collection of nodes selected throughout the brain would yield comparable fingerprint identification accuracy rather than using the nodes of the defined Yeo networks. We created two random networks by randomly selecting a subset of nodes from the Schaefer parcellation, of 22 and 91 nodes, respectively matching the size of the limbic and default networks in our study. Using the 22-node random network yielded worse accuracy than any other network at 16% but using the 91-node random network yielded high accuracy at 94% (Supp Fig 2.2A).

2.4.2 - Both self-identifiability and others-identifiability change non-linearly and in parallel across the lifespan

We found, using quadratic regressions and nested likelihood ratio tests, that both self-identifiability and others-identifiability differed non-linearly across the lifespan across all networks (both within- and between-network edges) (Figure 2.3). Using Stimson's equation for quadratic models, (Stimson et al., 1978) we further found that both self-identifiability and others-identifiability appeared to decrease until 49-63 years of age, before increasing (Figure 2.3). Results of all models, except for others-identifiability in the limbic network, remained significant when bootstrapping and controlling for sex, handedness, motion and number of fMRI frames available. Results were also very similar when using the Power atlas (Supp Fig 2.3B) across all networks for the self-identifiability, and for the whole brain, default, frontoparietal, and dorsal attention networks for the others-identifiability. We also found the same results when using our two random networks described in the previous section (Supp Fig 2.2B).

A. Within-network edges



B. Between-network edges

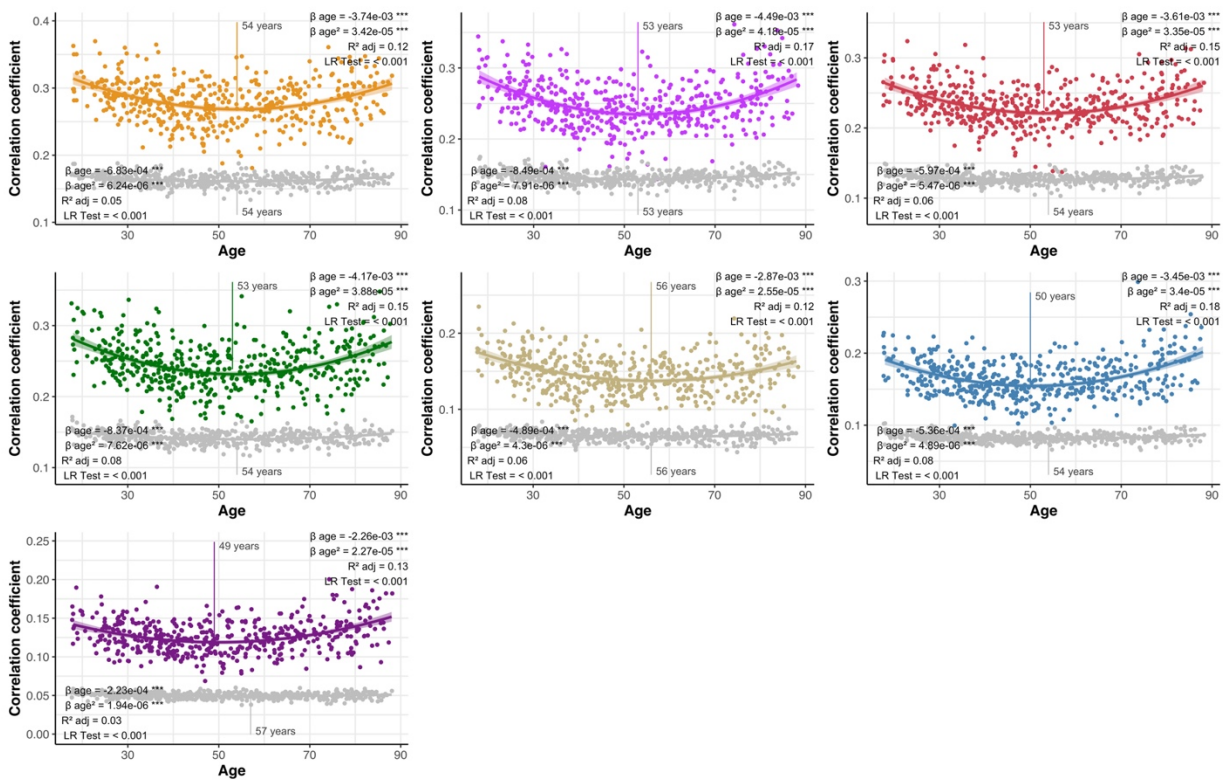


Figure 2.3 – Differences in self- and others-identifiability across the lifespan

Change in self- (colors) and others-identifiability (grey) are represented using either within-network edges (A.) or between-network edges (B.). Each graph represents a different network, following acronyms and color schemes of Figure 1B. The beta coefficient of the age term and its quadratic term are presented at the top of the graph. We also present the adjusted R^2 of the model and the p -value of the nested likelihood ratio indicating the non-linearity of the relationship. The p -value of predictors surviving inclusion of covariates and execution of the bootstrapping are indicated by asterisks ($p < 0.001 = ***$, $p < 0.01 = **$, $p < 0.05 = *$, $p < 0.1 = \circ$). The age at which the curve changed direction was calculated from Stimson's equation (Stimson et al., 1978) and is illustrated on the graphs.

To ensure that the non-linearity of our results wasn't driven by the oldest participants having higher self- and others-identifiability, we excluded participants above 80 years of age and repeated the analyses. We found nearly identical results (Supp Fig 2.4). Finally, we tested whether results would be similar when functional connectivity was generated using product-moment correlations of the blood-oxygen level dependent (BOLD) signal between nodes instead of using partial correlations. We found few associations between self-identifiability and age using this method. However, in networks where the association existed, it exhibited a U-shape (Supp Fig 2.5).

2.4.3 - Regions contributing to self-identifiability across the lifespan

To determine which FC edges contributed to self-identifiability, we used an elastic net model paired with the age-group sliding window approach. Specifically, we aimed to

determine which combination of FC edges across the brain were predictive of self-identifiability in both a training and a testing set, in each age window. We applied these elastic net models to each age window across our sliding-window parameters. We report the model performance of the elastic net models in the left-out test set (i.e., whether edges identified in the training model also predicted self-identifiability in the left-out test set). We also report the nodal density for each node in each age window. The nodal density indicates the extent to which edges from a given node contributes to self-identifiability (Amico & Goñi, 2018). For each node, we summed the number of edges identified by the elastic net as being important for prediction within each node and divided this number by the total number of edges per node (400). While we only report the results for the window size 100 and step size 40, the results were identical across sliding window parameters.

Overall, prediction of self-identifiability within each age window did not generalize to any left-out samples and exhibited poor model performance across all age windows (Supp Fig 2.6). Furthermore, no specific nodes had more predictive edges than others (Figure 2.4). In fact, in many windows, the elastic net did not identify any combination of edges that were predictive of self-identifiability. These results suggest that no combination of FC brain edges can reliably predict self-identifiability across individuals.

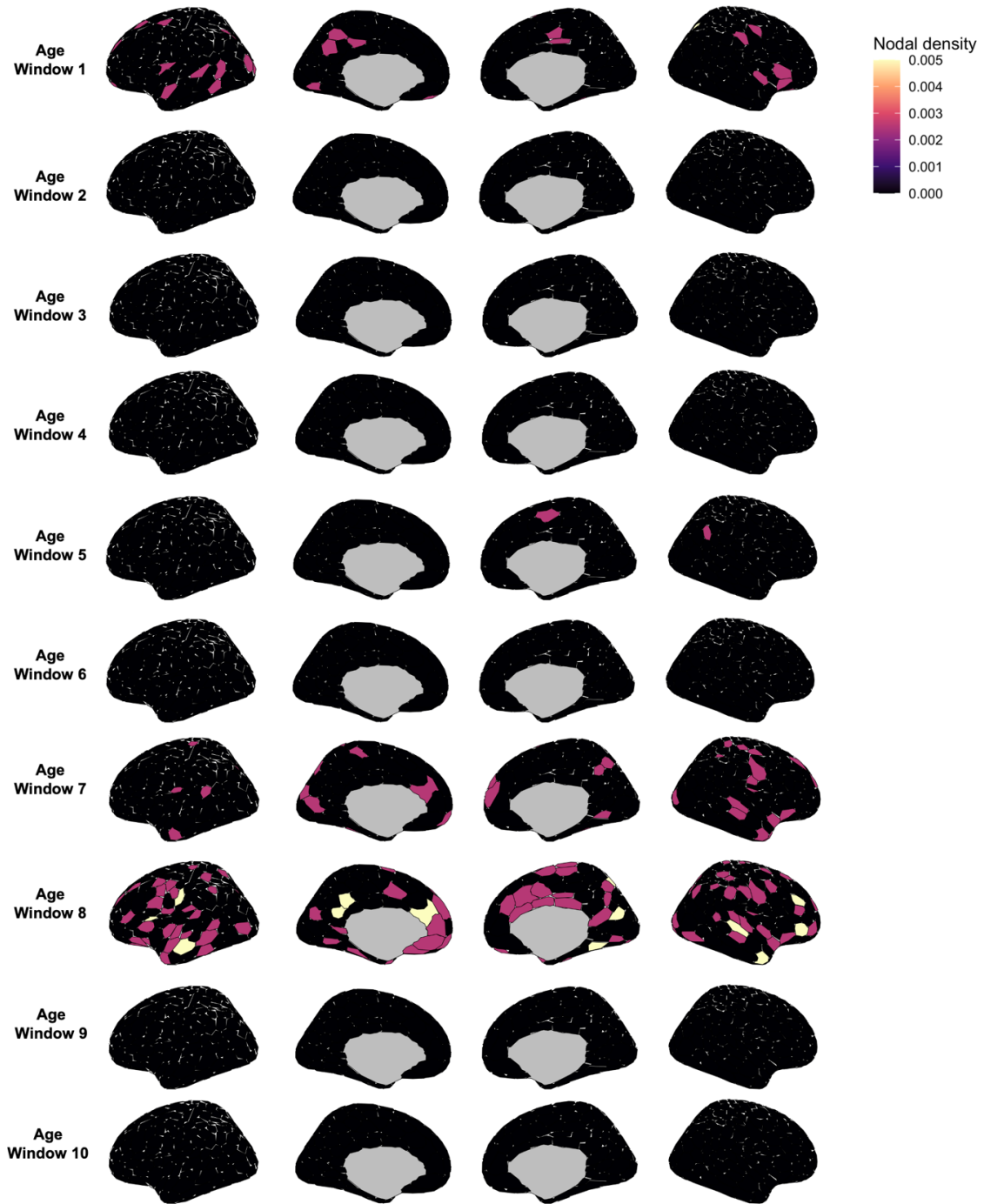


Figure 2.4 – Distribution of nodes predicting self-identifiability across the brain

For each age window (see sliding-window approach, Figure 2.1C), we plot the nodal density (sum of number of edges identified by the elastic net as being predictive of self-

identifiability divided by the total number of nodes) using the Schaefer atlas (400 nodes). A higher nodal density indicates that the node had a higher proportion of edges contributing to self-identifiability. Average age in each window match averages in Figure 2.2.

A potential issue with using the elastic net model with our data is the massive number of predictors in the model (79,800 edges) and the sparse nature of the FC matrices derived from partial correlations rather than product–moment correlations. This could explain the lack of generalizability in the left-out test sets, as well as the lack of nodes identified consistently as predictive. To ensure that our results were not driven by these limitations, we adapted three more methods to verify these results: a connectome predictive modelling approach, an intra-class correlation approach and a clustering approach. The connectome predictive modelling and intra-class correlation approach tested whether FC in individual edges in specific networks were driving self-identifiability. Alternatively, the clustering approach aimed to confirm whether patterns of individual FC were shared across the brain in each age window. Detailed discussions of these methods are found in Supplementary materials. All these additional analyses converged toward the same conclusion as the elastic net model: regions contributing to self-identifiability vary across the lifespan and between individuals (Supp Figs 2.7 to 2.14).

2.4.4 - Variability in FC, but not variability in BOLD features, differ over the lifespan

We additionally tested whether other markers of variability in fMRI signal differed over the lifespan (Supp Fig 2.15). To this end, we derived two types of measures, variability in FC and variability in BOLD temporal similarity profile. Within-individual

variability in FC was defined as the variance coefficient of FC values within a given network for a given individual. We defined the between-individual variability in FC as the distance (subtraction) between the variability in FC of an individual to the average variability in FC of the group. Variability in temporal similarity profile was defined in the same way but using BOLD signal feature profiles instead of FC (Shafiei et al., 2020). More information on these measures is available in the Methods section. For both measures we calculated a within-individual variance measure and between-individual variance measure. These were calculated at the whole-brain and network levels, and for each fMRI condition (Rest and Task). In contrast to the fingerprinting results, within-individual variability in FC decreased linearly across the lifespan in all networks, and between-individual variability in FC did not change with age in any network. No association were found between age and variability in temporal profile similarity.

Finally, we tested whether a non-linear change in amplitude of the BOLD signal with age could be driving the non-linear association between self-identifiability and age. Amplitude was calculated as the average of the amplitude of the BOLD signal for all nodes in a given network, for each participant. We found that there was no association between amplitude of the BOLD signal and age in the Rest modality. In the Task modality, amplitude of the BOLD signal was associated non-linearly with age (Supp Fig 2.16), but self-identifiability was not associated with BOLD signal amplitude (Supp Fig 2.17). We conclude that it is very unlikely that the BOLD signal amplitude drives the non-linear association between self-identifiability and age.

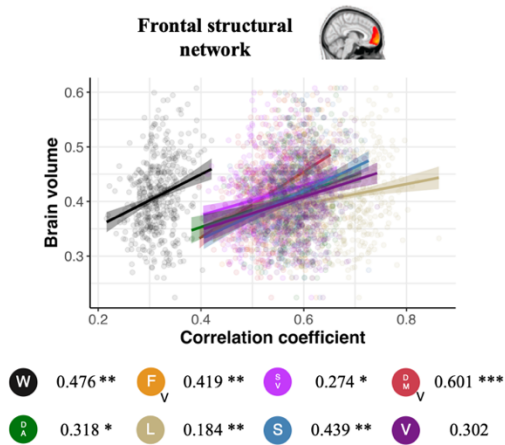
2.4.5 - Self-identifiability is associated with grey matter volume

Our initial results suggest that fingerprint accuracy is reliably achieved in adults over the lifespan. This is likely achieved due to the variability across people in the strongest FC patterns across the brain. We finally wanted to assess whether this identifiability was associated with age-sensitive variables, such as brain volume. To do so, we used three morphometric networks derived from an independent study as our outcome of interest (Pichet Binette et al., 2020): one frontal network (strongest age-related changes), a limbic network, which includes the hippocampus and the medial temporal lobe (moderate associations with both Alzheimer's disease and age-related changes) and an occipital network (weakest age-related effect). Grey matter volume was extracted for all three networks and used in our analyses.

Lower self-identifiability was associated with lower grey matter volume in the frontal structural network over and above the effect of age and other covariates (Figure 2.5). This connectome-wide result was recapitulated in the within- and between-network self-identifiability metrics (except for self-identifiability in the visual networks for within-network edges and visual and somatomotor networks for between-network edges).

Others-identifiability was not associated with brain volume (Supp Fig 2.18). Using our markers of variability in FC and BOLD signal, we found that decreased within-individual variability in FC was associated with decreased brain volume across networks (Supp Fig 2.19) but to a lower extent than self-identifiability. Similarly to others-identifiability, there was no association between between-individual variability in FC and brain volume. We also did not find any association between variability of temporal profile similarity and brain volume.

A. Within-network edges



B. Between-network edges

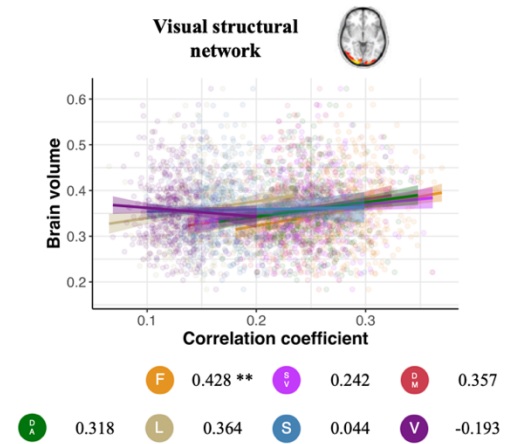
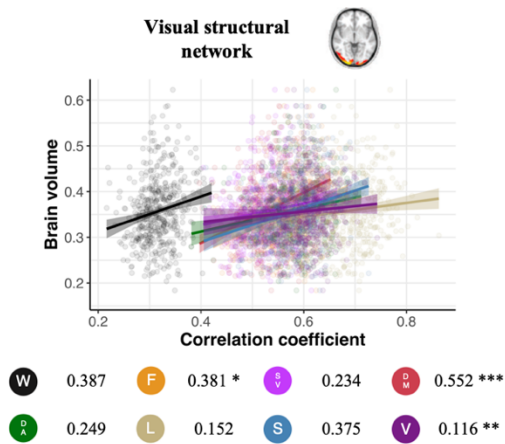
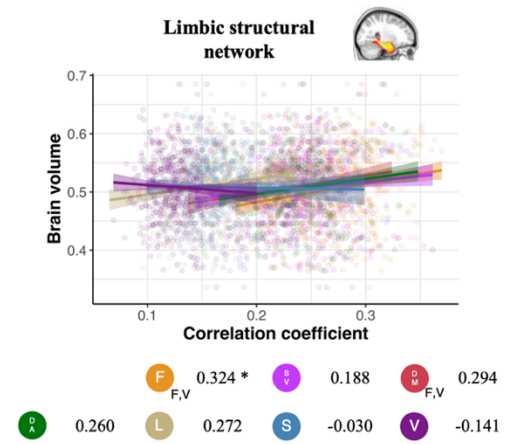
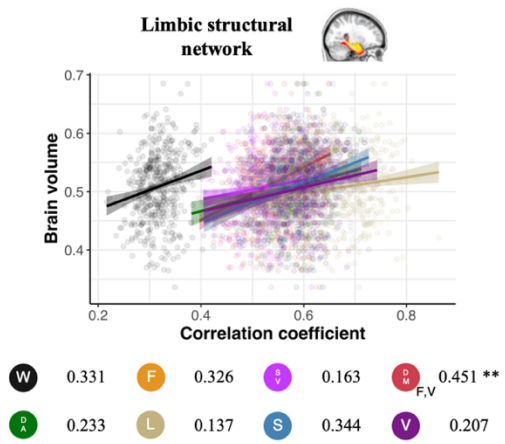
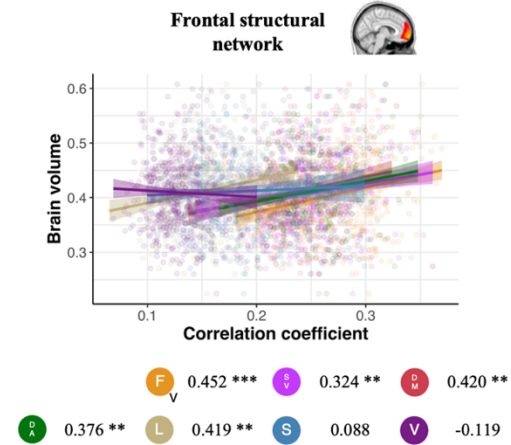


Figure 2.5 – Association between grey matter volume and self-identifiability

Scatterplots presenting the association between self-identifiability, derived using **A.** within- and **B.** between-network edges, and grey matter volume in three grey matter

*morphometric networks: frontal structural network (age-sensitive network), limbic structural network (Alzheimer's/age-related network) and visual structural network ("control" network). Data points, regression slopes and bubbles below the graph follow the color scheme of Figure 2.1B. The beta coefficient of the relationship between the self-identifiability and the brain volume is indicated beside each network bubble. The p-value of each predictor surviving comparison with covariates and bootstrapping is denoted by asterisks next to the beta coefficient ($p < 0.001 = ***$, $p < 0.01 = **$, $p < 0.05 = *$). Models surviving all confounders for all three morphometric networks were compared using Vuong's test for non-nested models. A letter at the bottom right of the network acronym indicates that the association was stronger using that specific structural network compared to the other networks referred to by the letter (V = Visual, F = Frontal, L = Limbic).*

2.5 – Discussion

We found that connectome-based fingerprinting is reliable across the lifespan. Fingerprint identification accuracy was robust even though self-identifiability and others-identifiability show a non-linear cross-sectional distribution across the lifespan. We also found that the highest weighted edges contributing to self-identifiability varied across individuals. This inter-individual variability was observed within each decade of life. Furthermore, relative to whole-brain and within-network FC, between-network FC provided more reliable identification estimates and the number of nodes (and related edges) were more important than their localization to identify individuals using brain functional properties. Finally, we found that self-identifiability (but not others-identifiability) was associated with frontal brain volume, a morphometric feature known to atrophy with advancing age (Pichet Binette et al., 2020).

Our findings indicate that fingerprinting remain robust across the lifespan, despite observed age-related changes in FC in older adulthood (Geerligs et al., 2015; Zonneveld et al., 2019). We found high fingerprinting identification accuracy across the lifespan, with perfect to nearly perfect identifiability accuracy in the whole brain connectomes and in the frontoparietal and default mode networks. Higher identification rates for associative cortical FC compared to unimodal networks has been found previously (Airan et al., 2016; Amico & Goñi, 2018; Finn et al., 2015; Horien et al., 2018, 2019; Van De Ville et al., 2021; Vanderwal et al., 2021) and has been suggested to be the result of high inter-individual variability in FC within these regions (Geerligs et al., 2015; Mueller et al., 2013). While this might partly be the case, networks such as the default mode network include a larger number of nodes than some unimodal networks. In supplementary analyses we showed

that we could achieve almost perfect identification using a large random network composed of the same number of nodes as the ones used in the default mode network. This identification was significantly diminished in a random network that included the same number of nodes as the ones used in the limbic network. These results suggesting that high identification may largely depend on the amount of information provided to perform this identification. This is in line with previous studies suggesting that finer-grained parcellations—i.e., more nodes—yield higher identification accuracy (Finn et al., 2015). The amount of information available for each participant might therefore be more important than the specific cortical topography when identifying individuals.

Next, we explicated fingerprint identification accuracy into its two components: self-identifiability and others-identifiability (Amico & Goñi, 2018). We found that both components have a non-linear trajectory across the lifespan. These U-shaped trajectories comprise high scores in young adults, which decrease into middle age and increase in older adulthood. This phenomenon was present across networks, and impacted metrics of self-identifiability more than others-identifiability. While U-shape trajectories have previously been reported in functional and structural lifespan studies (DuPre & Spreng, 2017; Kupis et al., 2021; Nadig et al., 2021), the exact cause of this phenomenon is unknown. This non-linear trajectory could be explained by a number of factors. Inter-individual heterogeneity in anatomy is most variable in early and late life, with more homogeneity observed between middle-aged adults (Nadig et al., 2021). This variance could boost individual identifiability in the youngest and oldest participants. Additionally, middle-aged women may have lower self-identifiability between fMRI sessions due to perimenopausal fluctuations in estrogen and progesterone (Pritschet et al., 2020), which

impact brain function on multiple scales. Previous studies in young adults found no longitudinal change in fingerprinting accuracy over a 2-to-3 year follow-up (Ousdal et al., 2020), suggesting that a longitudinal lifespan approach is needed to better characterize age-related change occurring over decades.

We also found that change occurring with age in self-identifiability and others-identifiability mainly occurs in parallel in all networks, including the random networks, which likely explain why the high identification accuracy is preserved across the lifespan despite age-related changes in its two components. As long as the balance between self-identifiability and others-identifiability is preserved, healthy individuals can be identified among a large group of individuals with similar accuracy (Horien et al., 2019; Kaufmann et al., 2018). Findings from developmental cohorts suggest that fingerprint metrics increase rapidly from a few days after birth and stabilize in young adults (Horien et al., 2019; Hu et al., 2022; Jalbrzikowski et al., 2020; Kaufmann et al., 2018; Vanderwal et al., 2021). Additionally, neuropsychiatric symptoms lead to a decrease in self-identifiability (Kaufmann et al., 2017, 2018). From a developmental perspective, fingerprints stabilize in early adulthood, but may be disrupted when the brain is affected by an overt neuropsychiatric or neurological disorder, or sub-clinical perturbations, resulting in mid-life declines in identifiability. The older adult cohort could represent either a stabilization of these effects, or a more carefully screened sample of healthy individuals that persist in the developmental stability of identification.

Our findings are consistent with work suggesting that fMRI connectivity is composed of distinct, unique individual-specific and shared task-specific components (Gratton et al., 2018; Mantwill et al., 2022). Using four different approaches (elastic net,

connectome predictive modelling, edge-wise intraclass correlation and clustering) we did not find consistent edges contributing to self-identifiability in our sample across individuals. This aligns with our large random network yielding high identification accuracy, suggesting that brain signatures, and their associated brain regions, are unique across individuals. These analytical approaches reinforce the finding that between-individual variance in functional brain connectomics are critical to the identification of individual functional fingerprints.

Finally, we aimed to determine whether individual-level FC fingerprint metrics were associated with brain volume. We compared brain volume associations with self-identifiability and others-identifiability. Whole brain connectomes, within-network FC and between-network FC self-identifiability was associated with brain volume in frontal areas known to be particularly affected by normal age-related atrophy (Pichet Binette et al., 2020). We also found consistent associations for self-identifiability between default and frontoparietal networks and brain volume in the hippocampus and medial temporal lobe (limbic structural network; known to be vulnerable in Alzheimer's disease). The occipital structural regions were preserved over the lifespan and did not impact self-identifiability (Pichet Binette et al., 2020). In contrast, there was no consistent association between others-identifiability and brain volume.

Self-identifiability may be associated with a number of factors that differentially impact individuals over the lifespan (Kaufmann et al., 2017, 2018). For instance, the default network is affected by a wide range of neurological disorders (de Lange et al., 2019) and aging (Zonneveld et al., 2019). Consistent with this idea, reduced fingerprint identifiability within the default network has been associated with mental health disorders

in youth (Kaufmann et al., 2017) and reduced brain volume in older adults (Ousdal et al., 2020). Individual-level FC measures, rather than group-level measures, may be more appropriate to detect age- or disease-related functional changes (Finn & Constable, 2016), either by directly accounting for inter-individual differences (Finn & Rosenberg, 2021) or, at least partially, ignoring group-level noise in fMRI signal (Amico & Goñi, 2018). Targeting individual-level differences might be particularly important in aging research, as aging individuals present high diversity of lifestyle and medical history, leading to diverse age-related outcomes (Daskalopoulou et al., 2019).

As an additional note, the findings above also expand methodological aspects in the field of fingerprinting. First, we used partial correlation to generate FC matrices, which were then used for fingerprinting. Partial correlations resulted in higher identification rates in our study compared to product–moment correlations. Partial correlations produce sparse matrices excluding, to some extent, noise inherent to fMRI (Marrelec et al., 2006). Other methods aiming at removing noise in FC matrices have also found success in improving fingerprint identification accuracy (Amico & Goñi, 2018). As noise affects individuals across the sample in a similar manner (Amico & Goñi, 2018), removing noise should therefore better isolate individual-specific features. Second, we computed identification using between-network edges as well as within-network edges. In most cases, between-network edges provided better identification rates compared to within-network edges. To our knowledge, all studies on fingerprinting to date have used within-network edges to compute identification. However, while within-network edges represent communities of nodes working tightly together (Sporns & Betzel, 2016), between-network connections are necessary to various brain functions. In aging in particular, the

segregation of these networks tends to change (Chan et al., 2014) and as such between-network edges may better represent overall brain network communications. Our study therefore also suggests potential methodological aspects to consider in future fingerprinting studies, particularly when considering aging populations.

2.5.1 – Strengths and limitations

The main limitation of this study is its cross-sectional nature. As such, it is difficult to determine how fingerprint metrics change during the lifespan within individuals, limiting the interpretation of our conclusions. Future work would benefit from longitudinal studies examining identifiability across scans separated by many years. Similarly, due to quality control issues, eldest participants in our cohort were under-represented, and as such, the non-linearity of our findings need to be interpreted with caution. However, supporting the non-linearity of the findings, the non-linearity between age and self-identifiability was still preserved when removing the oldest participants. Finally, we only included two fMRI modalities in our analyses. As other studies have shown that the choice of the task can influence the ability to fingerprint, future studies should replicate our findings using other combinations of fMRI tasks.

2.5.2 – Conclusion

Across our analyses, we found that FC patterns allow for precise fingerprinting between individuals and that this discrimination is reliable across the lifespan. High identification rates were observed across the Cam-CAN cohort, accompanied by age-related effects on individual-level (self-identifiability) and group-level (others-identifiability) FC patterns. Accurate fingerprinting of FC was observed across the lifespan, even though edges contributing to self-identifiability differed between individuals across networks and

across the decades of life. Finally, we show that individual-level self-identifiability (instead of group-level others-identifiability) is associated with brain volume in regions vulnerable to age-related atrophy. Together, the present findings illuminate the potential utility of individual-level measures that demarcate age-related brain change. Group-level differences in FC have revealed reliable patterns attributed to the aging brain. However, individual differences in FC patterns are likely to play a key role in predicting brain health and associated functional outcomes.

2.6 – Material and methods

2.6.1 – Participants

Data used in the preparation of this work were obtained from the Cam-CAN repository (available at <http://www.mrc-cbu.cam.ac.uk/datasets/camcan/>). The Cam-CAN cohort is a lifespan cross-sectional population-based cohort, composed of cognitively healthy participants aged between 18 and 89 years of age residing in the United Kingdom. Full details for the study participants and recruitment can be found elsewhere (Shafiq et al., 2014; Taylor et al., 2017). Participants underwent several brain imaging procedures at one timepoint. Special attention was given to recruiting persons from different decades and to balance both men and women. This study was approved by the Cambridgeshire 2 Research Ethics Committee (reference: 10/H0308/50).

2.6.2 – Magnetic resonance imaging

Full details on the imaging data collection and on the fMRI tasks used are available elsewhere (Taylor et al., 2017). Briefly, MRI data were acquired on a 3T Siemens TIM Trio scanner with a 32-channel head coil for a one 1-hour session. T1-weighted MPRAGE sequences were acquired for structural imaging, and T2*-weighted EPI sequences were acquired for fMRI imaging (261 volumes with 32 axial slices each; slice thickness of 3.7 mm; interslice gap of 0.74 mm; TR =1970 ms; TE =30 ms; flip angle =78 degrees; FOV =192 mm × 192 mm; voxel-size = 3 mm × 3 mm × 4.44 mm). Participants underwent two different fMRI conditions during one session: a Resting state condition (Rest), where participants were asked to keep their eyes closed for 8min 40s and a sensorimotor task (Task), also of 8min 40s in which participants were asked to press a button when audio-visual stimuli were presented.

Functional images from the two modalities were preprocessed using the NeuroImaging Analysis Kit, version 0.12.4 (NIAK; <http://niak.simexp-lab.org/>; Bellec et al., 2011; Gonneaud et al., 2020). The first three volumes of each run were suppressed to allow the magnetisation to reach equilibrium. Images were slice-timing corrected and rigid-body motion parameters were estimated for each time frame. For registration, T1-weighted images were linearly and non-linearly registered to MNI space. The rigid-body transform, fMRI-to-T1 transform, and T1-to-stereotaxic transform were all combined, and the functional volumes were resampled in the MNI space at a 3 mm isotropic resolution. To account for potentially excessive motion, frame displacement was calculated for each volume and those with more than 0.5 frame displacement were removed with one prior adjacent frame and two consecutive frames after. Timeseries with less than 40% of their original data after removing excessive motion were discarded from subsequent analyses (Orban et al., 2015). Next, slow time drifts, cerebrospinal fluid, average white matter signal, and motion artifacts (first principal components of the six rigid-body motion parameters, and their squares) were removed from the fMRI time series, and fMRI volumes were smoothed with a 6mm Gaussian kernel. Finally, fMRI timeseries for each region of the Schaefer atlas ($n = 400$) were extracted using Nilearn 0.6.2 (Abraham et al., 2014). Partial correlations were used to generate FC between regions, accounting for the signal in all other brain regions. This process generates sparser functional connectivity matrices that are thought to account for more noise than using simple product-moment correlation and represent more direct connections between regions (Marrelec et al., 2006; Zalesky et al., 2012). We generated FC matrices for the task and resting-state fMRI runs.

All structural images were pre-processed using Statistical Parametric Mapping (SPM12, <http://www.fil.ion.ucl.ac.uk/spm/software/spm12/>) in MATLAB version 2012a, as part of a previous study (Pichet Binette et al., 2020). Images were segmented into grey matter, white matter, and CSF components. Then, a group-specific template was created using the Diffeomorphic Anatomical Registration through Exponentiated Lie Algebra toolbox (DARTEL) (Ashburner, 2007), which was then registered non-linearly to the MNI-ICBM152 template. Finally, each individual participant's grey matter map was registered back to the group template, before being smoothed with an 8mm³ isotropic Gaussian kernel.

2.6.3 – Sliding-window analysis

Across multiple analyses, we used a between-participant sliding-window approach to study differences across the lifespan in a semi-continuous manner (Váša et al., 2018; Figure 2.1C). First, participants were ordered by age (from youngest to oldest). Then, we iteratively selected subsamples of overlapping participants varying two parameters: window size (i.e., the number of participants in each subsample) and step size (i.e., the number of participants skipped before selecting the next window). We used window sizes of 100 or 150 participants and used a step size of either 25 or 40 participants. As such, participants in adjacent windows overlapped by 60 to 80%. Main analyses report results using a window size of 100 and step size of 40, while results using other parameters are reported in supplementary analyses.

2.6.4 – Fingerprinting

Our main interest was functional connectome fingerprinting, which encompasses three measures of interest: fingerprint identification accuracy (Finn et al., 2015), self-

identifiability and others-identifiability (Amico & Goñi, 2018). In the fingerprinting framework, the FC matrix of a given individual obtained from one fMRI condition is correlated to the FC matrix of the same individual obtained during a different fMRI condition by computing the correlation coefficient of the vectorized upper triangle z-values between sessions. This results in a within-individual correlation (i.e., self-identifiability). This process is repeated for all within and between participant FC matrices, permitting the computation of both within and between-individual similarities (i.e., others-identifiability). Finally, fingerprint identification accuracy is estimated from both self- and others-identifiability measures: a fingerprint is considered identifiable when self-identifiability exceeds the magnitude of others-identifiability (Amico & Goñi, 2018; Finn et al., 2015); see Figure 2.1A. for schematic overview). This process was done for the whole brain connectome as well as for within-network and between-network edges for each network.

The fingerprint framework was adapted from the original methodologies by Finn et al. (2015) and Amico & Goñi (2018). The FC obtained for the Rest and Task modalities were first normalized using Fisher's r-to-z transform. Product-moment correlations were then used to correlate FC matrices obtained from the Rest and Task conditions, deriving self-identifiability and others-identifiability. These values were then stored in a similarity matrix. For each row of the matrix, a fingerprint identification was considered accurate if self-identifiability (diagonal elements of the matrix) was higher than any other others-identifiability (off-diagonal elements of the matrix). Self-identifiability and others-identifiability were computed based on the FC between 400 parcels. Additionally, the parcel information corresponding to the Yeo seven networks was leveraged to demarcate

within-network FC. Then, we composed aggregates of between-network FC by taking any edges between each other network. For example, if the visual network was composed of nodes 1 to 61 (rows and columns 1 to 61 in the matrix), within-network edges comprised edges where both rows and columns were between 1 to 61. Between-network edges comprised edges in rows 1 to 61 but in columns 62 to 400 (Yeo et al., 2011).

Additionally, we created two random networks to test whether we could find high identification accuracy using edges belonging to a random assortment of nodes rather than using predefined networks. We selected two random sets of nodes across the brain. The number of nodes chosen were 22 and 91, to match the size of the smallest (limbic) and largest (default) networks (Schaefer et al., 2018; Yeo et al., 2011) included in our study. Fingerprinting methodology described above was applied to the edges of these two random networks.

2.6.5 - Predicting self-identifiability using combinations of edges

We adapted an elastic net approach to predict self-identifiability from the FC edges in our sample. Specifically, we used the sliding window method to select subsamples of participants across the lifespan. Within each window, we first removed the diagonal and lower triangle of the functional connectivity matrices of the participants and flattened the remaining 79,800 edges. The connectivity values were then standardized, and participants were randomly split in a training and testing subset (85% training, 15% testing). Connectivity values across all 79,800 edges were used to predict self-identifiability. In the training set, we used a 5 k-fold cross-validation with a grid search to select the optimal L1 ratio for our elastic net model. Once the optimal L1 ratio was selected, an elastic net model was fitted on the entire training set. The model was then

used to predict self-identifiability in the testing set. Performance in the testing set was reported as the variance explained (R^2) and the RMSE.

The elastic net outputs coefficients indicating which edges significantly contributed to model performance. To determine their topography in the brain, we adapted a nodal density approach (Amico & Goñi, 2018). Briefly, edges were resized to a 400x400 functional connectivity matrix format and binarized. Then, the sum of the binary coefficients for each node (i.e., each row of the matrix) was divided by the number of edges for that node (i.e., 400). This yields a nodal density measure for all 400 nodes of the Schaefer atlas, where more density indicates that edges in that node are more important. These results were then projected to a brain map.

2.6.6 – Age-related outcome: Structural aging morphometric network

We tested the relationship between functional fingerprint metrics (self-identifiability and others-identifiability) and structural age-related changes. Three morphometric networks derived in an independent study were used as our outcome of interest (Pichet Binette et al., 2020). Briefly, a large cohort of cognitively unimpaired younger and older adults and participants on the Alzheimer disease spectrum were grouped and independent component analysis was used to derive statistically independent structural brain networks. Then, volume in each component was used in a receiver operating characteristic analysis to determine whether brain volume could accurately classify individuals in their corresponding group. From this study, we chose one frontal network (ICA01 in the original study which was the network showing the strongest age-related changes), a limbic network (ICA10 that showed moderate associations with both Alzheimer's disease and age-related changes) and an occipital network (ICA15 that

showed the weakest age-related effect). Grey matter volume was then extracted for all three morphometric networks for each participant. These morphometric networks were chosen rather than using parcel-level or network-level gray matter measures as we wanted age-associated gray matter measures and as their association with fingerprint measures could be more directly comparable between networks.

2.6.7 – Supplementary analyses on FC variability

Additionally, we also determined whether other markers of variability in fMRI signal changed during the aging process. We derived two types of measures, variability in FC and variability in blood-oxygen level dependant (BOLD) temporal similarity profile.

Both types of measures were calculated using custom Python scripts. Variability in FC for each individual was computed as the variance coefficient of FC coefficients at a whole brain level and within each network of interest. To obtain between-individual variability, we first computed the average variability in FC across the sample. Then, for each individual, we computed the absolute distance between their variability and the mean variability of the group. A greater distance indicates more between-individuals variability.

Variability within- and between-individuals in BOLD signal features was computed as the variance in temporal profile similarity of BOLD signal features (Shafiei et al., 2020). To do so, BOLD signals features were extracted from each brain region using the highly comparative time-series analysis toolbox (Fulcher et al., 2013; Fulcher & Jones, 2017). Timeseries were first z-scored and then fed to the toolbox where 7700 features are extracted from the BOLD signal. Because the number of fMRI frames varied between individuals after the preprocessing, some features had missing or constant values across

participants, and were therefore dropped. This resulted in a final 6192 features remaining. Extracted features were then z-scored again to ensure comparability between features. For each participant, the extracted features timeseries for each region were correlated using product–moment correlations to determine how similar timeseries were between each brain region, resulting in a 400x400 temporal similarity profile similarity matrix. Finally, variability in temporal similarity profile was computed identically to the variability in FC.

As a final verification, we computed BOLD signal amplitude and related this measure to age and self-identifiability. In each of the 400 brain regions, for each participant, the amplitude of the timeseries were computed by subtracting the minimum from the maximum BOLD value. Then, the amplitude of the nodes within the network was averaged to obtain a single amplitude measure for each network for each participant.

2.6.8 – Software

The sliding-window, fingerprinting framework, elastic net, edge-wise intraclass correlation analyses, connectome predictive modelling, clustering and variability in FC analyses were adapted and developed using Python 3.8.5 (Python Software Foundation, <https://www.python.org/>); NumPy 1.19.1 (Harris et al., 2020); pandas 1.1.3 (McKinney, 2010; The pandas development team, 2020); scikit-learn 0.24.0 (Abraham et al., 2014); SciPy 1.7.1 (Virtanen et al., 2020); pingouin 0.5.2 (Vallat, 2018) on Beluga, a high-performance computing resource hosted by the Digital Research Alliance of Canada, running on CentOS 7.9. The temporal similarity profile analysis was done using MATLAB2021B (highly comparative time-series analysis toolbox (Fulcher et al., 2013; Fulcher & Jones, 2017)) and Python 3.8.5. All statistical analyses and graphs were done

in R v4.1.2 (R Core Team, 2020) (tidyverse 1.3.0 (Wickham et al., 2019); boot 1.3-28 (Canty & Ripley, 2021; Davidson & Hinkley, 1997); patchwork 1.1.1(Lin Pedersen, 2020); ggnewscale 0.4.8 (Campitelli, 2022); ggseg 1.6.5 (Mowinckel & Vidal-Piñero, 2020)) using R Studio ("Ghost Orchid" Release [077589bc, 2021-09-20]) for macOS Monterey 12.6. All code related to the analyses are available at <https://github.com/villeneuvevilleneuve/projects>. The code related to the fingerprinting analysis was also adapted to the openly available sihnp Python package: <https://sihnp.readthedocs.io/>

2.6.9 – Statistical analyses

Fingerprint identifiability was computed for all networks for the Rest and Task conditions for both within- and between-network edges. Percentage of identified individuals with confidence intervals were calculated. Paired McNemar tests were used to compare identification in a given network to the identification of the same network using a different fingerprint type (i.e., using within- vs. between-network edges). We used this approach to compare network performance in fingerprint identifiability within each modality pair (e.g., comparing proportion of identification using the default vs. somatomotor networks). A family-wise Bonferroni correction was applied to each set of comparisons to account for multiple comparisons. Finally, we used the sliding-window approach where the fingerprint identification accuracy in each age window was computed and visualized.

To study the relationship between self-identifiability and age, and others-identifiability and age, we used multiple linear regression models. We used polynomial (quadratic) regressions when the linearity assumption was violated and, in that case, used

Stimson's equation to derive the peak's coordinates (Stimson et al., 1978). Assumption violation was determined by comparing fitted to residual values. We also used nested likelihood ratio tests to test whether models using quadratic terms outperformed linear models on model fit to confirm the non-linearity of the relationship. Each model included common confounders known to affect either FC or fingerprints as covariates of no interest: the number of frames post-scrubbing (Amico & Goñi, 2018; Horien et al., 2018; Xu et al., 2016), the mean frame displacement (i.e., movement; Amico & Goñi, 2018; Geerligts et al., 2017; Guo et al., 2012; Horien et al., 2018; Jalbrzikowski et al., 2020), the sex of participants (Finn et al., 2017) and a continuous handedness measure (Bailey et al., 2020). One model was generated for each network for both self-identifiability using within- and using between-network edges (45 models total). The same number of models was generated to study the association between others-identifiability and age. Due to the high number of regressions, we applied a bootstrap resampling procedure to each model as a way to account for multiple comparison (Westfall, 2011). Specifically, we generated bootstrapped bias-corrected and accelerated confidence intervals for the β -coefficients (where coefficients not overlapping with 0 were considered significant) of the main exposure. All analyses were repeated using within- and between-individual variability in FC and BOLD signal (i.e., variability in FC and variability in temporal similarity profiles) in each fMRI task in each network and within the whole brain.

All procedures described above were reapplied to study the relationship between fingerprint metrics and brain volume. Individual variability in FC and temporal similarity profile were also associated with age and with gray matter volume using the methodology described above. These metrics were used to determine whether other fMRI measures

would also show inter-individual variability across the lifespan. To test whether the association was stronger in the frontal structural network, the limbic structural network or the visual structural network, we used Vuong's test for non-nested models (Vuong et al., 1989). Models were repeated including all covariates with and without age.

2.7 – Acknowledgements

The authors would like to thank Jonathan Gallego Rudolf, Yara Yakoub, Ting Qiu and Julien Menes for useful feedback on the project, and Gabriel St-Onge for technical help in implementing the connectome predictive modelling. We would also like to thank the reviewers who provided their time to review this paper and for their thoughtful insight into our results, which significantly strengthened the paper. Data collection and sharing for this project was provided by the Cambridge Centre for Ageing and Neuroscience (Cam-CAN). Cam-CAN funding was provided by the UK Biotechnology and Biological Sciences Research Council (grant number BB/H008217/1), together with support from the UK Medical Research Council and University of Cambridge, UK. Computations were enabled in part by support from Calcul Québec (calculquebec.ca) and the Digital Research Alliance of Canada (alliancecan.ca), who provided access to the Beluga High-Performance Computing resource. This research was undertaken thanks in part to funding from the Canada First Research Excellence Fund and Fonds de recherche du Québec, awarded to the Healthy Brains, Healthy Lives initiative at McGill University. FS acknowledges support from Healthy Brains, Healthy Lives, Mitacs and the Fonds de Recherche Santé - Québec. The funding organizations did not have a role in writing the manuscript.

2.9 – References of Chapter 2

- Abraham, A., Pedregosa, F., Eickenberg, M., Gervais, P., Mueller, A., Kossaifi, J., Gramfort, A., Thirion, B., & Varoquaux, G. (2014). Machine learning for neuroimaging with scikit-learn. *Frontiers in Neuroinformatics*, 8(FEB), 1–10. <https://doi.org/10.3389/fninf.2014.00014>
- Airan, R. D., Vogelstein, J. T., Pillai, J. J., Caffo, B., Pekar, J. J., & Sair, H. I. (2016). Factors affecting characterization and localization of interindividual differences in functional connectivity using MRI. *Human Brain Mapping*, 37(5), 1986–1997. <https://doi.org/10.1002/hbm.23150>
- Amico, E., & Goñi, J. (2018). The quest for identifiability in human functional connectomes. *Scientific Reports*, 8(1), 1–14. <https://doi.org/10.1038/s41598-018-25089-1>
- Ashburner, J. (2007). A fast diffeomorphic image registration algorithm. *NeuroImage*, 38(1), 95–113. <https://doi.org/10.1016/j.neuroimage.2007.07.007>
- Bailey, L. M., McMillan, L. E., & Newman, A. J. (2020). A sinister subject: Quantifying handedness-based recruitment biases in current neuroimaging research. *European Journal of Neuroscience*, 51(7), 1642–1656. <https://doi.org/10.1111/ejn.14542>
- Bellec, P., Carbonell, V., Perlberg, C., Lepage, O., Lyttelton, V., Fonov, A., Janke, J., Tohka, A., & Evans, A. (2011). A neuroimaging analysis kit for Matlab and Octave. *Proceedings of the 17th International Conference on Functional Mapping of the Human Brain*.
- Binette, A. P., Gonneaud, J., Vogel, J. W., La Joie, R., Rosa-Neto, P., Louis Collins, D.,

- Poirier, J., Breitner, J. C. S., Villeneuve, S., Vachon-Pressseau, E., Tremblay-Mercier, J., & Madjar, C. (2020). Morphometric network differences in ageing versus Alzheimer's disease dementia. *Brain*, 143(2), 635–649.
<https://doi.org/10.1093/brain/awz414>
- Campitelli, E. (2022). `_ggnewscale`: Multiple Fill and Colour Scales in “ggplot2” [R].
- Canty, A., & Ripley, B. (2021). `boot`: Bootstrap R (S-Plus) Functions. (1.3-28).
- Chan, M. Y., Park, D. C., Savalia, N. K., Petersen, S. E., & Wig, G. S. (2014). Decreased segregation of brain systems across the healthy adult lifespan. *Proceedings of the National Academy of Sciences of the United States of America*, 111(46), E4997–E5006. <https://doi.org/10.1073/pnas.1415122111>
- Chen, P. Y., Chiou, J. M., Yang, Y. F., Chen, Y. T., Hsieh, H. L., Chang, Y. L., & Tseng, W. Y. I. (2016). Heterogeneous aging effects on functional connectivity in different cortical regions: A resting-state functional MRI study using functional data analysis. *PLoS ONE*, 11(9), 1–21.
<https://doi.org/10.1371/journal.pone.0162028>
- da Silva Castanheira, J., Orozco Perez, H. D., Misic, B., & Baillet, S. (2021). Brief segments of neurophysiological activity enable individual differentiation. *Nature Communications*, 12(1), 1–11. <https://doi.org/10.1038/s41467-021-25895-8>
- Daskalopoulou, C., Koukounari, A., Wu, Y. T., Terrera, G. M., Caballero, F. F., de la Fuente, J., Tyrovolas, S., Panagiotakos, D. B., Prince, M., & Prina, M. (2019). Healthy ageing trajectories and lifestyle behaviour: The Mexican Health and Aging Study. *Scientific Reports*, 9(1), 1–10. <https://doi.org/10.1038/s41598-019-47238-w>

- Davidson, A. C., & Hinkley, D. V. (1997). *Bootstrap Methods and Their Applications*. Cambridge University Press.
- de Lange, S. C., Scholtens, L. H., van den Berg, L. H., Boks, M. P., Bozzali, M., Cahn, W., Dannlowski, U., Durston, S., Geuze, E., van Haren, N. E. M., Hillegers, M. H. J., Koch, K., Jurado, M. Á., Mancini, M., Marqués-Iturria, I., Meinert, S., Ophoff, R. A., Reess, T. J., Reppe, J., ... van den Heuvel, M. P. (2019). Shared vulnerability for connectome alterations across psychiatric and neurological brain disorders. *Nature Human Behaviour*, 3(9), 988–998.
<https://doi.org/10.1038/s41562-019-0659-6>
- DuPre, E., & Spreng, R. N. (2017). Structural covariance networks across the life span, from 6 to 94 years of age. *Network Neuroscience*, 1(3), 302–323.
https://doi.org/10.1162/netn_a_00016
- Finn, E. S., & Rosenberg, M. D. (2021). Beyond fingerprinting: Choosing predictive connectomes over reliable connectomes. *NeuroImage*, 239(June), 118254.
<https://doi.org/10.1016/j.neuroimage.2021.118254>
- Finn, E. S., Scheinost, D., Finn, D. M., Shen, X., Papademetris, X., & Constable, R. T. (2017). Can brain state be manipulated to emphasize individual differences in functional connectivity? *NeuroImage*, 160(March), 140–151.
<https://doi.org/10.1016/j.neuroimage.2017.03.064>
- Finn, E. S., Shen, X., Scheinost, D., Rosenberg, M. D., Huang, J., Chun, M. M., Papademetris, X., & Constable, R. T. (2015). Functional connectome fingerprinting: Identifying individuals using patterns of brain connectivity. *Nature Neuroscience*, 18(11), 1664–1671. <https://doi.org/10.1038/nn.4135>

- Finn, E. S., & Todd Constable, R. (2016). Individual variation in functional brain connectivity: Implications for personalized approaches to psychiatric disease. *Dialogues in Clinical Neuroscience*, 18(3), 277–287.
- Fulcher, B. D., & Jones, N. S. (2017). hctsa: A Computational Framework for Automated Time-Series Phenotyping Using Massive Feature Extraction. *Cell Systems*, 5(5), 527-531.e3. <https://doi.org/10.1016/j.cels.2017.10.001>
- Fulcher, B. D., Little, M. A., & Jones, N. S. (2013). Highly comparative time-series analysis: The empirical structure of time series and their methods. *Journal of the Royal Society Interface*, 10(83). <https://doi.org/10.1098/rsif.2013.0048>
- Geerligs, L., Rubinov, M., Tyler, L. K., Brayne, C., Bullmore, E. T., Calder, A. C., Cusack, R., Dalgleish, T., Duncan, J., Henson, R. N., Matthews, F. E., Marslen-Wilson, W. D., Rowe, J. B., Shafto, M. A., Campbell, K., Cheung, T., Davis, S., Geerligs, L., Kievit, R., ... Henson, R. N. (2015). State and trait components of functional connectivity: Individual differences vary with mental state. *Journal of Neuroscience*, 35(41), 13949–13961. <https://doi.org/10.1523/JNEUROSCI.1324-15.2015>
- Geerligs, L., Tsvetanov, K. A., Cam-CAN, & Henson, R. N. (2017). Challenges in measuring individual differences in functional connectivity using fMRI: The case of healthy aging. *Human Brain Mapping*, 38(8), 4125–4156. <https://doi.org/10.1002/hbm.23653>
- Gómez-Robles, A., Hopkins, W. D., Schapiro, S. J., & Sherwood, C. C. (2015). Relaxed

genetic control of cortical organization in human brains compared with chimpanzees. *Proceedings of the National Academy of Sciences*, 112(48), 14799–14804. <https://doi.org/10.1073/pnas.1512646112>

Gonneaud, J., Baria, A. T., Binette, A. P., Gordon, B. A., Chhatwal, J. P., Cruchaga, C., Jucker, M., Levin, J., Salloway, S., Farlow, M., Gauthier, S., Benzinger, T. L. S., Morris, J. C., Bateman, R. J., Breitner, J. C. S., Poirier, J., Vachon-Preseau, E., & Villeneuve, S. (2020). Functional brain age prediction suggests accelerated aging in preclinical familial Alzheimer's disease, irrespective of fibrillar amyloid-beta pathology. *BioRxiv*, 0, 1–24. <https://doi.org/10.1101/2020.05.06.076745>

Gonneaud, J., Baria, A. T., Pichet Binette, A., Gordon, B. A., Chhatwal, J. P., Cruchaga, C., Jucker, M., Levin, J., Salloway, S., Farlow, M., Gauthier, S., Benzinger, T. L. S., Morris, J. C., Bateman, R. J., Breitner, J. C. S., Poirier, J., Vachon-Preseau, E., Villeneuve, S., Alzheimer's Disease Neuroimaging Initiative (ADNI), ... Vachon-Preseau, E. (2021). Accelerated functional brain aging in pre-clinical familial Alzheimer's disease. *Nature Communications*, 12(1), 5346. <https://doi.org/10.1038/s41467-021-25492-9>

Gratton, C., Laumann, T. O., Nielsen, A. N., Greene, D. J., Gordon, E. M., Gilmore, A. W., Nelson, S. M., Coalson, R. S., Snyder, A. Z., Schlaggar, B. L., Dosenbach, N. U. F., & Petersen, S. E. (2018). Functional Brain Networks Are Dominated by Stable Group and Individual Factors, Not Cognitive or Daily Variation. *Neuron*, 98(2), 439-452.e5. <https://doi.org/10.1016/j.neuron.2018.03.035>

Guo, C. C., Kurth, F., Zhou, J., Mayer, E. A., Eickhoff, S. B., Kramer, J. H., & Seeley, W.

- W. (2012). One-year test-retest reliability of intrinsic connectivity network fMRI in older adults. *NeuroImage*, 61(4), 1471–1483.
<https://doi.org/10.1016/j.neuroimage.2012.03.027>
- Harris, C. R., Millman, K. J., van der Walt, S. J., Gommers, R., Virtanen, P., Cournapeau, D., Wieser, E., Taylor, J., Berg, S., Smith, N. J., Kern, R., Picus, M., Hoyer, S., van Kerkwijk, M. H., Brett, M., Haldane, A., del Río, J. F., Wiebe, M., Peterson, P., ... Oliphant, T. E. (2020). Array programming with NumPy. *Nature*, 585(7825), 357–362. <https://doi.org/10.1038/s41586-020-2649-2>
- Horien, C., Noble, S., Finn, E. S., Shen, X., Scheinost, D., & Constable, T. (2018). Considering factors affecting the connectome-based identification process: Comment on Waller et al. *NeuroImage*, 01(203), 172–175.
<https://doi.org/10.1016/j.neuroimage.2017.12.045>.Considering
- Horien, C., Shen, X., Scheinost, D., & Constable, R. T. (2019). The individual functional connectome is unique and stable over months to years. *NeuroImage*, 189(February), 676–687. <https://doi.org/10.1016/j.neuroimage.2019.02.002>
- Hu, D., Wang, F., Zhang, H., Wu, Z., Zhou, Z., Li, G. G., Wang, L., Lin, W., & Li, G. G. (2022). Existence of Functional Connectome Fingerprint during Infancy and Its Stability over Months. *The Journal of Neuroscience*, 42(3), 377–389.
<https://doi.org/10.1523/jneurosci.0480-21.2021>
- Jalbrzikowski, M., Liu, F., Foran, W., Klei, L., Calabro, F. J., Roeder, K., Devlin, B., & Luna, B. (2020). Functional connectome fingerprinting accuracy in youths and adults is similar when examined on the same day and 1.5-years apart. *Human Brain Mapping*, 41(15), 4187–4199. <https://doi.org/10.1002/hbm.25118>

- Kaufmann, T., Alnæs, D., Brandt, C. L., Bettella, F., Djurovic, S., Andreassen, O. A., & Westlye, L. T. (2018). Stability of the brain functional connectome fingerprint in individuals with schizophrenia. *JAMA Psychiatry*, 75(7), 749–751. <https://doi.org/10.1001/jamapsychiatry.2018.0844>
- Kaufmann, T., Alnæs, D., Doan, N. T., Brandt, C. L., Andreassen, O. A., & Westlye, L. T. (2017). Delayed stabilization and individualization in connectome development are related to psychiatric disorders. *Nature Neuroscience*, 20(4), 513–515. <https://doi.org/10.1038/nn.4511>
- Kupis, L., Goodman, Z. T., Kornfeld, S., Hoang, S., Romero, C., Dirks, B., Dehoney, J., Chang, C., Spreng, R. N., Nomi, J. S., & Uddin, L. Q. (2021). Brain Dynamics Underlying Cognitive Flexibility Across the Lifespan. *Cerebral Cortex*, 31(11), 5263–5274. <https://doi.org/10.1093/cercor/bhab156>
- Lin Pedersen, T. (2020). patchwork: The Composer of Plots (1.1.1).
- Mansour L, S., Tian, Y., Yeo, B. T. T., Cropley, V., & Zalesky, A. (2020). High-resolution connectomic fingerprints: Mapping neural identity and behavior. *NeuroImage*, 229(December 2020). <https://doi.org/10.1016/j.neuroimage.2020.117695>
- Mantwill, M., Gell, M., Krohn, S., & Finke, C. (2022). Brain connectivity fingerprinting and behavioural prediction rest on distinct functional systems of the human connectome. *Communications Biology*, 5(1), 261. <https://doi.org/10.1038/s42003-022-03185-3>
- Marrelec, G., Krainik, A., Duffau, H., Péligrini-Issac, M., Lehericy, S., Doyon, J., &

- Benali, H. (2006). Partial correlation for functional brain interactivity investigation in functional MRI. *NeuroImage*, 32(1), 228–237.
<https://doi.org/10.1016/j.neuroimage.2005.12.057>
- McKinney, W. (2010). Data Structures for Statistical Computing in Python. In S. J. van der Walt & K. J. Millman (Eds.), *Proceedings of the 9th Python in Science Conference* (pp. 56–61). <https://doi.org/10.25080/Majora-92bf1922-00a>
- Mowinckel, A. M., & Vidal-Piñeiro, D. (2020). Visualization of Brain Statistics With R Packages ggseg and ggseg3d. *Advances in Methods and Practices in Psychological Science*, 3(4), 466–483.
<https://doi.org/10.1177/2515245920928009>
- Mueller, S., Wang, D., Fox, M. D., Yeo, B. T. T., Sepulcre, J., Sabuncu, M. R., Shafee, R., Lu, J., & Liu, H. (2013). Individual Variability in Functional Connectivity Architecture of the Human Brain. *Neuron*, 77(3), 586–595.
<https://doi.org/10.1016/j.neuron.2012.12.028>
- Nadig, A., Seidlitz, J., McDermott, C. L., Liu, S., Bethlehem, R., Moore, T. M., Mallard, T. T., Clasen, L. S., Blumenthal, J. D., Lalonde, F., Gur, R. E. R. C. R. E., Gur, R. E. R. C. R. E., Bullmore, E. T., Satterthwaite, T. D., & Raznahan, A. (2021). Morphological integration of the human brain across adolescence and adulthood. *Proceedings of the National Academy of Sciences of the United States of America*, 118(14), 1–10. <https://doi.org/10.1073/pnas.2023860118>
- Orban, P., Madjar, C., Savard, M., Dansereau, C., Tam, A., Das, S., Evans, A. C., Rosa-Neto, P., Breitner, J. C. S., Bellec, P., Aisen, P., Pascoal, T. A., Anthal, E., Appleby, M., Barkun, A., Beaudry, T., Benbouhoud, F., Bohbot, V., Brandt, J., ...

- Wang, S. (2015). Test-retest resting-state fMRI in healthy elderly persons with a family history of Alzheimer's disease. *Scientific Data*, 2, 1–11.
<https://doi.org/10.1038/sdata.2015.43>
- Ousdal, O. T., Kaufmann, T., Kolskår, K., Vik, A., Wehling, E., Lundervold, A. J., Lundervold, A., & Westlye, L. T. (2020). Longitudinal stability of the brain functional connectome is associated with episodic memory performance in aging. *Human Brain Mapping*, 41(3), 697–709. <https://doi.org/10.1002/hbm.24833>
- Power, J. D., Cohen, A. L., Nelson, S. M., Wig, G. S., Barnes, K. A., Church, J. A., Vogel, A. C., Laumann, T. O., Miezin, F. M., Schlaggar, B. L., & Petersen, S. E. (2011). Functional Network Organization of the Human Brain. *Neuron*, 72(4), 665–678. <https://doi.org/10.1016/j.neuron.2011.09.006>
- Pritschet, L., Santander, T., Taylor, C. M., Layher, E., Yu, S., Miller, M. B., Grafton, S. T., & Jacobs, E. G. (2020). Functional reorganization of brain networks across the human menstrual cycle. *NeuroImage*, 220, 117091.
<https://doi.org/10.1016/j.neuroimage.2020.117091>
- R Core Team. (2020). R: A language and environment for statistical computing. R Foundation for Statistical Computing.
- Schaefer, A., Kong, R., Gordon, E. M., Laumann, T. O., Zuo, X.-N., Holmes, A. J., Eickhoff, S. B., & Yeo, B. T. T. (2018). Local-Global Parcellation of the Human Cerebral Cortex from Intrinsic Functional Connectivity MRI. *Cerebral Cortex*, 28(9), 3095–3114. <https://doi.org/10.1093/cercor/bhx179>
- Setton, R., Mwilambwe-Tshilobo, L., Girn, M., Lockrow, A. W., Baracchini, G., Hughes,

- C., Lowe, A. J., Cassidy, B. N., Li, J., Luh, W.-M., Bzdok, D., Leahy, R. M., Ge, T., Margulies, D. S., Misić, B., Bernhardt, B. C., Stevens, W. D., De Brigard, F., Kundu, P., ... Spreng, R. N. (2022). Age differences in the functional architecture of the human brain. *Cerebral Cortex*, bhac056.
<https://doi.org/10.1093/cercor/bhac056>
- Shafiei, G., Markello, R. D., De Wael, R. V., Bernhardt, B. C., Fulcher, B. D., & Misić, B. (2020). Topographic gradients of intrinsic dynamics across neocortex. *ELife*, 9, 1–24. <https://doi.org/10.7554/eLife.62116>
- Shafto, M. A., Tyler, L. K., Dixon, M., Taylor, J. R., Rowe, J. B., Cusack, R., Calder, A. J., Marslen-Wilson, W. D., Duncan, J., Dalgleish, T., Henson, R. N., Brayne, C., Bullmore, E., Campbell, K., Cheung, T., Davis, S., Geerlings, L., Kievit, R., McCarrey, A., ... Matthews, F. E. (2014). The Cambridge Centre for Ageing and Neuroscience (Cam-CAN) study protocol: A cross-sectional, lifespan, multidisciplinary examination of healthy cognitive ageing. *BMC Neurology*, 14(1), 1–25. <https://doi.org/10.1186/s12883-014-0204-1>
- Sporns, O., & Betzel, R. F. (2016). Modular brain networks. *Annual Review of Psychology*, 67(September 2015), 613–640. <https://doi.org/10.1146/annurev-psych-122414-033634>
- Stimson, J. A., Carmines, E. G., & Zeller, R. A. (1978). Interpreting Polynomial Regression. *Sociological Methods & Research*, 6(4), 515–524.
- Taylor, J. R., Williams, N., Cusack, R., Auer, T., Shafto, M. A., Dixon, M., Tyler, L. K., Cam-CAN, & Henson, R. N. (2017). The Cambridge Centre for Ageing and Neuroscience (Cam-CAN) data repository: Structural and functional MRI, MEG,

- and cognitive data from a cross-sectional adult lifespan sample. *NeuroImage*, 144, 262–269. <https://doi.org/10.1016/j.neuroimage.2015.09.018>
- The pandas development team. (2020). pandas-dev/pandas: Pandas (1.1.3). Zenodo. <https://doi.org/10.5281/zenodo.3509134>
- Vallat, R. (2018). Pingouin: Statistics in Python. *Journal of Open Source Software*, 3(31), 1026. <https://doi.org/10.21105/joss.01026>
- Van De Ville, D., Farouj, Y., Preti, M. G., Liégeois, R., & Amico, E. (2021). When makes you unique: Temporality of the human brain fingerprint. *Science Advances*, 7(42), 1–11. <https://doi.org/10.1126/sciadv.abj0751>
- Vanderwal, T., Eilbott, J., Finn, E. S., Craddock, R. C., Turnbull, A., & Castellanos, F. X. (2017). Individual differences in functional connectivity during naturalistic viewing conditions. *NeuroImage*, 157(April), 521–530. <https://doi.org/10.1016/j.neuroimage.2017.06.027>
- Vanderwal, T., Eilbott, J., Kelly, C., Frew, S. R., Woodward, T. S., Milham, M. P., & Castellanos, F. X. (2021). Stability and similarity of the pediatric connectome as developmental measures. *NeuroImage*, 226(November 2019), 117537. <https://doi.org/10.1016/j.neuroimage.2020.117537>
- Váša, F., Seidlitz, J., Romero-Garcia, R., Whitaker, K. J., Rosenthal, G., Vértes, P. E., Shinn, M., Alexander-Bloch, A., Fonagy, P., Dolan, R. J., Jones, P. B., Goodyer, I. M., Sporns, O., & Bullmore, E. T. (2018). Adolescent tuning of association cortex in human structural brain networks. *Cerebral Cortex*, 28(1), 281–294. <https://doi.org/10.1093/cercor/bhx249>
- Virtanen, P., Gommers, R., Oliphant, T. E., Haberland, M., Reddy, T., Cournapeau, D.,

- Burovski, E., Peterson, P., Weckesser, W., Bright, J., van der Walt, S. J., Brett, M., Wilson, J., Millman, K. J., Mayorov, N., Nelson, A. R. J., Jones, E., Kern, R., Larson, E., ... Vázquez-Baeza, Y. (2020). SciPy 1.0: Fundamental algorithms for scientific computing in Python. *Nature Methods*, 17(3), 261–272.
<https://doi.org/10.1038/s41592-019-0686-2>
- Vuong, Q. H., Econometrica, S., & Mar, N. (1989). Likelihood Ratio Tests for Model Selection and Non-Nested Hypotheses Published by: The Econometric Society. *Econometrica*, 57(2), 307–333.
- Westfall, P. H. (2011). On using the bootstrap for multiple comparisons. *Journal of Biopharmaceutical Statistics*, 21(6), 1187–1205.
<https://doi.org/10.1080/10543406.2011.607751>
- Wickham, H., Averick, M., Bryan, J., Chang, W., D’Agostino McGowan, L., François, R., Grolemund, G., Hayes, A., Henry, L., Hester, J., Kuhn, M., Lin Pedersen, T., Miller, E., Milton Bache, S., Muller, K., Ooms, J., Robinson, D., Paige Seidel, D., Spinu, V., ... Yutani, H. (2019). Welcome to the tidyverse. *Journal of Open Source Software*, 4(43), 1686. <https://doi.org/10.21105/joss.01686>
- Xu, T., Opitz, A., Craddock, R. C., Wright, M. J., Zuo, X. N., & Milham, M. P. (2016). Assessing Variations in Areal Organization for the Intrinsic Brain: From Fingerprints to Reliability. *Cerebral Cortex*, 26(11), 4192–4211.
<https://doi.org/10.1093/cercor/bhw241>
- Yeo, T. B., Krienen, F. M., Sepulcre, J., Sabuncu, M. R., Lashkari, D., Hollinshead, M., Roffman, J. L., Smoller, J. W., Zöllei, L., Polimeni, J. R., Fisch, B., Liu, H., & Buckner, R. L. (2011). The organization of the human cerebral cortex estimated

by intrinsic functional connectivity. *Journal of Neurophysiology*, 106(3), 1125–1165. <https://doi.org/10.1152/jn.00338.2011>

Zalesky, A., Fornito, A., & Bullmore, E. (2012). On the use of correlation as a measure of network connectivity. *NeuroImage*, 60(4), 2096–2106. <https://doi.org/10.1016/j.neuroimage.2012.02.001>

Zonneveld, H. I., Pruijm, R. H., Bos, D., Vrooman, H. A., Muetzel, R. L., Hofman, A., Rombouts, S. A., van der Lugt, A., Niessen, W. J., Ikram, M. A., & Vernooij, M. W. (2019). Patterns of functional connectivity in an aging population: The Rotterdam Study. *NeuroImage*, 189(September 2018), 432–444. <https://doi.org/10.1016/j.neuroimage.2019.01.041>

2.10 – Supplementary material of Chapter 2

2.10.1 – Methods

Identifying regions contributing to fingerprinting metrics

a. Connectome predictive modelling

We tested whether edges most associated with fingerprint metrics changed during the lifespan by adapting a connectome predictive modelling approach. (Shen et al., 2017) Procedures are illustrated in Supp Fig 2.7 and can be divided in three major sections: I) Sample selection, II) Cross-validation and III) Generalizability.

In the sample selection section, we used the sliding-window approach described in the methods section of the manuscript. Once windows were derived, each window was split in a training and testing set, where 85% of the participants were retained for training and 15% for testing the generalizability of the model. (Varoquaux et al., 2017)

During the cross-validation section, we used a leave-one-out procedure (1) (Supp Fig 2.7C). (Scheinost et al., 2019) In each iteration, each of the 160,000 FC edges for participants in the training set were correlated to their measured fingerprint metrics of interest (self-identifiability or others-identifiability) using product–moment correlations (2). Edges with significant ($p < 0.01$) negative (lower FC associated with higher fingerprint metric) and positive (higher FC associated with higher fingerprint metric) correlations ($p < 0.01$) were kept and considered as potential predictors of the fingerprint metric of interest (3). The fingerprint metric of interest was calculated at the whole-sample level, and not within individual sliding windows. We then created two binary masks at the whole-brain level; one including significant edges from positive correlations and the other including significant edges from negative correlations (4). After discarding the lower

triangle of the binary masks (symmetric projection of the upper triangle), FC values in the significant edges were then summed to obtain a single value per participant for each mask (5). These sums were used to train the models to predict the fingerprint metric of interest (6). We used two different algorithms to train the models: a simple linear regression and a support vector regression with radial basis function kernel. For the support vector regression, both the feature and outcome were scaled to a mean of 0 and standard deviation of 1 before training the model. Hyperparameters (C, gamma and epsilon) for the final model were determined during cross-validation using a grid search technique. The positive and negative masks were then applied separately to the left-out participant (7) and their FC sum (8) was used to validate the models (9). As a last step we developed a positive and a negative cross-validated binary mask, where edges that were significant across 95% of the cross-validation runs were kept (10), and the rest was discarded. This process was done to identify FC edges that were recurrently predictive across participants of a given age group bin.

In the generalization section, we tested the predictive value of the positively associated and negatively associated models using the corresponding cross-validated binary masks in the test set (i.e., participants that were not used to develop the predictive models). The FC values in the cross-validated binary masks were summed for each participant of the test set (11) and used to predict the fingerprint metrics (12). Model generalizability in the test set was assessed by correlating the predicted and measured fingerprint metrics in the test set participants and by measuring the root mean square error.

Finally, we used the averaged cross-validated positive and negative binary masks to determine which inter-regional FC values were associated with our fingerprint metrics across the lifespan using the between-individual sliding window approach. Specifically, we divided the masks for each subsample in within- and between-network edges for each of the Yeo networks. Then, we calculated the proportion of predictive edges in each network by dividing the number of predictive edges over the total number of edges in the network. These proportions were then plotted for visualization.

b. Edge-wise intraclass correlation

We adapted the edge-wise intraclass correlation (ICC) methodology from Amico and Goñi (2018) (see Supp Fig 2.10) to determine which edges contributed to self- and others-identifiability across the lifespan. In our context, we refer to intra-rater reliability ICC measures (as opposed to inter-rater reliability); i.e., how similar a score is for different targets within each rater. (Shrout & Fleiss, 1979) Specifically, we use the ICC form referred to as ICC(3,1) in the original publication (Koo & Li, 2016; Shrout & Fleiss, 1979) for single fixed raters. We consider two types of raters. For the first type, we consider each participant as a rater, and we consider targets as the FC of a given edge for both modalities. In this analysis, the ICC reflects how consistent the value of the edge is between the Rest and Task sessions for each participant. When the edge values of both tasks are close to one another (i.e., the difference between the two values is small), across all raters, then the ICC value for an edge would be high. Conversely, if the edge values are very different between the Rest and Task sessions across all raters, then the ICC value for an edge would be low. This first ICC measure relates to self-identifiability. While self-identifiability is derived from correlating the entire functional connectivity of a

given network during rest to the entire functional connectivity of the same network during the task, edges with consistent values (i.e., high ICC) between Rest and Task are likely to contribute to higher self-identifiability due to their similarity in each participant. For the second intra-rater ICC, we set the raters as the fMRI conditions and the targets as the FC of the edge of individual participants within each condition. In this analysis, the ICC reflects how consistent the value of an edge is across participants within each modality. If the value of the edge is consistent across all participants in both the rest and task conditions individually, the resulting ICC will be high. Conversely, if the edge value differs between participants in each modality, this would result in a low ICC. This second ICC measure relates to others-identifiability. Others-identifiability is computed by correlating the functional connectivity of one participant to the functional connectivity of a different participant. As such, if an edge has consistent values across participants in each modality, it will likely result in a higher others-identifiability. This process was done for every age window, and FC edge, yielding two matrices of 160,000 edges per age bin. The lower triangle was ignored for the rest of the analyses.

Once edge-wise ICC were derived, we first thresholded the coefficients to retain the edges contributing most to self- or others-identifiability by using values above the 95th percentile. Then, we computed the mean and standard deviation of the ICC for both within- and between-network FC. Finally, the ICC in each edge retained after thresholding was binarized: values above the 95th percentile were set to one and the rest were set to zero. The mean and standard deviation of the ICC values were then plotted for each age window.

Then, we aimed to determine whether edges identified as contributing most to self- and others-identifiability would remain the same through the lifespan. To do so, we used the binarized matrices of the ICC and the Jaccard Similarity Index (Jaccard, 1912). The Jaccard Similarity Index measures the size of the intersection of two binary arrays over their union, yielding a score ranging from zero to one, where one is a perfect overlap between the two arrays. We applied this measure by comparing the overlap of the binary arrays between each pair of adjacent age group bins (e.g., the binary array of the youngest group compared to the binary array of the second youngest group). Higher values indicate the highest weighted edges that predict identifiability overlap between adjacent groups. We also applied this method to compare the overlap between the binary arrays of the edges contributing most to self-identifiability and the binary arrays of the edges contributing most to others-identifiability. As the Jaccard Index represents a proportion of overlap by network, we can compute a 95% confidence interval of that proportion, by calculating the standard deviation of the proportion and multiplying it by the desired degree of confidence.

Finally, we checked whether certain nodes have edges which contribute predominantly to self- and others-identifiability. Based on methodology by Amico & Goñi (2018), we computed the nodal density of each node in the binarized ICC matrix. Briefly, each row of the matrix was summed, ignoring the diagonal. Then, the sum was divided by the number of edges. This yields a nodal density measure for all 400 nodes of the Schaefer atlas. These results were then projected onto a parcellation.

c. Clustering

To determine if specific edges overlapped between individual- and group-level FC patterns, we adopted a K-means clustering approach. Specifically, the FC edges of the upper triangle of FC matrix (79,800 edges) of all participants within each age window were averaged across participants to obtain a group-level average of FC. Then, we used a K-means clustering approach to cluster the group-level average edges. We chose a 7-cluster solution to match the number of expected networks from the Schaefer parcellation used throughout the paper. The labels assigned by the clustering algorithm for each edge were saved. Then, we repeated the procedure but this time at the individual-level; we applied a 7-cluster K-means clustering algorithm to cluster the 79,800 edges of each participant. Finally, we computed the overlap of individual- and group-level clusters using the Jaccard coefficient. Specifically, for each cluster (from 1 to 7), we computed the average overlap between individual participants and the group-level FC average, where '1' indicates a perfect overlap of the cluster assignments and '0' indicates poor overlap of the cluster assignments.

2.10.2 – Results

Regions predictive of fingerprint metrics

a. Connectome Predictive Modelling

As a complementary analysis, we used a connectome predictive modelling approach (Shen et al., 2017) to determine if any individual FC edges were predictive of self-identifiability and others-identifiability across adjacent age windows, across different sliding-window parameters (Supp Fig 2.8 and 2.9).

The connectome predictive modelling approach (Shen et al., 2017) first selected edges most associated with self-identifiability using a leave-one-out cross-validation after holding out 15% of the sample, and FC in the remaining associated edges were used to train linear and support vector regression models predicting self-identifiability. This procedure was done in each age window separately. Edges associated with self-identifiability in 95% of the cross-validations in each age window were deemed as contributing to self-identifiability. Prediction within each age window did not generalize to left-out samples, and no single network had more predictive edges for self-identifiability. Using a random set of edges instead of doing feature selection also yielded similar results (not shown). Predicting the self-identifiability across the entire sample, instead of within each age window, yielded similar results (not shown).

b. Edge-wise intraclass correlation

We used an intra-class correlation (ICC) analysis (Supp Fig 2.10), as proposed by Amico and Goñi (2018), paired with the age-group-bin sliding window approach (Figure 2.1B) to assesses intra-rater reliability. Specifically, we measured to which extent the connectivity values in each edge were consistent within each individual across the Rest and Task condition. High consistency (i.e., higher ICC) indicated that the edge contributed to self-identifiability within each participant. We also measured to which extent the connectivity values in each edge were consistent within each fMRI condition across participants. In this case high consistency (i.e., higher ICC) indicated that the edge contributed to others-identifiability in each fMRI modality. This process yielded two ICC values for each edge. Additional explanation on how the intra-rater reliability was derived is available in the supplementary methods section. The sliding window approach was

used to estimate whether the top 95% edge-weights in each window remained consistent across the lifespan. Within each age window, we thresholded the ICC values at the 95th percentile to retain edges contributing the most to each of self- and others-identifiability.

Thresholded ICC values indicated that edges contributing the most to self-identifiability were not consistent across individuals as they showed very low ICC values despite retaining only the highest 95th percentile edge values (i.e., poor consistency within raters between Rest and Task modality), while edges contributing the highest to others-identifiability were more consistent across individuals (i.e., high consistency within modalities between individual participants; Supp Fig 2.11A). This was observed across all age windows, across the whole brain connectome, within- and between-networks, and using different sliding window parameters (i.e., size of subsamples and number of participants from adjacent age-group bins). We did not find evidence that edges within or between any one network were more similar across individuals for edges contributing to self- or to others-identifiability (overlapping confidence intervals). Similar results were observed using different window parameters (not shown).

Next, we evaluated whether the edges contributing the highest to self- and others-identifiability were similar between subsamples across the lifespan (Supp Fig 2.11B). Thresholded edges were binarized: ICC values above the 95th percentile were set as one and the rest set as zero. We then computed what proportion of the retained edges overlapped between the different age windows using the Jaccard Similarity Index, ranging from 0 (no overlap) to 1 (perfect overlap). (Jaccard, 1912) A strong overlap, consistent across adjacent age groups, would indicate that edges contributing to either self- or others-identifiability were similar across individuals over the lifespan. We found that the

overlap of edges contributing to the highest self-identifiability was low between age windows: less than 25% of edges within each network overlapped between age windows. The only exceptions were the visual and somatomotor networks, where the overlap was closer to 50% and 30%, respectively. In contrast, edges contributing the highest to others-identifiability across individuals were similar across different age windows across the lifespan: between 50% to 75% of edges within each network overlapped between different age windows. This was the case whether using the whole brain connectome, within- or between-network edges, and using different sliding window parameters (not shown).

We tested the extent edges contributing to self-identifiability also contributed to others-identifiability (Supp Fig 2.11C). Within each age window, we computed the Jaccard Similarity Index between the binarized ICC values for edges contributing to self-identifiability and the binarized ICC values for edges contributing to others-identifiability. Here, a strong overlap indicates that edges contributing to self-identifiability also contributed to others-identifiability. We found that, across age windows, edges contributing to self-identifiability showed little overlap (low Jaccard Index) with edges contributing to others-identifiability. This finding was consistent when using either whole brain connectome, within- or between-network edges, or when changing the window parameters (not shown).

Finally, we computed and plotted to which extent each node had a high number of edges contributing to self- (Supp Fig 2.12) or others-identifiability (Supp Fig 2.13). Following Amico & Goñi (2018), we computed the nodal density for each of the 400 nodes included in the Schaefer atlas. For each node, we summed the number of edges above the 95th percentile contributing to either self- or others-identifiability and divided this

number by the total number of edges per region (400). The resulting nodal density indicates to which extent edges from a given node contribute to self- or others-identifiability. Overall, consistent with our previous result, all nodes tended to contribute relatively similarly to self-identifiability.

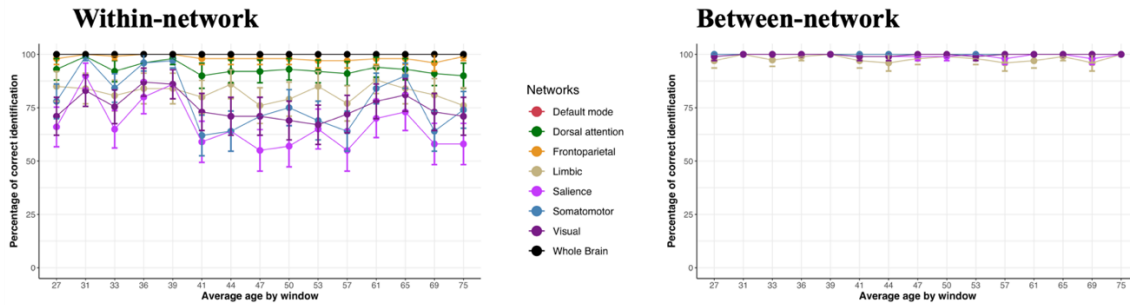
c. Clustering

We additionally used a clustering approach to confirm that FC patterns across the whole brain at the individual-level differed from group-level FC. This was to confirm that there were no evident patterns of individual-level FC that were shared across individuals and age windows, which we would expect to see if specific edges contributed to self-identifiability. In each age window, we applied a 7-cluster K-means clustering approach to FC edges in two ways: on the average FC values of all edges at group-level and on the FC values of all edges for each participant separately. We then computed the overlap between the clusters obtained at the group-level and at the individual-level, with the reasoning that individual-level cluster assignments should overlap strongly with group-level assignments if FC patterns are more similar across individuals. In line with the other previous analyses, we found very little overlap between the clusters obtained at the group-level and the clusters obtained at the individual-level (average Jaccard score across cluster labels and windows of 0.06; Supp Fig 2.14). Furthermore, the overlap between individual- and group-level clusters varied between age windows, highlighting again that slightly different group selection yields different results.

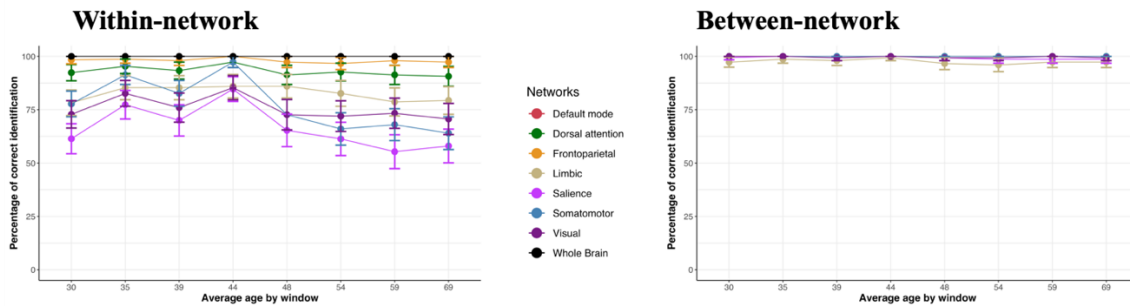
2.10.3 – Supplementary Figures

Supplementary Figure 2.1

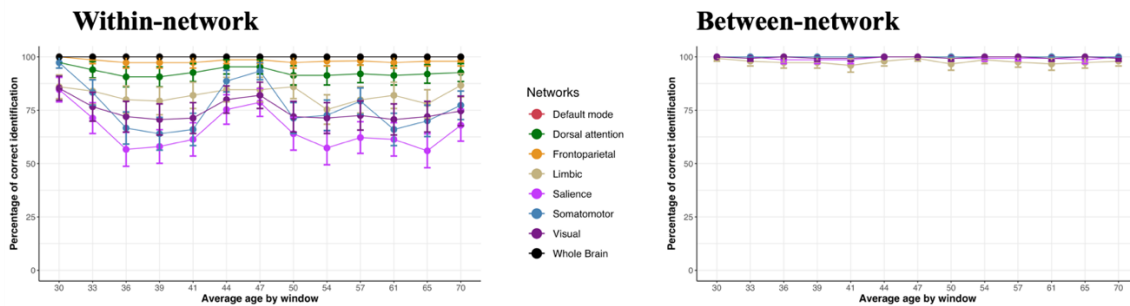
A. Identification accuracy across aging (Window size = 100, step size = 25)



B. Identification accuracy across aging (Window size = 150, step size = 40)



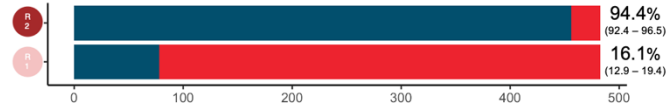
C. Identification accuracy across aging (Window size = 150, step size = 25)



Supplementary Figure 2.1 - Fingerprint identification accuracy across the lifespan using different window parameters. Like in Figure 2.2B, we illustrate the fingerprint identification accuracy using a sliding window approach, varying the size of the window (100 or 150) and the step size (40 or 25). Figure 2.2B uses a window size of 100 and a step size of 40. Accuracy using within-network (left) and between-network (right) edges are represented.

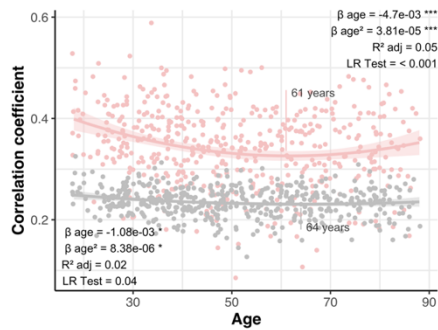
Supplementary Figure 2.2

A. Fingerprint identification accuracy in randomly selected nodes across the lifespan (Schaefer atlas)

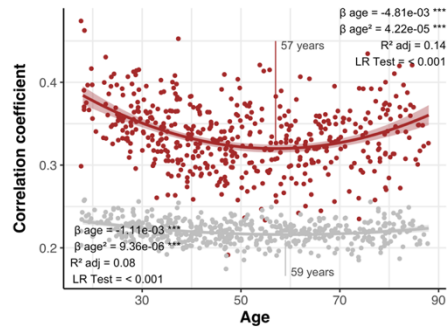


B. Self- and others-identifiability in randomly selected nodes across the lifespan (Schaefer atlas)

Small random network (22 nodes)

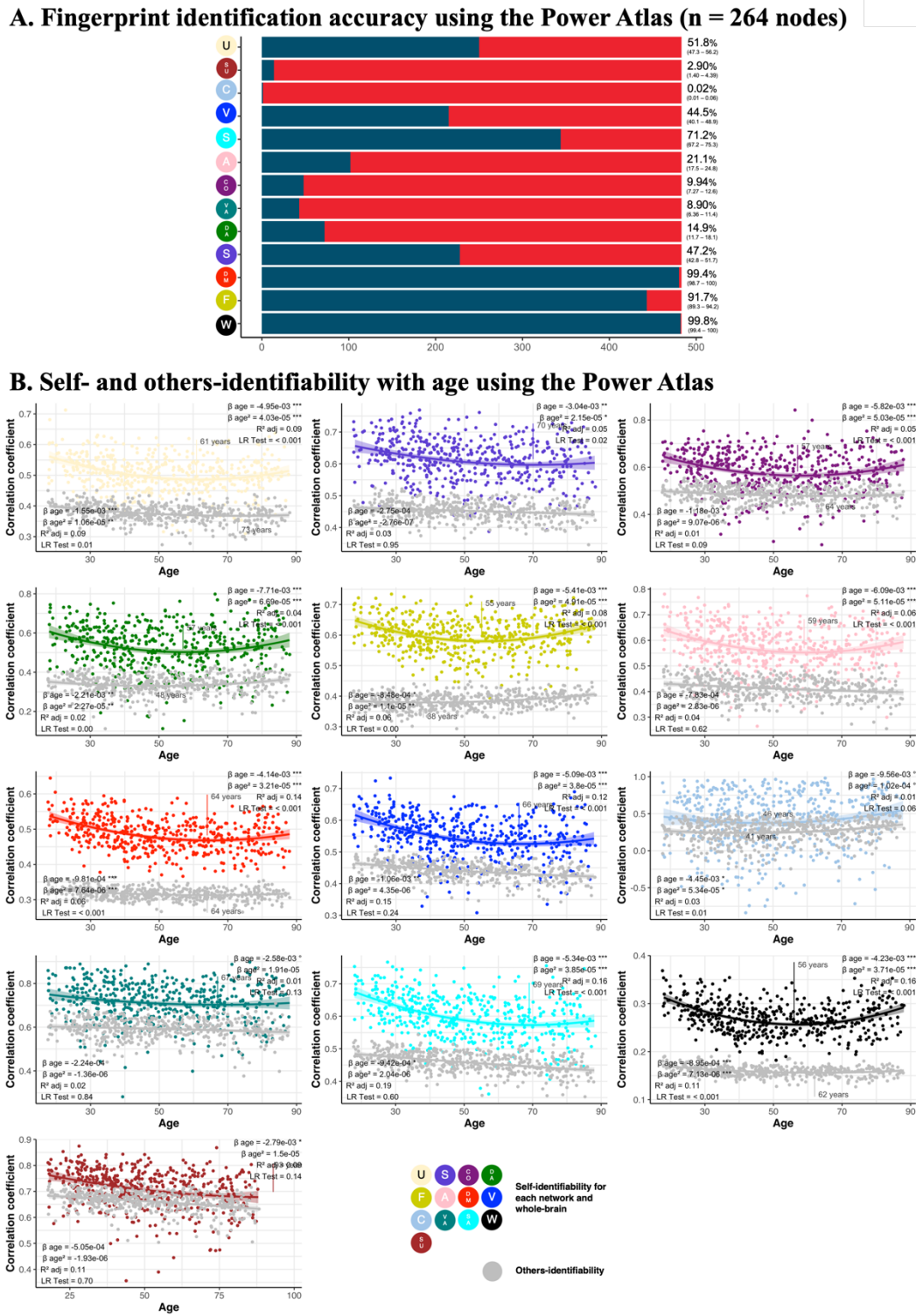


Large random network (91 nodes)



Supplementary Figure 2.2 – Fingerprint identification accuracy, and self- and others-identifiability using a randomized subset of nodes. We randomly selected two subsets of nodes from the Schaefer atlas across all regions and calculated the fingerprint identification accuracy (panel **A**) and the self- and others-identifiability (panel **B**) in both networks. The number of nodes were chosen to mirror the number of nodes in the smallest (limbic – 22 nodes) and the largest (default-mode – 91 nodes) Yeo networks using the Schaefer atlas. Edges within the randomly selected nodes were used to calculate the accuracy and the identifiability.

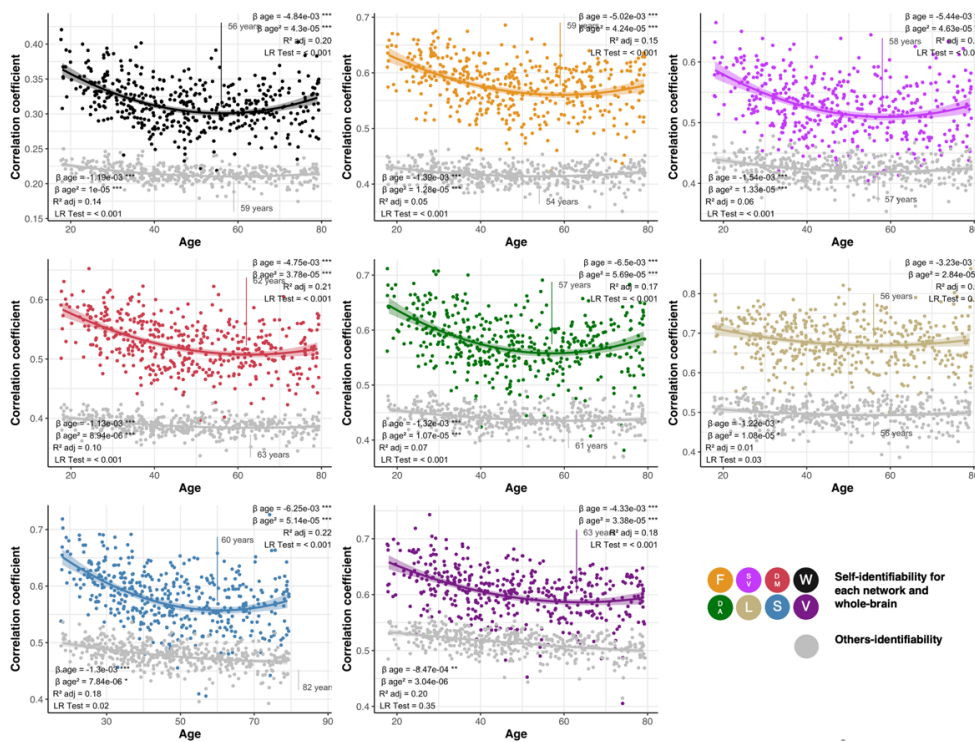
Supplementary Figure 2.3



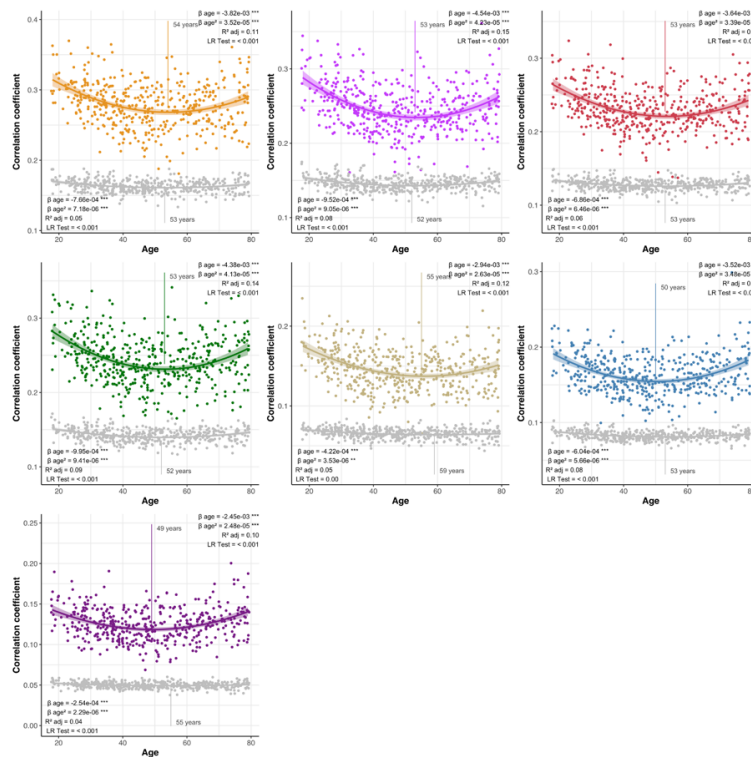
Supplementary Figure 2.3 – Fingerprint identification accuracy, and self- and others-identifiability using the Power atlas. *We replicated our results from Figure 2.2A and Figure 2.3A using a different brain parcellation: the Power atlas (Power et al. 2011). All networks from the Power atlas were replicated and the network acronyms are as follow: U (beige) = Uncertain, SA (light purple) = Salience, CO (dark purple) = Cingulo-opercular, DA (dark green) = Dorsal attention, F (light green) = Frontoparietal, A (pink) = Auditory, DM (red) = Default-mode, V (blue) = Visual, C (light blue) = Cerebellar, VA (teal) = Ventral attention, S (cyan) = Somatomotor, W (black) = Whole brain, SU (brown) = Subcortical.*

Supplementary Figure 2.4

A. Within-network edges

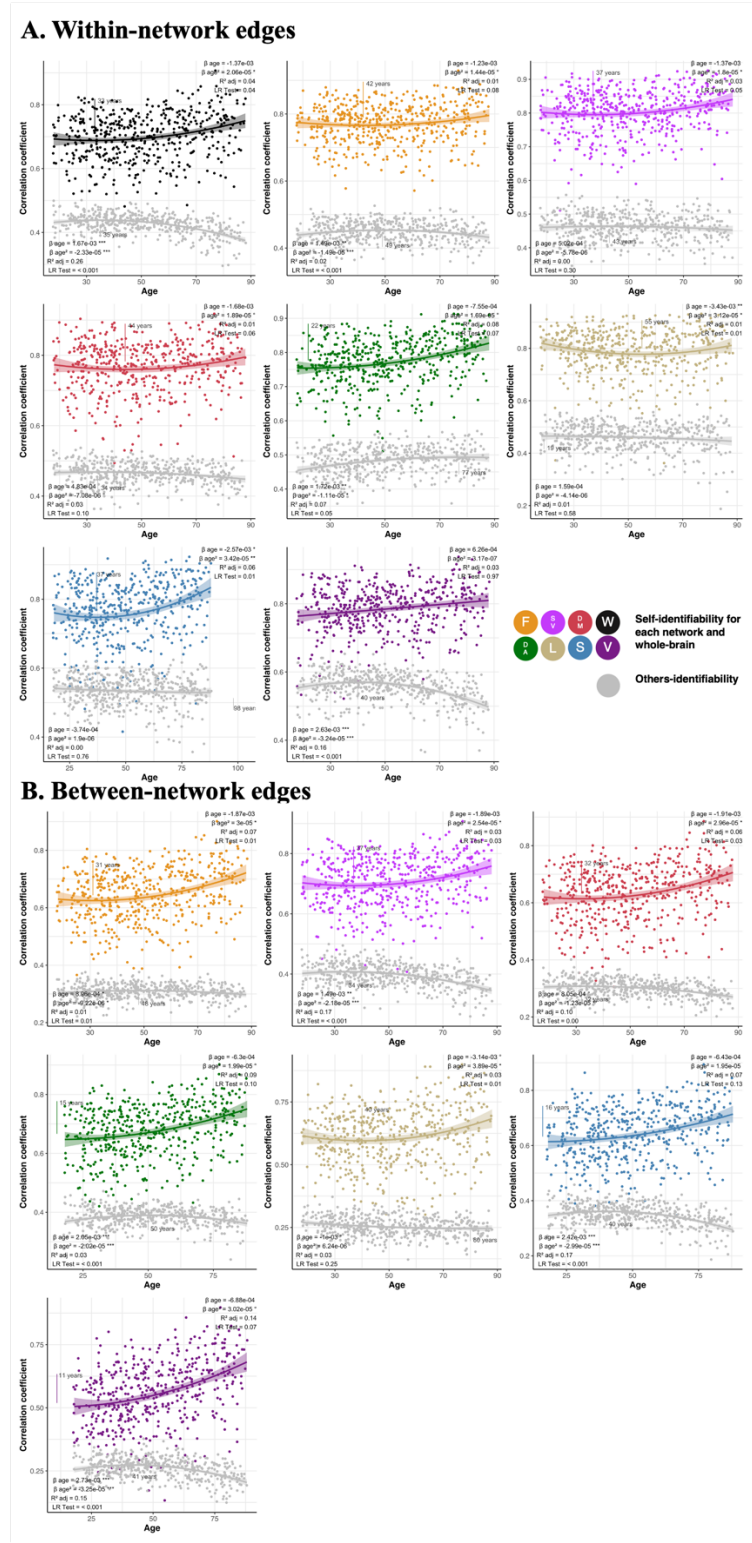


B. Between-network edges



Supplementary Figure 2.4 – Differences in self- and others-identifiability across the lifespan, excluding the last decade. *Change in self-identifiability (colors) and others-identifiability (grey) are represented using either within-network edges (A.) or between-network edges (B.). Each graph represents a different network, following acronyms and color schemes of Figure 1B. The beta coefficient of the age term and its quadratic term are presented at the top of the graph. We also present the adjusted R^2 of the model and the p -value of the nested likelihood ratio indicating the non-linearity of the relationship. The p -value of predictors surviving inclusion of covariates and execution of the bootstrapping are indicated by asterisks ($p < 0.001 = ***$, $p < 0.01 = **$, $p < 0.05 = *$). The age at which the curve changed direction was calculated from Stimson's equation and is illustrated on the graphs. Participants aged 80-89 were excluded.*

Supplementary Figure 2.5

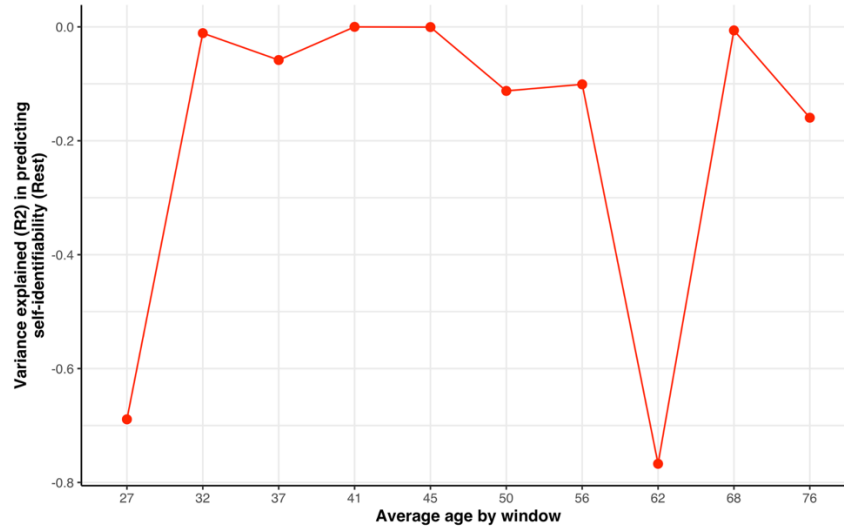


Supplementary figure 2.5 – Association between self- and others-identifiability and age across the lifespan using product–moment-calculated functional connectivity.

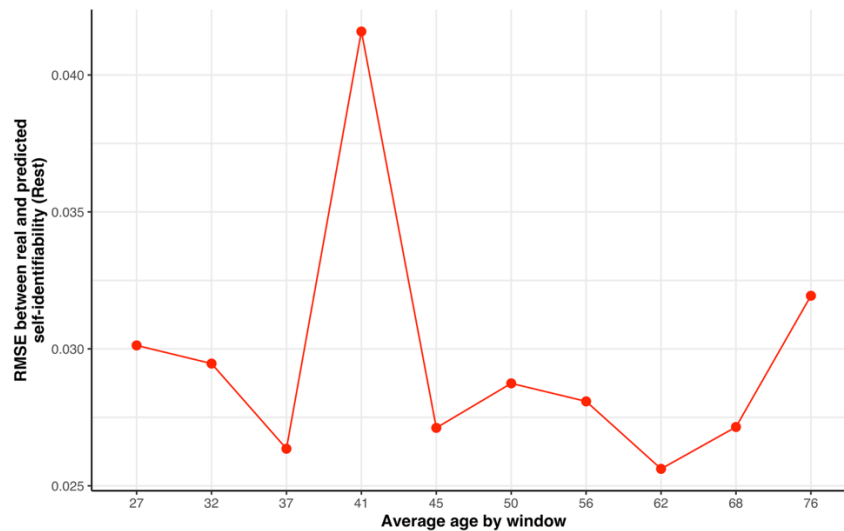
*Change in self-identifiability (colors) and others-identifiability (grey) are represented using either within-network edges (A.) or between-network edges (B.). Each graph represents a different network, following acronyms and color schemes of Figure 2.1B. The beta coefficient of the age term and its quadratic term are presented at the top of the graph. We also present the adjusted R^2 of the model and the p-value of the nested likelihood ratio indicating the non-linearity of the relationship. The p-value of predictors surviving inclusion of covariates and execution of the bootstrapping are indicated by asterisks ($p < 0.001 = ***$, $p < 0.01 = **$, $p < 0.05 = *$). The age at which the curve changed direction was calculated from Stimson's equation and is illustrated on the graphs.*

Supplementary figure 2.6

A. Variance explained of predicted self-identifiability using elastic nets (Rest modality)

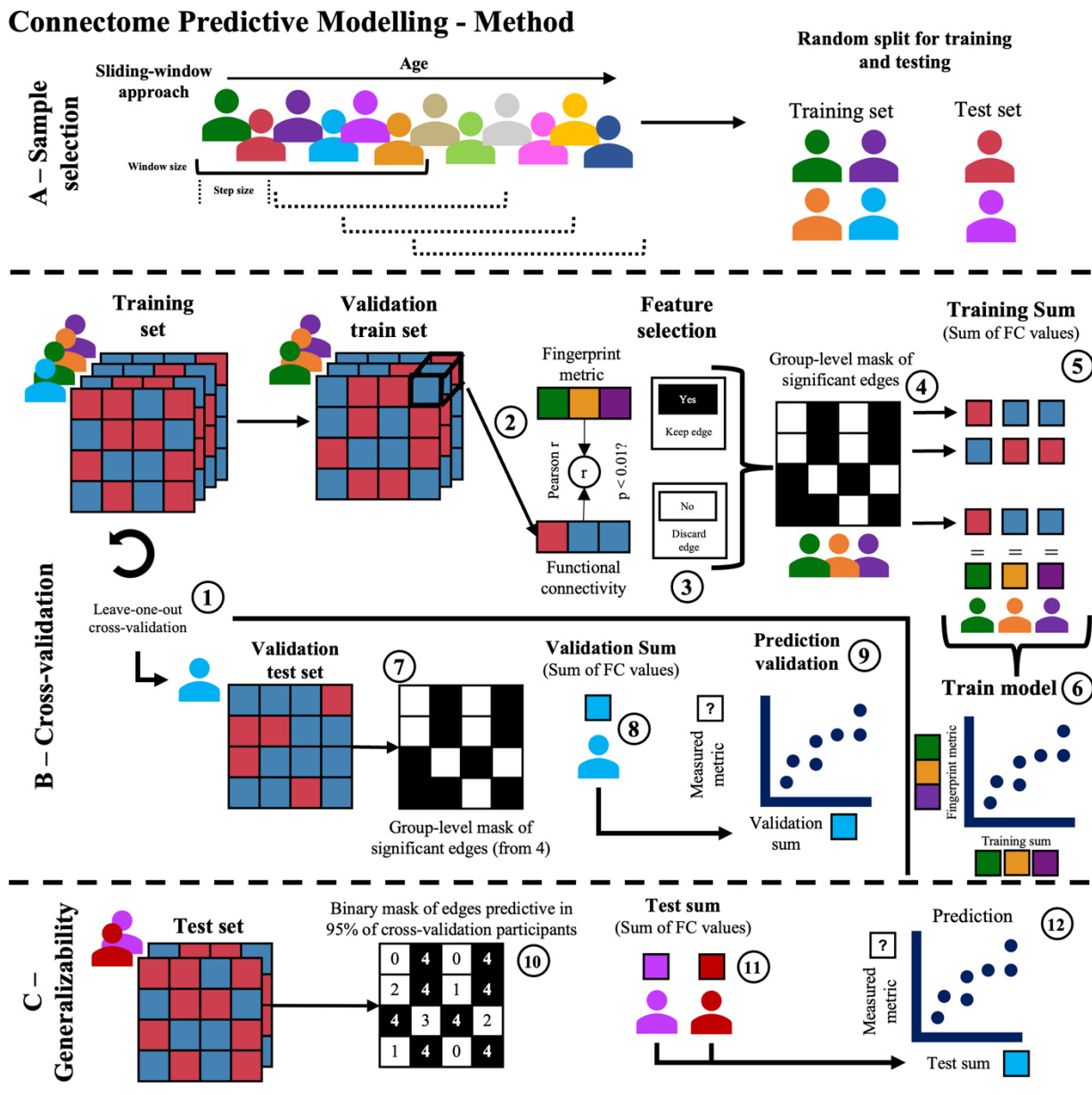


B. Root mean squared error of predicted self-identifiability using elastic nets (Rest modality)



Supplementary Figure 2.6 – Model performance of elastic net models predicting self-identifiability from FC edges. Performance of the elastic net models is presented with two metrics: variance explained (R^2 ; A) and root mean square error (RMSE; B) for each age window using a window size of 100 and a step size of 40.

Supplementary Figure 2.7

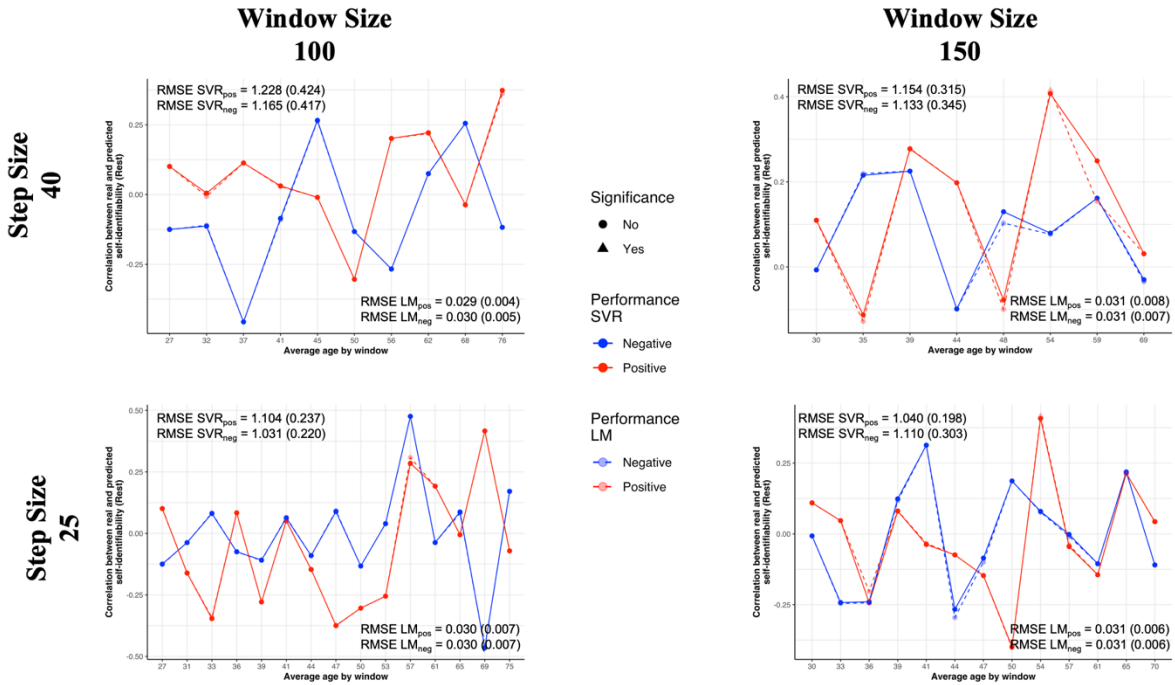


Supplementary Figure 2.7 - Illustration of the connectome predictive modelling

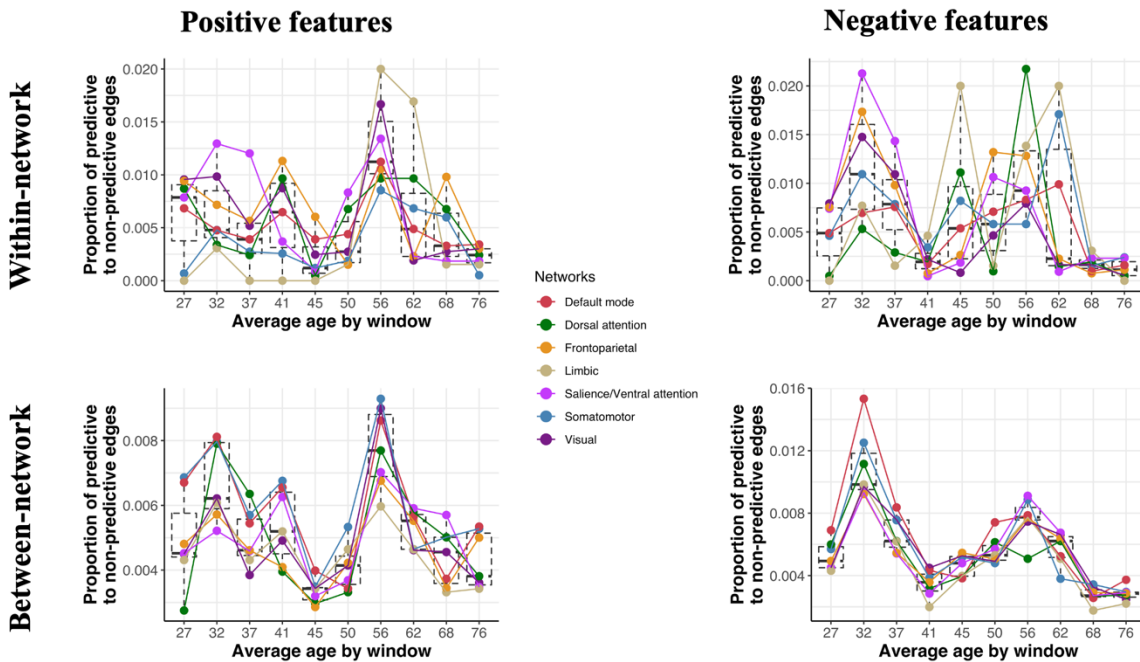
Illustration of the connectome predictive modelling in a simulated sample. The modelling is done in three main steps: Sample selection, Cross-validation, and Generalizability. Briefly, subsets of participants are chosen using a sliding-window approach. Then, functional connectivity in each edge is correlated to the fingerprint metric of interest during the cross-validation. Significantly correlated edges are used to form a mask in which we sum the FC values. These sums are then used to train a model predicting the fingerprint metric of interest. For each cross-validation, the mask derived in step 4 is applied to the left-out participant (step 7) and the sum of FC values of that participant is used to predict the fingerprint metric. In the final generalization step, edges predictive of the fingerprint metric in 95% of participants are kept. We then sum the FC values within these significant edges and use the sums to predict the fingerprint metric in the participants of the left-out test set (step 12). Both the self- and others-identifiability used in the modelling are calculated in the whole sample before the modelling.

Supplementary Figure 2.8

A. Model performance for self-identifiability (Rest modality)



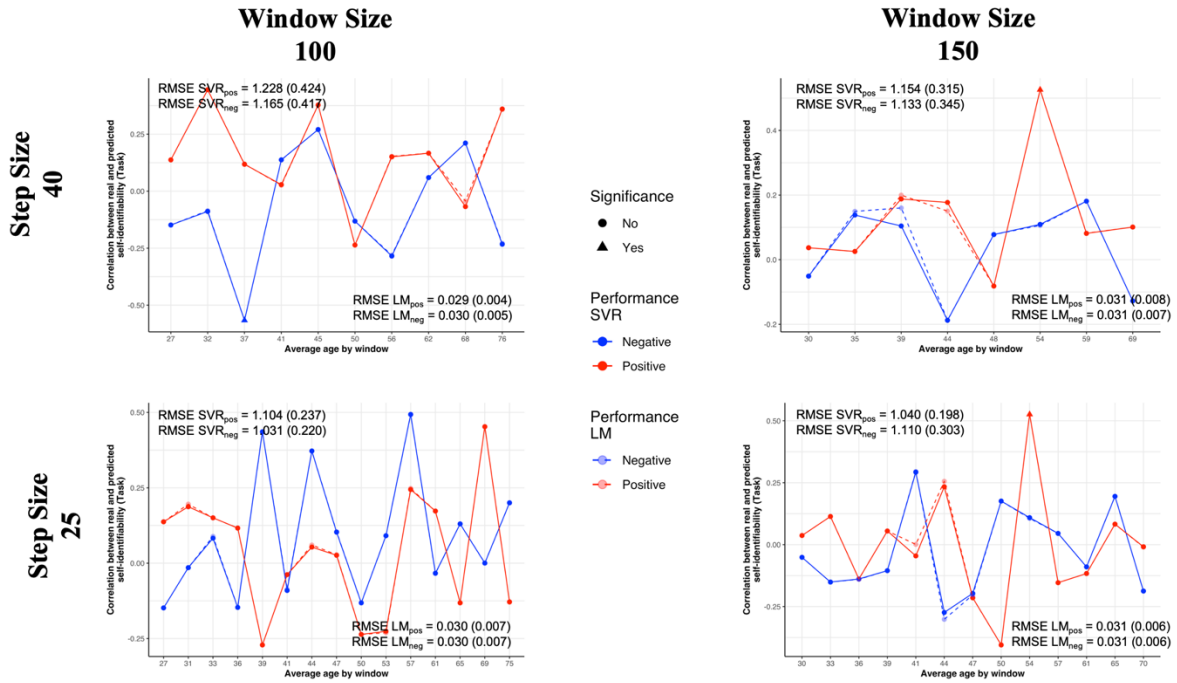
B. Edges involved in prediction (Rest; Sliding-window: 100, 40)



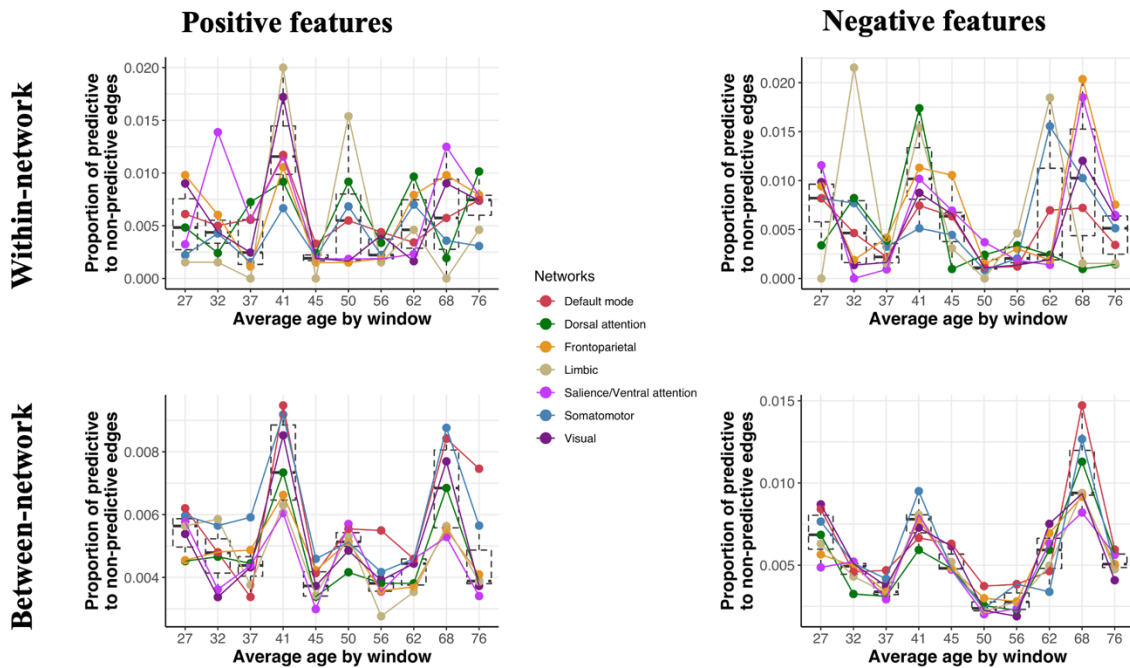
Supplementary Figure 2.8 – Connectome predictive modelling performance and predictive edges of self-identifiability (Rest modality). *Point and line graphs representing **A.** model performance (correlation of predicted and measured fingerprint values in the test set) and **B.** network over-representation of predictive edges in predicting self-identifiability. In **A.**, models using support vector regression (SVR) are presented in dashed lines and models using linear models (LM) are presented in solid lines. Average root mean square error (RMSE) across windows is presented in each graph. Graphs are presented by window size (number of participants) and step size (difference in participants included compared to previous windows). In **B.**, representative example of the proportion of edges predictive of self-identifiability in each network following cross-validation. The proportion is the number of predictive edges over the total size of the network.*

Supplementary Figure 2.9

A. Model performance for self-identifiability (Task modality)



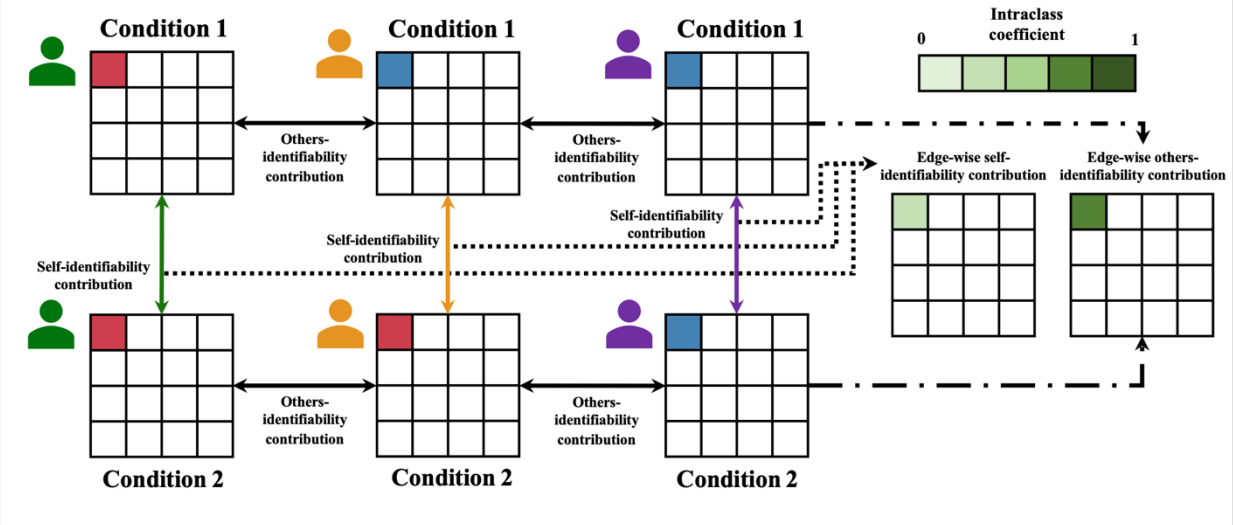
B. Edges involved in prediction (Task; Sliding-window: 100, 40)



Supplementary Figure 2.9 - Connectome predictive modelling performance and predictive edges of self-identifiability (Task modality). *Point and line graphs representing **A.** model performance (correlation of predicted and measured fingerprint values in the test set) and **B.** network over-representation of predictive edges in predicting self-identifiability. In **A.**, models using support vector regression (SVR) are presented in dashed lines and models using linear models (LM) are presented in solid lines. Average root mean square error (RMSE) across windows is presented in each graph. Graphs are presented by window size (number of participants) and step size (difference in participants included compared to previous windows). In **B.**, representative example of the proportion of edges predictive of self-identifiability in each network following cross-validation. The proportion is the number of predictive edges over the total size of the network.*

Supplementary Figure 2.10

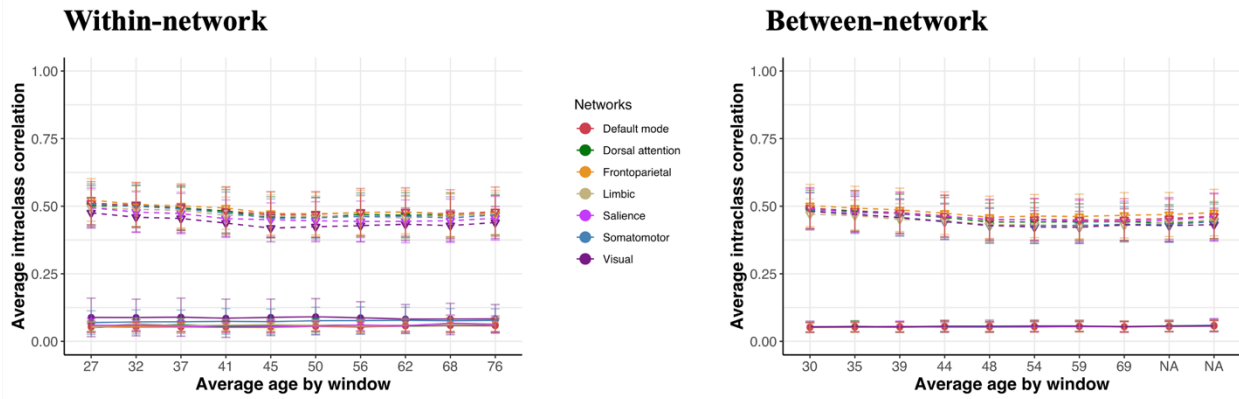
Edge-wise intraclass correlation



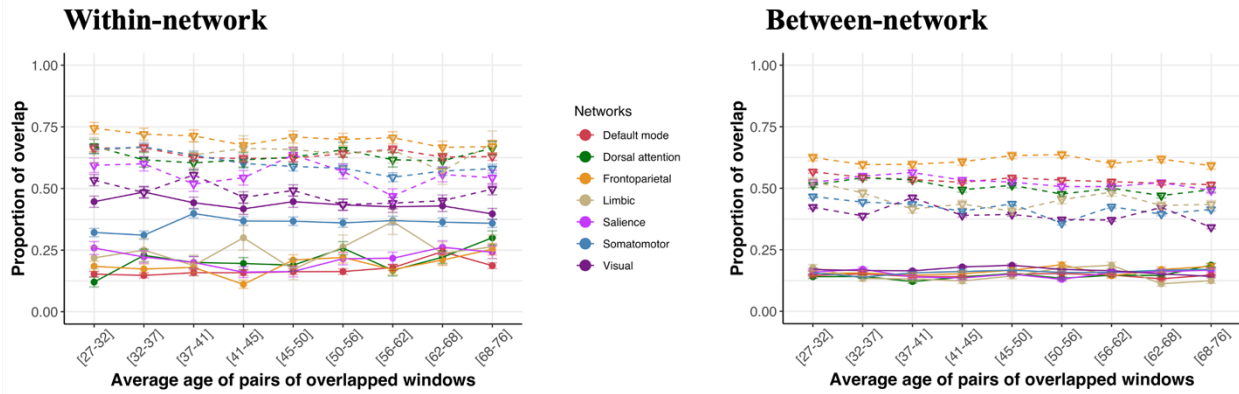
Supplementary Figure 2.10 - Illustration of the edge-wise intra-class correlation (ICC) methodology adapted from Amico & Goñi (2018). For each edge, we derive that edge's contribution to self-identifiability and to others-identifiability (ICC coefficient ranging from 0 to 1). A high ICC for self-identifiability indicates that the edge's contribution to self-identifiability is shared across individuals. In contrast, a high ICC for others-identifiability indicates that the edge's contribution to others-identifiability is shared across individuals.

Supplementary Figure 2.11

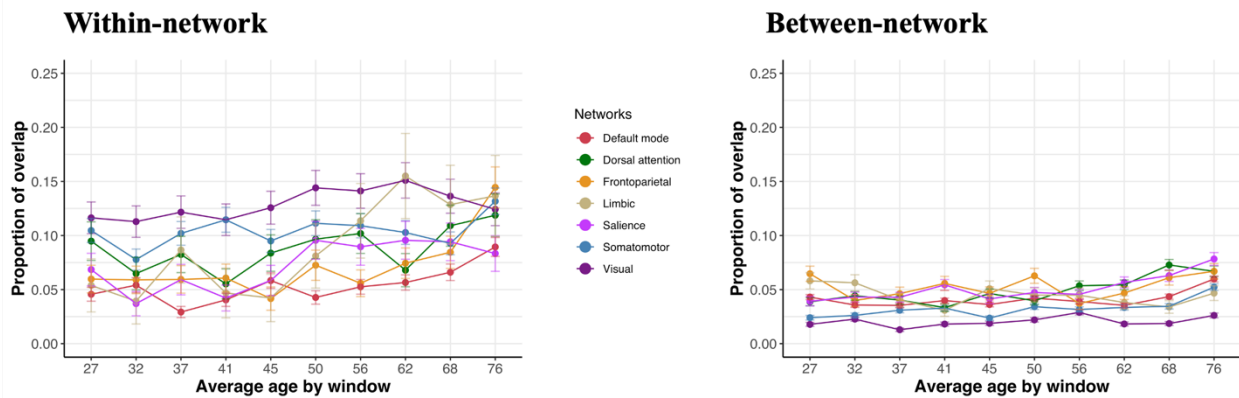
A. Average edge-wise intraclass correlation by network



B. Overlap of edges contributing the most to self- or others-identifiability during aging



C. Overlap of edges contributing the most to self- and to others-identifiability



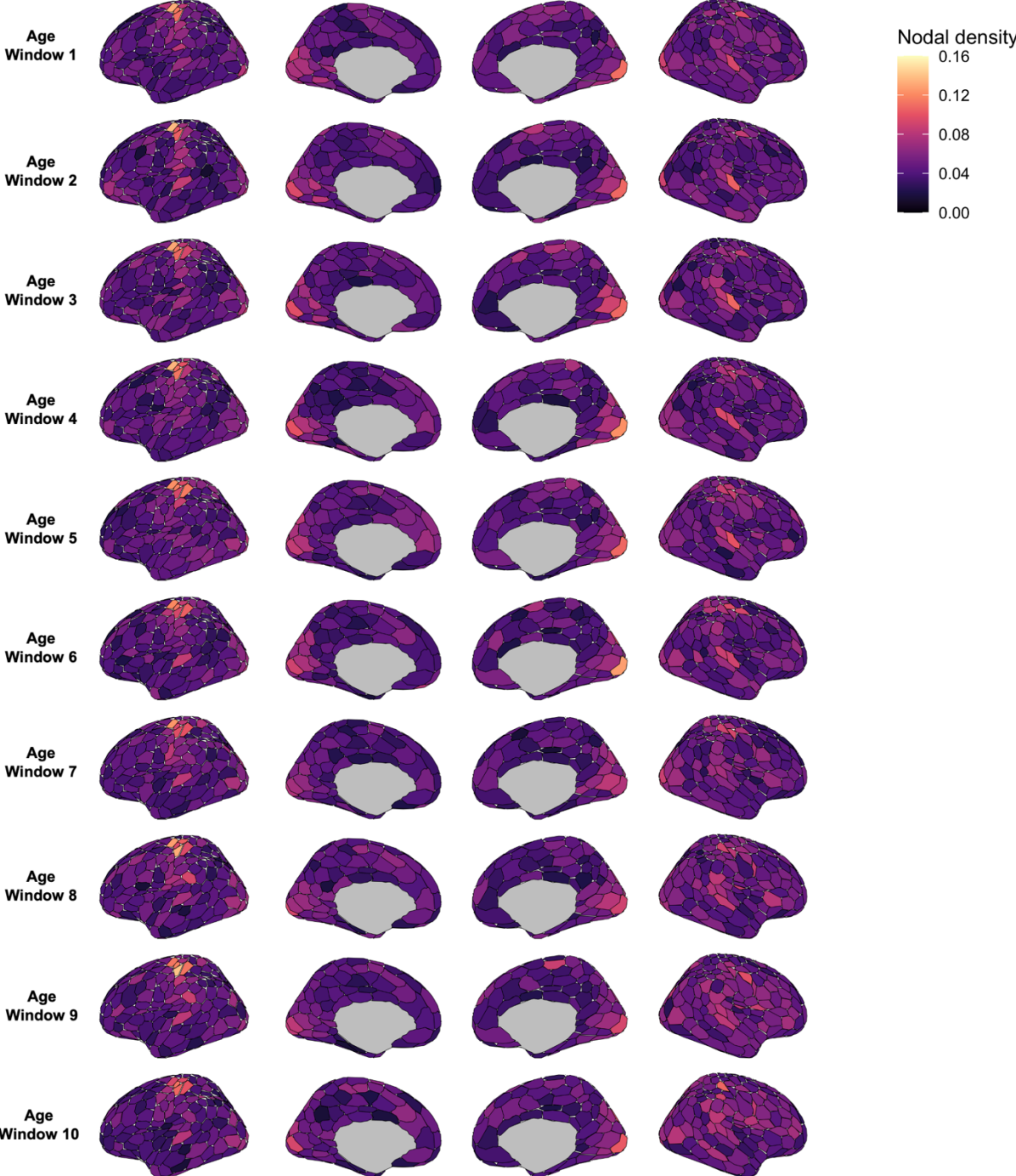
Supplementary Figure 2.11 - Edge-wise contribution to self- and others-identifiability (window size = 100, step size = 40)

A. Average intraclass correlation (ICC) coefficients by network—for within- and between-network edges—in edges contributing the highest to self- and others-identifiability (values within each age window above the 95th percentile). Full circles and lines represent the average ICC of edges contributing the highest to self-identifiability while downward facing triangles and dashed lines represent the average ICC of edges contributing the highest to others-identifiability. Each average is accompanied by the standard deviation as an error bar.

B. Overlap of edges contributing the most to self- (full lines and circles) and to others-identifiability (dashed lines and triangles), as measured by the Jaccard Similarity Index (0 = no overlap, 1 = perfect overlap). The average age of age windows demonstrating overlap are indicated in square brackets. The 95% confidence interval of the standard error for the proportion of overlap, as a function of each network size, is illustrated with error bars.

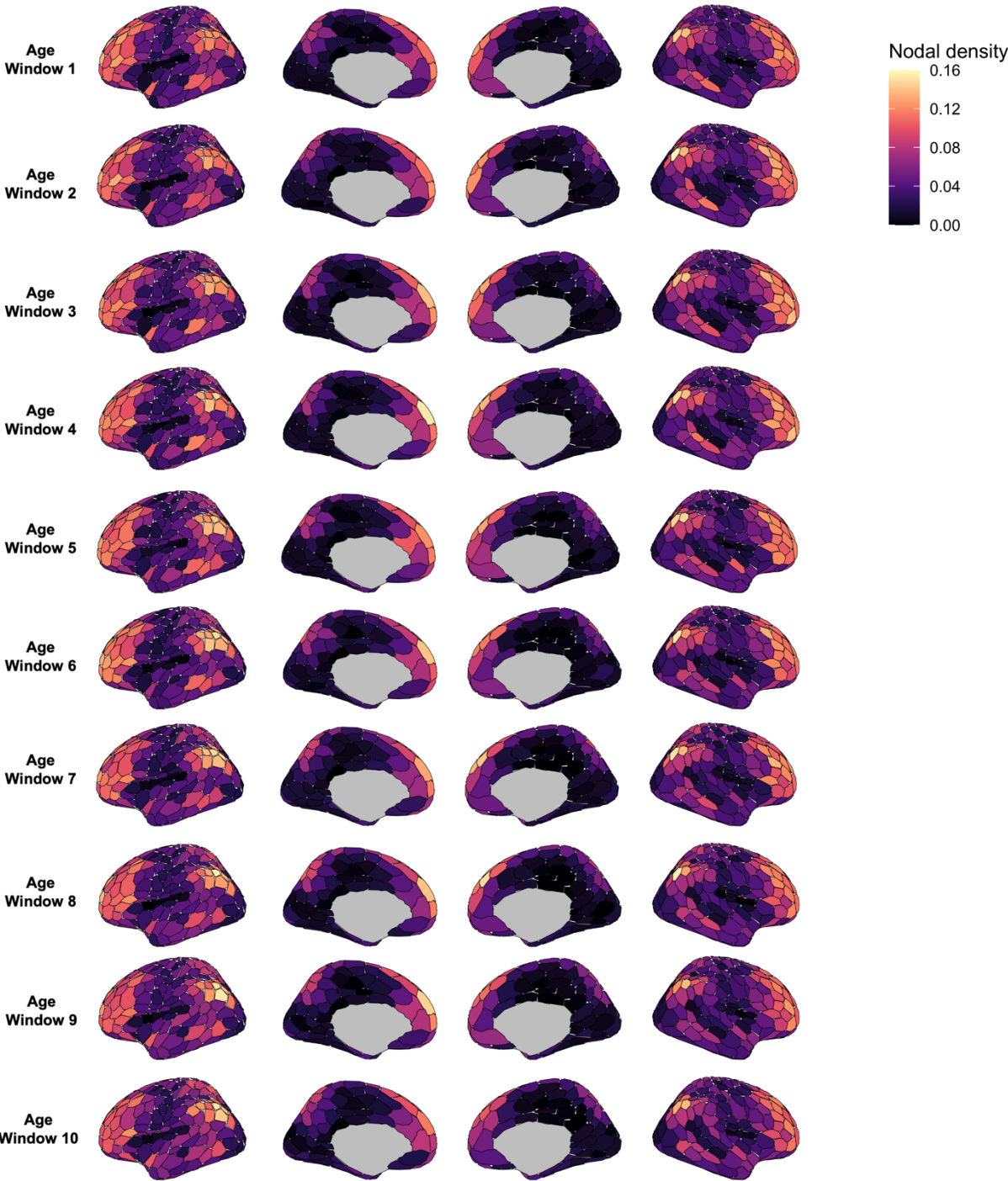
C. Overlap of edges contributing the most to both self- and others-identifiability within each age window as measured by the Jaccard Similarity Index. The 95% confidence interval of the standard error for the proportion of overlap is illustrated with error bars.

Supplementary Figure 2.12



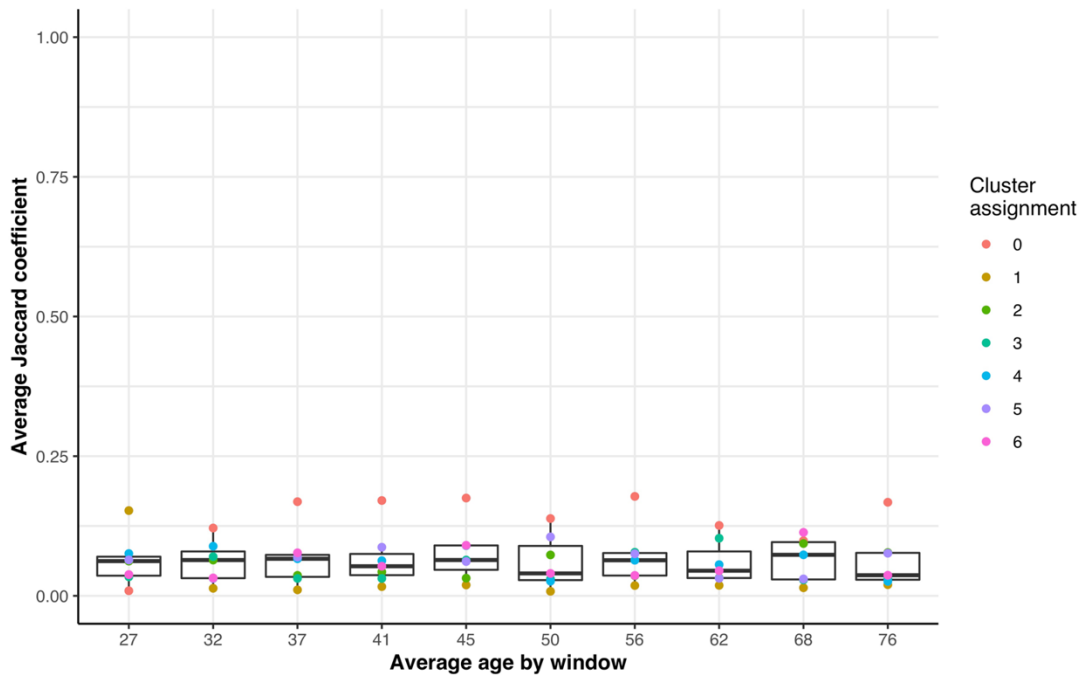
Supplementary Figure 2.12 – Nodal density of edges highly contributing to self-identifiability. *For each age window, we plot the nodal density (sum of number of edges above the 95th percentile threshold of the highest intraclass correlation divided by the number of edges for a given node) using the Schaefer atlas (400 nodes). A higher nodal density means that the node had a higher proportion of edges contributing to self-identifiability.*

Supplementary Figure 2.13



Supplementary Figure 2.13 – Nodal density of edges highly contributing to others-identifiability. *For each age window, we plot the nodal density (sum of edges above the 95th percentile threshold of the highest intraclass correlation divided by the number of edges for a given node) using the Schaefer atlas (400 nodes). A higher nodal density means that the node had a higher proportion of edges contributing to others-identifiability.*

Supplementary Figure 2.14

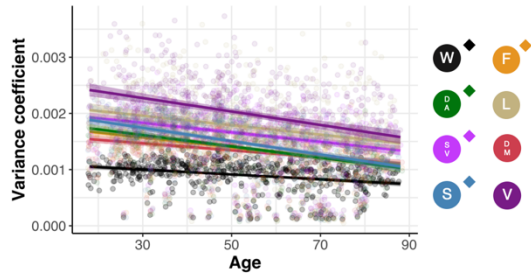


Supplementary Figure 2.14 – Average overlap between group-level and individual-level clustering of functional connectivity edges. For each cluster label derived by the 7-cluster K-means, we computed the average overlap between the cluster labels assigned to group-level connectivity and the individual-level connectivity using the Jaccard coefficient. A coefficient closer to 1 indicates that the clusters overlap more between group- and individual-level connectivity, while a coefficient closer to 0 indicates that the clusters overlap less between group- and individual-level connectivity.

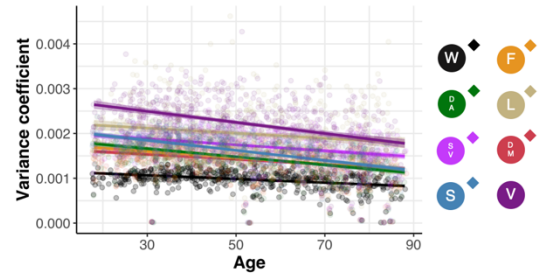
Supplementary Figure 2.15

A. Within-individual variability in FC

Rest

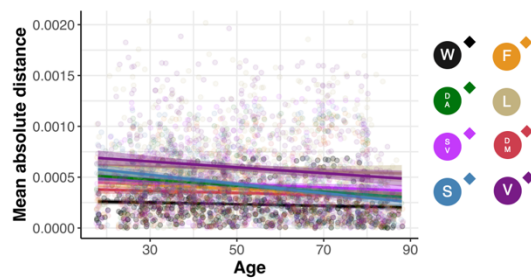


Task

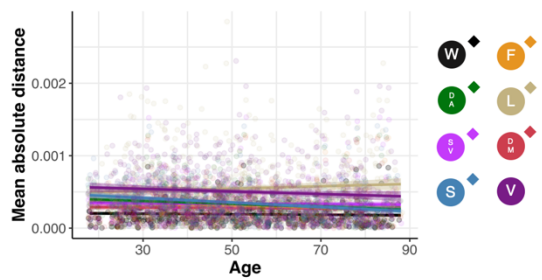


B. Between-individual variability in FC

Rest

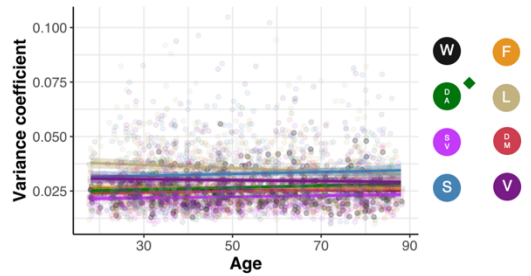


Task

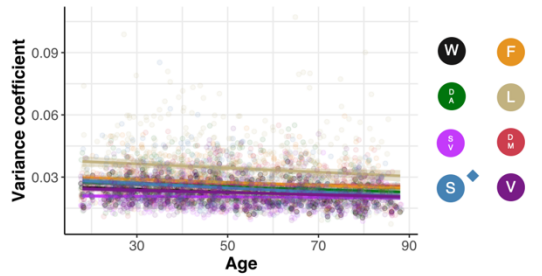


C. Within-individual variability in temporal similarity profile

Rest

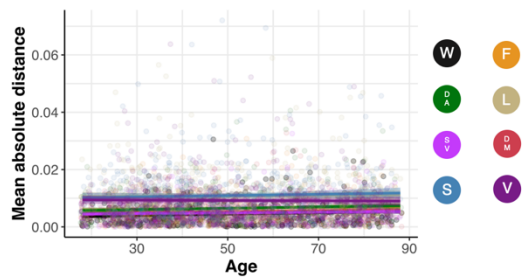


Task

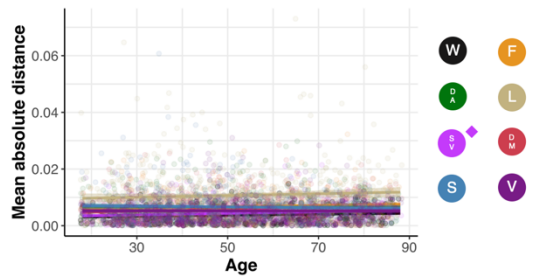


D. Between-individual variability in temporal similarity profile

Rest



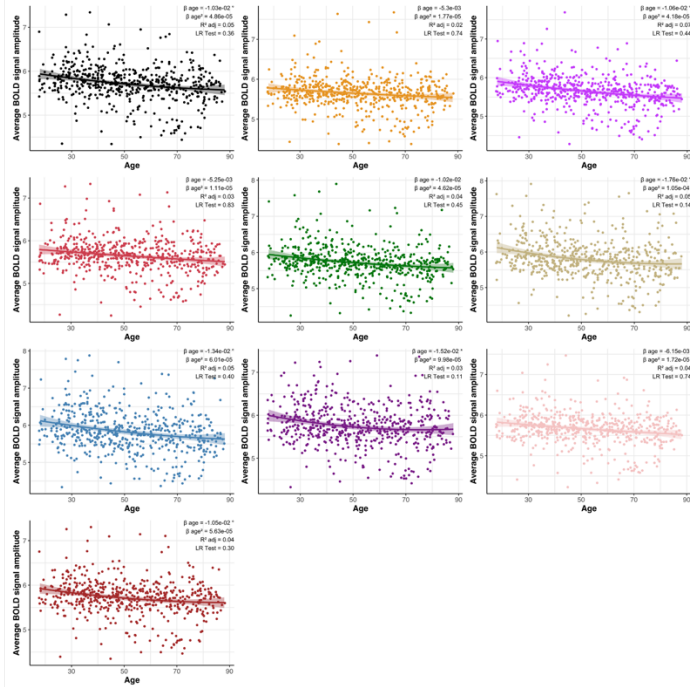
Task



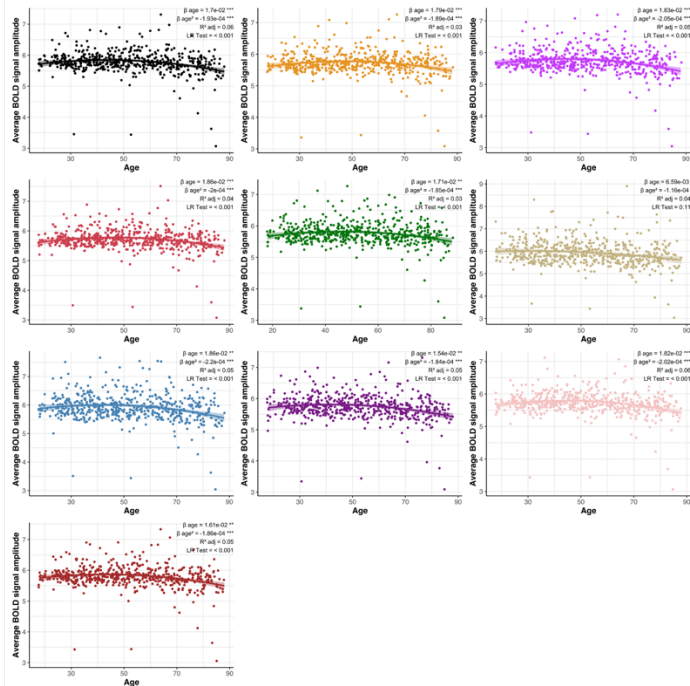
Supplementary Figure 2.15 - Change in within- and between-individual variability in functional connectivity across the lifespan and across tasks. *This figure presents the association between FC variability within- (panel **A.**) and between-individual (panel **B.**) and age. It also presents the association between variability in temporal similarity profile within- (panel **C.**) and between-individuals (panel **D.**). Each network is color-coded based on the abbreviation and color scheme presented in Figure 2.1B. A lozenge next to the network acronym representing the network at the bottom of each graph indicates that the model survived controlling for confounders and bootstrap resampling.*

Supplementary figure 2.16

A. Relationship between BOLD signal amplitude and age in the Rest modality



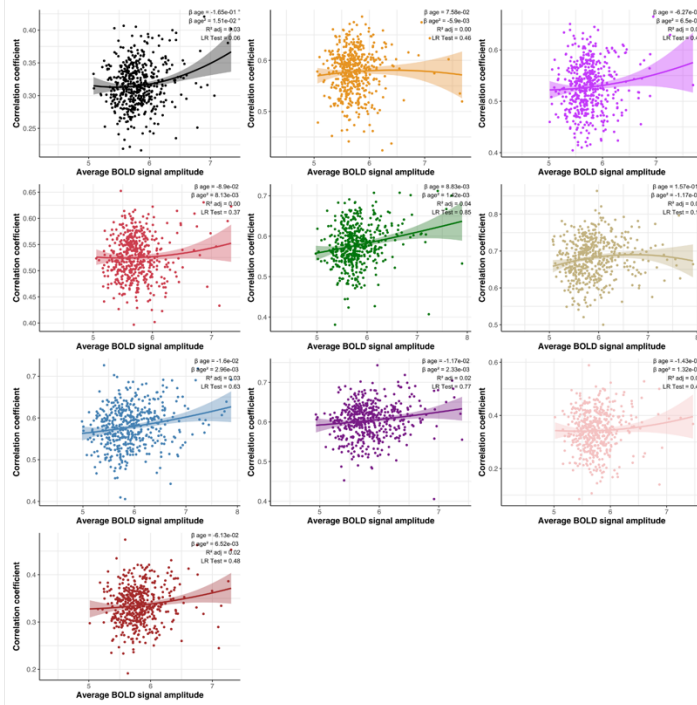
B. Relationship between BOLD signal amplitude and age in the Task modality



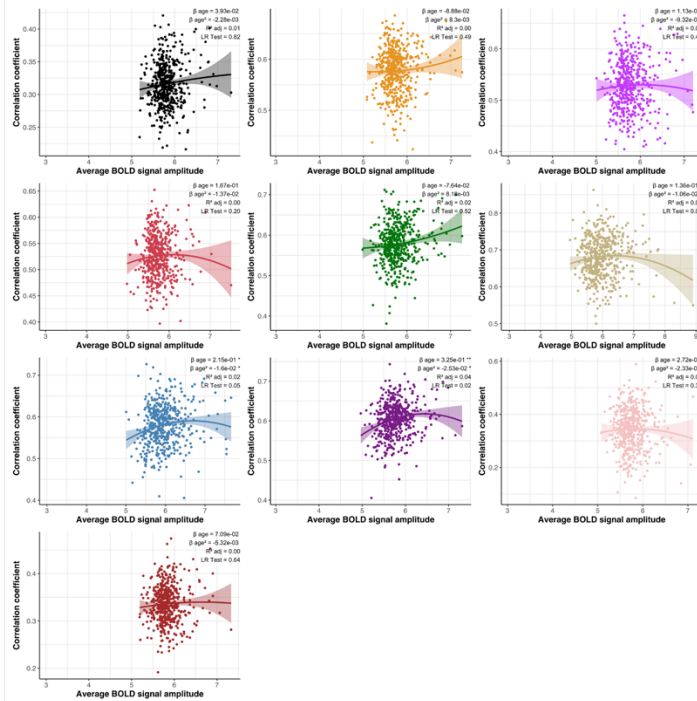
Supplementary Figure 2.16 – Association between BOLD signal amplitude and age across the lifespan. *The amplitude of the fMRI BOLD signal was computed in both the Rest (A) and Task (B) modality separately. Then, the amplitude was related to age using a non-linear (quadratic) model. The beta coefficient of the age term and its quadratic term are presented at the top of the graph. We also present the adjusted R^2 of the model and the p -value of the nested likelihood ratio indicating the non-linearity of the relationship. The p -value of predictors surviving inclusion of covariates and execution of the bootstrapping are indicated by asterisks ($p < 0.001 = ***$, $p < 0.01 = **$, $p < 0.05 = *$, $p < 0.1 = \circ$).*

Supplementary Figure 2.17

A. Relationship between BOLD signal amplitude in the Rest modality and self-identifiability



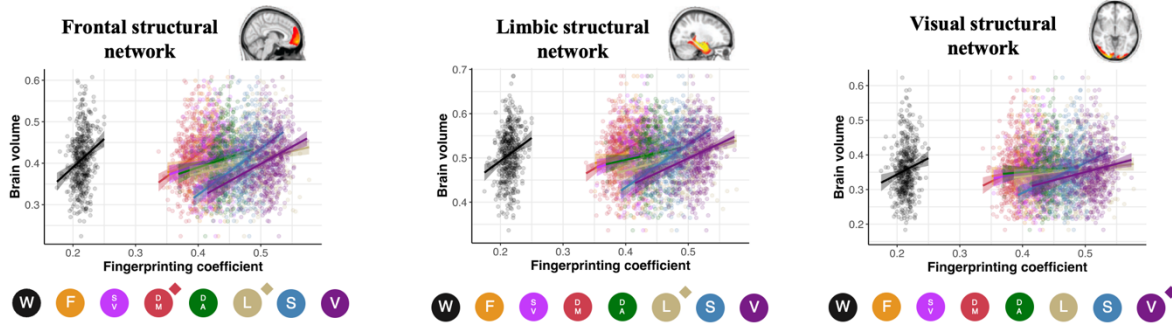
B. Relationship between BOLD signal amplitude in the Task modality and self-identifiability



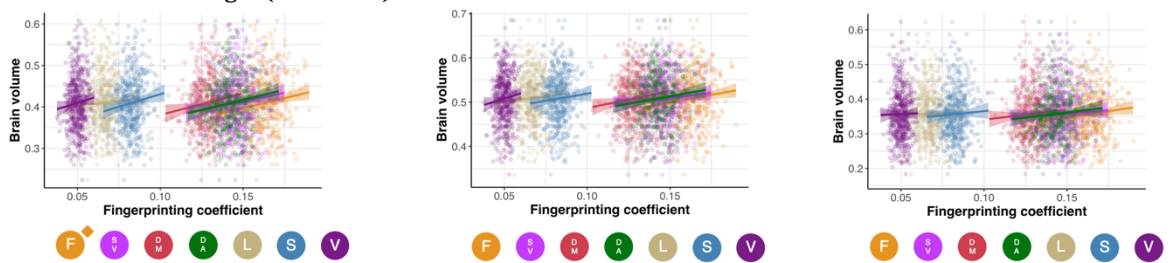
Supplementary Figure 2.17 – Association between BOLD signal amplitude and self-identifiability across the lifespan. *The average amplitude of the fMRI BOLD signal was computed in both the Rest (A) and Task (B) modality separately. Then, the amplitude was related to age using a non-linear (quadratic) model. The beta coefficient of the age term and its quadratic term are presented at the top of the graph. We also present the adjusted R^2 of the model and the p-value of the nested likelihood ratio indicating the non-linearity of the relationship. The p-value of predictors surviving inclusion of covariates and execution of the bootstrapping are indicated by asterisks ($p < 0.001 = ***$, $p < 0.01 = **$, $p < 0.05 = *$, $p < 0.1 = \text{‡}$).*

Supplementary Figure 2.18

A. Within-network edges (Rest-Task)



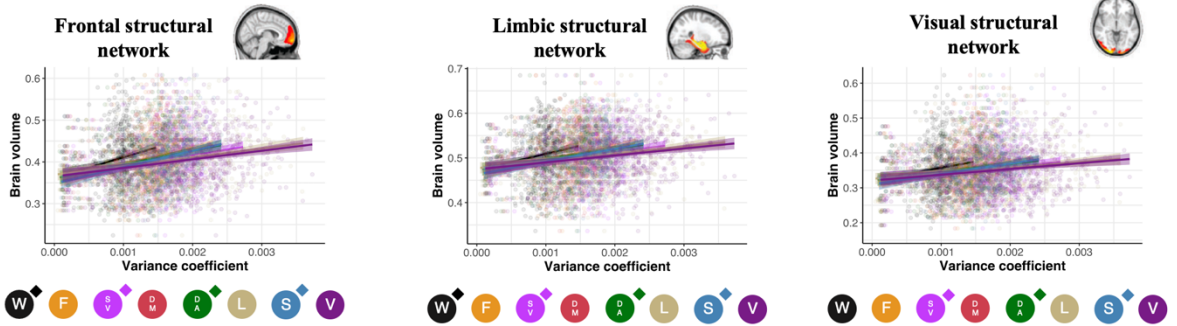
B. Between-network edges (Rest-Task)



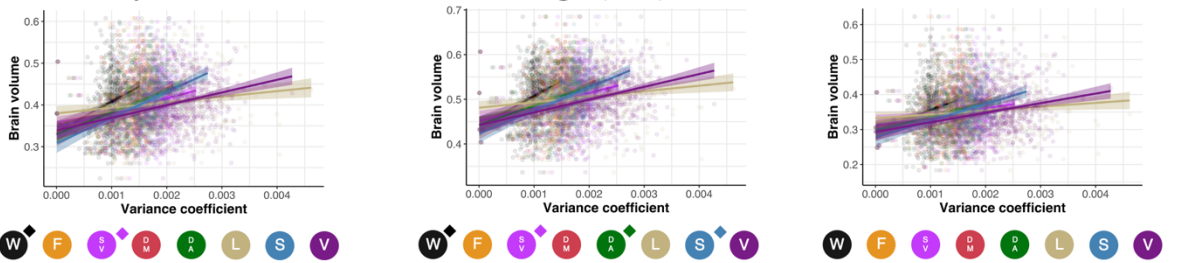
Supplementary Figure 2.18 - Association between grey matter volume and others-identifiability. Scatterplots presenting the association between others-identifiability and grey matter volume in three morphometric networks: frontal structural network (age-sensitive network), limbic structural network (Alzheimer's/age-related network) and visual structural network ("control" network). Data points, regression slopes and bubbles below the graph follow the color scheme of Figure 2.1B. A "◆" at the upper right of the bubble indicates that the association survived when using bootstrapping and controlling for covariates (including age). Panel **A**. presents the results for within-network edges while panel **B**. presents the results for the between-network edges.

Supplementary Figure 2.19

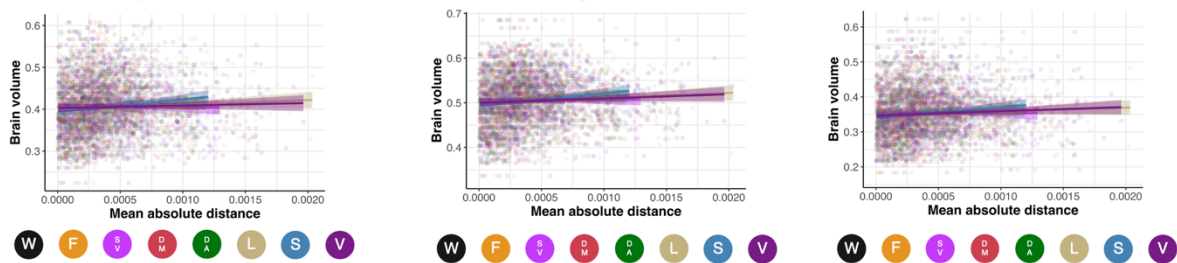
A. FC variability within-individuals within-network edges (Rest)



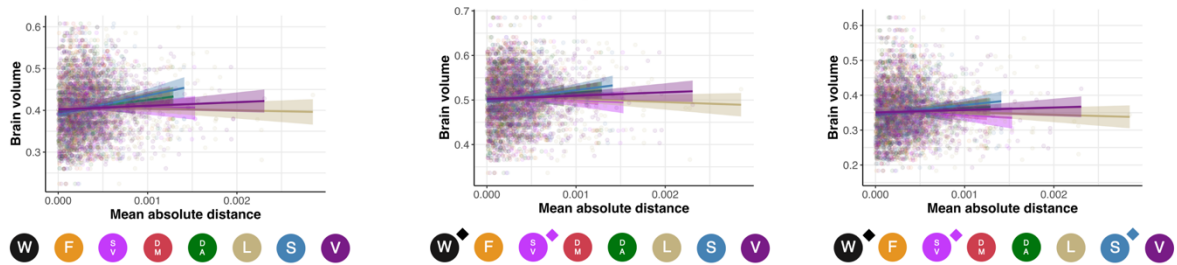
B. FC variability within-individuals within-network edges (Task)



C. FC variability between individuals within-network edges (Rest)



D. FC variability between individuals within-network edges (Task)



Supplementary Figure 2.19 – FC variability and grey matter associations.

*Scatterplots presenting the association between within-individual (panels **A.** and **B.**) and between-individual variability in FC (panels **C.** and **D.**), and grey matter volume in three morphometric networks: frontal structural network (age-sensitive network), limbic structural network (Alzheimer's/age-related network) and visual structural network ("control" network). Data points, regression slopes and bubbles below the graph follow the color scheme of Figure 2.1B. A "◆" at the upper right of the bubble indicates that the association survived when using bootstrapping and controlling for covariates (including age).*

Supplementary Table 2.1 – McNemar tests comparing fingerprint identification accuracy obtained from within-network edges and between-network edges

Network	Within-network accuracy	Between-network accuracy	Statistic
Visual	75.6 (71.7-79.4)	99.8 (99.4-100)	χ^2 (df = 1, p < 0.001) = 113.08
Somatomotor	80.7 (77.2-84.3)	100 (-)	n/a
Limbic	81.2 (77.7-84.6)	97.9 (96.7-99.2)	χ^2 (df = 1, p < 0.001) = 63.92
Dorsal attention	93.2 (90.9-95.4)	100 (-)	n/a
Default mode	100 (-)	100 (-)	n/a
Salience	69.6 (65.6-73.7)	99.6 (99.0-100)	χ^2 (df = 1, p < 0.001) = 143.01
Frontoparietal	98.3 (97.2-99.5)	100 (-)	n/a

In cases where all participants were identified accurately, the McNemar test cannot be calculated.

Supplementary Table 2.2 – McNemar tests comparing the fingerprint identification accuracy between networks (within-network edges)

	Visual (75.6%)	Somato- motor (80.7%)	Limbic (81.2%)	Dorsal attention (93.2%)	Default mode (100%)	Salience (69.6%)	Fronto- parietal (98.3%)
Visual (75.6%)		χ^2 (df = 1, p = 0.037) = 4.331	χ^2 (df = 1, p = 0.012) = 6.322	χ^2 (df = 1, p < 0.001) = 62.284	n/a	χ^2 (df = 1, p = 0.0293) = 4.752	χ^2 (df = 1, p < 0.001) = 104.22
Somato-motor (80.7%)			χ^2 (df = 1, p = 0.603) = 0.271	χ^2 (df = 1, p < 0.001) = 44.444	n/a	χ^2 (df = 1, p < 0.001) = 23.025	χ^2 (df = 1, p < 0.001) = 79.281
Limbic (81.2%)				χ^2 (df = 1, p < 0.001) = 30.533	n/a	χ^2 (df = 1, p < 0.001) = 23.841	χ^2 (df = 1, p < 0.001) = 65.878
Dorsal attention (93.2%)					n/a	χ^2 (df = 1, p < 0.001) = 97.714	χ^2 (df = 1, p < 0.001) = 17.633
Default mode (100%)						n/a	n/a
Salience (69.6%)							χ^2 (df = 1, p < 0.001) = 133.17
Fronto-parietal (98.3%)							

McNemar tests were calculated for every pair of networks that didn't have perfect identification accuracy. To simplify the table, only the upper half was completed (the diagonal yields a chi-square of 0, and the lower half would be exactly symmetric to the upper half)

Supplementary Table 2.3 – McNemar tests comparing fingerprint identification accuracy from product–moment-derived FC and from partial correlation derived FC (within-network edges)

Network	Product–moment FC	Partial correlation FC	Statistic
Visual	76.6 (72.8-80.4)	75.6 (71.7-79.4)	χ^2 (df = 1, p = 0.705) = 0.144
Somatomotor	77.7 (73.9-81.4)	80.7 (77.2-84.3)	χ^2 (df = 1, p = 0.301) = 1.070
Limbic	79.3 (75.7-82.9)	81.2 (77.7-84.6)	χ^2 (df = 1, p = 0.423) = 0.643
Dorsal attention	91.9 (89.5-94.4)	93.2 (90.9-95.4)	χ^2 (df = 1, p = 0.450) = 0.571
Default mode	96.3 (94.6-98.0)	100 (-)	n/a
Salience	97.7 (96.4-99.1)	69.6 (65.6-73.7)	χ^2 (df = 1, p < 0.001) = 123.14
Frontoparietal	98.3 (97.2-99.5)	98.3 (97.2-99.5)	χ^2 (df = 1, p = 1) = 0
Whole brain	95.4 (93.6-97.3)	100 (-)	n/a

In cases where all the sample was identified accurately, the McNemar test cannot be calculated.

Supplementary Table 2.4 – McNemar tests comparing fingerprint identification accuracy from product–moment-derived FC and from partial correlation derived FC (between-network edges)

Network	Product–moment FC	Partial correlation FC	Statistic
Visual	66.7 (62.5-70.9)	99.8 (99.4-100)	χ^2 (df = 1, p < 0.001) = 158.01
Somatomotor	80.3 (76.8-83.8)	100 (-)	n/a
Limbic	90.0 (87.4-92.7)	97.9 (96.7-99.2)	χ^2 (df = 1, p < 0.001) = 24.45
Dorsal attention	93.2 (90.9-95.4)	100 (-)	n/a
Default mode	91.1 (88.6-93.6)	100 (-)	n/a
Saliency	92.5 (90.2-94.9)	99.6 (99.0-100)	χ^2 (df = 1, p < 0.001) = 28.658
Frontoparietal	94.9 (93.1-97.0)	100 (-)	n/a

In cases where all the sample was identified accurately, the McNemar test cannot be calculated.

2.10.4 – Supplementary references

- Jaccard, P. (1912). THE DISTRIBUTION OF THE FLORA IN THE ALPINE ZONE. *New Phytologist*, 11(2), 37–50. <https://doi.org/10.1111/j.1469-8137.1912.tb05611.x>
- Koo, T., & Li, M. (2016). A Guideline of Selecting and Reporting Intraclass Correlation Coefficients for Reliability Research. *J Chiropr Med*, 15(2), 155–163.
- Scheinost, D., Noble, S., Horien, C., Greene, A. S., Lake, E. M., Salehi, M., Gao, S., Shen, X., O'Connor, D., Barron, D. S., Yip, S. W., Rosenberg, M. D., & Constable, R. T. (2019). Ten simple rules for predictive modeling of individual differences in neuroimaging. *NeuroImage*, 193(March), 35–45. <https://doi.org/10.1016/j.neuroimage.2019.02.057>
- Shen, X., Finn, E. S., Scheinost, D., Rosenberg, M. D., Chun, M. M., Papademetris, X., & Constable, R. T. (2017). Using connectome-based predictive modeling to predict individual behavior from brain connectivity. *Nature Protocols*, 12(3), 506–518. <https://doi.org/10.1038/nprot.2016.178>
- Shrout, P. E., & Fleiss, J. L. (1979). Intraclass Correlations: Uses in Assessing Rater Reliability. *Psychological Bulletin*, 86(2), 420–428.
- Varoquaux, G., Raamana, P. R., Engemann, D. A., Hoyos-Idrobo, A., Schwartz, Y., & Thirion, B. (2017). Assessing and tuning brain decoders: Cross-validation, caveats, and guidelines. *NeuroImage*, 145(October 2016), 166–179. <https://doi.org/10.1016/j.neuroimage.2016.10.038>

Chapter 3 - Tau accumulation and its spatial progression in the late onset Alzheimer's disease spectrum

Frédéric St-Onge^{1,2}, Marianne Chapleau³, John CS Breitner^{2,4}, Sylvia Villeneuve^{2,4,5†},
and Alexa Pichet Binette^{6,†}, for the Alzheimer's Disease Neuroimaging Initiative*

1 Integrated Program in Neuroscience, Faculty of medicine, McGill University, Montreal, Qc, H3A 2B4, Canada

2 Research Center of the Douglas Mental Health University Institute, Montreal, Qc, H4H 1R3, Canada

3 Faculty of medicine, University of California San Francisco, San Francisco, CA, 94143, United-States

4 Department of psychiatry, Faculty of medicine, McGill University, Montreal, QC, H3A 1Y2, Canada

5 McConnell Brain Imaging Centre, Montreal Neurological Institute, Montreal, QC, H3A 2B4, Canada

6 Clinical Memory Research Unit, Faculty of Medicine, Lund University, Malmö, 205 02, Sweden

† Co-senior authors

*Data used in preparation of this article were obtained from the Alzheimer's Disease Neuroimaging Initiative (ADNI) database (adni.loni.usc.edu). As such, the investigators within the ADNI contributed to the design and implementation of ADNI and/or provided data but did not participate in analysis or writing of this report. A complete listing of ADNI investigators can be found at:

http://adni.loni.usc.edu/wp-content/uploads/how_to_apply/ADNI_Acknowledgement_List.pdf

3.1 – Preface

Results from Chapter 2 indicated that interindividual differences remain in functional networks all throughout life, no matter the age of participants. We also showed that these differences were associated with age-related grey matter volume. Overall, this suggests that interindividual differences can have an impact on other variables we measure and associate with the brain. This last point is echoed in the literature, as studies suggest that individual-specific functional connectivity is associated with lifestyle variables in healthy populations (Bijsterbosch et al., 2018; Mansour et al., 2020) and clinical information in patients with schizophrenia (Kaufmann et al., 2018), with different psychopathologies (Kaufmann et al., 2017) or with cognitive decline (Sorrentino et al., 2020).

Taken together, the literature and Chapter 2 suggest that interindividual differences in the brain can help bridge our understanding of the brain and its role in disease-related variables. This doesn't only have implications in cognitively unimpaired participants, but also impacts how we understand disorders. For example, research in recent years has indicated that there is significant heterogeneity in the brains of patients with AD (Ferreira et al., 2020). This heterogeneity seems particularly important in predicting the spread of tau pathology—one of the main hallmarks of AD associated with cognitive decline (Ossenkoppele et al., 2018)—where individualized markers of tau pathology outperform group-level markers (Franzmeier et al., 2020; Leuzy et al., 2023) to track the pathology. However, this clashes somewhat with previous literature indicating that tau pathology follows a stereotypical gradient from the middle temporal to the sensorimotor cortex (Braak & Braak, 1991; Therriault, Pascoal, Lussier, et al., 2022).

As such, in Chapter 3, we developed a tool, the spatial extent, that computes the extent to which tau pathology has spread in the brains of participants at the individual level. This was done so we could specifically study interindividual differences in the accumulation of tau pathology and compare it to the traditionally accepted patterns of tau pathology. We also related this spread at the individual level to cognition in order to establish a potential clinical relevance of individual-level markers of tau pathology.

3.2 – Abstract

The accumulation of tau abnormality in sporadic Alzheimer's disease is believed typically to follow neuropathologically defined Braak staging. Recent *in-vivo* positron emission tomography (PET) evidence challenges this belief, however, as accumulation patterns for tau appear heterogeneous among individuals with varying clinical expressions of Alzheimer's disease. We, therefore, sought a better understanding of the spatial distribution of tau in the preclinical and clinical phases of sporadic Alzheimer's disease and its association with cognitive decline.

Longitudinal tau-PET data (1,370 scans) from 832 participants (463 cognitively unimpaired, 277 with mild cognitive impairment and 92 with Alzheimer's disease dementia) were obtained from the Alzheimer's Disease Neuroimaging Initiative. Among these, we defined thresholds of abnormal tau deposition in 70 brain regions from the Desikan atlas, and for each group of regions characteristic of Braak staging. We summed each scan's number of regions with abnormal tau deposition to form a spatial extent index. We then examined patterns of tau pathology cross-sectionally and longitudinally and assessed their heterogeneity. Finally, we compared our spatial extent index of tau uptake with a temporal meta region of interest—a commonly used proxy of tau burden—assessing their association with cognitive scores and clinical progression.

More than 80% of amyloid-beta positive participants across diagnostic groups followed typical Braak staging, both cross-sectionally and longitudinally. Within each Braak stage, however, the pattern of abnormality demonstrated significant heterogeneity such that the overlap of abnormal regions across participants averaged less than 50%, particularly in persons with mild cognitive impairment. Accumulation of tau progressed

more rapidly among cognitively unimpaired and participants with mild cognitive impairment (1.2 newly abnormal regions per year) compared to participants with Alzheimer's disease dementia (less than one newly abnormal region per year). Comparing the association of tau pathology and cognitive performance our spatial extent index was superior to the temporal meta-ROI for identifying associations with memory in cognitively unimpaired individuals and explained more variance for measures of executive function and language in mild cognitive impairment and Alzheimer's disease dementia participants.

Thus, while participants broadly followed Braak stages, significant individual regional heterogeneity of tau binding was observed at each clinical stage. Progression of the spatial extent of tau pathology appears to be fastest in cognitively unimpaired and persons with mild cognitive impairment. Exploring the spatial distribution of tau deposits throughout the entire brain may uncover further pathological variations and their correlation with cognitive impairments.

3.3 – Introduction

The first positron emission tomography (PET) tracers of tau pathology were developed almost a decade ago (Xia et al., 2013). These tracers have advanced our understanding of the role of tau pathology in aging and Alzheimer’s disease (Leuzy et al., 2019; Lowe et al., 2016; Marquié et al., 2015; Schöll et al., 2016). However, several questions remain, including the spatial progression of the disease across the whole brain. Our principal aim was to provide a comprehensive view and the clinical relevance of cross-sectional and longitudinal tau-PET binding in late-onset sporadic Alzheimer’s disease. Using data from the Alzheimer’s disease neuroimaging initiative (ADNI) we here report the abnormal tau PET binding patterns in individuals classified as being cognitively unimpaired [CU] or having mild cognitive impairment [MCI] or Alzheimer’s disease dementia. We also report the amount and the spatial extent of tau abnormality across these clinical groups both cross-sectionally and over time. Finally, we describe their association with cognitive impairment.

The progression of tau pathology in the brain is generally believed to follow a stereotypical pattern approximating the Braak stages defined post-mortem, where tau starts accumulating in medial temporal regions (Braak I-II) before accumulating in limbic regions (Braak III-IV) and finally to the whole cortical mantle (Braak V-VI). (Braak & Braak, 1991) Many PET studies have confirmed this pattern in-vivo (Sanchez et al., 2021; Schöll et al., 2016; Therriault et al., 2022), and studies investigating associations between tau and clinical variables usually average tau from a predefined set of temporal regions (i.e., a temporal meta-region of interest or ROI) to approximate the early stages of tau

accumulation (Jack et al., 2017; Ossenkoppele et al., 2018; Strikwerda-Brown et al., 2022).

Reports in recent years have highlighted the limitations of this homogenous approach as tau progression patterns can differ across individuals (Franzmeier et al., 2020; Vogel et al., 2021) and between different disease variants (La Joie et al., 2020; Ossenkoppele et al., 2020; Singleton et al., 2021). These inter-individual differences would seem important to track longitudinal changes, and it has been suggested that tau accumulation is better captured when using individualized ROIs (Franzmeier et al., 2020; Leuzy et al., 2023). Inter-individual differences in tau pathology may become particularly critical when tracking clinical progression. The evidence thus far highlights that tau, rather than amyloid-beta ($A\beta$) alone, is a reliable indicator of future clinical progression (Ossenkoppele et al., 2022; Strikwerda-Brown et al., 2022), and is well associated with cognitive change in the early stages of Alzheimer's disease (Biel et al., 2021; Hanseeuw et al., 2019; Ossenkoppele et al., 2021; Pontecorvo et al., 2017, 2019). Therefore, if tau patterns and their progression are indeed heterogeneous, it is likely that tracking tau with a single set of regions across participants may misrepresent a significant portion of them.

Leveraging 1,370 tau PET scan visits from 832 ADNI participants across the Alzheimer's disease spectrum, we characterized the spatial extent of tau pathology across the whole brain (70 brain regions) both cross-sectionally and longitudinally. We summarized these measures by developing a novel index, the spatial extent index. This index accounts for individual differences in tau-PET patterns by evaluating the extent of tau pathology for any single individual across the whole brain. We then evaluated how the spatial extent index related to performance in different cognitive domains. We

compared this approach with more traditional measures of Braak staging and tau-PET uptake in a temporal meta-region of interest (ROI) (Jack et al., 2017). We hypothesized that a region-specific analysis of tau-PET abnormality would offer a more useful measure of cognitive impairment than other approaches that rely on tracer uptake in one set of regions across all individuals.

3.4 – Methods

3.4.1 – Participants

We used data from ADNI, a multi-site study launched in 2003 as a public-private partnership. The primary goal of ADNI has been to test whether serial MRI, PET, other biological markers, and clinical and neuropsychological assessment can be combined to measure the progression of MCI and early Alzheimer's disease. For up-to-date information, see www.adni-info.org. We conducted the analyses using ADNI longitudinal data available in May 2022. We included participants who had at least one available tau (flortaucipir) and one A β (florbetapir or florbetaben) PET scan, and who had an available diagnostic assessment within two years from the tau scan in ADNI3.

3.4.2 – PET acquisition and processing

We used fully preprocessed data from the ADNI consortium. Details on PET acquisition and preprocessing procedures can be found elsewhere (<http://adni.loni.usc.edu/methods/documents/>). Briefly, for tau-PET, the flortaucipir tracer ([¹⁸F] AV-1451) was used and images were acquired 75-105 minutes post-injection. For A β -PET, florbetapir or florbetaben were used, and images were acquired 50-70- and 90-110-minutes post-injection, respectively. Briefly, PET images were realigned, averaged, resliced to 1.5mm³ and smoothed to a resolution of 8mm³ full width at half-maximum. Then, the closest T1-weighted MRI available for a participant was processed and segmented using FreeSurfer 7.1.1, and co-registered to the PET scan using SPM. SUVRs were extracted from each cortical region of the Desikan atlas (Desikan et al., 2006). The inferior cerebellum was used as the reference region for flortaucipir, and the whole cerebellum was the reference region for A β -PET. As suggested by the ADNI PET

core group, we divided the SUVR values provided by ADNI by the SUVR values in the reference region for each tracer.

A β -PET positivity status was determined according to the cutoff derived from the ADNI PET core based on a neocortical composite region: participants exceeding 1.11 SUVR for florbetapir or 1.08 SUVR for florbetaben were considered positive. We also converted the SUVR values into centiloid units for supplementary analyses, following established formulas from the ADNI PET core (Royse et al., 2021).

3.4.3 – Regional tau-PET and other measures of interest

Our main interest was to study the patterns of elevated regional tau-PET uptake across the brain at the individual level. For this aim, we derived an SUVR cutoff for each brain region of interest using Gaussian-mixture modeling (GMM) on the entire cross-sectional sample of ADNI participants. This procedure is illustrated in Figure 3.1. We fitted a two-component GMM for each region and used the SUVR closest to the 50% probability of belonging to the abnormal (high values) distribution as the regional cutoff, as done previously (Pichet Binette et al., 2022; Vogel et al., 2020). The GMMs were initialized using k-means and parametrized using scikit-learn's v1.2.1 default settings. We ensured that a two-component solution was a better fit compared to a single-component solution by verifying that the Bayesian Information Criterion of the two-component solution was higher. The brain regions of interest were the 34 bilateral cortical regions of the Desikan atlas (Desikan et al., 2006) and the amygdalae. We then binarized the tau SUVR from each region, and values at or exceeding the cutoff were coded as one and a score lower than the cutoff as zero. From there, we derived our main measure of interest: the spatial extent index, which is the sum of regions exceeding the regional thresholds for a given

participant. Regional thresholds for each region are provided in Supplementary Table 3.1. The main results were replicated by setting regional thresholds based on 2 standard deviations from the mean of the tau SUVR of CU A β - participants and deriving the spatial extent with these alternative thresholds (see Supplementary Results, Supplementary Tables 3.2 and 3.5, and Supplementary Fig. 3.9 to 3.13).

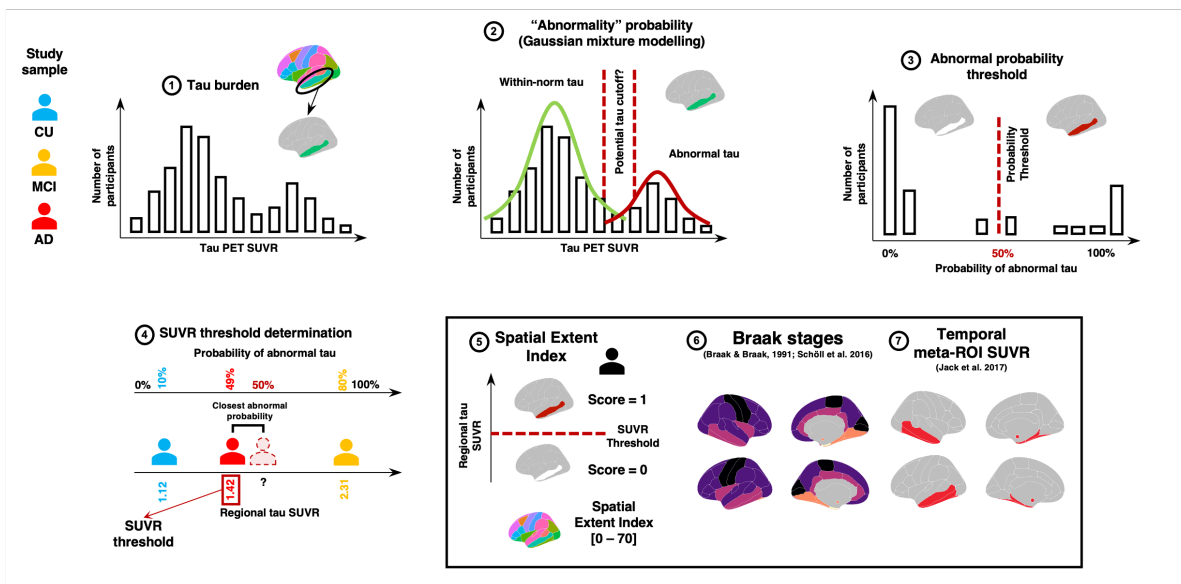


Figure 3.1 Spatial extent methodology. For each cortical region of the Desikan atlas and the bilateral amygdalae, we extract the standardized uptake value ratio (SUVR) of our participants (1). Then, a two-component gaussian mixture modelling technique is applied to the SUVR values in each region (2-3). The second distribution is considered to reflect abnormally high SUVR tau values. We extract the probability that each participant belongs to the “abnormal” distribution and establish a threshold that individuals with over 50% probability are considered positive for the given region (4). Once thresholds are derived across all regions, we derive the spatial extent index for each participant by summing the number of positive regions across the brain. (5). We also apply the same

methodology to the average SUVR within each aggregate composing Braak stages I and III through VI (warmer to colder colors) (6). To compare our spatial extent index in the cognition analyses, we also compute the average SUVR in a classic temporal meta-ROI. (7) CU = Cognitively unimpaired, MCI = Mild cognitive impairment, AD = Alzheimer's disease. Figure adapted from sihnpy's documentation (<https://sihnpy.readthedocs.io/>) with permission of the first author.

We also derived a more typical temporal meta-ROI (Jack et al., 2017) and the regions composing the Braak staging scheme (Braak & Braak, 1991; Schöll et al., 2016; Therriault et al., 2022). The temporal meta-ROI was the average SUVR from key regions harboring elevated tau-PET SUVR in Alzheimer's disease: the entorhinal cortex, the parahippocampal, inferior temporal, the middle temporal and fusiform gyri, and the amygdalae (Jack et al., 2017). In the Braak Staging scheme, pathology accumulation follows a predetermined order ranging from Braak I to VI until the whole cortical mantle is affected by tau (see Supplementary Table 1 for all regions included in each stage) (Braak & Braak, 1991; Therriault et al., 2022). Braak II (hippocampus) was excluded from our analyses owing to the known choroid plexus off-target binding effect of the flortaucipir tau-PET tracer (Lowe et al., 2016). We averaged the tau-PET SUVR values in bilateral regions comprising each Braak stage, following methods described previously (McSweeney et al., 2020; Schöll et al., 2016). We then applied the GMM approach, as described in Figure 3.1, to determine a data-driven threshold for each Braak stage. These thresholds were then applied to assign which individuals were positive on each Braak stage.

A subset of 195 participants had at least two tau-PET scans for longitudinal analyses, with 100 having three such scans. The same regional binarization of positive (score 1) or negative (score 0) using the regional cutoffs was applied to all time points.

3.4.4 – Neuropsychological measures

To compare the clinical implications of our regional index score vs. a typical meta-ROI analysis, we compared the association of each with composite cognitive scores for memory, executive function (Gibbons et al., 2012), language and visuo-spatial performance (Mukherjee et al., 2022). The cognitive performance data were taken as the test timepoint closest in time to tau-PET. As well, we assessed cognitive decline in participants by estimating slopes of annual change for each cognitive composite score using linear mixed effects models with random slopes and intercepts. For these analyses the cognitive score at each visit was the outcome, with the exposure being time since the initial cognitive test score in ADNI. These analyses considered all ADNI visits for the whole sample, thereby maximizing the number of timepoints contributing to estimates of individual slopes. For all cognitive domains, models met assumptions of linearity, homoscedasticity, and normality of residuals, except for the visuospatial score, where very small change over time was observed.

3.4.5 – Statistical analyses

All statistical analyses were run using Python v3.9.2 (numpy v1.23.1; pandas v1.4.3; scipy v1.9.3; scikit-learn v1.2.1; matplotlib v3.6.3), R v4.2.0 (Packages: lme4 v1.1-30; tidyverse v1.3.1; lmerTest v3.1-3; lmerTest 0.9-40; nonnest2 v0.5-5; tableone v0.13.2; patchwork v1.1.2; ggseg v1.6.5; ggnewscale v0.4.7; glue v1.6.2; MASS v7.3-59; cocor

v1.1-4; performance v0.10.1; pscl v1.5.5.1) and R Studio "Prairie Trillium" Release (1db809b8, 2022-05-16) for macOS.

3.4.5.1 – Demographics

We compared groups on their demographic information by their diagnostic status separately for A β + and A β - participants using one-way ANOVA and Tukey post-hoc tests being used for continuous variables and chi-square tests for categorical variables.

3.4.5.2 – Cross-sectional characterization of tau

We first compared tau levels of A β -positive vs. A β -negative individuals. For the three diagnostic groups of CU, MCI, or Alzheimer's disease dementia, we compared our spatial extent index with the temporal meta-ROI SUVR contrasting A β + and A β - individuals within each clinical group using ANOVA and post-hoc Tukey tests. Logistic regression complemented this analysis by quantifying the probability of having a spatial extent index of at least one based on a continuous burden of A β pathology (centiloid values). The linearity of log odds of having a spatial extent of at least one to centiloid values was verified. As tau-PET binding was typically low in A β - participants, all subsequent analyses were done separately in each diagnostic group in the A β + sample. We calculated the extent to which each participant's tau pathology was consistent with Braak staging. To do this, at each Braak stage, we computed the percentage of participants who were tau-positive both at their more advanced Braak stage and at all previous stages (e.g., if a participant was positive on Braak IV, and was also positive on Braak III and I, then this participant was judged to have data in accord with Braak staging).

3.4.5.3 – Longitudinal characterization of tau

We used linear mixed-effect models to calculate the annual change of the tau spatial extent and the temporal meta-ROI (tau as the outcome; time since first tau scan as exposure) with random slopes and intercepts for each participant for the temporal meta-ROI. As the spatial extent index represents a count of regions, we used a Poisson mixed model to model the longitudinal change correcting for zero inflation as the models significantly underfitted the zero counts. At the group level, we used linear mixed-effect models with random slopes and intercepts to track the annual change in positivity across the cohort and the annual change in SUVR in each brain region and plotted the regions on a template brain map. We calculated the extent to which Braak stages were followed by participants longitudinally. For each Braak stage, we computed the percentage of participants who became positive at each stage, and who were already positive or progressed in the previous Braak stages (e.g., if a participant became positive on Braak IV at their last visit and was already positive or progressed in Braak III and I, the participant followed the Braak stages).

3.4.5.4 – Tau-PET heterogeneity

We computed the overlap between the patterns of abnormal tau at baseline or over time between participants in the same diagnostic group using the Jaccard Similarity index. The index ranges from zero to one where zero indicates that not a single positive region overlaps between participants, and one indicates that all positive regions between two participants perfectly overlap. We then averaged the values so that each participant would be left with a single value representing, on average, how similar their tau positivity pattern

was to the rest of their diagnostic group at the whole brain level. Analyses were always restricted to individuals with at least one positive region.

3.4.5.5 – Associations with demographic variables and cognition

We assessed whether the spatial extent index was associated with demographic characteristics (i.e., age, gender, education and ApoE4 genotype) using linear models, controlling for the other three factors. Then, we studied the association between our tau spatial index measures at baseline and the cognitive performance at the time of the PET, and the cognitive decline (slope) across all available cognitive visits using linear models. Beta, standardized beta, P-values and model fit (R^2 and AIC), are reported. Models were adjusted for age, sex and education and were also subjected to a false discovery rate (FDR) multiple comparison correction. Differences in model fit between different tau measures were assessed using Vuong's closeness test (i.e., non-nested likelihood ratio test; Vuong et al., 1989). As complementary analyses, we also assessed the association between tau uptake and cognitive performance in each of the 70 brain regions. Tau SUVR in each region was associated with cognitive performance and cognitive decline for each diagnostic group, controlling for age, sex, and education. Within each group, a False Discovery Rate (FDR) correction was applied.

As complimentary analyses, we assessed the association between tau uptake and cognitive performance in each of the 70 brain regions. Tau SUVR in each region was associated with cognitive performance and cognitive decline for each diagnostic group, controlling for age, sex, and education. Within each group, a False Discovery Rate (FDR) correction was applied to avoid multiple comparison issues. Beta coefficients of the surviving relationships were plotted on brain templates.

3.4.6 – Data availability

Data used in this study come from the Alzheimer’s disease neuroimaging initiative (ADNI). Investigators interested in obtaining the data can apply for access on ADNI’s website: <https://adni.loni.usc.edu/>. The code used to compute the spatial extent measures is publicly available in *sihnpy* as of version v0.2, a Python package freely available for download (<https://sihnpy.readthedocs.io/>). The code used for the statistical analyses and for the figures is also made available freely on Github (<https://github.com/villeneuve/ projects>).

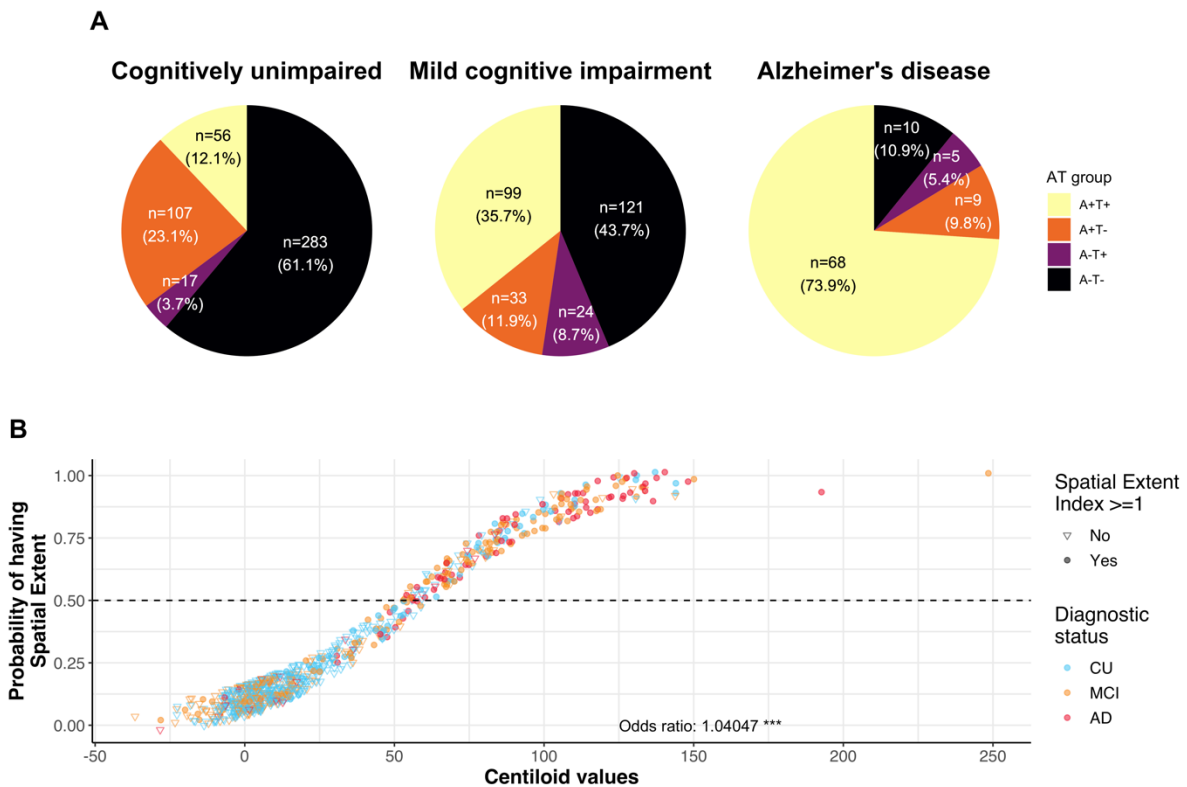


Figure 3.2 Amyloid and tau status in the cohort. (A) A β /tau (AT) status in the included participants from ADNI. A β positivity was established using ADNI’s tracer-specific recommendations for both florbetapir and florbetaben. Tau positivity was defined as having at least one region positive for tau pathology (spatial extent index of one and

above). **(B)** Scatterplot of the probability of having at least one positive tau region (i.e., spatial extent index equal to or higher than one) as a function of the A β load (in centiloid). The probability was extracted from a logistic regression. Odds ratio (and confidence interval) derived from a logistic regression is presented at the bottom of the graph. Note that the points were jittered by a factor of 0.065x0.065 for visualization purposes.

3.5 – Results

3.5.1 – Participants

A total of 1,370 tau scans from 832 unique participants had at least one A β - and tau-PET scan. At the time of the baseline tau scan, 463 participants were cognitively unimpaired (CU), 277 had mild cognitive impairment (MCI) and 92 had Alzheimer's disease dementia. About half of the sample (51%) were female, and 34% had at least one ApoE4 allele. Participants were on average 73.56 ± 7.95 years old. Overall, 35.1% (n = 107) of CU individuals, 47.7% (n = 132) individuals with MCI, and 83.7% (n = 77) individuals with AD were A β -positive. Full demographic information is available in Table 3.1.

In the A β -positive sample, 12.1% (n = 56) of CU participants, 36.1% (n = 100) of MCI and 73.9% (n = 68) of Alzheimer's disease patients had at least one region of tau positivity (Fig. 3.2A, heatmap in Fig. 3.3A). In the A β -negative sample, a small percentage of participants had at least one tau-positive region (heatmap in Supplementary Fig. 3.1B and Supplementary Fig. 3.2) and had lower tau SUVR in the temporal meta-ROI (Supplementary Fig. 3.2). Every increase of 1 A β centiloid unit increased the odds of having at least one brain region with abnormal tau tracer uptake abnormal by 4% (Fig. 3.2B). Considering these findings, and our focus on tau pathology, we restricted the rest of the main analyses to A β -positive individuals (n = 372).

3.5.2 – Cross-sectional tau-PET patterns

We found that, across diagnostic groups, the entorhinal cortex (Braak I) was the region most positive across A β -positive individuals (CU = 17.2%, MCI = 59.9%,

Alzheimer's disease = 74.7%; Fig. 3.3B, Supplementary Fig. 3.3 & Supplementary Table 3.2).

Table 3.1 – Demographic information

	A β -negative (n=460)			A β -positive (n=372)		
	CU (n=300)	MCI (n=145)	AD (n=15)	CU (n=163)	MCI (n=132)	AD (n=77)
Sex, n Females, (%)	176 (58.67)	56 (38.62)	5 (33.33)	96 (58.90)	65 (49.24)	32 (41.56)
APOE4 carriers, n (%)	66 (22.00)	23 (15.86)	5 (33.33)	73 (44.79)	70 (53.03)	48 (62.34)
Age (years)	71.48 (7.31)	73.72 (8.48)	73.83 (8.43)	74.82 (7.57)	74.36 (7.39)	77.35 (8.93)
Education (years)	16.83 (2.30)	16.32 (2.74)	16.07 (2.60)	16.64 (2.34)	15.99 (2.49)	15.55 (2.48)
Centiloid values	4.09 (8.11)	1.18 (10.53)	1.63 (11.27)	53.47 (30.83)	75.78 (35.15)	90.14 (32.86)
Memory composite score	1.08 (0.61) ^{b,c}	0.52 (0.62) ^{a,c}	-0.55 (0.48) ^{a,b}	1.00 (0.62) ^{b,c}	0.07 (0.59) ^{a,c}	-0.77 (0.57) ^{a,b}
Executive composite score	1.20 (0.82) ^{b,c}	0.61 (0.82) ^{a,c}	-0.47 (0.95) ^{a,b}	0.92 (0.77) ^{b,c}	0.19 (0.92) ^{a,c}	-0.79 (1.16) ^{a,b}
Language composite score	0.89 (0.51) ^{b,c}	0.52 (0.50) ^{a,c}	-0.21 (0.39) ^{a,b}	0.75 (0.49) ^{b,c}	0.41 (0.55) ^{a,c}	-0.18 (0.61) ^{a,b}
Visuospatial composite score	0.13 (0.29) ^b	0.01 (0.34) ^a	-0.07 (0.44)	0.06 (0.36) ^c	0.00 (0.38) ^c	-0.43 (0.72) ^{a,b}
Longitudinal sub-sample	CU (n=96)	MCI (n=40)	AD (n=10)	CU (n=90)	MCI (n=66)	AD (n=39)
Average number of tau PET scan per participant	2.56 (0.87)	2.52 (0.72)	2.20 (0.42)	2.68 (0.75)	2.58 (0.66)	2.54 (0.60)
Average number of cognitive visits per participant	6.24 (3.45)	8.75 (5.59) ^{a, c}	3.80 (3.88)	6.18 (3.83)	5.55 (4.21)	4.54 (4.02)

a : significantly different from CU group, b: significantly different from MCI group, c: significantly different from AD group. Values correspond to mean (standard deviation) unless otherwise specified. APOE4 positivity corresponds to having at least 1 e4 allele. Statistical tests were performed within each of A β -negative and A β -positive groups.

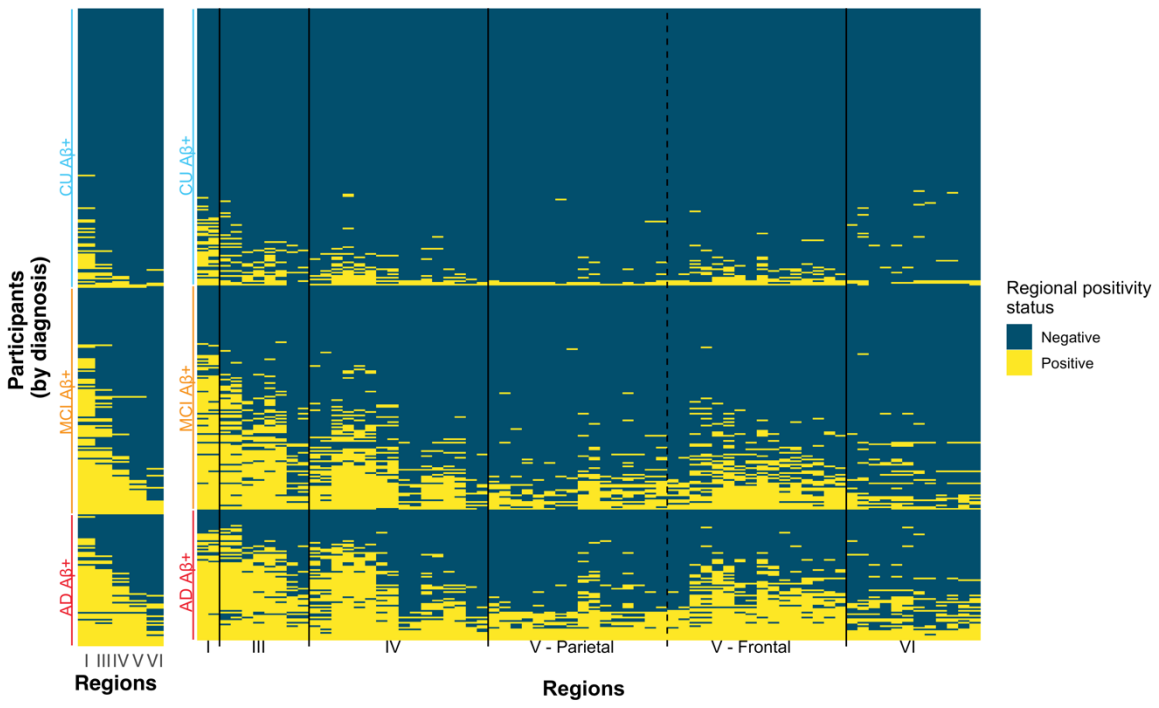
In all diagnostic groups, the five regions that were most often tau positive after the entorhinal cortex were, in order, the inferior temporal (Braak IV), the amygdalae (Braak III), the parahippocampal gyri (Braak III), the middle temporal (Braak IV) and the fusiform gyri (Braak III). All the regions above constituted the temporal meta-ROI (Jack et al., 2017). Similarly, we found that participants largely follow the Braak staging scheme (Fig. 3.3A): across all Braak stages up to and including Braak V, over 91% of participants positive on any given Braak stage were also positive on all previous Braak stages.

3.5.3 – Longitudinal tau-PET patterns

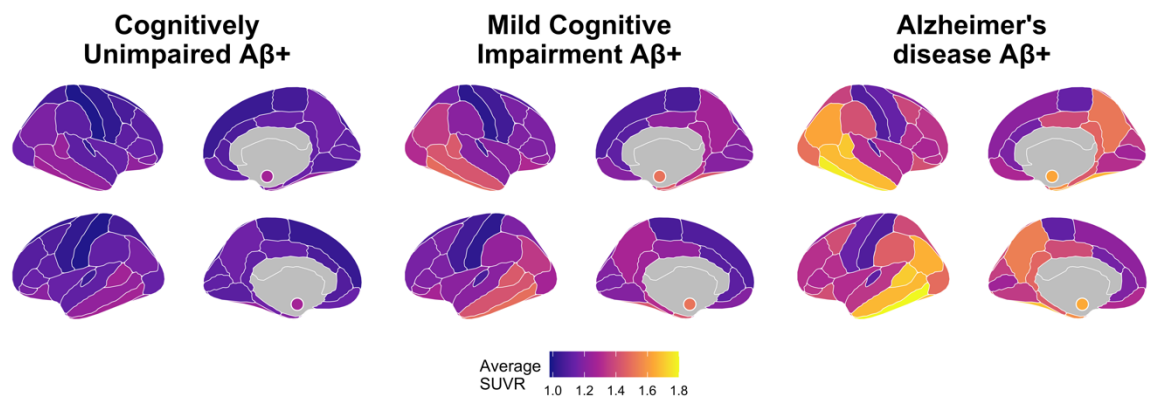
We repeated the analyses in our longitudinal sample (n = 195). Specifically, we assessed whether participants becoming positive in a Braak stage at their last tau scan were either already positive in preceding Braak stages or also progressed in previous stages during the follow-up period.

We quantified which brain regions were negative at baseline and became positive over time (progressor), were positive at baseline and became negative over time (regressor), were positive at both visits (stable positive) or were negative at both visits (stable negative). Similar to the cross-sectional results, we found that participants largely followed the Braak staging scheme (Fig. 3.4A): across all Braak stages up to and including Braak V, over 80% of participants who progressed on a Braak stage at follow-up were already positive or progressed on all previous Braak stages.

A



B



C

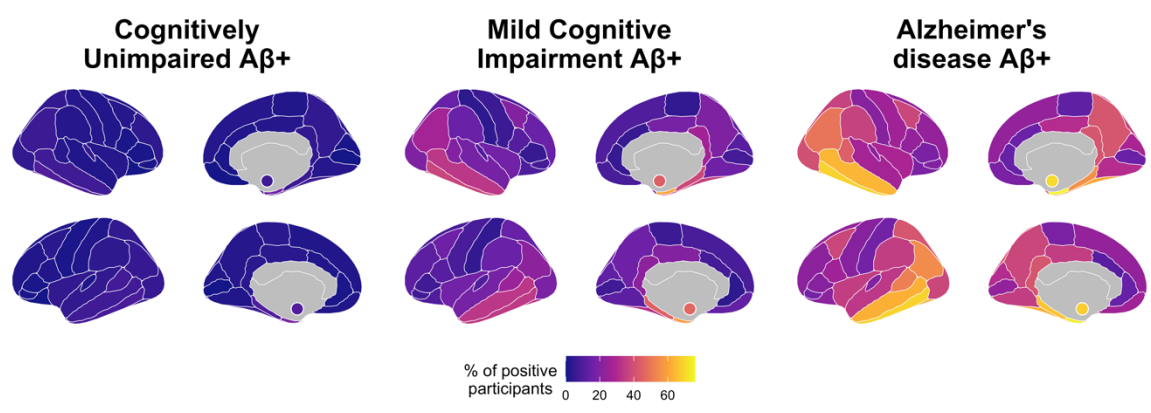


Figure 3.3 Spatial extent of abnormal tau deposition in amyloid positive participants of the ADNI cohort. (A) Based on the method discussed in Figure 3.1, abnormality thresholds were determined for each **I. Braak stages (except stage II)** and for each **II. region of the cortical mantle and the bilateral amygdalae (70 regions)**. One row on the heatmap correspond to an individual participant, while each column represents a distinct cortical region. Within each diagnostic group, participants were sorted from individuals with lowest to highest spatial extent index. Regions on the x-axis in **II.** are sorted by Braak stages. **(B)** Regional average SUVR, by diagnostic status. **(C)** Brain maps representing the percentage of participants having abnormal levels of tau in each region, by diagnostic status.

Patterns of progression across the brain however were different between clinical stages (Fig. 3.4; Supplementary Table 3.3). Specifically, CU participants mostly progressed in the entorhinal cortex (Braak I) while tau abnormality in participants with MCI progressed across the entire cortex, and few participants with Alzheimer's disease dementia accrued additional tau abnormal regions (Fig. 3.4C). Based on the tau spatial extent, the annual rate of regions progressing from negative to positive was 1.2 region per year in participants with MCI, which was similar to CU (1.3 region/year) but higher than participants with Alzheimer's disease dementia (0.988 region/year). (Supplementary Fig. 3.4B). CU and MCI showed a significant rate of change over time compared to participants with Alzheimer's disease dementia, which was similar in the temporal meta-ROI.

Few regressions from positive to negative were observed. In terms of Braak stages, 4 participants with MCI and 3 participants with Alzheimer's disease dementia (4%

of total participants) regressed from a Braak positive to a negative status (usually Braak III, V or VI). In most cases, the participants only regressed on a single Braak stage. At the regional level, thirty participants (15%) had at least one individual region regressing from positive to negative. The rate of regression was lower in CU (3%) and participants with MCI (18%) compared to participants with Alzheimer's disease dementia (38%), which could be explained by the higher number of positive regions in these participants.

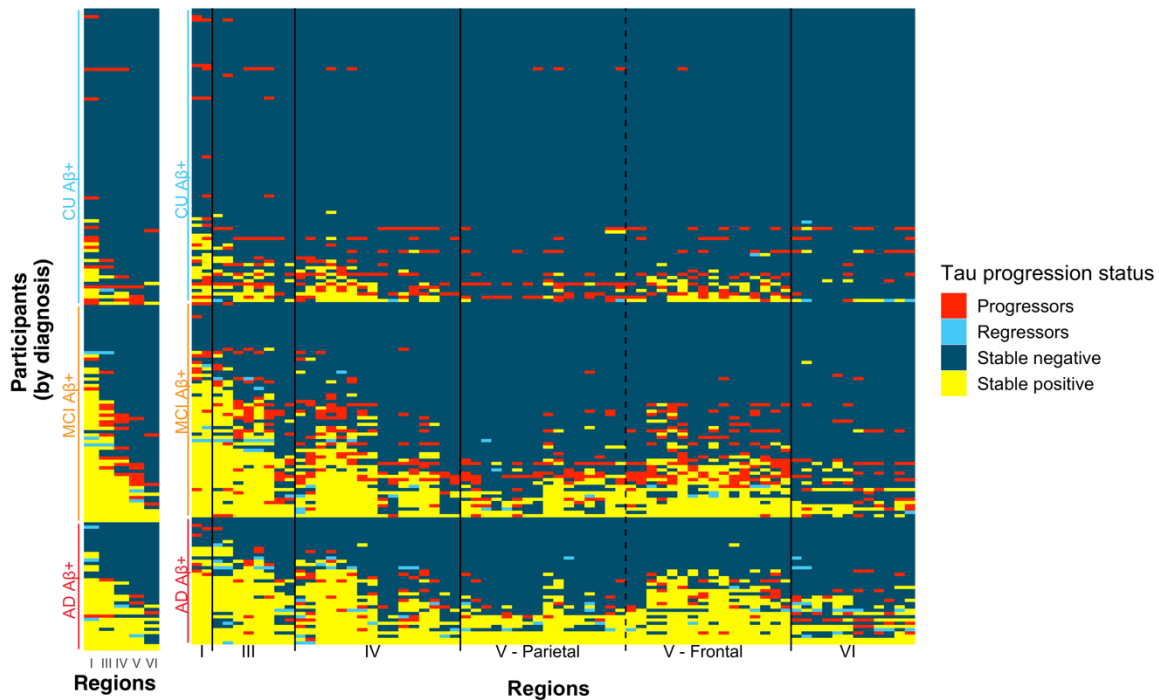
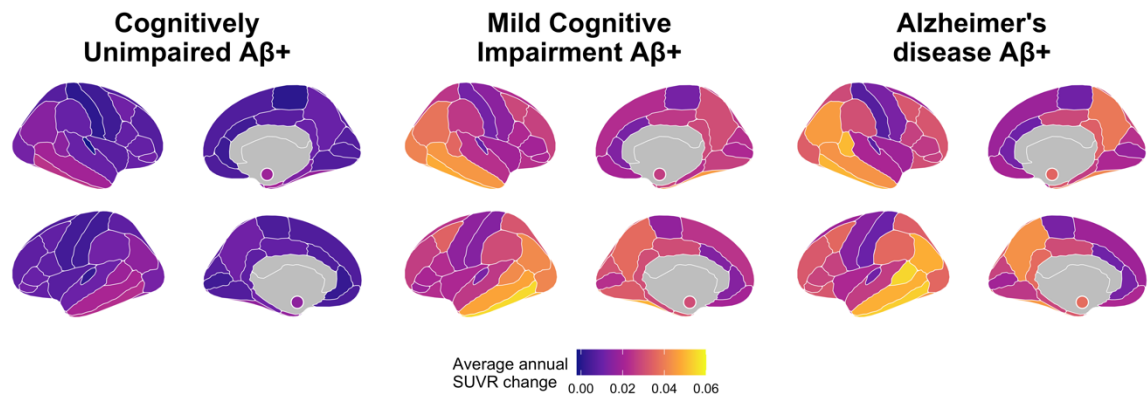
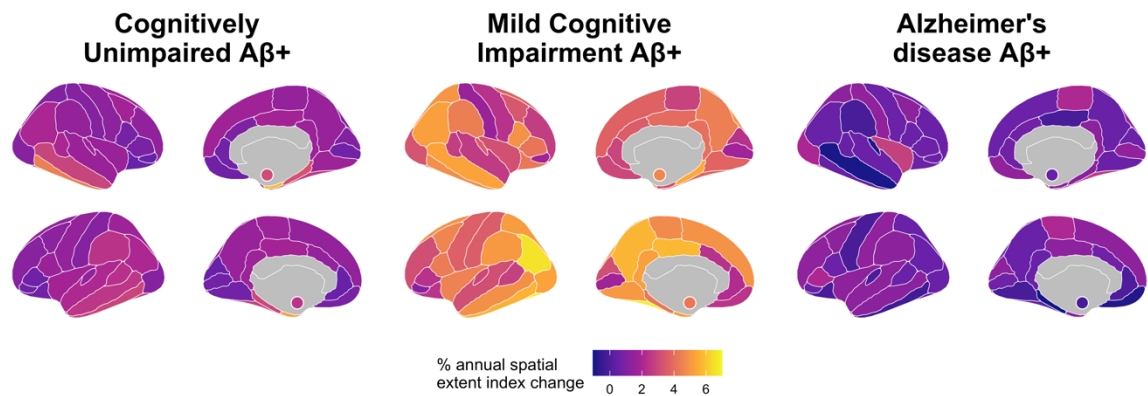
A**B****C**

Figure 3.4 Spatial localization of abnormal tau accumulation over time in amyloid-positive participants of the ADNI cohort. (A) Abnormal accumulation is presented by (I.) Braak stages and (II.) all 70 individual brain regions of the Desikan atlas. Colors denote the change in the region between the baseline and the last available visit. A stable region (negative or positive; blue or yellow) did not change status during the follow-up. A progressing region (red) was originally negative and subsequently became positive over time. A regressing region (teal) was originally positive and became negative over time. (B) Brain maps presenting the average SUVR change per region per year. (C) Brain maps representing the percentage of participants becoming tau positive in each region annually. In both (B) and (C), values in the bilateral amygdalae are represented by small colored circles in the medial view of the brain, and the annual change is calculated in each region using linear mixed effect models with random slopes and intercepts. Only participants with at least three tau scans ($n = 100$) were kept for (B) and (C) to ensure a constant sample across the longitudinal follow-ups.

Overall, we found that participants overwhelmingly followed the Braak staging scheme, demonstrated cross-sectionally and longitudinally, except for the very last Braak stage. However, we also show that there are substantial individual differences in abnormal regions at baseline and in the regional progression of tau pathology.

3.5.4 – Heterogeneity of regional tau-PET abnormality

While abnormal tau accumulation followed Braak staging, regional tau abnormality across the whole brain and within each Braak stage showed heterogeneity across individuals (Fig. 3.3A; Supplementary Table 3.2). CU participants demonstrated the least heterogeneity with an average overlap of 0.74 (± 0.15), participants with MCI had an

average overlap of 0.58 (\pm 0.14) and participants with Alzheimer's disease dementia demonstrated the most heterogeneity with an average overlap of 0.46 (\pm 0.08). Within each Braak stage, the difference in heterogeneity was greatest between CU and MCI, with the MCI group showing more heterogeneity in the pattern of tau abnormal regions. The difference between MCI and AD was less pronounced and often not significant (Supplementary Fig. 3.5A). Results were also similar when considering heterogeneity in the progression of regional tau abnormality over time (Supplementary Fig. 3.5B).

3.5.5 - Associations with demographic information, cognitive profiles and cognitive decline

Given the heterogeneity in regions showing tau abnormality at the individual level across the AD continuum, we then evaluated if the measure of tau spatial extent could yield stronger associations with demographics and cognitive measures than the classical temporal meta-ROI. Of note, the temporal meta-ROI SUVR and the spatial extent correlated well with each other, showing the highest correlation in the MCI group, followed by Alzheimer's disease and CU (Supplementary Fig. 3.2C).

Younger participants with MCI (Spatial extent index: $\beta_{std} = -0.22$, $p < 0.05$, $R^2_{adj} = 0.08$; Temporal meta-ROI SUVR: $\beta_{std} = -0.20$, $p < 0.05$, $R^2_{adj} = 0.07$) or Alzheimer's disease dementia (Spatial extent index: $\beta_{std} = -0.65$, $p < 0.001$, $R^2_{adj} = 0.39$; Temporal meta-ROI SUVR: $\beta_{std} = -0.46$, $p < 0.001$, $R^2_{adj} = 0.17$) had higher spatial extent index and temporal meta-ROI SUVR (Supplementary Fig. 3.6). We also found that ApoE4 carriers in the MCI group had greater tau levels ($\beta_{std} = 0.41$, $p < 0.05$, $R^2_{adj} = 0.09$ for the spatial extent index; $\beta_{std} = 0.49$, $p < 0.05$, $R^2_{adj} = 0.10$ for Temporal meta-ROI

SUVR). Sex and education were not associated with the spatial extent index or the temporal meta-ROI.

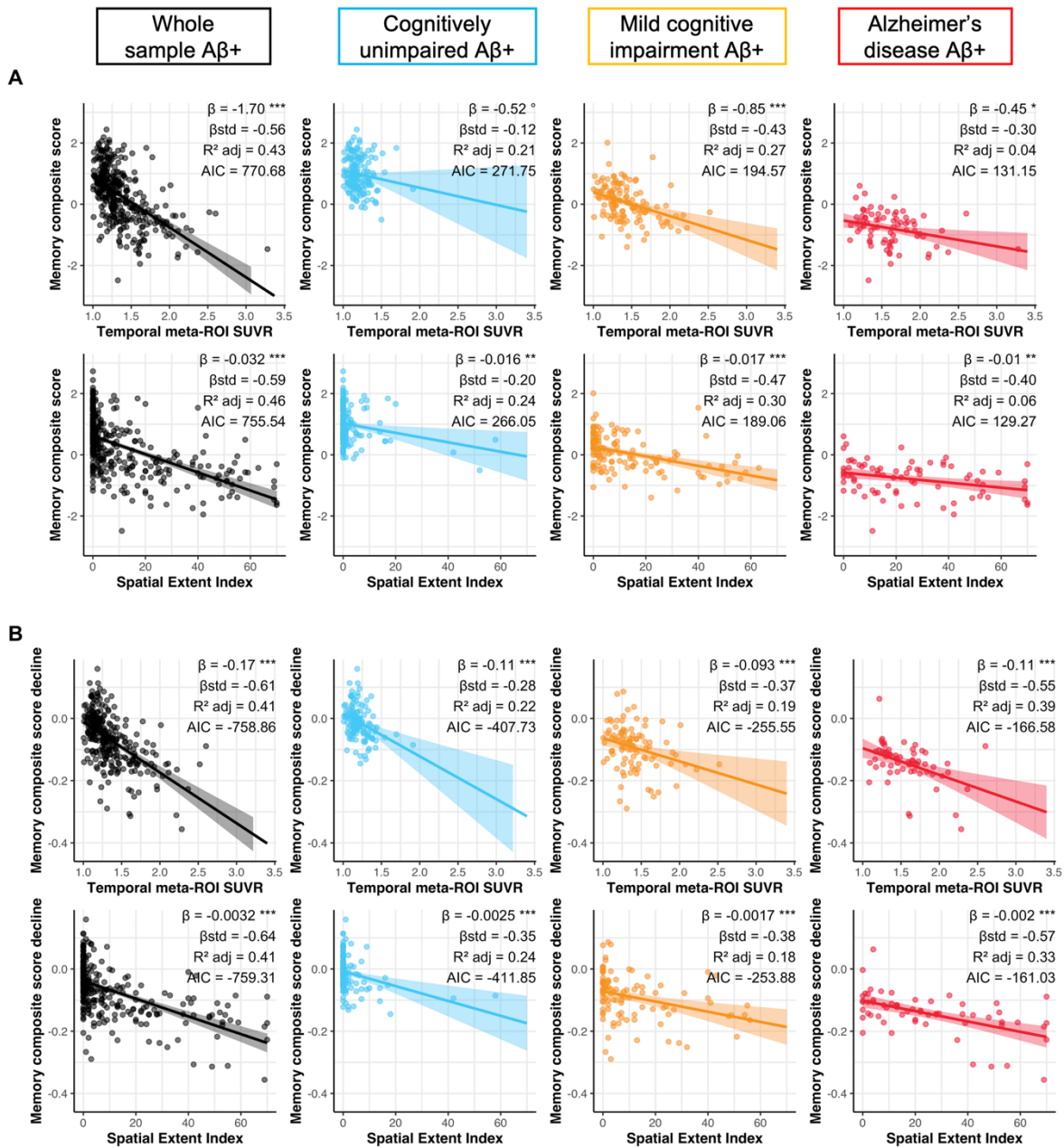


Figure 3.5 Association between tau-PET measures, and memory performance and decline. (A) Memory performance closest in time to the tau-PET scan and (B) memory decline computed across the study period were associated to both temporal meta-ROI

*SUVr and spatial extent index in A β -positive participants using linear regressions. Cognitive decline was computed for each participant with more than two cognitive timepoints using linear mixed effect models with random slopes and intercepts. In each panel, columns represent a diagnostic group (leftmost/black: whole sample, second from the left/blue: cognitively unimpaired, second from the right/orange: mild cognitive impairment, right-most/red: Alzheimer's disease). Simple and standardized β coefficients, adjusted R^2 and AIC, controlled for age sex and education, are shown on the graphs. P-value of models are indicated next to the simple beta coefficients. ($^{\circ}$: $P < 0.1$, * : $P < 0.05$, ** : $P < 0.01$, *** $P < 0.001$) Results remained significant after a multiple comparison false discovery rate (FDR) correction.*

In CU participants, the spatial extent index was associated with the memory composite score (*standardized [std] $\beta = -0.20$, $P = 0.01$, $R^2_{adj} = 0.24$*) (Fig. 3.5) while the temporal meta-ROI was not (*std $\beta = -0.12$, $P > 0.10$, $R^2_{adj} = 0.21$*). The difference in model fit was not significant (*Vuong's $z = -1.13$, $P = 0.13$*), however, suggesting that the spatial extent index provided only a marginally better model fit when compared to the more traditional temporal meta-ROI. In CU participants, neither the spatial extent index nor the temporal meta-ROI were associated with any other cognitive composite (executive, language or visuospatial) (Supplementary Fig. 3.5-3.7). In participants with MCI, both the spatial extent index and the temporal meta-ROI were nearly equally associated with the memory composite, and there were no differences in model fit (*Vuong's $z = -1.35$, $P = 0.089$*). However, the association between the executive composite (*Vuong's $z = -2.77$, $p = 0.003$*), as well as the language composite (*Vuong's $z = -1.89$, $p = 0.029$*) and the spatial extent index was stronger than that with the temporal meta-ROI. There was no

association between the spatial extent index or the meta-ROI and the visuospatial composite. In participants with Alzheimer's disease, results were similar to participants with MCI: spatial extent index and temporal meta-ROI were both equally associated with the memory and the spatial extent index was more strongly associated with the executive composite than the temporal meta-ROI (*Vuong's* $z = -1.88$, $P = 0.030$). However, the spatial extent index was not more strongly associated with the language composite compared to the temporal meta-ROI SUVR (*Vuong's* $z = 0.04$, $P = 0.516$). There was no association between the spatial extent index or the temporal meta-ROI and the visuospatial composite. Looking at cognitive decline, the spatial extent index was more strongly associated with executive function decline compared to the temporal meta-ROI SUVR in participants with MCI (*Vuong's* $z = -1.695$, $P = 0.045$). In all other cognitive domains, the temporal meta-ROI and spatial extent index offered a similar model fit for cognitive decline.

In supplementary analyses, we also investigated regional associations between tau-PET SUVR and cognition (Fig. 3.6A). In CU participants, no individual region was associated with cognitive performance on any composite score. In participants with MCI, tau levels most associated with memory were largely comprised of regions within the temporal lobe, with some weaker associations in the parietal and frontal lobes. Tau levels most associated with executive functions comprised regions across the cortex. Associations with language were almost unilaterally restricted to the left temporal lobe. No associations survived multiple corrections for the visuospatial composite. Results were similar for participants with Alzheimer's disease dementia with one exception;

region-wise associations with the visuospatial composite were significant and spanned outside of the temporal lobe.

Looking at the association between baseline tau and longitudinal cognitive decline, region-wise analyses between tau SUVR and cognitive decline largely replicated our findings at the cross-sectional level (Fig. 3.6B).

We also repeated the main analyses when deriving the spatial extent using alternative regional thresholds based on two standard deviations from CU A β - participants (see Supplementary Results and Supplementary Fig. 3.10 to 3.14). Briefly, analyses related to memory and executive function remained similar. The notable difference was that the group of A-T+ significantly increased in CU and MCI, as tau thresholds, mostly in regions outside of the temporal lobe, were lowered.

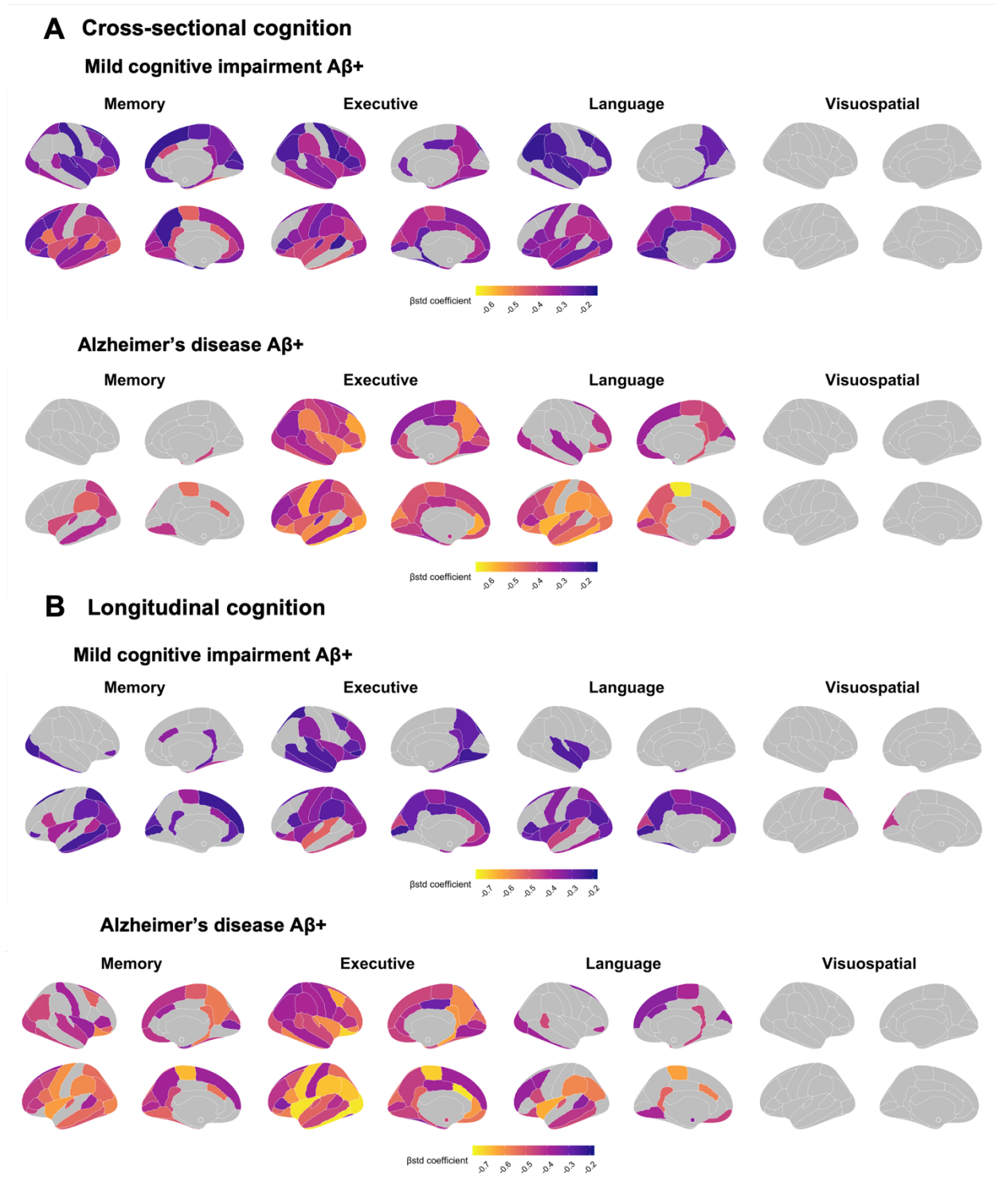


Figure 3.6 Region-wise associations between regional tau-PET SUVR and cognitive performance and decline in participants with MCI and Alzheimer's disease.

Association between tau-PET SUVR and cognitive performance (A) and cognitive decline (B) in participants with MCI and with Alzheimer's disease across four cognitive domains (memory, executive functioning, language and visuospatial). Cognitive decline was computed for each participant with more than two cognitive timepoints using linear mixed effect models with random slopes and intercepts. The standardized β coefficients of the associations between tau-PET SUVR in a specific region and each cognition measure is displayed if it survives adjustment for age, sex and education and a multiple comparison false discovery rate (FDR) correction ($P_{corrected} < 0.05$).

3.6 – Discussion

We found that tau accumulation in late-onset sporadic Alzheimer's disease, tau pathology and follows broad stages of pathological progression (i.e., Braak stages) uniformly across individuals, with early accumulation largely constrained to temporal lobe regions. However, abnormality in cortical tau at a finer-grain regional level is heterogeneous between participants, particularly as clinical symptoms progress. This effect was strongest in participants with mild cognitive impairment, who also showed the fastest region-to-region accumulation of abnormal tau across the whole brain. Finally, we also found that in cognitively unimpaired individuals the association between tau and memory was only significant using the spatial extent index while in participants with MCI or Alzheimer's disease dementia the spatial extent index was more strongly associated with executive function performance than temporal meta-ROI SUVR.

In line with the literature (Braak & Braak, 1991), we found that tau pathology usually accumulates in the entorhinal cortex (Braak I) before accumulating in other temporal regions (Braak III-IV; Berron et al., 2021; Krishnadas et al., 2023; Lee et al., 2022; Sanchez et al., 2021; Vogel et al., 2020) and finally large frontal and parietal regions (Braak V-VI; Therriault et al., 2022). Similarly to previous work (Lee et al., 2022; Ozlen et al., 2022; Sanchez et al., 2021; Vogel et al., 2020), this accumulation of abnormal amounts of tau pathology was mostly restricted to participants with high levels of A β —as opposed to A β -negative participants who showed little tau abnormality. An addition from our study is that these stages are followed not just cross-sectionally, but also over time. Overall, our results recapitulate and solidify our current understand that tau pathology

largely accumulates following the broad Braak stages in late onset sporadic Alzheimer's disease.

Despite these uniform broad inter-individual patterns, we found that within Braak stages, tau abnormality is regionally and inter-individually heterogeneous, especially in more advanced disease stages (i.e., MCI or Alzheimer's disease). Alzheimer's disease is known to present many different clinical variants (Weintraub et al., 2012) and heterogeneous neuroimaging profiles (Ferreira et al., 2020; Ossenkoppele et al., 2020). Specifically looking at tau pathology, several "subtypes" of tau pathology have been suggested (Vogel et al., 2021) and different clinical variants of AD have also shown distinct tau deposition patterns (La Joie et al., 2020; Singleton et al., 2021). Other studies have used continuous variables of heterogeneity rather than subtypes, but always aggregating large swaths of brain regions together in smaller samples and with limited insight in more advanced participants (Mohanty et al., 2023; C. B. Young et al., 2022). Furthermore, using individualized tau measures have been shown to better associate with future accumulation of tau pathology compared to using only Braak stages, demonstrating substantial inter-individual variability (Franzmeier et al., 2020). As such, it is possible that while a large portion of the cortex may become abnormal following a specific sequence, regional patterns may differ between individuals. This was also suggested by a recent study which highlighted that despite tau pathology accumulating mostly in the temporal lobe, individualized regions of interest better capture change in tau overtime (Leuzy et al., 2023). Our results suggest that this heterogeneity emerges in participants with MCI. Specifically, these participants accumulated abnormal amounts of tau pathology across the entire brain faster than CU participants and participants with Alzheimer's disease,

highlighting that the heterogenous accumulation of pathology appears once tau appears outside of the temporal lobe. To note, we also found that higher levels of tau pathology at baseline were associated with faster accumulation of tau pathology over time across diagnostic groups, but that the spatial extent seems to plateau at the stage of Alzheimer's disease dementia. This suggest that there is a stage of the disease where the number of abnormal regions is reached, even though tangles (i.e., SUVR) continue to accumulate. This is somewhat contrary to A β pathology which seems to plateau over time at the late stage of the disease (Jagust & Landau, 2021). Overall, these results suggest that fine-grain regional heterogeneity exists in tau deposition and accumulation, despite broad stages being followed uniformly, and that this heterogeneity starts to appear in participants with MCI.

Another key finding from the study is that the extent of tau pathology across the brain is associated with cognitive performance across cognitive domains on par with tau in the temporal meta-ROI in most domains, except for memory in cognitively unimpaired individuals and executive functioning in individuals with cognitive impairments where spatial extent of tau was more strongly associated with cognition than the temporal meta-ROI. Literature in recent years has repetitively shown that tau—rather than A β —is the pathological hallmark most strongly associated with cognitive decline (Ossenkoppele et al., 2021). This is also echoed by research on Alzheimer's disease clinical variants. Previous work demonstrated that, while A β deposition patterns were similar across individuals from different clinical variants, tau patterns differ according to the variants, often affecting regions responsible for the main cognitive domain affected (La Joie et al., 2020; Singleton et al., 2021). This distinct topography of tau for each cognitive domain

was also found in our study: tau was associated with the memory composite mostly in the temporal and frontal lobes bilaterally, tau was associated with the executive composite across the brain and tau was associated with language mostly unilaterally to the left hemisphere. Overall, our results suggest that regional tau topography is associated with specific cognitive domains, and that leveraging the spatial extent index may uncover stronger associations between tau and cognitive performances.

3.6.1 – Strengths and limitations

The strengths of our study include a large sample size and a large longitudinal tau-PET sample. Cognition was collected over a long follow-up period; for at least 5 years in most cases.

Our study also has some limitations to acknowledge. We staged disease progression following the clinical diagnosis as attributed by physicians from memory clinics. However, not everyone with the same clinical label may be at the same “biological” stage of the disease, i.e., two individuals with an MCI diagnosis may not have the same tau-PET patterns simply because they haven’t started to present symptoms at the same time (Vogel et al., 2021; A. L. Young et al., 2018). As such, the heterogeneity observed within each clinical diagnosis could be due to participants being at more advanced disease stages. Furthermore, we use the overlap of spatial extent patterns to define heterogeneity which somewhat lacks spatial resolution. It is possible that the same index, e.g., 0.5, represents the positive overlap of a small set of regions spatially close to one another or the overlap of a large set of regions spatially distant from one another. Nonetheless, our results are reassuring: if biological staging had been the driver of the heterogeneity in the tau patterns cross-sectionally, our longitudinal results would have

shown that participants had less (not more) heterogeneity, and we replicated most of the findings of heterogeneity within each Braak stage.

Our main method to derive the spatial extent index relies on unsupervised GMM, where participants are clustered in either one of two groups: “normal” or “abnormal” tau. Some of the limitations of these methods include the need to set in advance certain components of the models, including the number of clusters—two in the case of this paper—which may preclude more complex underlying patterns in the data. However, we ensured that a two-component method was a better fit compared to a single component using the Bayesian Information Criterion. Due to the data-driven nature of the method, should the proportion of participants with high levels of tau included change, the thresholds will also likely change. However, in supplementary analyses, we showed that GMM thresholds were likely less influenced by outliers in the data compared to other methods for deriving thresholds such as 2 standard deviations from CU A β - participants. This suggests that other traditional methods are likely plagued by the same issue, and the main results of the paper were not dependent on the choice of how to derive the thresholds.

A major limitation is ADNI’s inclusion criteria. By design, ADNI includes participants with amnesic disease presentation (Weiner et al., 2017). However, atypical variants of AD may not present with memory impairment at the forefront of their cognitive complaints (Weintraub et al., 2012). As such, ADNI’s sample may be by design very homogenous. This could explain why the spatial extent performed relatively similarly to the meta-ROI across cognitive composites. Despite this homogenous sample, we still found

heterogeneous tau patterns and diverse tau-cognition associations, and a stronger association of individualized measures with executive functioning and language.

Many participants have the same visuospatial score cross-sectionally and over time, which could stem from an error in the database. Any results related to this composite index should be carefully considered in this context.

Finally, due to molecular limitations of the Flortaucipir tracer which presents off-target binding in the hippocampus, we excluded this region from our spatial extent index. However, there is convincing evidence that some patients with Alzheimer's disease dementia will present more (medial temporal subtype) or less (hippocampal sparing subtype) neurodegeneration in the hippocampus (Ferreira et al., 2020), suggesting that tau within the hippocampus is also an important source of heterogeneity which is missed by the spatial extent index from the current paper. Future research should aim to confirm these findings using tau-PET tracers less sensitive to off-target binding in the hippocampus such as MK6240.

3.6.2 – Conclusion

While our study confirms that participants accumulate tau pathology following the broad Braak stages, we also demonstrate that regional accumulation is subject to significant heterogeneity—particularly as the disease progresses. This heterogeneity seems to take hold during the MCI stage, as these participants accrue more tau abnormal regions faster than both CU and participants with Alzheimer's disease dementia. We also illustrate that the topography of the tau pathology is differentially associated with cognitive domains, and that using the spatial extent (i.e., tau abnormality across the brain) can lead to stronger associations with executive functioning in MCI and individuals with

Alzheimer's disease dementia. Taken together, our results suggest that using a method that captures regional tau might help uncover associations with cognition, and we propose a simple research method to investigate these regionalities going forward.

3.7 – Acknowledgements

The authors would like to acknowledge Valentin Ourry, Yara Yakoub, Ting Qiu, Mohammadali Javanray, Jonathan Gallego Rudolf, Bery Mohammediyan and Alfonso Fajardo for providing advice on the study research design. We would also like to acknowledge the participants of the ADNI cohort for dedicating their time and energy to collect the data used in this study and the staff working on organizing the ADNI data for making the data available to researchers worldwide.

3.8 – Funding

FSO was funded by a scholarship from the Fonds de Recherche en Santé – Québec. APB is supported by a postdoctoral fellowship from the Fonds de Recherche en Santé – Québec (298314).

Part of data collection and sharing for this project was funded by the Alzheimer's Disease Neuroimaging Initiative (ADNI) (National Institutes of Health Grant U01 AG024904) and DOD ADNI (Department of Defense award number W81XWH-12-20012). ADNI is funded by the National Institute on Aging, the National Institute of Biomedical Imaging and Bioengineering, and through generous contributions from the following: AbbVie, Alzheimer's Association; Alzheimer's Drug Discovery Foundation; Araclon Biotech; BioClinica, Inc.; Biogen; BristolMyers Squibb Company; CereSpir, Inc.; Cogstate; Eisai Inc.; Elan Pharmaceuticals, Inc.; Eli Lilly and Company; EuroImmun; F. Hoffmann-LaRoche Ltd and its affiliated company Genentech, Inc.; Fujirebio; GE Healthcare; IXICO Ltd.; Janssen Alzheimer Immunotherapy Research & Development, LLC.; Johnson & Johnson Pharmaceutical Research & Development LLC.; Lumosity; Lundbeck; Merck & Co., Inc.; MesoScale Diagnostics, LLC.; NeuroRxResearch; Neurotrack Technologies; Novartis Pharmaceuticals Corporation; Pfizer Inc.; Piramal Imaging; Servier; Takeda Pharmaceutical Company; and Transition Therapeutics. The Canadian Institutes of Health Research is providing funds to support ADNI clinical sites in Canada. Private sector contributions are facilitated by the Foundation for the National Institutes of Health (www.fnih.org). The grantee organization is the Northern California Institute for Research and Education, and the study is coordinated by the Alzheimer's Therapeutic Research Institute at the University of Southern California. ADNI data are

disseminated by the Laboratory for Neuro Imaging at the University of Southern California.

3.9 – Competing interests

The authors report no competing interests.

3.10 – References of Chapter 3

- Berron, D., Vogel, J. W., Insel, P. S., Pereira, J. B., Xie, L., Wisse, L. E. M., Yushkevich, P. A., Palmqvist, S., Mattsson-Carlgren, N., Stomrud, E., Smith, R., Strandberg, O., & Hansson, O. (2021). Early stages of tau pathology and its associations with functional connectivity, atrophy and memory. *Brain*, 2021. <https://doi.org/10.1093/brain/awab114>
- Biel, D., Brendel, M., Rubinski, A., Buerger, K., Janowitz, D., Dichgans, M., Franzmeier, N., & for the Alzheimer's Disease Neuroimaging Initiative (ADNI). (2021). Tau-PET and in vivo Braak-staging as prognostic markers of future cognitive decline in cognitively normal to demented individuals. *Alzheimer's Research & Therapy*, 13(1), 137. <https://doi.org/10.1186/s13195-021-00880-x>
- Braak, H., & Braak, E. (1991). Neuropathological staging of Alzheimer-related changes. *Acta Neuropathologica*, 82, 239–259.
- Desikan, R. S., Ségonne, F., Fischl, B., Quinn, B. T., Dickerson, B. C., Blacker, D., Buckner, R. L., Dale, A. M., Maguire, R. P., Hyman, B. T., Albert, M. S., & Killiany, R. J. (2006). An automated labeling system for subdividing the human cerebral cortex on MRI scans into gyral based regions of interest. *NeuroImage*, 31(3), 968–980. <https://doi.org/10.1016/j.neuroimage.2006.01.021>
- Ferreira, D., Nordberg, A., & Westman, E. (2020). Biological subtypes of Alzheimer disease: A systematic review and meta-analysis. *Neurology*, 94(10), 436–448. <https://doi.org/10.1212/WNL.00000000000009058>
- Franzmeier, N., Dewenter, A., Frontzkowski, L., Dichgans, M., Rubinski, A., Neitzel, J., Smith, R., Strandberg, O., Ossenkoppele, R., Buerger, K., Duering, M., Hansson,

- O., & Ewers, M. (2020). Patient-centered connectivity-based prediction of tau pathology spread in Alzheimer's disease. *Science Advances*, 6(48).
<https://doi.org/10.1126/sciadv.abd1327>
- Gibbons, L. E., Carle, A. C., Mackin, R. S., Harvey, D., Mukherjee, S., Insel, P., Curtis, S. M. K., Mungas, D., & Crane, P. K. (2012). A composite score for executive functioning, validated in Alzheimer's Disease Neuroimaging Initiative (ADNI) participants with baseline mild cognitive impairment. *Brain Imaging and Behavior*, 6(4), 517–527. <https://doi.org/10.1007/s11682-012-9176-1>
- Hanseeuw, B. J., Betensky, R. A., Jacobs, H. I. L., Schultz, A. P., Sepulcre, J., Becker, J. A., Cosio, D. M. O., Farrell, M., Quiroz, Y. T., Mormino, E. C., Buckley, R. F., Papp, K. V., Amariglio, R. A., Dewachter, I., Ivanoiu, A., Huijbers, W., Hedden, T., Marshall, G. A., Chhatwal, J. P., ... Johnson, K. (2019). Association of Amyloid and Tau with Cognition in Preclinical Alzheimer Disease: A Longitudinal Study. *JAMA Neurology*, 76(8), 915–924.
<https://doi.org/10.1001/jamaneurol.2019.1424>
- Jack, C. R., Wiste, H. J., Weigand, S. D., Therneau, T. M., Lowe, V. J., Knopman, D. S., Gunter, J. L., Senjem, M. L., Jones, D. T., Kantarci, K., Machulda, M. M., Mielke, M. M., Roberts, R. O., Vemuri, P., Reyes, D. A., & Petersen, R. C. (2017). Defining imaging biomarker cut points for brain aging and Alzheimer's disease. *Alzheimer's and Dementia*, 13(3), 205–216.
<https://doi.org/10.1016/j.jalz.2016.08.005>
- Jagust, W. J., & Landau, S. M. (2021). Temporal Dynamics of Beta-amyloid Accumulation in Aging and Alzheimer's Disease. *Neurology*,

10.1212/WNL.0000000000011524.

<https://doi.org/10.1212/wnl.0000000000011524>

Krishnadas, N., Doré, V., Robertson, J. S., Ward, L., Fowler, C., Masters, C. L., Bourgeat, P., Fripp, J., Villemagne, V. L., & Rowe, C. C. (2023). Rates of regional tau accumulation in ageing and across the Alzheimer's disease continuum: An AIBL 18F-MK6240 PET study. *EBioMedicine*, 88, 104450. <https://doi.org/10.1016/j.ebiom.2023.104450>

La Joie, R., Visani, A. V., Lesman-Segev, O. H., Baker, S. L., Edwards, L., Iaccarino, L., Soleimani-Meigooni, D. N., Mellinger, T., Janabi, M., Miller, Z. A., Perry, D. C., Pham, J., Strom, A., Gorno-Tempini, M. L., Rosen, H. J., Miller, B. L., Jagust, W. J., & Rabinovici, G. D. (2020). Association of APOE4 and clinical variability in Alzheimer disease with the pattern of tau- and amyloid-PET. *Neurology*, 10.1212/WNL.0000000000011270. <https://doi.org/10.1212/wnl.0000000000011270>

Lee, W. J., Brown, J. A., Kim, H. R., Seong, J., Seeley, W. W., Lee, W. J., Brown, J. A., Kim, H. R., Joie, R. L., Cho, H., & Lyoo, C. H. (2022). *Article Regional A b -tau interactions promote onset and acceleration of Alzheimer ' s disease tau spreading Article Regional A b -tau interactions promote onset and acceleration of Alzheimer ' s disease tau spreading*. 1–12. <https://doi.org/10.1016/j.neuron.2022.03.034>

Leuzy, A., Chiotis, K., Lemoine, L., Gillberg, P.-G., Almkvist, O., Rodriguez-Vieitez, E., & Nordberg, A. (2019). Tau PET imaging in neurodegenerative tauopathies—Still

a challenge. *Molecular Psychiatry*, 24(8), 1112–1134.

<https://doi.org/10.1038/s41380-018-0342-8>

Leuzy, A., Pichet Binette, A., Vogel, J. W., Klein, G., Borroni, E., Tonietto, M., Strandberg, O., Mattsson-Carlgrén, N., Palmqvist, S., Pontecorvo, M. J., Iaccarino, L., Stomrud, E., Ossenkoppele, R., Smith, R., Hansson, O., & Alzheimer's Disease Neuroimaging Initiative. (2023). Comparison of Group-Level and Individualized Brain Regions for Measuring Change in Longitudinal Tau Positron Emission Tomography in Alzheimer Disease. *JAMA Neurology*.
<https://doi.org/10.1001/jamaneurol.2023.1067>

Lowe, V. J., Curran, G., Fang, P., Liesinger, A. M., Josephs, K. A., Parisi, J. E., Kantarci, K., Boeve, B. F., Pandey, M. K., Bruinsma, T., Knopman, D. S., Jones, D. T., Petrucelli, L., Cook, C. N., Graff-Radford, N. R., Dickson, D. W., Petersen, R. C., Jack, C. R., & Murray, M. E. (2016). An autoradiographic evaluation of AV-1451 Tau PET in dementia. *Acta Neuropathologica Communications*, 4(1), 58.
<https://doi.org/10.1186/s40478-016-0315-6>

Marquié, M., Normandin, M. D., Vanderburg, C. R., Costantino, I. M., Bien, E. A., Rycyna, L. G., Klunk, W. E., Mathis, C. A., Ikonomic, M. D., Debnath, M. L., Vasdev, N., Dickerson, B. C., Gomperts, S. N., Growdon, J. H., Johnson, K. A., Frosch, M. P., Hyman, B. T., & Gómez-Isla, T. (2015). Validating novel tau positron emission tomography tracer [F-18]-AV-1451 (T807) on postmortem brain tissue: Validation of PET Tracer. *Annals of Neurology*, 78(5), 787–800.
<https://doi.org/10.1002/ana.24517>

- McSweeney, M., Pichet Binette, A., Meyer, P. F., Gonneaud, J., Bedetti, C., Ozlen, H., Labonté, A., Rosa-Neto, P., Breitner, J., Poirier, J., & Villeneuve, S. (2020). Intermediate flortaucipir uptake is associated with A β -PET and CSF tau in asymptomatic adults. *Neurology*, *94*(11), e1190–e1200.
<https://doi.org/10.1212/WNL.00000000000008905>
- Mukherjee, S., Choi, S.-E., Lee, M. L., Scollard, P., Trittschuh, E. H., Mez, J., Saykin, A. J., Gibbons, L. E., Sanders, R. E., Zaman, A. F., Teylan, M. A., Kukull, W. A., Barnes, L. L., Bennett, D. A., Lacroix, A. Z., Larson, E. B., Cuccaro, M., Mercado, S., Dumitrescu, L., ... Crane, P. K. (2022). Cognitive domain harmonization and cocalibration in studies of older adults. *Neuropsychology*.
<https://doi.org/10.1037/neu0000835>
- Ossenkoppele, R., Lyoo, C. H., Sudre, C. H., van Westen, D., Cho, H., Ryu, Y. H., Choi, J. Y., Smith, R., Strandberg, O., Palmqvist, S., Westman, E., Tsai, R., Kramer, J., Boxer, A. L., Gorno-Tempini, M. L., La Joie, R., Miller, B. L., Rabinovici, G. D., & Hansson, O. (2020). Distinct tau PET patterns in atrophy-defined subtypes of Alzheimer's disease. *Alzheimer's and Dementia*, *16*(2), 335–344.
<https://doi.org/10.1016/j.jalz.2019.08.201>
- Ossenkoppele, R., Pichet Binette, A., Groot, C., Smith, R., Strandberg, O., Palmqvist, S., Stomrud, E., Tideman, P., Ohlsson, T., Jögi, J., Johnson, K., Sperling, R., Dore, V., Masters, C. L., Rowe, C., Visser, D., van Berckel, B. N. M., van der Flier, W. M., Baker, S., ... Hansson, O. (2022). Amyloid and tau PET-positive cognitively unimpaired individuals are at high risk for future cognitive decline.

Nature Medicine, 28(11), 2381–2387. <https://doi.org/10.1038/s41591-022-02049-x>

Ossenkoppele, R., Rabinovici, G. D., Smith, R., Cho, H., Scholl, M., Strandberg, O., Palmqvist, S., Mattsson, N., Janelidze, S., Santillo, A., Ohlsson, T., Jogi, J., Tsai, R., La Joie, R., Kramer, J., Boxer, A. L., Gorno-Tempini, M. L., Miller, B. L., Choi, J. Y., ... Hansson, O. (2018). Discriminative accuracy of [18F]flortaucipir positron emission tomography for Alzheimer disease vs other neurodegenerative disorders. *JAMA - Journal of the American Medical Association*, 320(11), 1151–1162. <https://doi.org/10.1001/jama.2018.12917>

Ossenkoppele, R., Smith, R., Mattsson-Carlsson, N., Groot, C., Leuzy, A., Strandberg, O., Palmqvist, S., Olsson, T., Jögi, J., Stormrud, E., Cho, H., Ryu, Y. H., Choi, J. Y., Boxer, A. L., Gorno-Tempini, M. L., Miller, B. L., Soleimani-Meigooni, D., Iaccarino, L., La Joie, R., ... Hansson, O. (2021). Accuracy of Tau Positron Emission Tomography as a Prognostic Marker in Preclinical and Prodromal Alzheimer Disease: A Head-to-Head Comparison against Amyloid Positron Emission Tomography and Magnetic Resonance Imaging. *JAMA Neurology*, 78(8), 961–971. <https://doi.org/10.1001/jamaneurol.2021.1858>

Ozlen, H., Pichet Binette, A., Köbe, T., Meyer, P.-F., Gonneaud, J., St-Onge, F., Provost, K., Soucy, J.-P., Rosa-Neto, P., Breitner, J., Poirier, J., Villeneuve, S., Tam, A., Labonte, A., Pichet Binette, A., Faubert, A.-M., Mathieu, A., Madjar, C., Carrier, C. E., ... Yang, H.-S. (2022). Spatial Extent of Amyloid- β Levels and Associations With Tau-PET and Cognition. *JAMA Neurology*. <https://doi.org/10.1001/jamaneurol.2022.2442>

- Pichet Binette, A., Franzmeier, N., Spotorno, N., Ewers, M., Brendel, M., Biel, D., Alzheimer's Disease Neuroimaging Initiative, Weiner, M., Aisen, P., Petersen, R., Jack, C. R., Jagust, W., Trojanowki, J. Q., Toga, A. W., Beckett, L., Green, R. C., Saykin, A. J., Morris, J., Shaw, L. M., ... Hansson, O. (2022). Amyloid-associated increases in soluble tau relate to tau aggregation rates and cognitive decline in early Alzheimer's disease. *Nature Communications*, *13*(1), 6635.
<https://doi.org/10.1038/s41467-022-34129-4>
- Pontecorvo, M. J., Devous, M. D., Kennedy, I., Navitsky, M., Lu, M., Galante, N., Salloway, S., Doraiswamy, P. M., Southeikal, S., Arora, A. K., McGeehan, A., Lim, N. C., Xiong, H., Trucchio, S. P., Joshi, A. D., Shcherbinin, S., Teske, B., Fleisher, A. S., & Mintun, M. A. (2019). A multicentre longitudinal study of flortaucipir (18F) in normal ageing, mild cognitive impairment and Alzheimer's disease dementia. *Brain*, *142*(6), 1723–1735.
<https://doi.org/10.1093/brain/awz090>
- Pontecorvo, M. J., Devous, M. D., Navitsky, M., Lu, M., Salloway, S., Schaerf, F. W., Jennings, D., Arora, A. K., McGeehan, A., Lim, N. C., Xiong, H., Joshi, A. D., Siderowf, A., & Mintun, M. A. (2017). Relationships between flortaucipir PET tau binding and amyloid burden, clinical diagnosis, age and cognition. *Brain*, *140*(3), 748–763. <https://doi.org/10.1093/brain/aww334>
- Royse, S. K., Minhas, D. S., Lopresti, B. J., Murphy, A., Ward, T., Koeppe, R. A., Bullich, S., DeSanti, S., Jagust, W. J., Landau, S. M., & for the Alzheimer's Disease Neuroimaging Initiative. (2021). Validation of amyloid PET positivity

- thresholds in centiloids: A multisite PET study approach. *Alzheimer's Research & Therapy*, 13(1), 99. <https://doi.org/10.1186/s13195-021-00836-1>
- Sanchez, J. S., Becker, J. A., Jacobs, H. I. L., Hanseeuw, B. J., Jiang, S., Schultz, A. P., Properzi, M. J., Katz, S. R., Beiser, A., Satizabal, C. L., O'Donnell, A., DeCarli, C., Killiany, R., El Fakhri, G., Normandin, M. D., Gómez-Isla, T., Quiroz, Y. T., Rentz, D. M., Sperling, R. A., ... Johnson, K. A. (2021). The cortical origin and initial spread of medial temporal tauopathy in Alzheimer's disease assessed with positron emission tomography. *Science Translational Medicine*, 13(577). <https://doi.org/10.1126/scitranslmed.abc0655>
- Schöll, M., Lockhart, S. N., Schonhaut, D. R., O'Neil, J. P., Janabi, M., Ossenkuppele, R., Baker, S. L., Vogel, J. W., Faria, J., Schwimmer, H. D., Rabinovici, G. D., & Jagust, W. J. (2016). PET Imaging of Tau Deposition in the Aging Human Brain. *Neuron*, 89(5), 971–982. <https://doi.org/10.1016/j.neuron.2016.01.028>
- Singleton, E. H., Hansson, O., Pijnenburg, Y. A. M., Joie, R. L., Mantyh, W. G., Tideman, P., Stomrud, E., Leuzy, A., Johansson, M., Strandberg, O., Smith, R., Berendrecht, E., Miller, B., Iaccarino, L., Edwards, L., Storm, A., Wolters, E., Coomans, E. M., Visser, D., ... Ossenkuppele, R. (2021). Heterogeneous distribution of tau pathology in the behavioral variant of Alzheimer's disease. *Journal of Neurology, Neurosurgery and Psychiatry*, 0, 1–9. <https://doi.org/10.1136/jnnp-2020-325497>
- Strikwerda-Brown, C., Hobbs, D. A., Gonneaud, J., St-Onge, F., Binette, A. P., Ozlen, H., Provost, K., Soucy, J.-P., Buckley, R. F., Benzinger, T. L. S., Morris, J. C., Villemagne, V. L., Doré, V., Sperling, R. A., Johnson, K. A., Rowe, C. C., Gordon,

- B. A., Poirier, J., Breitner, J. C. S., ... Bourgeat, P. (2022). Association of Elevated Amyloid and Tau Positron Emission Tomography Signal With Near-Term Development of Alzheimer Disease Symptoms in Older Adults Without Cognitive Impairment. *JAMA Neurology*, 79(10), 975.
<https://doi.org/10.1001/jamaneurol.2022.2379>
- Therriault, J., Pascoal, T. A., Lussier, F. Z., Tissot, C., Chamoun, M., Bezgin, G., Servaes, S., Benedet, A. L., Ashton, N. J., Karikari, T. K., Lantero-Rodriguez, J., Kunach, P., Wang, Y.-T., Fernandez-Arias, J., Massarweh, G., Vitali, P., Soucy, J.-P., Saha-Chaudhuri, P., Blennow, K., ... Rosa-Neto, P. (2022). Biomarker modeling of Alzheimer's disease using PET-based Braak staging. *Nature Aging*, 2(6), 526–535. <https://doi.org/10.1038/s43587-022-00204-0>
- Vogel, J. W., Iturria-Medina, Y., Strandberg, O. T., Smith, R., Levitis, E., Evans, A. C., & Hansson, O. (2020). Spread of pathological tau proteins through communicating neurons in human Alzheimer's disease. *Nature Communications*, 11(1), 2612.
<https://doi.org/10.1038/s41467-020-15701-2>
- Vogel, J. W., Young, A. L., Oxtoby, N. P., Smith, R., Ossenkoppele, R., Strandberg, O. T., Joie, R. L., Aksman, L. M., Grothe, M. J., Devous, M. D., Rabinovici, G. D., Alexander, D. C., Lyoo, C. H., Evans, A. C., & Hansson, O. (2021). Four distinct trajectories of tau deposition identified in Alzheimer's disease. *Nature Medicine*.
<https://doi.org/10.1038/s41591-021-01309-6>
- Vuong, Q. H., Econometrica, S., & Mar, N. (1989). Likelihood Ratio Tests for Model Selection and Non-Nested Hypotheses Published by: The Econometric Society. *Econometrica*, 57(2), 307–333.

- Weiner, M. W., Veitch, D. P., Aisen, P. S., Beckett, L. A., Cairns, N. J., Green, R. C., Harvey, D., Jack, C. R., Jagust, W., Morris, J. C., Petersen, R. C., Salazar, J., Saykin, A. J., Shaw, L. M., Toga, A. W., Trojanowski, J. Q., & Alzheimer's Disease Neuroimaging Initiative. (2017). The Alzheimer's Disease Neuroimaging Initiative 3: Continued innovation for clinical trial improvement. *Alzheimer's & Dementia*, 13(5), 561–571. <https://doi.org/10.1016/j.jalz.2016.10.006>
- Weintraub, S., Wicklund, A. H., & Salmon, D. P. (2012). The neuropsychological profile of Alzheimer disease. *Cold Spring Harbor Perspectives in Medicine*, 2(4). <https://doi.org/10.1101/cshperspect.a006171>
- Xia, C., Arteaga, J., Chen, G., Gangadharmath, U., Gomez, L. F., Kasi, D., Lam, C., Liang, Q., Liu, C., Mocharla, V. P., Mu, F., Sinha, A., Su, H., Szardenings, A. K., Walsh, J. C., Wang, E., Yu, C., Zhang, W., Zhao, T., & Kolb, H. C. (2013). [¹⁸F]T807, a novel tau positron emission tomography imaging agent for Alzheimer's disease. *Alzheimer's & Dementia*, 9(6), 666–676. <https://doi.org/10.1016/j.jalz.2012.11.008>
- Young, A. L., Marinescu, R. V., Oxtoby, N. P., Bocchetta, M., Yong, K., Firth, N. C., Cash, D. M., Thomas, D. L., Dick, K. M., Cardoso, J., van Swieten, J., Borroni, B., Galimberti, D., Masellis, M., Tartaglia, M. C., Rowe, J. B., Graff, C., Tagliavini, F., Frisoni, G. B., ... Furst, A. J. (2018). Uncovering the heterogeneity and temporal complexity of neurodegenerative diseases with Subtype and Stage Inference. *Nature Communications*, 9(1), 1–16. <https://doi.org/10.1038/s41467-018-05892-0>

3.11 – Supplementary results

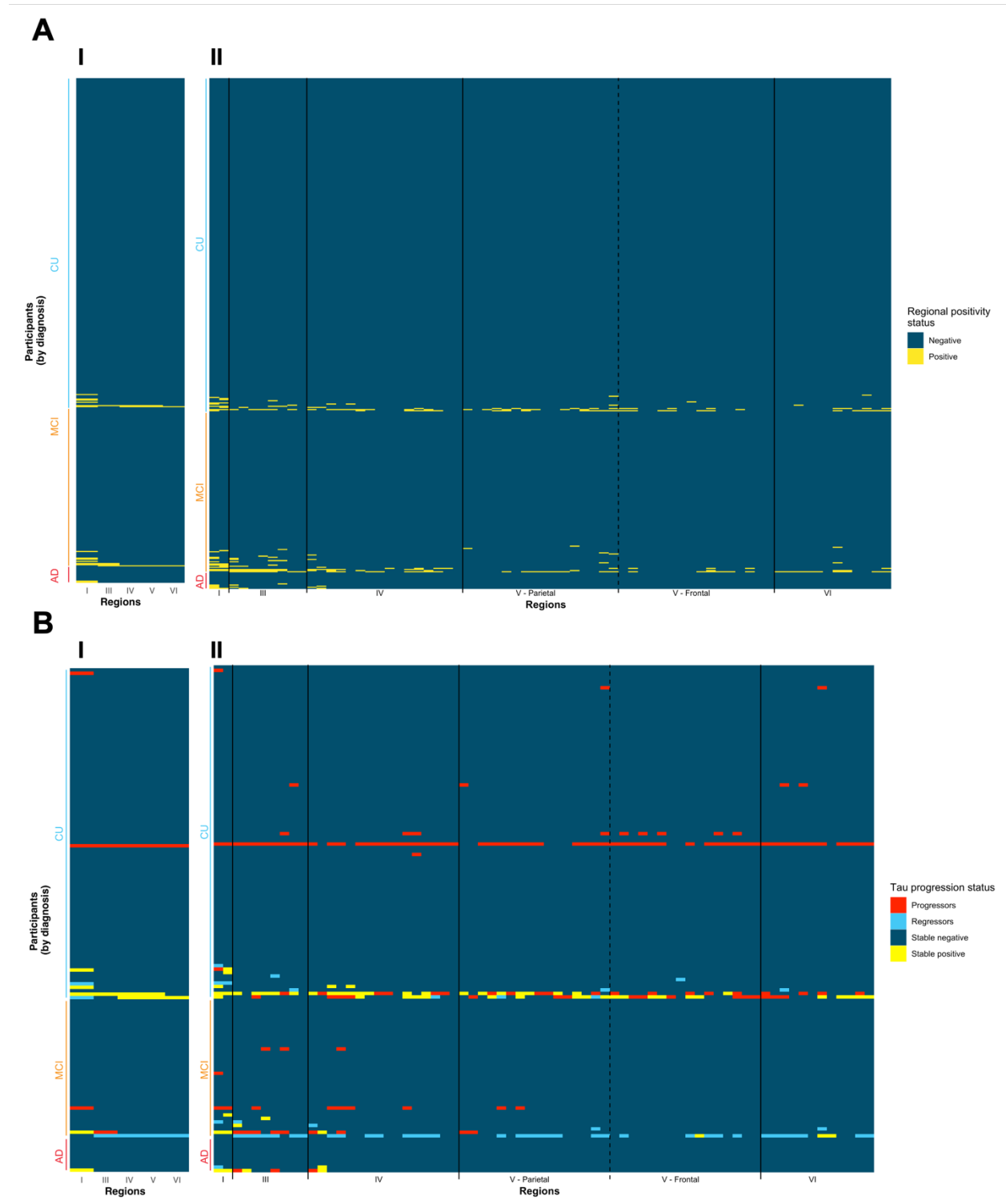
We replicated our main results using a spatial extent index derived from regional thresholds using 2 standard deviation from the mean of CU A β - participants instead of the GMM approach. Using the CU-based thresholds, we recharacterized AT status in the cohort (Supplementary Figure 3.9; original Figure 3.2A). The proportion of A+T+ (12.1% to 18.4%; $\chi^2 = 27.034$, $p < 0.001$) and A-T+ (3.2% to 14.9%; $\chi^2 = 50.019$, $p < 0.001$) increased in CU participants with the CU-based thresholds. We found similar results in participants with MCI for the proportion of A+T+ (36.1% to 41.1%; $\chi^2 = 13.067$, $p < 0.001$) and the proportion of A-T+ participants (8.7% to 16.9%; $\chi^2 = 21.043$, $p < 0.001$). The proportions did not change in participants with AD. Additionally, the proportion of A-T+ participants increased more than the proportion of A+T+ participants in CU participants ($\chi^2 = 5.975$, $p = 0.015$), but not in participants with MCI ($\chi^2 = 1.290$, $p = 0.256$). Recreating the heatmap represented in Figure 3.3A using the CU-based thresholds (Supplementary Figure 3.10), we found that our previous main findings remained: Braak stages were followed across all Braak stages up to and including Braak V in over 84% of participants, while patterns were heterogenous within regions.

We tested whether spatial extent index derived from CU A β - thresholds would retain its advantage over the temporal meta-ROI SUVR in cognitive performance (Supplementary Figure 3.12) and decline (Supplementary Figure 3.13). Overall, the CU-derived spatial extent index was associated similarly with cognition than the GMM-based measure across cognitive domains. However, the CU-derived spatial extent index was no longer superior to the temporal meta-ROI SUVR in the association with executive performance at baseline in participants with MCI ($z = -0.742$, $p = 0.771$) or AD ($z = -1.534$,

$p = 0.063$) and over time for participants with MCI ($z = -0.007$, $p = 0.497$). It was also no longer superior for the language performance at baseline in participants with MCI ($z = -0.983$, $p = 0.163$). Interestingly, in some language and visuospatial associations, less cognitive decline was associated with more CU-based spatial extent index.

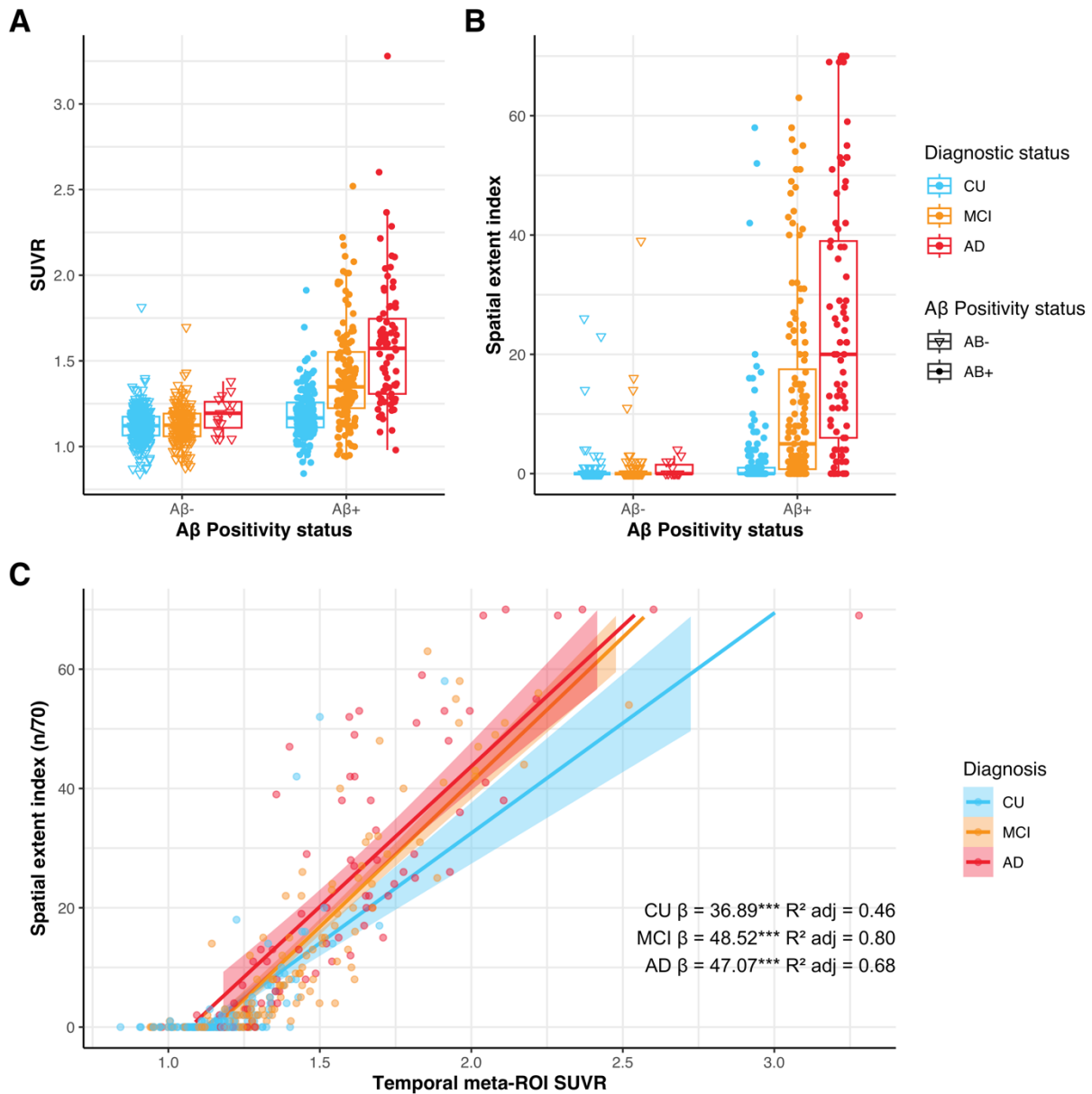
We investigated what could be driving the differences between both methods. First, we found that, on average, thresholds from the GMM were 0.10 SUVR ($t = 20.57$, $df = 69$, $p < 0.001$) higher than thresholds from CU A β - participants, but this varied across the brain where left temporal regions presented the least difference between methods and frontal regions presenting the most (Supplementary Figure 3.9A). Second, we investigated the extent to which the distribution of tau in CU A β - participants influenced the thresholds derived from both methods. We considered the distribution of tau using the max-min range (spread of the entire data). Considering the total range of each region, spatial extent from the GMM ($r = 0.31$, $p = 0.009$; Supplementary Figure 3.9C) was associated with the range, but the spatial extent from the 2SD CU A β - method showed a stronger association with the total range ($r = 0.66$, $p < 0.001$; Supplementary Figure 3.9D), which was higher than the spatial extent from the GMM ($z = -5.43$, $p < 0.001$).

Supplementary Figure 3.1



Supplementary Figure 3.1 Spatial extent of abnormal tau deposition and accumulation in amyloid negative participants of the ADNI cohort. (A) Based on the method discussed in Figure 3.1, abnormality thresholds were determined for each (I.) Braak stages (except stage II) and for each (II.) region of the cortical mantle and the bilateral amygdalae (70 regions). One row on the heatmap correspond to an individual participant, while each column represents a distinct cortical region. Within each diagnostic group, participants were sorted from individuals with lowest to highest spatial extent index. Regions on the x-axis in II. are sorted by Braak stages. (B) Abnormal accumulation is presented by (I.) Braak stages and (II.) all 70 individual brain regions of the Desikan atlas. Colors denote the change in the region between the baseline and the last available visit. A stable region (negative or positive; blue or yellow) did not change status during the follow-up. A progressing region (red) was originally negative and subsequently became positive over time. A regressing region (teal) was originally positive and became negative over time.

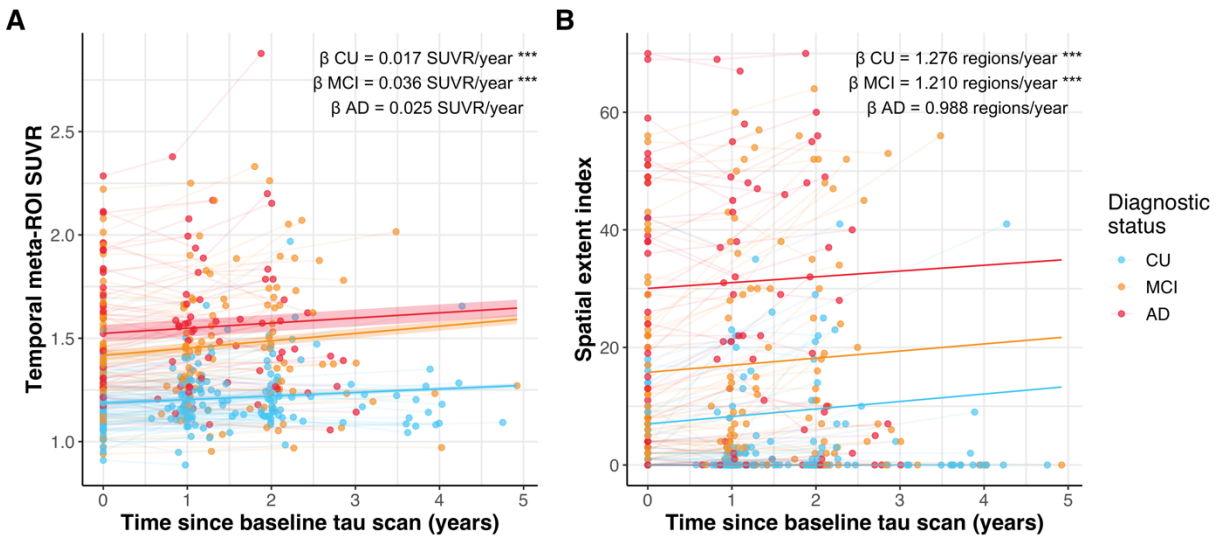
Supplementary Figure 3.2



Supplementary Figure 3.2 Tau measures by amyloid and clinical status. (A) Average tau SUVR within the temporal meta-ROI by amyloid positivity and diagnostic status. **(B)** Spatial extent index (i.e., number of tau abnormal regions) by amyloid positivity and diagnostic status. In both panels, ANOVAs were used to compare tau measures between Aβ⁻ and Aβ⁺ participants (e.g., Aβ⁻ compared to Aβ⁺ cognitively unimpaired participants).

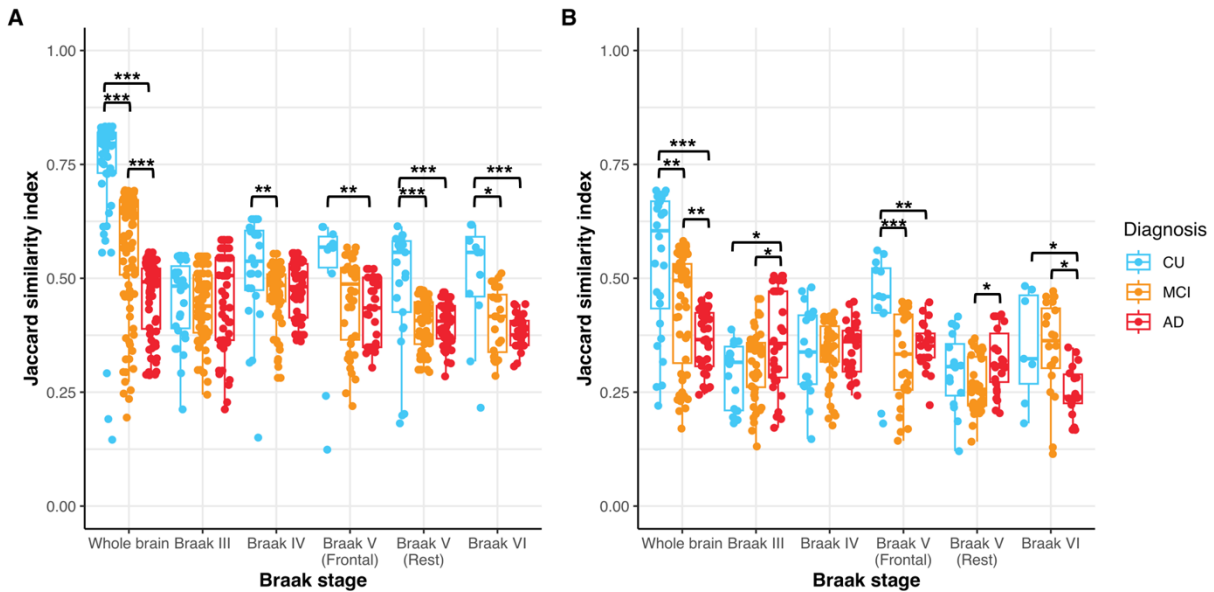
*As all analyses yielded that A β + had more tau—across all diagnostic groups—at $P < 0.001$ significance, we did not plot the model significance on the figure. (C) Association using linear models between temporal meta-ROI SUVR and spatial extent index in A β + participants of each diagnostic group. Beta coefficients and adjusted R^2 are presented at the bottom of the graph (***) = $P < 0.001$).*

Supplementary Figure 3.3



Supplementary Figure 3.3 Annual change in tau-PET measures. Annual change of (A) standardized uptake value ratio (SUVR) in the temporal meta-ROI and annual change of (B) spatial extent index in CU (blue), MCI (orange) and AD (red). Rates of annual change, computed with linear mixed models for temporal meta-ROI SUVR and zero-inflated Poisson mixed models for the spatial extent index, are presented at the top right corner of the graphs. Models' significance when controlling for age, sex and education are denoted by stars next to the rate. Brackets and stars between two slopes denote a significant group difference in the rate of change (* = $P < 0.05$).

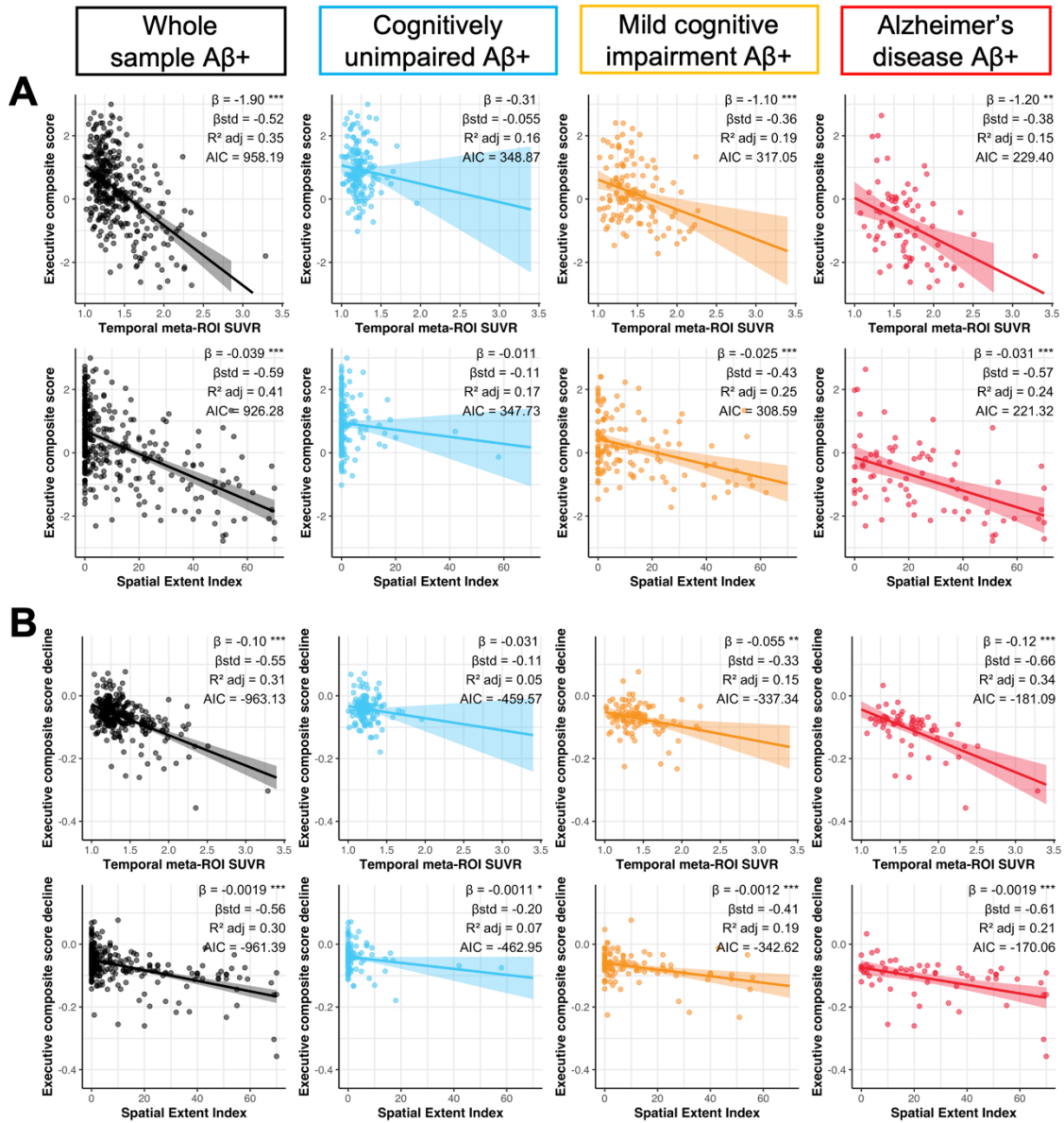
Supplementary Figure 3.4



Supplementary Figure 3.4 Heterogeneity in tau-PET spatial extent at baseline and longitudinally. (A) Across the whole brain and within each Braak stage, we computed how, on average, the patterns of tau abnormality (i.e., positivity for specific sets of brain regions) overlapped between participants of the same diagnostic group using the Jaccard similarity index. An index closer to one means a bigger overlap on average between participants in terms of regions that are positive, while an index closer to zero means more heterogeneity on average between participants. For each diagnostic group, we only retained participants who had at least one tau positive region. (B). Across the brain we computed how, on average, the patterns of change in tau abnormality (i.e., stability, progression, or regression for specific sets of brain regions) overlapped between participants of the same diagnostic group using the same method described in (A). In both (A) and (B), difference in average similarity was compared using Kruskal-Wallis tests. Post-hoc Dunn tests (with Bonferroni correction) were conducted when the result

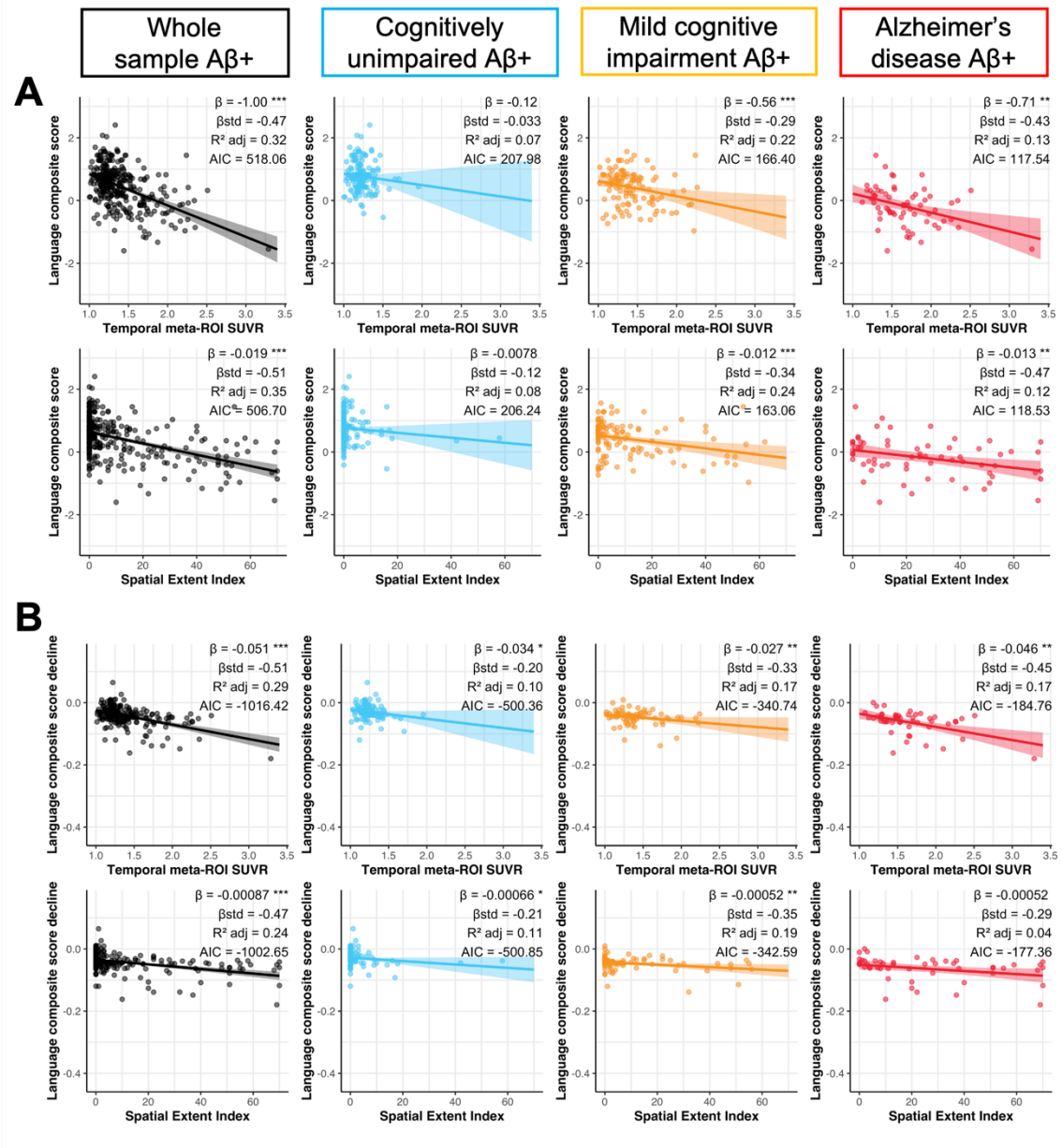
was significant. * = $P < 0.05$, ** = $P < 0.01$, *** = $P < 0.001$. CU = Cognitively unimpaired,
MCI = Mild cognitive impairment, AD = Alzheimer's disease

Supplementary Figure 3.5



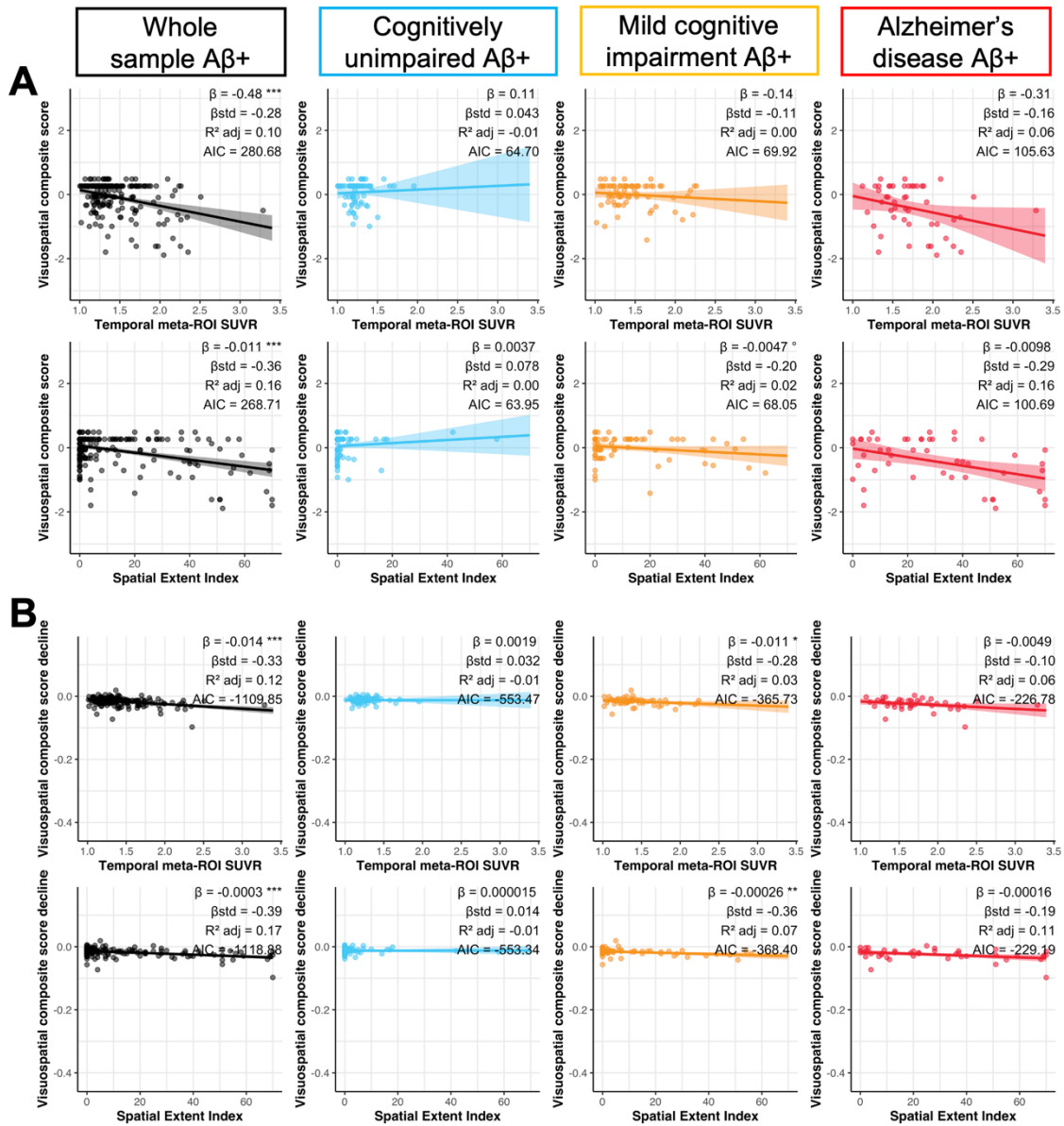
Supplementary Figure 3.5 Association between tau-PET measures, and executive functioning performance and decline. (A) Executive functioning performance closest in time to the tau-PET scan and (B) executive functioning decline computed across the study period were associated to both temporal meta-ROI SUVR and spatial extent index in A β ⁺ participants using linear regressions. Cognitive decline was computed for each participant with more than two cognitive timepoints using linear mixed effect models with random slopes and intercepts. In each panel, columns represent a diagnostic group (leftmost/black: whole sample, second from the left/blue: cognitively unimpaired, second from the right/orange: mild cognitive impairment, right-most/red: Alzheimer's disease). Simple and standardized β coefficients, adjusted R^2 and AIC, controlled for age sex and education, are shown on the graphs. P-value of models are indicated next to the simple beta coefficients. ($^{\circ}$: $P < 0.1$, * : $P < 0.05$, ** : $P < 0.01$, *** $P < 0.001$) Results remained significant after a multiple comparison false discovery rate (FDR) correction.

Supplementary Figure 3.6



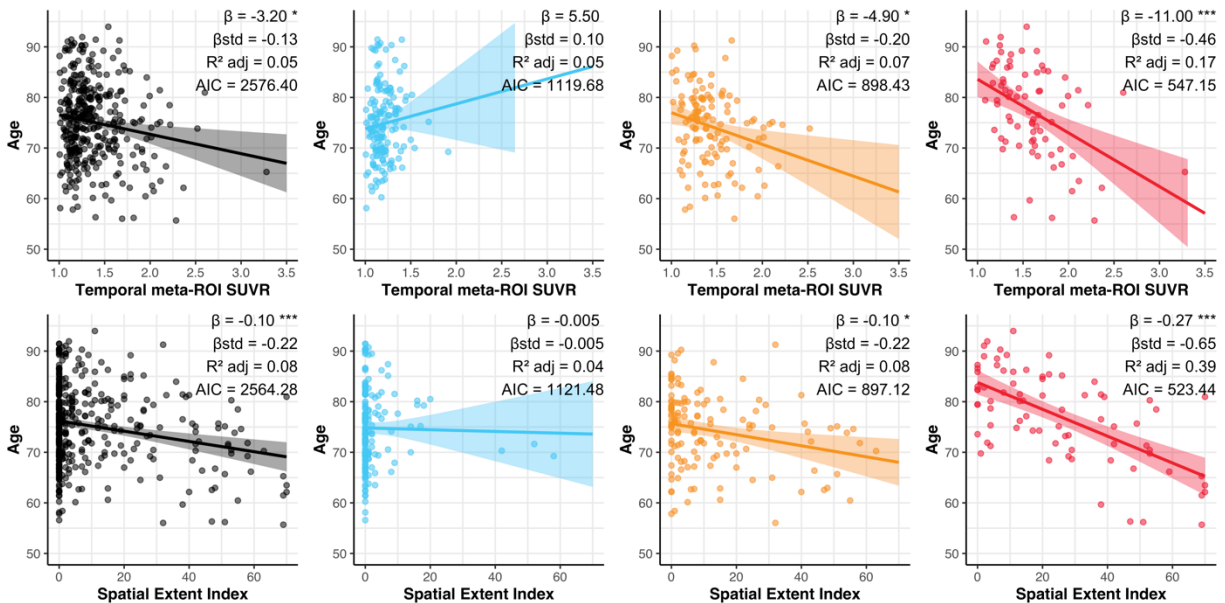
Supplementary Figure 3.6 Association between tau-PET measures, and language performance and decline. (A) Language performance closest in time to the tau-PET scan and (B) language decline computed across the study period were associated to both temporal meta-ROI SUVR and spatial extent index in A β ⁺ participants using linear regressions. Cognitive decline was computed for each participant with more than two cognitive timepoints using linear mixed effect models with random slopes and intercepts. In each panel, columns represent a diagnostic group (leftmost/black: whole sample, second from the left/blue: cognitively unimpaired, second from the right/orange: mild cognitive impairment, right-most/red: Alzheimer's disease). Simple and standardized β coefficients, adjusted R^2 and AIC, controlled for age sex and education, are shown on the graphs. P-value of models are indicated next to the simple beta coefficients. (° : $P < 0.1$, * : $P < 0.05$, ** : $P < 0.01$, *** $P < 0.001$) Results remained significant after a multiple comparison false discovery rate (FDR) correction.

Supplementary Figure 3.7



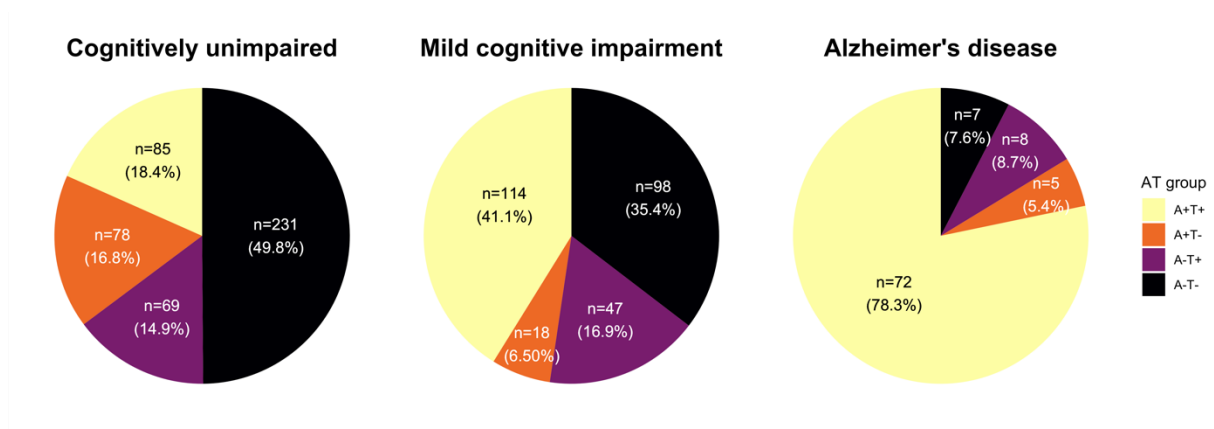
Supplementary Figure 3.7 Association between tau-PET measures, and visuospatial performance and decline. (A) Visuospatial performance closest in time to the tau-PET scan and (B) visuospatial decline computed across the study period were associated to both temporal meta-ROI SUVR and spatial extent index in $A\beta+$ participants using linear regressions. Cognitive decline was computed for each participant with more than two cognitive timepoints using linear mixed effect models with random slopes and intercepts. In each panel, columns represent a diagnostic group (leftmost/black: whole sample, second from the left/blue: cognitively unimpaired, second from the right/orange: mild cognitive impairment, right-most/red: Alzheimer's disease). Simple and standardized β coefficients, adjusted R^2 and AIC, controlled for age sex and education, are shown on the graphs. P-value of models are indicated next to the simple beta coefficients. ($^{\circ}$: $P < 0.1$, * : $P < 0.05$, ** : $P < 0.01$, *** $P < 0.001$) Results remained significant after a multiple comparison false discovery rate (FDR) correction.

Supplementary Figure 3.8



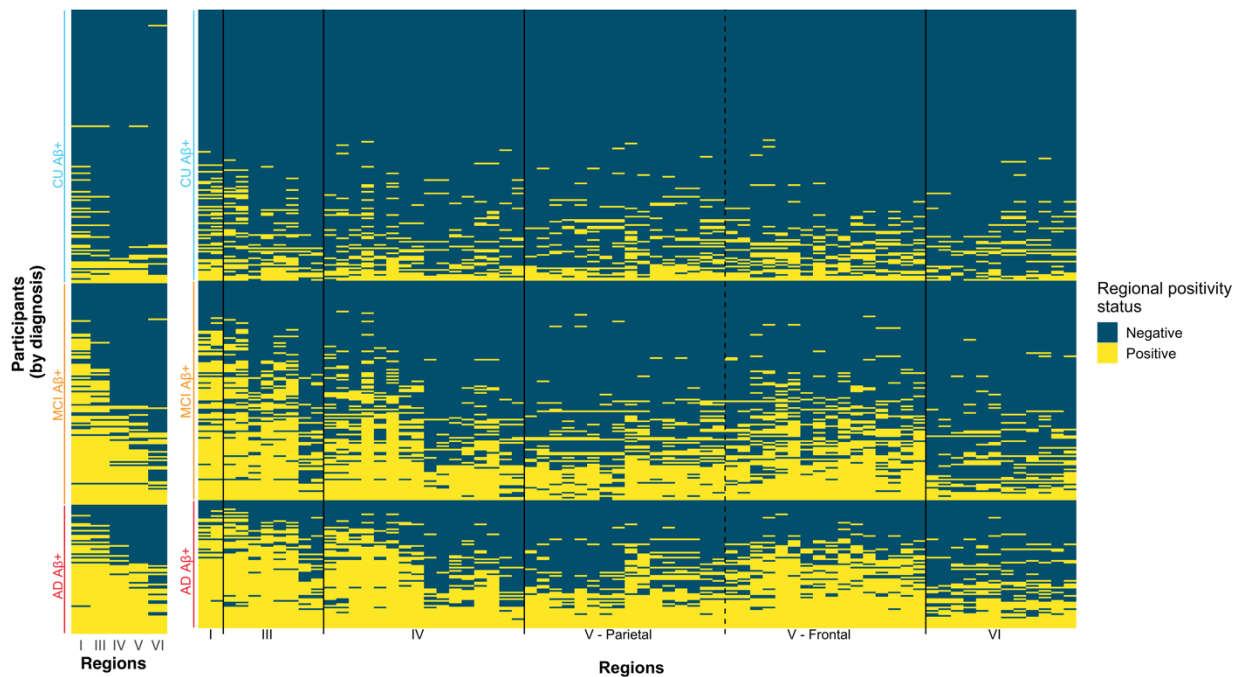
Supplementary Figure 3.8 Association between tau measures and age. Age at baseline was associated with temporal meta-ROI SUVR (first row) and spatial extent index (second row) in $A\beta^+$ participants using linear regressions. In each panel, columns represent a diagnostic group (leftmost/black: whole sample, second from the left/blue: cognitively unimpaired, second from the right/orange: mild cognitive impairment, rightmost/red: Alzheimer's disease). Simple and standardized β coefficients, adjusted R^2 and AIC, controlled for sex and education, are shown on the graphs. P-values of models are indicated next to the simple beta coefficients. ($^{\circ}$: $P < 0.1$, * : $P < 0.05$, ** : $P < 0.01$, *** $P < 0.001$) Results remained significant after a multiple comparison false discovery rate (FDR) correction.

Supplementary Figure 3.9



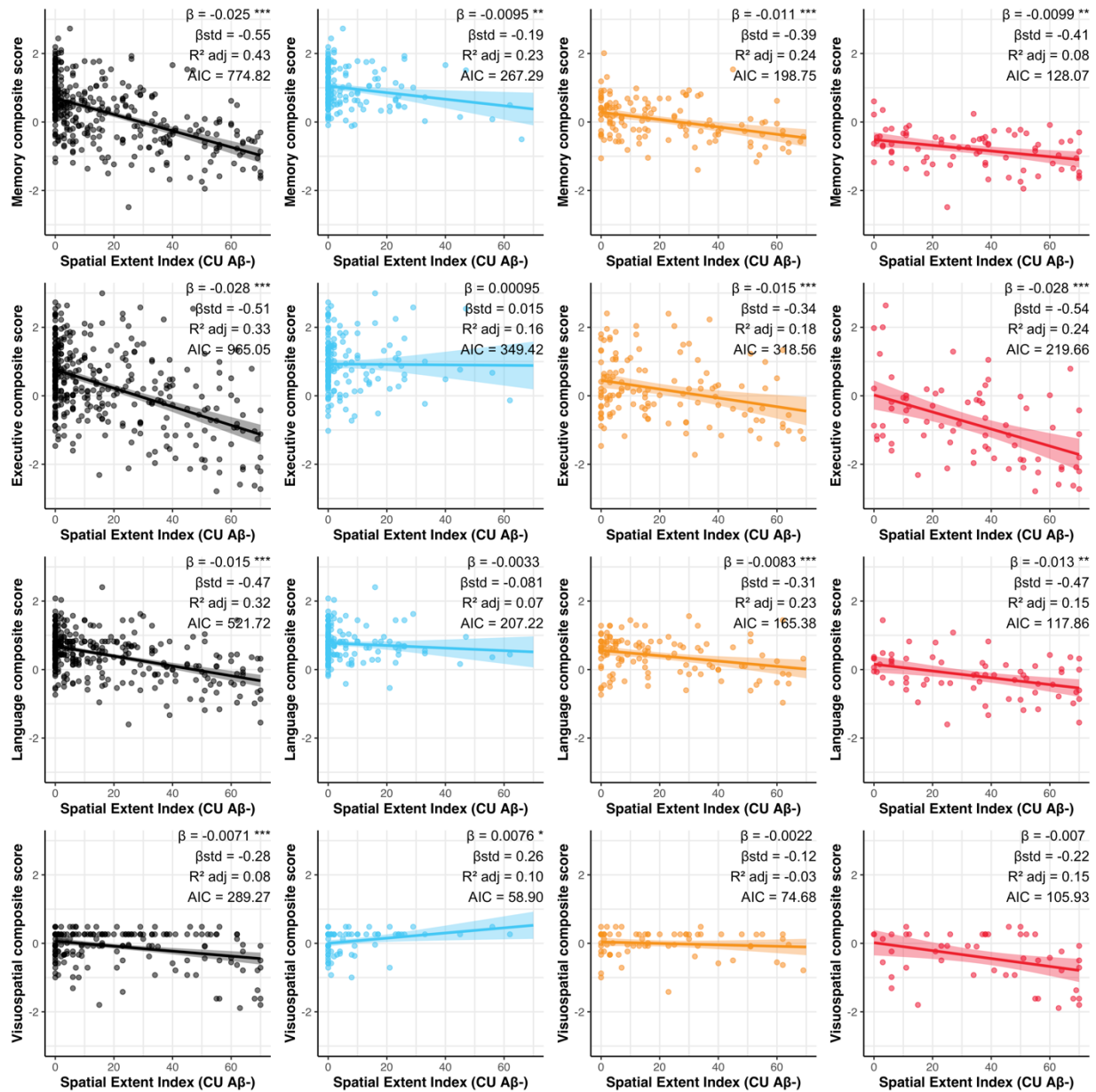
Supplementary Figure 3.9 Amyloid and tau status in the cohort using thresholds from cognitively unimpaired $A\beta$ - participants. $A\beta$ positivity was established using ADNI's tracer-specific recommendations for both Florbetapir and Florbetaben. Tau positivity was defined as having at least one region positive for tau pathology (spatial extent index of one and above). The spatial extent was derived across regions by using the mean plus two standard deviations of tau-PET values in CU $A\beta$ - participants.

Supplementary Figure 3.10



Supplementary Figure 3.10 Spatial extent using CU-based thresholds for abnormal tau deposition in amyloid-positive participants of the ADNI cohort. *Replication of Figure 3A, but the regional spatial extent was instead derived from thresholds based on the mean plus two standard deviations of CU A β - participants. Abnormality thresholds were determined for each **I.** Braak stages (except stage II) and for each **II.** region of the cortical mantle and the bilateral amygdalae (70 regions). One row on the heatmap correspond to an individual participant, while each column represents a distinct cortical region. Within each diagnostic group, participants were sorted from individuals with lowest to highest spatial extent index. Regions on the x-axis in **II.** are sorted by Braak stages.*

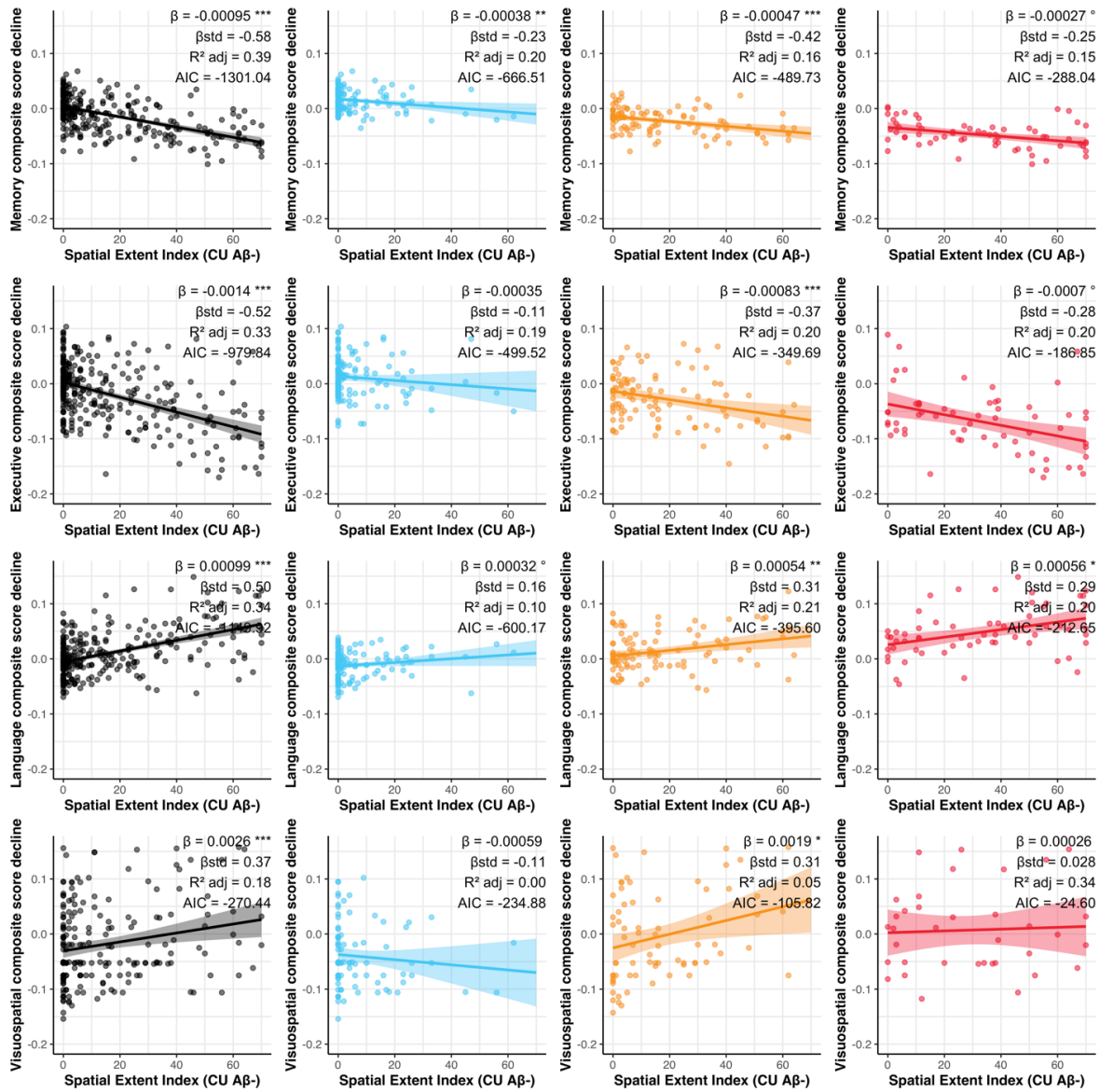
Supplementary Figure 3.11



Supplementary Figure 3.11 Association between spatial extent index derived from CU A β - thresholds, and cognitive performance. Association between the cognitive performance closest in time to the tau-PET scan and cognitive performance at baseline. Each row represents a cognitive measure (from top to bottom, memory, executive function, language and visuospatial) and each column represents a diagnostic group

*(leftmost/black: whole sample, (leftmost/black: whole sample, second from the left/blue: cognitively unimpaired, second from the right/orange: mild cognitive impairment, rightmost/red: Alzheimer's disease). Simple and standardized β coefficients, adjusted R^2 and AIC, controlled for age sex and education, are shown on the graphs. P-value of models are indicated next to the simple beta coefficients. ($^{\circ}$: $P < 0.1$, * : $P < 0.05$, ** : $P < 0.01$, *** $P < 0.001$) Results remained significant after a multiple comparison false discovery rate (FDR) correction.*

Supplementary Figure 3.12

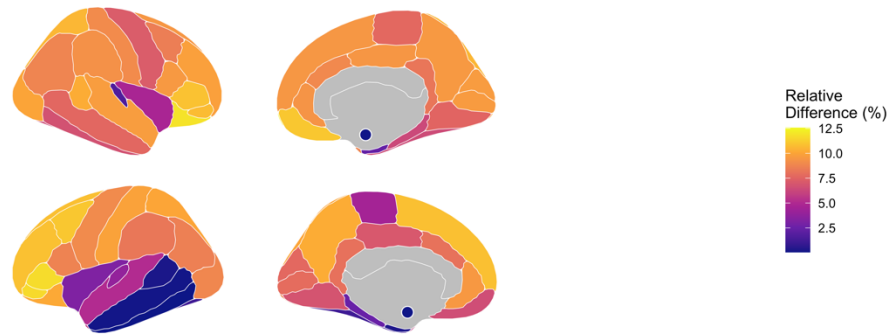


Supplementary Figure 3.12 Association between spatial extent index derived from CU Aβ- thresholds, and cognitive decline. For each domain, cognitive decline was computed for each participant with more than two timepoints using linear mixed-effect models with random slopes and intercepts. Each row represents a cognitive domain (from top to bottom, memory, executive function, language and visuospatial) and each column represents a diagnostic group (leftmost/black: whole sample,

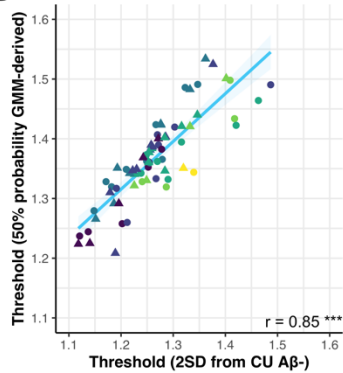
*(leftmost/black: whole sample, second from the left/blue: cognitively unimpaired, second from the right/orange: mild cognitive impairment, right-most/red: Alzheimer's disease). Simple and standardized β coefficients, adjusted R^2 and AIC, controlled for age sex and education, are shown on the graphs. P-value of models are indicated next to the simple beta coefficients. ($^{\circ}$: $P < 0.1$, * : $P < 0.05$, ** : $P < 0.01$, *** $P < 0.001$) Results remained significant after a multiple comparison false discovery rate (FDR) correction.*

Supplementary Figure 3.13

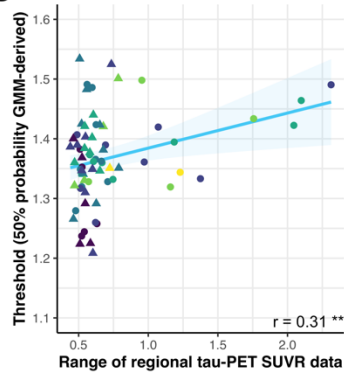
A



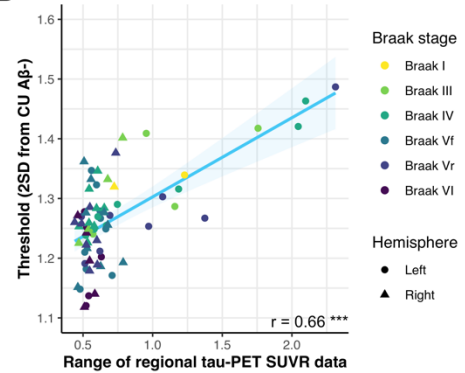
B



C



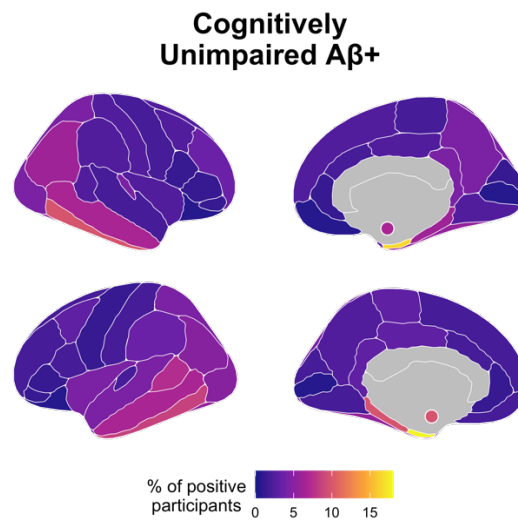
D



Supplementary Figure 3.13 Comparison of spatial extent approaches. A) *The percent difference in thresholds for tau-PET positivity across brain regions derived from applying GMM on the whole ADNI sample or by taking 2SD from the mean of CU A β -. On average, thresholds from the GMM were 0.10 SUVR higher than the 2SD method. The small sphere in the medial view of the brain represents the amygdala.* B) *Correlation between thresholds from the GMM method and 2SD from the mean of CU A β -. C) Correlation between the regional thresholds derived from the GMM and the range (max-min) of SUVR values in all regions. D) Correlation between the regional thresholds derived from the 2SD CU A β - method and the range (min-max) of SUVR values in all regions. In all three panels, each point corresponds to a brain region, with the colour*

representing their Braak stage and the shape the left or the right hemisphere (** : $P < 0.01$, *** $P < 0.001$).

Supplementary Figure 3.14



Supplementary Figure 3.14 Spatial extent of tau abnormality in CU A β + participants **at baseline.** *Replication of Figure 3C for CU A β +* participants, but with a colour scale allowing to see the pattern specific to this group.

Supplementary Table 3.1 – Regional thresholds of tau positivity

Braak stage	Region	Threshold value (SUVR)	
		LH	RH
I	entorhinal	1.344	1.349
	amygdala	1.498	1.501
III	fusiform	1.434	1.421
	parahippocampal	1.319	1.330
	lingual	1.328	1.322
	temporalpole	1.395	1.402
IV	inferiortemporal	1.464	1.440
	middletemporal	1.423	1.421
	isthmuscingulate	1.360	1.360
	caudalanteriorcingulate	1.342	1.372
	insula	1.332	1.346
	posteriorcingulate	1.362	1.384
	rostralanteriorcingulate	1.414	1.391
	lateraloccipital	1.390	1.390
V ₁	inferiorparietal	1.420	1.403
	superiortemporal	1.333	1.347
	bankssts	1.490	1.525
	precuneus	1.407	1.387
	superiorparietal	1.317	1.310
	supramarginal	1.361	1.349
	transversetemporal	1.260	1.209
	parsopectoralis	1.362	1.381
V ₂	parsoorbitalis	1.486	1.483
	parstriangularis	1.424	1.423
	frontalpole	1.328	1.357
	caudalmiddlefrontal	1.320	1.292
	lateralorbitofrontal	1.491	1.534
	medialorbitofrontal	1.462	1.425
	rostralmiddlefrontal	1.349	1.342
	superiorfrontal	1.280	1.266
VI	pericalcarine	1.382	1.400
	cuneus	1.353	1.369
	paracentral	1.258	1.292
	postcentral	1.237	1.229
	precentral	1.244	1.225

LH = Left hemisphere, RH = Right hemisphere, SUV_R = Standardized uptake value ratio. V₂ represents Braak V region in the frontal lobe while V₁ regroups the remaining Braak V regions.

Supplementary Table 3.2 Regional thresholds of tau positivity based on 2 standard deviation from cognitively unimpaired A β - participants

Braak stage	Region	Threshold value (SUVR)	
		LH	RH
I	entorhinal	1.339	1.320
	amygdala	1.409	1.402
III	fusiform	1.418	1.332
	parahippocampal	1.287	1.249
	lingual	1.240	1.225
IV	temporalpole	1.316	1.284
	inferiortemporal	1.463	1.346
	middletemporal	1.421	1.316
	isthmuscingulate	1.255	1.253
	caudalanteriorcingulate	1.238	1.226
	insula	1.290	1.284
	posteriorcingulate	1.270	1.259
	rostralanteriorcingulate	1.249	1.254
V ₁	lateraloccipital	1.249	1.256
	inferiorparietal	1.323	1.332
	superiortemporal	1.267	1.277
	bankssts	1.171	1.193
	precuneus	1.182	1.186
	superiorparietal	1.347	1.362
	supramarginal	1.279	1.276
	transversetemporal	1.210	1.217
V ₂	parsopercularis	1.148	1.151
	parsorbitalis	1.272	1.258
	parstriangularis	1.303	1.285
	frontalpole	1.267	1.222
	caudalmiddlefrontal	1.487	1.376
	lateralorbitofrontal	1.270	1.260
	medialorbitofrontal	1.191	1.179
	rostralmiddlefrontal	1.253	1.230
	superiorfrontal	1.212	1.189
VI	pericalcarine	1.278	1.272
	cuneus	1.252	1.243
	paracentral	1.202	1.196
	postcentral	1.121	1.118
	precentral	1.137	1.140

LH = Left hemisphere, RH = Right hemisphere, SUVR = Standardized uptake value ratio. V₂ represents Braak V region in the frontal lobe while V₁ regroups the remaining Braak V regions.

Supplementary Table 3.3 – Regional tau abnormality across regions of interest

Braak stage	Region	CU A β +		MCI A β +		AD A β +		CU A β -		MCI A β -		AD A β -	
		(n = 163)		(n = 132)		(n = 77)		(n = 300)		(n = 145)		(n = 15)	
		LH	RH	LH	RH	LH	RH	LH	RH	LH	RH	LH	RH
I	entorhinal *	17.8	16.6	58.3	61.4	74	75.3	2	2	6.2	4.8	26.7	6.7
III	amygdala *	9.8	6.7	46.2	43.9	67.5	70.1	0.3	0.3	4.8	2.8	13.3	6.7
	fusiform *	5.5	5.5	31.8	35.6	62.3	61	0.3	0.3	2.1	2.8	0	0
	parahippocampal *	9.8	6.1	44.7	37.9	66.2	55.8	1	0.3	4.1	2.8	0	6.7
	lingual	1.8	2.5	12.1	15.9	35.1	31.2	0.7	0	0.7	0.7	0	0
IV	temporalpole	2.5	3.7	23.5	18.9	48.1	41.6	0.7	0.3	2.8	1.4	6.7	13.3
	inferiortemporal *	8.6	9.8	34.1	37.1	68.8	68.8	0.7	0.3	2.1	1.4	0	0
	middletemporal *	6.7	6.7	33.3	33.3	62.3	63.6	0.7	0.7	0	0.7	0	0
	isthmuscingulate	3.1	4.3	22	26.5	41.6	41.6	0.3	0	0.7	0.7	0	0
	caudalanteriorcingulate	1.8	1.8	7.6	5.3	11.7	13	0	0	0.7	0	0	0
	insula	4.3	2.5	16.7	16.7	35.1	28.6	0.7	0.7	1.4	2.1	0	0
	posteriorcingulate	3.1	2.5	19.7	17.4	35.1	31.2	0.7	0.3	1.4	1.4	0	0
	rostralanteriorcingulate	1.2	0.6	2.3	4.5	11.7	11.7	0	0	0.7	0	0	0
V ₁	lateraloccipital	4.9	4.3	18.2	18.9	37.7	40.3	0.3	0	0.7	0	0	0
	inferiorparietal	4.9	6.1	22	27.3	54.5	49.4	0.3	0.7	0	0	0	0
	superiortemporal	4.3	1.8	17.4	17.4	33.8	27.3	0.7	0.3	0.7	0	0	0
	bankssts	7.4	2.5	25	19.7	51.9	44.2	0.7	0.3	0.7	0.7	0	0
	precuneus	2.5	4.3	15.9	18.9	37.7	41.6	0	0	0.7	0.7	0	0
	superiorparietal	4.3	4.3	14.4	14.4	41.6	36.4	0.3	0.3	0.7	1.4	0	0
	supramarginal	3.7	2.5	15.2	15.2	35.1	36.4	0.7	0.7	0	0	0	0
	transversetemporal	1.8	4.3	9.8	9.8	19.5	22.1	0.3	1.3	2.1	2.1	0	0
V ₂	parsopercularis	1.8	1.2	11.4	10.6	26	23.4	0.7	0.7	0	1.4	0	0
	parsorbitalis	1.2	1.2	6.8	7.6	16.9	19.5	0	0	0	0	0	0
	parstriangularis	1.2	1.2	6.8	5.3	20.8	18.2	0.3	0.7	0	0	0	0
	frontalpole	1.2	0.6	3.8	4.5	15.6	16.9	0	0.3	0	0	0	0
	caudalmiddlefrontal	3.1	2.5	15.9	19.7	37.7	37.7	0.3	0.7	0.7	2.1	0	0
	lateralorbitofrontal	0.6	0.6	9.8	9.1	22.1	18.2	0	0	0.7	0.7	0	0
	medialorbitofrontal	1.2	0.6	4.5	8.3	14.3	18.2	0.3	0	0	1.4	0	0
	rostralmiddlefrontal	1.8	3.7	12.1	15.2	22.1	23.4	0	0	0	0	0	0
superiorfrontal	1.8	2.5	8.3	9.8	23.4	23.4	0	0	0.7	0.7	0	0	
VI	pericalcarine	0.6	0.6	6.8	7.6	23.4	15.6	0.3	0	0.7	0.7	0	0
	cuneus	1.8	1.2	12.9	11.4	31.2	28.6	0	0	0.7	0	0	0
	paracentral	3.1	1.8	6.1	4.5	18.2	13	0.7	0.3	2.8	1.4	0	0
	postcentral	1.8	2.5	4.5	3	16.9	20.8	0.3	1	0	0	0	0
	precentral	1.2	1.8	8.3	6.1	20.8	26	0.3	0.7	0.7	1.4	0	0

CU = Cognitively unimpaired, MCI = Mild cognitive impairment, AD = Alzheimer's disease, LH = Left hemisphere, RH = Right hemisphere, A β = Amyloid. V₂ represents Braak V region in the frontal lobe while V₁ regroups the remaining Braak V regions. An asterisk next to the region name indicate that this region is part of the temporal meta region of interest (Jack et al., 2017)

Supplementary Table 3.4 – Regional tau abnormality progression across regions of interest

Braak stage	Region	CU A β +		MCI A β +		AD A β +		CU A β -		MCI A β -		AD A β -	
		(n = 90)		(n = 66)		(n = 39)		(n = 96)		(n = 40)		(n = 10)	
		LH	RH	LH	RH	LH	RH	LH	RH	LH	RH	LH	RH
I	entorhinal *	8.9	14.4	12.1	4.5	10.3	5.1	3.1	1.0	5.0	2.5	0.0	0.0
	amygdala *	3.3	6.7	10.6	9.1	2.6	0.0	1.0	1.0	2.5	2.5	10.0	0.0
III	fusiform *	4.4	4.4	16.7	12.1	2.6	10.3	2.1	1.0	5.0	2.5	0.0	0.0
	parahippocampal *	7.8	7.8	6.1	13.6	5.1	5.1	1.0	3.1	2.5	5.0	10.0	0.0
	lingual	2.2	1.1	10.6	9.1	2.6	2.6	2.1	1.0	0.0	0.0	0.0	0.0
	temporalpole	6.7	5.6	12.1	16.7	12.8	15.4	1.0	1.0	2.5	0.0	10.0	0.0
	inferiortemporal *	4.4	4.4	12.1	13.6	2.6	7.7	2.1	2.1	2.5	7.5	0.0	0.0
	middletemporal *	5.6	6.7	12.1	12.1	5.1	2.6	1.0	1.0	2.5	0.0	0.0	0.0
IV	isthmuscingulate	4.4	2.2	10.6	4.5	7.7	5.1	1.0	2.1	0.0	0.0	0.0	0.0
	caudalanteriorcingulate	4.4	0.0	6.1	4.5	2.6	0.0	2.1	1.0	0.0	0.0	0.0	0.0
	insula	4.4	6.7	7.6	6.1	12.8	7.7	2.1	3.1	2.5	0.0	0.0	0.0
	posteriorcingulate	4.4	3.3	10.6	7.6	7.7	7.7	1.0	2.1	0.0	0.0	0.0	0.0
	rostralanteriorcingulate	2.2	1.1	3.0	3.0	5.1	0.0	2.1	1.0	0.0	0.0	0.0	0.0
	lateraloccipital	2.2	2.2	12.1	9.1	5.1	7.7	1.0	1.0	2.5	2.5	0.0	0.0
	inferiorparietal	1.1	4.4	15.2	13.6	0.0	2.6	1.0	2.1	0.0	0.0	0.0	0.0
	superiortemporal	4.4	7.8	7.6	6.1	5.1	10.3	1.0	2.1	2.5	0.0	0.0	0.0
V ₁	bankssts	1.1	5.6	6.1	9.1	0.0	2.6	1.0	1.0	2.5	0.0	0.0	0.0
	precuneus	2.2	2.2	12.1	12.1	5.1	0.0	2.1	1.0	0.0	0.0	0.0	0.0
	superiorparietal	3.3	3.3	10.6	12.1	2.6	7.7	1.0	1.0	0.0	0.0	0.0	0.0
	supramarginal	4.4	4.4	10.6	12.1	12.8	2.6	1.0	1.0	0.0	0.0	0.0	0.0
	transversetemporal	4.4	1.1	3.0	9.1	10.3	2.6	2.1	3.1	0.0	0.0	0.0	0.0
	parsopercularis	4.4	2.2	7.6	12.1	5.1	5.1	2.1	2.1	0.0	0.0	0.0	0.0
	parsorbitalis	2.2	1.1	3.0	0.0	2.6	0.0	2.1	3.1	0.0	0.0	0.0	0.0
	parstriangularis	2.2	1.1	1.5	9.1	5.1	0.0	2.1	2.1	0.0	0.0	0.0	0.0
	frontalpole	2.2	2.2	1.5	4.5	2.6	0.0	1.0	0.0	0.0	0.0	0.0	0.0
V ₂	caudalmiddlefrontal	3.3	7.8	7.6	4.5	2.6	2.6	2.1	0.0	0.0	0.0	0.0	0.0
	lateralorbitofrontal	3.3	1.1	7.6	7.6	0.0	0.0	2.1	2.1	0.0	0.0	0.0	0.0
	medialorbitofrontal	2.2	2.2	7.6	7.6	7.7	2.6	1.0	4.2	0.0	0.0	0.0	0.0
	rostralmiddlefrontal	4.4	5.6	4.5	3.0	7.7	2.6	2.1	2.1	0.0	0.0	0.0	0.0
	superiorfrontal	3.3	4.4	10.6	7.6	5.1	0.0	3.1	2.1	0.0	0.0	0.0	0.0
	pericalcarine	1.1	1.1	0.0	1.5	2.6	5.1	3.1	1.0	0.0	0.0	0.0	0.0
	cuneus	0.0	3.3	4.5	4.5	5.1	2.6	3.1	1.0	0.0	0.0	0.0	0.0
VI	paracentral	1.1	2.2	9.1	6.1	12.8	7.7	3.1	1.0	0.0	0.0	0.0	0.0
	postcentral	0.0	2.2	7.6	1.5	5.1	7.7	1.0	1.0	0.0	0.0	0.0	0.0
	precentral	2.2	4.4	7.6	7.6	2.6	5.1	2.1	1.0	0.0	0.0	0.0	0.0

Numbers are in percentages. CU = Cognitively unimpaired, MCI = Mild cognitive impairment, AD = Alzheimer's disease, LH = Left hemisphere, RH = Right hemisphere, A β = Amyloid. V₂ represents Braak V region in the frontal lobe while V₁ regroups the remaining Braak V regions. An asterisk next to the region name indicate that this region is part of the temporal meta region of interest (Jack et al., 2017)

Supplementary Table 3.5 Braak stages thresholds

Region	Threshold value	
	GMM-based	CU-based
Braak I	1.325	1.299
Braak III	1.359	1.274
Braak IV	1.347	1.249
Braak V	1.331	1.204
Braak VI	1.260	1.155
Temporal meta-ROI	1.398	1.311

Thresholds were derived by taking the composite regions and using the GMM method described in Figure 1, or using the mean plus two standard deviation of CU A β - participants

Chapter 4 – General discussion

4.1 – Summary of thesis conclusions

The overall goal of this thesis was to investigate the extent of interindividual differences in the brain of participants across the lifespan and in Alzheimer’s disease. We first characterized functional connectome fingerprints and their integrity in a lifespan cognitively unimpaired cohort using functional MRI. Then, we identified interindividual differences in tau-PET patterns of participants on the spectrum of Alzheimer’s disease using positron emission tomography.

In the first project (Chapter 2), we found that interindividual differences measured using functional magnetic resonance imaging—despite significant population-level changes in older adults recorded in the literature—persist through the entire lifespan. Furthermore, this signature doesn’t seem to involve the same regions for every participant: each participant has a unique set of regions contributing best to their own fingerprint. Finally, lower self-identifiability was associated with lower grey matter volume in age-vulnerable regions, suggesting that these interindividual differences are not only an inherent property of the brain: they may also be associated with clinically relevant outcomes.

Next, we investigated whether these interindividual differences could influence our understanding of pathology patterns observed in a clinical population, specifically on tau-PET patterns in Alzheimer’s disease (Chapter 3). We show that while some patterns are shared across individuals (i.e., following the Braak stages), abnormality in individual regions differs drastically across individuals, particularly during clinical progression. We also show that accounting for these differences in individual-specific tau-PET patterns

can result in better associations for cognitive deficits outside of memory impairment, perhaps due to the localization of the associations between tau and cognition across the cortex.

Through both projects, we concurrently developed *sihnpy*, a Python-based package which contains the tools we adapted and developed in Chapters 2 and 3. The package—presented in the Annex—is fully downloadable and made open to the entire scientific community. This toolbox will provide scientists with concrete methods to investigate interindividual differences and transparently replicate findings from Chapters 2 and 3. Interindividual differences are not limited to the brains of participants included in research studies. I also applied the spatial extent index developed in *sihnpy* to quantify the spread of amyloid pathology at an individual level in a data science project conducted during an internship in industry. These results are also presented in the Annex.

4.2 – The brain is made of shared and idiosyncratic patterns

A common theme echoed across the thesis is that the brain exhibits shared, group-level characteristics, but there are important interindividual differences. This idea is not novel as others suggested this from data from a small group of younger adults (Gratton et al., 2018). However, this thesis emphasizes that this is a phenomenon that is preserved even when the brain undergoes significant transformation such as aging or AD.

In aging for instance, there have been multiple consistent studies showing that functional connectivity in older adults tends to decrease within networks and increase between networks (i.e., decreased segregation) (Chan et al., 2014). However, in Chapter 2, we demonstrated that functional connectivity has a high degree of uniqueness that is preserved throughout life. Similarly, in AD, many studies consistently identify that

pathology follows stereotypical patterns such as Thal phases for amyloid (i.e., neocortical to subcortical) (Thal et al., 2002) or Braak for tau (i.e., early middle temporal to late sensorimotor cortex) (Braak & Braak, 1991). In Chapter 3, we show that this pattern for tau is not uniformly followed across all participants and it is therefore heterogenous.

These findings have significant implications for neuroimaging research. Many mainstream methods for analyzing brain data relies on some level of group-averaging like selecting anatomical borders for segmenting the brain (Desikan et al., 2006), warping the brain of an individual to a group-level template (Ashburner, 2007) or averaging a brain variable within a group (Brett et al., 2011). Considering that individuals demonstrate significant heterogeneity, it is possible that these methods lead to biased estimates that are not easily replicable in other cohorts. In parallel, the field of neuroimaging is going through a replication crisis, where studies asking the same scientific question do not obtain the same results (Botvinik-Nezer et al., 2020). Multiple factors can play into this lack of replication, including the lack of consensus in terms of methodology used to obtain the results (Botvinik-Nezer et al., 2020; Xifra-porxas et al., 2020) and limited sample sizes (Marek et al., 2022). These factors aim mostly to reduce the variability between different cohorts to obtain consistent results across teams.

However, what this thesis argues is that there is significant heterogeneity even within cohorts considered homogenous which should also be accounted. Potentially promising solutions that could help with these issues include the *sihnpy* package which proposes measures to account for these differences, but other methods also exist at different steps of the analysis pipeline. Preprocessing methods such as hyperalignment, which aligns individual brains to a group-level template while preserving individual-level

topographical information (Haxby et al., 2020) can help early in the process to mitigate the impact of interindividual differences on results. Many new methods are also appearing to account for these differences in data analyses. For instance, brain charts (Bethlehem et al., 2022) offer a way to account for population-level changes in the brain but directly acknowledge variability between individuals. Other methods, such as creating individualized masks for predicting pathology accumulation have been shown to outperform group-level methods in AD (Franzmeier et al., 2020; Leuzy et al., 2023).

Overall, one main message from this thesis is that the brain is made of group- and individual-level patterns that can be measured and are of great magnitude: individual differences are a core aspect of the brain, healthy or pathological. Researchers should account for this when considering preprocessing and analysis of their neuroimaging data.

4.3 – Interindividual differences impact our understanding of the brain

Another point driven by this thesis is that interindividual differences are not simply noise (Brett et al., 2011; Poldrack et al., 2011); they are associated with other variables related to healthy and pathological aging.

In a cognitively unimpaired lifespan cohort (Chapter 2), we found that lower self-identifiability—an individual-specific measure of functional connectivity—was associated with lower grey matter volume in age-related brain regions. This is similar to existing literature where lower self-identifiability over time was associated with lower total grey matter volume in older adults (Ousdal et al., 2020). In participants with MCI and AD, we found that tau (Chapter 3) at the individual level (i.e., spatial extent index) outperformed traditional group-level measures when measuring certain cognitive domains.

Individual-specific functional connectivity measures have been known to associate with health and behavior profiles of young CU healthy participants (Bijsterbosch et al., 2018; Mansour et al., 2020), indicating potential clinical usefulness. In more clinical settings, fingerprint measures of functional connectivity were shown to be systematically different between patients with schizophrenia (Kaufmann et al., 2018) or patients with varied psychopathologies (Kaufmann et al., 2017) during development, suggesting that fingerprints could capture individual-specific indicators of disease. More relevant to this thesis, a few preliminary studies have also found that individual-specific markers of functional connectivity can help distinguish participants with MCI or AD (Sorrentino et al., 2020) and identify cognitive deficits in these populations (Svaldi et al., 2021). This suggests significant heterogeneity in brain features of participants on the AD spectrum.

Amyloid, tau, and subsequently atrophy, are often considered the trifecta of cognitive decline in AD: amyloid lays down the foundation for the disease, tau then spreads and consequently triggers neuronal death (i.e., atrophy). All three brain features have been consistently associated with either clinical progression of AD (Ossenkoppele et al., 2022; Strikwerda-Brown et al., 2022), though amyloid seems to be less associated with cognition than tau pathology (Ossenkoppele et al., 2018; Ozlen et al., 2022; Parent et al., 2023). Despite the many studies indicating heterogeneity in amyloid (Collij et al., 2022), tau (Vogel et al., 2021) and atrophy (Ferreira et al., 2020), few leveraged or accounted for this heterogeneity and fewer still studied whether this heterogeneity directly impacts clinical measures. We could also not find studies using individually defined measures of amyloid-PET, but group-level subtypes of amyloid patterns were associated with diverging clinical patterns (Y. Sun et al., 2023). Individually defined tau-PET burden

at baseline was shown to better capture longitudinal change in tau-PET over time (Franzmeier et al., 2020; Leuzy et al., 2023), but individually defined measures of tau-PET have never been associated with cognition. One study using individual-specific measures of atrophy found significant associations with cognition but did not establish whether these measures outperformed group-based measures (Verdi et al., 2023). This thesis provides evidence that individual-specific measures of pathology—specifically tau—can improve associations between pathology and specific cognitive domains, reinforcing the idea that heterogeneity can provide meaningful clinical information. Results should be replicated with amyloid and atrophy.

This will be particularly important when considering clinical trials and interventions in AD. Despite decades of research, patients with AD have very few options to treat the disease (J. L. Cummings et al., 2014) due to the frequent failure of clinical trials. Newer treatment options are emerging, such as Aducanumab (J. Cummings et al., 2021), Lecanumab (Van Dyck et al., 2023) and Donanemab (Sims et al., 2023), but benefits on cognition remain minimal and side effects are prevalent, and—in some cases—life-threatening. Many reasons are cited for the chronic failure of clinical trials in AD, including targeting a wrong or unimportant molecular process or targeting patients too late in the disease process where the damage cannot be reversed. However, another potential source highlighted by this thesis is between-individual heterogeneity.

Currently, in the US, only between 7 and 20% of patients with neurological disorders using the highest-selling drugs designed to treat these disorders gain meaningful clinical benefits from using the drugs (Schork, 2015). This is partly due to the idea that in a pool of patients sharing a diagnosis, on average, at least a significant

proportion will respond to the drug as expected (Iturria-Medina et al., 2018). In AD, it is well known that participants can present with different symptoms and clinical variants, with their specific patterns of tau-PET pathology matching these symptoms (La Joie et al., 2020). Consequently, in AD drug trials, stringent inclusion criteria are often applied to ensure that participants present with the same disease phenotype (i.e., amnesic) as patients should present the same disease etiology and, consequently, should respond similarly to the same treatment (Van Dyck et al., 2023). However, this thesis sheds some doubt on this approach. In Chapter 3, we focused our results on participants from the ADNI cohort. Like clinical trials, ADNI has stringent inclusion criteria meant to primarily recruit patients with amnesic disease presentation. While theoretically, they should share similar disease patterns and progression, we found heterogeneity in these measures.

Overall, the findings in this thesis are critical for trials as they indicate that even with stringent criteria meant to retain a homogenous group of participants, there is still significant heterogeneity in biomarkers, changing with the progression of the disease and yielding stronger associations with cognition. This could foreshadow poor disease outcomes, as is suggested in other neurological disorders (Schork, 2015) if treatments are given in the same way to every patient despite positive trial results. Researchers should continue investigating the impact of these interindividual differences, in AD and in other neurological disorders, particularly using trial data, to ensure that this variability is properly accounted for and to understand if and why certain groups of patients respond more or less to the interventions.

4.4 – Creating tools to assess and leverage interindividual differences

The main conclusions of this thesis point to heterogeneity being a core feature of the brain and affecting clinical measures. From a more practical point of view, very few tools are openly available for researchers to study this heterogeneity. We have already detailed some of the barriers in the general introduction of this thesis: there are not a lot of tools available to study interindividual differences, and fewer still are accessible. This lack of tools led us to develop a more practical project included in the annex of this thesis with the creation of *sihnpy*.

With the exception of the spatial extent, all of the ideas behind each of *sihnpy*'s modules were not newly developed during this Ph.D. work but were rather adapted from existing work during the writing of Chapter 2 and 3. The code for fingerprinting (Finn et al., 2015), sliding-window (Váša et al., 2018) and imbalance mapping (Nadig et al., 2021) were all available in MATLAB, R and R, respectively. While imbalance mapping was not included in the publications, it was developed in the package as a potential useful tool. The process behind the spatial extent—particularly the Gaussian Mixture method—to determine abnormality of pathology is not novel (Franzmeier et al., 2020; Ozlen et al., 2022; Vogel et al., 2020), but its systematic application across the whole brain and the subsequently resulting measures are novel. However, all of the existing methods had common flaws: they lacked documentation and structure for replication and widespread use. Most of the work in the development of *sihnpy* was, in fact, more related to refactoring the scripts to allow for greater scalability with different types of data, translating all of them to a single programmatic language, producing more extensive documentation with step-by-step instructions and ensuring its accessibility for a wide scientific audience.

One major issue in the field of neuroimaging is the lack of replication between studies (Botvinik-Nezer et al., 2020): different teams use different software or preprocessing methods to prepare and analyze data. One cause behind this is the strong diversity of tools and a lack of universal standards for methods to be used. In the case of the existing scripts for fingerprinting, sliding window and imbalance mapping, none of the original articles released the data used specifically with their methods, making replication by other users more difficult. This was also one of the driving forces behind *sihnpy*. Open data from the PREVENT-AD was preprocessed and integrated into *sihnpy*. Furthermore, *sihnpy*'s tutorial executes the data analyses step-by-step and show the users what the results should look like. This makes the reproduction of the methods more likely and less prone to errors when users test the methods before applying them to their data.

Contrary to the chapters of this thesis which resulted in static products (i.e., publications), *sihnpy* is a living tool. Left open to the scientific community on GitHub, it will continue to evolve as feedback and issues arise and with new modules being integrated. However, the goal behind *sihnpy* will always remain the adaptation of tools to investigate interindividual differences, be it the creation of new tools, or the integration of previously existing tools.

4.5 – Strengths and limitations

The field of interindividual differences in the brain is still young. We can reliably demonstrate their existence, but the potential for their utility remains still largely unexplored. While the work of this thesis paves the path for this research, many limitations must be acknowledged.

First, it is important to acknowledge that, despite the associations with clinically relevant variables across both studies, the role of the different measures in clinical research studies must be better defined. The spatial extent demonstrated the best capacity for clinical research, but while the gain in variance explained for tau (Chapter 3) is significant, this is only evident in circumscribed cognitive domains. More studies are needed to establish exactly how these measures could help with tracking clinically relevant processes in the brain.

Second, all the methods presented across chapters rely heavily on arbitrary choices. It is still unclear how choices from users can impact the results. However, in Chapter 2, we carefully studied the impact of different methodological choices on fingerprinting and sliding window approaches and detailed them extensively. However, the main messages remained the same. In Chapter 3, we tried to be as transparent as possible on the methods and the choices made so others could consider these choices when designing studies including these methodologies.

Third, though this was chosen by design, the study populations in Chapters 2 and 3 were largely homogenous: participants overwhelmingly identified as white, were all from highly industrialized nations and mostly had higher levels of education. In Chapter 3, participants were recruited from ADNI, which comprises participants with amnesic symptoms at the forefront of their clinical presentation, which does not represent a large proportion of patients with different clinical presentations. These choices were made initially mostly for practical reasons: very few datasets have lifespan neuroimaging data available yet, and very few tau-PET datasets are openly available yet, let alone datasets with significant diversity. Future studies should validate these results in more diverse

populations. However, the fact that we were able to find significant interindividual differences in highly homogenous cohorts reinforces the conclusion that interindividual differences are incredibly common.

Fourth, results in Chapter 3 use a coarse brain parcellation of 68 cortical regions. In Chapter 2, we demonstrate that an increase in brain resolution (i.e., more brain region) tends to increase identifiability suggesting that including more brain regions helps highlight the heterogeneity. As such, it is possible that including more brain regions for PET imaging would also increase the heterogeneity observed. Future research should confirm whether this is the case. However, despite the relatively coarse brain resolution, we were able to identify significant heterogeneity and relate it to clinical variables.

Fifth, the methodology used in Chapter 3 to capture abnormal tau-PET distribution binarizes information for each brain region. While this has the advantage of being easy to interpret (i.e., number of brain regions), particularly for clinical use, this binarization limits further interpretation of the data and precludes data patterns exclusive to continuous SUVR data.

4.6 – Future directions

In 2023, the year where this thesis is submitted, nearly 43.8 million individuals live with AD or related dementia worldwide (Nichols et al., 2019). Closer to home, nearly 10% of older adults over 65 years in the Canada live with AD, a proportion projected to double by 2050 (Alzheimer’s Society of Canada, 2022). This high prevalence, mixed with critical failures of clinical trials to treat the disease (J. L. Cummings et al., 2014), emphasizes the importance of developing accurate tools to identify patients and their prognoses.

The current thesis, suggesting high inter-individual differences between patients, points to personalized medicine as a future avenue of research. Personalized medicine tools offer individual-specific measures that can track the progress of the disease, accounting for each participant’s unique life trajectories and realities (Iturria-Medina et al., 2018). Already, individual-specific tools in AD and dementia demonstrate good prognostic ability to track disease progression over group-level measures (J. A. Brown et al., 2019; Franzmeier et al., 2020; Leuzy et al., 2023), emphasizing the advantages of these methods. This research field must expand and validate the clinical utility of these tools above and beyond existing ones.

This thesis, and most of the research on individual-specific measures, usually focus on descriptive or accurate modelling of the differences and often do not account for other important differences between individuals. There is a vast body of literature on many risk factors influencing pathology amount and progression in AD: decreased sleep and exercise, increased cardiovascular burden, certain personality types (Ourry et al., 2023), being a woman (Buckley et al., 2020) or a person of color (Morris et al., 2019), having specific genetic risk factors (Angelopoulou et al., 2021; Cai et al., 2023) or family history

(Arenaza-Urquijo et al., 2020), increased age and decreased education (Arce Rentería et al., 2019) are all factors associated with increased pathology and disease progression at the group-level. An advantage of personalized measures is that these factors are implicitly accounted for as each individual become their own reference point. Still, more research is needed to evaluate how each of the factors—and their combination—influences individual-specific measures. This will likely require massive amounts of data to ensure that all these factors are well represented in the data.

Another important aspect that should be addressed in personalized medicine research is that heterogeneity in the brain spans multiple modalities. This is implicit in this thesis, as we demonstrate heterogeneity in functional and molecular imaging, and this was also shown in other studies (Mansour et al., 2020). Still, the impact of this multimodal heterogeneity has not been studied extensively in AD, nor on its spread (Iturria-Medina et al., 2018). Incorporating information from multiple heterogenous sources of brain structure and function could help provide even more precise information in predicting outcomes in AD.

4.7 – General conclusions

The work in this thesis challenges traditional views in neuroimaging research by demonstrating that grouping individuals from populations thought to be homogeneous can miss significant and clinically relevant heterogeneity in both healthy and pathological cohorts and using functional, structural, and molecular imaging. We also propose a collection of tools that other researchers can use to study this heterogeneity. Researchers should carefully examine the impact of heterogeneity in brain features before grouping participants in their analyses.

IX - Reference list

- Airan, R. D., Vogelstein, J. T., Pillai, J. J., Caffo, B., Pekar, J. J., & Sair, H. I. (2016). Factors affecting characterization and localization of interindividual differences in functional connectivity using MRI. *Human Brain Mapping, 37*(5), 1986–1997. <https://doi.org/10.1002/hbm.23150>
- Alzheimer's Association. (2023). 2023 Alzheimer's disease facts and figures. *Alzheimer's & Dementia, 19*(4), 1598–1695. <https://doi.org/10.1002/alz.13016>
- Alzheimer's Society of Canada. (2022). *Navigating the path forward for dementia in Canada: Landmark study* (1).
- Amico, E., & Goñi, J. (2018). The quest for identifiability in human functional connectomes. *Scientific Reports, 8*(1), 1–14. <https://doi.org/10.1038/s41598-018-25089-1>
- Angelopoulou, E., Paudel, Y. N., Papageorgiou, S. G., & Piperi, C. (2021). APOE Genotype and Alzheimer's Disease: The Influence of Lifestyle and Environmental Factors. *ACS Chemical Neuroscience, 12*(15), 2749–2764. <https://doi.org/10.1021/acscemneuro.1c00295>
- Arce Rentería, M., Vonk, J. M. J., Felix, G., Avila, J. F., Zahodne, L. B., Dalchand, E., Frazer, K. M., Martinez, M. N., Shouel, H. L., & Manly, J. J. (2019). Illiteracy, dementia risk, and cognitive trajectories among older adults with low education. *Neurology, 93*(24), E2247–E2256. <https://doi.org/10.1212/WNL.00000000000008587>
- Arenaza-Urquijo, E. M., Salvadó, G., Operto, G., Minguillón, C., Sánchez-Benavides, G., Crous-Bou, M., Grau-Rivera, O., Sala-Vila, A., Falcón, C., Suárez-Calvet, M.,

- Zetterberg, H., Blennow, K., Gispert, J. D., & Molinuevo, J. L. (2020). Association of years to parent's sporadic onset and risk factors with neural integrity and Alzheimer biomarkers. *Neurology*, *95*(15), e2065–e2074.
<https://doi.org/10.1212/WNL.0000000000010527>
- Arrighi, H. M., Neumann, P. J., Lieberburg, I. M., & Townsend, R. J. (2010). Lethality of Alzheimer Disease and Its Impact on Nursing Home Placement. *Alzheimer Disease & Associated Disorders*, *24*(1), 90–95.
<https://doi.org/10.1097/WAD.0b013e31819fe7d1>
- Ashburner, J. (2007). A fast diffeomorphic image registration algorithm. *NeuroImage*, *38*(1), 95–113. <https://doi.org/10.1016/j.neuroimage.2007.07.007>
- Attems, J., & Jellinger, K. A. (2014). The overlap between vascular disease and Alzheimer's disease—Lessons from pathology. *BMC Medicine*, *12*(1), 1–12.
<https://doi.org/10.1186/s12916-014-0206-2>
- Bari, S., Amico, E., Vike, N., Talavage, T. M., & Goñi, J. (2019). Uncovering multi-site identifiability based on resting-state functional connectomes. *NeuroImage*, *202*(July). <https://doi.org/10.1016/j.neuroimage.2019.06.045>
- Bateman, R. J., Xiong, C., Benzinger, T. L. S., Fagan, A. M., Goate, A., & Fox, N. (2013). *Clinical and Biomarker Changes in Dominantly Inherited Alzheimer's Disease*. *367*(9), 795–804. <https://doi.org/10.1056/NEJMoa1202753>.Clinical
- Bejanin, A., Murray, M. E., Martin, P., Botha, H., Tosakulwong, N., Schwarz, C. G., Senjem, M. L., Chételat, G., Kantarci, K., Jack, C. R., Boeve, B. F., Knopman, D. S., Petersen, R. C., Giannini, C., Parisi, J. E., Dickson, D. W., Whitwell, J. L., & Josephs, K. A. (2019). Antemortem volume loss mirrors TDP-43 staging in older

adults with non-frontotemporal lobar degeneration. *Brain*, 142(11), 3621–3635.
<https://doi.org/10.1093/brain/awz277>

Benkarim, O., Paquola, C., Park, B., Kebets, V., Hong, S.-J., Vos De Wael, R., Zhang, S., Yeo, B. T. T., Eickenberg, M., Ge, T., Poline, J.-B., Bernhardt, B. C., & Bzdok, D. (2022). Population heterogeneity in clinical cohorts affects the predictive accuracy of brain imaging. *PLOS Biology*, 20(4), e3001627.
<https://doi.org/10.1371/journal.pbio.3001627>

Bertoux, M., Cassagnaud, P., Lebouvier, T., Lebert, F., Sarazin, M., Le Ber, I., Dubois, B., Auriacombe, S., Hannequin, D., Wallon, D., Ceccaldi, M., Maurage, C. A., Deramecourt, V., & Pasquier, F. (2020). Does amnesia specifically predict Alzheimer's pathology? A neuropathological study. *Neurobiology of Aging*, 95, 123–130. <https://doi.org/10.1016/j.neurobiolaging.2020.07.011>

Bethlehem, R. A. I., Seidlitz, J., White, S. R., Vogel, J. W., Anderson, K. M., Adamson, C., Adler, S., Alexopoulos, G. S., Anagnostou, E., Areces-Gonzalez, A., Astle, D. E., Auyeung, B., Ayub, M., Bae, J., Ball, G., Baron-Cohen, S., Beare, R., Bedford, S. A., Benegal, V., ... Alexander-Bloch, A. F. (2022). Brain charts for the human lifespan. *Nature*, 604(February). <https://doi.org/10.1038/s41586-022-04554-y>

Betzler, R. F., Bertolero, M. A., Gordon, E. M., Gratton, C., Dosenbach, N. U. F., & Bassett, D. S. (2019). The community structure of functional brain networks exhibits scale-specific patterns of inter- and intra-subject variability. *NeuroImage*, 202(September 2018), 115990.
<https://doi.org/10.1016/j.neuroimage.2019.07.003>

- Betzel, R. F., Byrge, L., He, Y., Goñi, J., Zuo, X. N., & Sporns, O. (2014). Changes in structural and functional connectivity among resting-state networks across the human lifespan. *NeuroImage*, *102*(P2), 345–357.
<https://doi.org/10.1016/j.neuroimage.2014.07.067>
- Bijsterbosch, J. D., Woolrich, M. W., Glasser, M. F., Robinson, E. C., Beckmann, C. F., Van Essen, D. C., Harrison, S. J., & Smith, S. M. (2018). The relationship between spatial configuration and functional connectivity of brain regions. *eLife*, *7*, 1–27.
- Binette, A. P., Gonneaud, J., Vogel, J. W., La Joie, R., Rosa-Neto, P., Louis Collins, D., Poirier, J., Breitner, J. C. S., Villeneuve, S., Vachon-Preseu, E., Tremblay-Mercier, J., & Madjar, C. (2020). Morphometric network differences in ageing versus Alzheimer’s disease dementia. *Brain*, *143*(2), 635–649.
<https://doi.org/10.1093/brain/awz414>
- Blennow, K., Galasko, D., Perneczky, R., Quevenco, F., Van Der Flier, W. M., Akinwonmi, A., Carboni, M., Jethwa, A., Suridjan, I., & Zetterberg, H. (2023). The potential clinical value of plasma biomarkers in Alzheimer’s disease. *Alzheimer’s & Dementia*, alz.13455. <https://doi.org/10.1002/alz.13455>
- Bloom, G. S. (2014). Amyloid- β and tau: The trigger and bullet in Alzheimer disease pathogenesis. *JAMA Neurology*, *71*(4), 505–508.
<https://doi.org/10.1001/jamaneurol.2013.5847>
- Bollack, A., Pemberton, H. G., Collij, L. E., Farrar, G., & Barkhof, F. (2023). *Longitudinal amyloid and tau PET imaging in Alzheimer’s disease: A systematic review of methodologies and factors affecting quantification.*

- Botvinik-Nezer, R., Holzmeister, F., Camerer, C. F., Dreber, A., Huber, J., Johannesson, M., Kirchler, M., Iwanir, R., Mumford, J. A., Adcock, R. A., Avesani, P., Baczkowski, B. M., Bajracharya, A., Bakst, L., Ball, S., Barilari, M., Bault, N., Beaton, D., Beitner, J., ... Schonberg, T. (2020). Variability in the analysis of a single neuroimaging dataset by many teams. *Nature*, *582*(7810), 84–88. <https://doi.org/10.1038/s41586-020-2314-9>
- Boyle, P. A., Yu, L., Leurgans, S. E., Wilson, R. S., Brookmeyer, R., Schneider, J. A., & Bennett, D. A. (2019). Attributable risk of Alzheimer's dementia attributed to age-related neuropathologies. *Annals of Neurology*, *85*(1), 114–124. <https://doi.org/10.1002/ana.25380>
- Braak, H., & Braak, E. (1991). Neuropathological staging of Alzheimer-related changes. *Acta Neuropathologica*, *82*, 239–259.
- Brett, M., Penny, W., & Kiebel, S. (2011). Parametric Procedures. In W. Penny, K. J. Friston, J. Ashburner, S. Kiebel, & T. E. Nichols (Eds.), *Statistical Parametric Mapping: The Analysis of Functional Brain Images* (Elsevier).
- Brown, J. A., Deng, J., Neuhaus, J., Sible, I. J., Sias, A. C., Lee, S. E., Kornak, J., Marx, G. A., Karydas, A. M., Spina, S., Grinberg, L. T., Coppola, G., Geschwind, D. H., Kramer, J. H., Gorno-Tempini, M. L., Miller, B. L., Rosen, H. J., & Seeley, W. W. (2019). Patient-Tailored, Connectivity-Based Forecasts of Spreading Brain Atrophy. *Neuron*, *104*(5), 856-868.e5. <https://doi.org/10.1016/j.neuron.2019.08.037>

- Brown, T. T. (2017). Individual differences in human brain development. *Wiley Interdisciplinary Reviews: Cognitive Science*, 8(1–2), 1–8.
<https://doi.org/10.1002/wcs.1389>
- Buckley, R. F., Scott, M. R., Jacobs, H. I. L. I., Schultz, A. P., Properzi, M. J., Amariglio, R. E., Hohman, T. J., Mayblyum, D. V., Rubinstein, Z. B., Manning, L., Hanseeuw, B. J., Mormino, E. C., Rentz, D. M., Johnson, K. A., Sperling, R. A., Amarglio, R. E., Hohman, T. J., Mayblyum, D. V., Rubinstein, Z. B., ... Sperling, R. A. (2020). Sex Mediates Relationships Between Regional Tau Pathology and Cognitive Decline. *Annals of Neurology*, 1–12. <https://doi.org/10.1002/ana.25878>
- Cai, Y., Du, J., Li, A., Zhu, Y., Xu, L., Sun, K., Ma, S., Guo, T., & for the Alzheimer's Disease Neuroimaging Initiative. (2023). Initial levels of β -amyloid and tau deposition have distinct effects on longitudinal tau accumulation in Alzheimer's disease. *Alzheimer's Research & Therapy*, 15(1), 30.
<https://doi.org/10.1186/s13195-023-01178-w>
- Chan, M. Y., Park, D. C., Savalia, N. K., Petersen, S. E., & Wig, G. S. (2014). Decreased segregation of brain systems across the healthy adult lifespan. *Proceedings of the National Academy of Sciences of the United States of America*, 111(46), E4997–E5006. <https://doi.org/10.1073/pnas.1415122111>
- Chen, P. Y., Chiou, J. M., Yang, Y. F., Chen, Y. T., Hsieh, H. L., Chang, Y. L., & Tseng, W. Y. I. (2016). Heterogeneous aging effects on functional connectivity in different cortical regions: A resting-state functional MRI study using functional data analysis. *PLoS ONE*, 11(9), 1–21.
<https://doi.org/10.1371/journal.pone.0162028>

- Chong, J. S. X., Ng, K. K., Tandi, J., Wang, C., Poh, J. H., Lo, J. C., Chee, M. W. L., & Zhou, J. H. (2019). Longitudinal changes in the cerebral cortex functional organization of healthy elderly. *Journal of Neuroscience*, *39*(28), 5534–5550. <https://doi.org/10.1523/JNEUROSCI.1451-18.2019>
- Collij, L. E., Salvadó, G., Wotschel, V., Mastenbroek, S. E., Schoenmakers, P., Heeman, F., Aksman, L., Wink, A. M., Berckel, B. N. M., van de Flier, W. M., Scheltens, P., Visser, P. J., Barkhof, F., Haller, S., Gispert, J. D., & Alves, I. L. (2022). Spatial-Temporal Patterns of Amyloid- β Accumulation: A Subtype and Stage Inference Model Analysis. *Neurology*, *0*, 10.1212/WNL.0000000000200148. <https://doi.org/10.1212/wnl.0000000000200148>
- Cummings, J., Aisen, P., Lemere, C., Atri, A., Sabbagh, M., & Salloway, S. (2021). Aducanumab produced a clinically meaningful benefit in association with amyloid lowering. *Alzheimer's Research & Therapy*, *13*(1), 98. <https://doi.org/10.1186/s13195-021-00838-z>
- Cummings, J. L., Morstorf, T., & Zhong, K. (2014). Alzheimer's disease drug-development pipeline: Few candidates, frequent failures. *Alzheimer's Research and Therapy*, *6*(4), 1–7. <https://doi.org/10.1186/alzrt269>
- da Silva Castanheira, J., Orozco Perez, H. D., Misic, B., & Baillet, S. (2021). Brief segments of neurophysiological activity enable individual differentiation. *Nature Communications*, *12*(1), 1–11. <https://doi.org/10.1038/s41467-021-25895-8>
- Demeter, D. V., Engelhardt, L. E., Mallett, R., Gordon, E. M., Nugiel, T., Harden, K. P., Tucker-Drob, E. M., Lewis-Peacock, J. A., & Church, J. A. (2020). Functional

Connectivity Fingerprints at Rest Are Similar across Youths and Adults and Vary with Genetic Similarity. *iScience*, 23(1), 100801.

<https://doi.org/10.1016/j.isci.2019.100801>

Desikan, R. S., Ségonne, F., Fischl, B., Quinn, B. T., Dickerson, B. C., Blacker, D.,

Buckner, R. L., Dale, A. M., Maguire, R. P., Hyman, B. T., Albert, M. S., &

Killiany, R. J. (2006). An automated labeling system for subdividing the human cerebral cortex on MRI scans into gyral based regions of interest. *NeuroImage*,

31(3), 968–980. <https://doi.org/10.1016/j.neuroimage.2006.01.021>

Duan, D., Xia, S., Reikik, I., Wu, Z., Wang, L., Lin, W., Gilmore, J. H., Shen, D., & Li, G.

(2020). Individual identification and individual variability analysis based on

cortical folding features in developing infant singletons and twins. *Human Brain*

Mapping, 41(8), 1985–2003. <https://doi.org/10.1002/hbm.24924>

Dubois, B., Villain, N., Frisoni, G. B., Rabinovici, G. D., Sabbagh, M., Cappa, S.,

Bejanin, A., Bombois, S., Epelbaum, S., Teichmann, M., Habert, M., Nordberg,

A., Blennow, K., Galasko, D., Stern, Y., Rowe, C. C., Salloway, S., Schneider, L.

S., Cummings, J. L., & Feldman, H. H. (2021). *Clinical diagnosis of Alzheimer's disease: Recommendations of the International Working Group*. 4422(21), 1–13.

[https://doi.org/10.1016/S1474-4422\(21\)00066-1](https://doi.org/10.1016/S1474-4422(21)00066-1)

DuPre, E., & Spreng, R. N. (2017). Structural covariance networks across the life span,

from 6 to 94 years of age. *Network Neuroscience*, 1(3), 302–323.

https://doi.org/10.1162/netn_a_00016

Engelborghs, S., Niemantsverdriet, E., Struyfs, H., Blennow, K., Brouns, R., Comabella,

M., Dujmovic, I., Van Der Flier, W., Frölich, L., Galimberti, D., Gnanapavan, S.,

- Hemmer, B., Hoff, E., Hort, J., Iacobaeus, E., Ingelsson, M., Jan De Jong, F., Jonsson, M., Khalil, M., ... Teunissen, C. E. (2017). Consensus guidelines for lumbar puncture in patients with neurological diseases. *Alzheimer's & Dementia: Diagnosis, Assessment & Disease Monitoring*, 8(1), 111–126.
<https://doi.org/10.1016/j.dadm.2017.04.007>
- Fantoni, E., Collij, L., Alves, I. L., Buckley, C., & Farrar, G. (2020). The spatial-temporal ordering of amyloid pathology and opportunities for PET imaging. *Journal of Nuclear Medicine*, 61(2), 166–171. <https://doi.org/10.2967/jnumed.119.235879>
- Ferreira, D., Nordberg, A., & Westman, E. (2020). Biological subtypes of Alzheimer disease: A systematic review and meta-analysis. *Neurology*, 94(10), 436–448.
<https://doi.org/10.1212/WNL.00000000000009058>
- Finn, E. S., Scheinost, D., Finn, D. M., Shen, X., Papademetris, X., & Constable, R. T. (2017). Can brain state be manipulated to emphasize individual differences in functional connectivity? *NeuroImage*, 160(March), 140–151.
<https://doi.org/10.1016/j.neuroimage.2017.03.064>
- Finn, E. S., Shen, X., Scheinost, D., Rosenberg, M. D., Huang, J., Chun, M. M., Papademetris, X., & Constable, R. T. (2015). Functional connectome fingerprinting: Identifying individuals using patterns of brain connectivity. *Nature Neuroscience*, 18(11), 1664–1671. <https://doi.org/10.1038/nn.4135>
- Franzmeier, N., Dewenter, A., Frontzkowski, L., Dichgans, M., Rubinski, A., Neitzel, J., Smith, R., Strandberg, O., Ossenkoppele, R., Buerger, K., Duering, M., Hansson, O., & Ewers, M. (2020). Patient-centered connectivity-based prediction of tau

pathology spread in Alzheimer's disease. *Science Advances*, 6(48).

<https://doi.org/10.1126/sciadv.abd1327>

Gallach, M., Mikhail Lette, M., Abdel-Wahab, M., Giammarile, F., Pellet, O., & Paez, D.

(2020). Addressing Global Inequities in Positron Emission Tomography-

Computed Tomography (PET-CT) for Cancer Management: A Statistical Model to Guide Strategic Planning. *Medical Science Monitor*, 26.

<https://doi.org/10.12659/MSM.926544>

Geerligs, L., Rubinov, M., Tyler, L. K., Brayne, C., Bullmore, E. T., Calder, A. C.,

Cusack, R., Dalgleish, T., Duncan, J., Henson, R. N., Matthews, F. E., Marslen-

Wilson, W. D., Rowe, J. B., Shafto, M. A., Campbell, K., Cheung, T., Davis, S.,

Geerligs, L., Kievit, R., ... Henson, R. N. (2015). State and trait components of

functional connectivity: Individual differences vary with mental state. *Journal of*

Neuroscience, 35(41), 13949–13961. [https://doi.org/10.1523/JNEUROSCI.1324-](https://doi.org/10.1523/JNEUROSCI.1324-15.2015)

15.2015

George, S., Duran, N., & Norris, K. (2014). A Systematic Review of Barriers and

Facilitators to Minority Research Participation Among African Americans, Latinos,

Asian Americans, and Pacific Islanders. *American Journal of Public Health*,

104(2), e16–e31. <https://doi.org/10.2105/AJPH.2013.301706>

Gilmore, J. H., Knickmeyer, R. C., & Gao, W. (2018). Imaging structural and functional

brain development in early childhood. *Nature Reviews Neuroscience*, 19(3), 123–

137. <https://doi.org/10.1038/nrn.2018.1>

Gorno-Tempini, M. L., Hillis, A. E., Weintraub, S., Kertesz, A., Mendez, M., Cappa, S.

F., Ogar, J. M., Rohrer, J. D., Black, S., Boeve, B. F., Manes, F., Dronkers, N. F.,

- Vandenberghe, R., Rascovsky, K., Patterson, K., Miller, B. L., Knopman, D. S., Hodges, J. R., Mesulam, M. M., & Grossman, M. (2011). Classification of primary progressive aphasia and its variants. *Neurology*, *76*(11), 1006–1014.
<https://doi.org/10.1212/WNL.0b013e31821103e6>
- Graff-Radford, J., Yong, K. X. X., Apostolova, L. G., Bouwman, F. H., Carrillo, M., Dickerson, B. C., Rabinovici, G. D., Schott, J. M., Jones, D. T., & Murray, M. E. (2021). New insights into atypical Alzheimer’s disease in the era of biomarkers. *The Lancet Neurology*, *20*(3), 222–234. [https://doi.org/10.1016/S1474-4422\(20\)30440-3](https://doi.org/10.1016/S1474-4422(20)30440-3)
- Gratton, C., Laumann, T. O., Nielsen, A. N., Greene, D. J., Gordon, E. M., Gilmore, A. W., Nelson, S. M., Coalson, R. S., Snyder, A. Z., Schlaggar, B. L., Dosenbach, N. U. F., & Petersen, S. E. (2018). Functional Brain Networks Are Dominated by Stable Group and Individual Factors, Not Cognitive or Daily Variation. *Neuron*, *98*(2), 439-452.e5. <https://doi.org/10.1016/j.neuron.2018.03.035>
- Greene, A. S., Gao, S., Scheinost, D., & Constable, R. T. (2018). Task-induced brain state manipulation improves prediction of individual traits. *Nature Communications*, *9*(1). <https://doi.org/10.1038/s41467-018-04920-3>
- Griffa, A., Amico, E., Liégeois, R., Van De Ville, D., & Preti, M. G. (2022). Brain structure-function coupling provides signatures for task decoding and individual fingerprinting. *NeuroImage*, *250*, 118970.
<https://doi.org/10.1016/j.neuroimage.2022.118970>

- Grothe, M. J., Barthel, H., Sepulcre, J., Dyrba, M., Sabri, O., & Teipel, S. J. (2017). In vivo staging of regional amyloid deposition. *Neurology*, *89*(20), 2031–2038.
<https://doi.org/10.1212/WNL.0000000000004643>
- Guo, T., Korman, D., Baker, S. L., Landau, S. M., & Jagust, W. J. (2021). Longitudinal Cognitive and Biomarker Measurements Support a Unidirectional Pathway in Alzheimer's Disease Pathophysiology. *Biological Psychiatry*, *89*(8), 786–794.
<https://doi.org/10.1016/j.biopsych.2020.06.029>
- Hansson, O., Edelmayer, R. M., Boxer, A. L., Carrillo, M. C., Mielke, M. M., Rabinovici, G. D., Salloway, S., Sperling, R., Zetterberg, H., & Teunissen, C. E. (2022). The Alzheimer's Association appropriate use recommendations for blood biomarkers in Alzheimer's disease. *Alzheimer's & Dementia*, *18*(12), 2669–2686.
<https://doi.org/10.1002/alz.12756>
- Hardy, J., & Selkoe, D. J. (2002). The amyloid hypothesis of Alzheimer's disease: Progress and problems on the road to therapeutics. *Science*, *297*(5580), 353–356. <https://doi.org/10.1126/science.1072994>
- Haxby, J. V., Guntupalli, J. S., Nastase, S. A., & Feilong, M. (2020). Hyperalignment: Modeling shared information encoded in idiosyncratic cortical topographies. *eLife*, *9*, 1–26. <https://doi.org/10.7554/eLife.56601>
- Horien, C., Noble, S., Finn, E. S., Shen, X., Scheinost, D., & Constable, T. (2018). Considering factors affecting the connectome-based identification process: Comment on Waller et al. *NeuroImage*, *01*(203), 172–175.
<https://doi.org/10.1016/j.neuroimage.2017.12.045.Considering>

- Horien, C., Shen, X., Scheinost, D., & Constable, R. T. (2019). The individual functional connectome is unique and stable over months to years. *NeuroImage*, 189(February), 676–687. <https://doi.org/10.1016/j.neuroimage.2019.02.002>
- Hu, D., Wang, F., Zhang, H., Wu, Z., Zhou, Z., Li, G. G., Wang, L., Lin, W., & Li, G. G. (2022). Existence of Functional Connectome Fingerprint during Infancy and Its Stability over Months. *The Journal of Neuroscience*, 42(3), 377–389. <https://doi.org/10.1523/jneurosci.0480-21.2021>
- Iturria-Medina, Y., Carbonell, F. M., & Evans, A. C. (2018). Multimodal imaging-based therapeutic fingerprints for optimizing personalized interventions: Application to neurodegeneration. *NeuroImage*, 179, 40–50. <https://doi.org/10.1016/j.neuroimage.2018.06.028>
- Jack, C. R., Bennett, D. A., Blennow, K., Carrillo, M. C., Dunn, B., Haeberlein, S. B., Holtzman, D. M., Jagust, W., Jessen, F., Karlawish, J., Liu, E., Molinuevo, J. L., Montine, T., Phelps, C., Rankin, K. P., Rowe, C. C., Scheltens, P., Siemers, E., Snyder, H. M., ... Silverberg, N. (2018). NIA-AA Research Framework: Toward a biological definition of Alzheimer's disease. *Alzheimer's and Dementia*, 14(4), 535–562. <https://doi.org/10.1016/j.jalz.2018.02.018>
- Jack, C. R., Knopman, D. S., Jagust, W. J., Petersen, R. C., Weiner, M. W., Aisen, P. S., Shaw, L. M., Vemuri, P., Wiste, H. J., Weigand, S. D., Lesnick, T. G., Pankratz, V. S., Donohue, M. C., & Trojanowski, J. Q. (2013). Tracking pathophysiological processes in Alzheimer's disease: An updated hypothetical model of dynamic biomarkers. *The Lancet Neurology*, 12(2), 207–216. [https://doi.org/10.1016/S1474-4422\(12\)70291-0](https://doi.org/10.1016/S1474-4422(12)70291-0)

- Jagust, W. (2018). Imaging the evolution and pathophysiology of Alzheimer disease. *Nature Reviews Neuroscience*, 19(11), 687–700. <https://doi.org/10.1038/s41583-018-0067-3>
- Jalbrzikowski, M., Liu, F., Foran, W., Klei, L., Calabro, F. J., Roeder, K., Devlin, B., & Luna, B. (2020). Functional connectome fingerprinting accuracy in youths and adults is similar when examined on the same day and 1.5-years apart. *Human Brain Mapping*, 41(15), 4187–4199. <https://doi.org/10.1002/hbm.25118>
- Kaufmann, T., Alnæs, D., Brandt, C. L., Bettella, F., Djurovic, S., Andreassen, O. A., & Westlye, L. T. (2018). Stability of the brain functional connectome fingerprint in individuals with schizophrenia. *JAMA Psychiatry*, 75(7), 749–751. <https://doi.org/10.1001/jamapsychiatry.2018.0844>
- Kaufmann, T., Alnæs, D., Doan, N. T., Brandt, C. L., Andreassen, O. A., & Westlye, L. T. (2017). Delayed stabilization and individualization in connectome development are related to psychiatric disorders. *Nature Neuroscience*, 20(4), 513–515. <https://doi.org/10.1038/nn.4511>
- Klunk, W. E., Engler, H., Nordberg, A., Wang, Y., Blomqvist, G., Holt, D. P., Bergström, M., Savitcheva, I., Huang, G.-F., Estrada, S., Ausén, B., Debnath, M. L., Barletta, J., Price, J. C., Sandell, J., Lopresti, B. J., Wall, A., Koivisto, P., Antoni, G., ... Långström, B. (2004). Imaging brain amyloid in Alzheimer's disease with Pittsburgh Compound-B: Imaging Amyloid in AD with PIB. *Annals of Neurology*, 55(3), 306–319. <https://doi.org/10.1002/ana.20009>
- Klunk, W. E., Koeppe, R. A., Price, J. C., Benzinger, T. L., Devous, M. D., Jagust, W. J., Johnson, K. A., Mathis, C. A., Minhas, D., Pontecorvo, M. J., Rowe, C. C.,

- Skovronsky, D. M., & Mintun, M. A. (2015). The Centiloid Project: Standardizing quantitative amyloid plaque estimation by PET. *Alzheimer's & Dementia*, *11*(1), 1. <https://doi.org/10.1016/j.jalz.2014.07.003>
- La Joie, R., Visani, A. V., Lesman-Segev, O. H., Baker, S. L., Edwards, L., Iaccarino, L., Soleimani-Meigooni, D. N., Mellinger, T., Janabi, M., Miller, Z. A., Perry, D. C., Pham, J., Strom, A., Gorno-Tempini, M. L., Rosen, H. J., Miller, B. L., Jagust, W. J., & Rabinovici, G. D. (2020). Association of APOE4 and clinical variability in Alzheimer disease with the pattern of tau- and amyloid-PET. *Neurology*, *10.1212/WNL.0000000000011270*.
<https://doi.org/10.1212/wnl.0000000000011270>
- Lehmann, M., Madison, C. M., Ghosh, P. M., Seeley, W. W., Mormino, E., Greicius, M. D., Gorno-Tempini, M. L., Kramer, J. H., Miller, B. L., Jagust, W. J., & Rabinovici, G. D. (2013). Intrinsic connectivity networks in healthy subjects explain clinical variability in Alzheimer's disease. *Proceedings of the National Academy of Sciences of the United States of America*, *110*(28), 11606–11611.
<https://doi.org/10.1073/pnas.1221536110>
- Leuzy, A., Pichet Binette, A., Vogel, J. W., Klein, G., Borroni, E., Tonietto, M., Strandberg, O., Mattsson-Carlgen, N., Palmqvist, S., Pontecorvo, M. J., Iaccarino, L., Stomrud, E., Ossenkoppele, R., Smith, R., Hansson, O., & Alzheimer's Disease Neuroimaging Initiative. (2023). Comparison of Group-Level and Individualized Brain Regions for Measuring Change in Longitudinal Tau Positron Emission Tomography in Alzheimer Disease. *JAMA Neurology*.
<https://doi.org/10.1001/jamaneurol.2023.1067>

- Liao, X., Cao, M., Xia, M., & He, Y. (2017). Individual differences and time-varying features of modular brain architecture. *NeuroImage*, *152*(February), 94–107. <https://doi.org/10.1016/j.neuroimage.2017.02.066>
- Lowe, V. J., Curran, G., Fang, P., Liesinger, A. M., Josephs, K. A., Parisi, J. E., Kantarci, K., Boeve, B. F., Pandey, M. K., Bruinsma, T., Knopman, D. S., Jones, D. T., Petrucelli, L., Cook, C. N., Graff-Radford, N. R., Dickson, D. W., Petersen, R. C., Jack, C. R., & Murray, M. E. (2016). An autoradiographic evaluation of AV-1451 Tau PET in dementia. *Acta Neuropathologica Communications*, *4*(1), 58. <https://doi.org/10.1186/s40478-016-0315-6>
- Ma, L., Tian, L., Hu, T., Jiang, T., & Zuo, N. (2021). Development of Individual Variability in Brain Functional Connectivity and Capability across the Adult Lifespan. *Cerebral Cortex*, *31*(8), 3925–3938. <https://doi.org/10.1093/cercor/bhab059>
- Mansour, S., Tian, Y., Yeo, B. T. T., Cropley, V., & Zalesky, A. (2020). High-resolution connectomic fingerprints: Mapping neural identity and behavior. *NeuroImage*, *229*(December 2020). <https://doi.org/10.1016/j.neuroimage.2020.117695>
- Mantwill, M., Gell, M., Krohn, S., & Finke, C. (2022). Brain connectivity fingerprinting and behavioural prediction rest on distinct functional systems of the human connectome. *Communications Biology*, *5*(1), 261. <https://doi.org/10.1038/s42003-022-03185-3>
- Marek, S., Tervo-Clemmens, B., Calabro, F. J., Montez, D. F., Kay, B. P., Hatoum, A. S., Donohue, M. R., Foran, W., Miller, R. L., Hendrickson, T. J., Malone, S. M., Kandala, S., Feczko, E., Miranda-Dominguez, O., Graham, A. M., Earl, E. A., Perrone, A. J., Cordova, M., Doyle, O., ... Dosenbach, N. U. F. (2022).

Reproducible brain-wide association studies require thousands of individuals.
Nature, 603(7902), 654–660. <https://doi.org/10.1038/s41586-022-04492-9>

Marquie, M., Normandin, M. D., Vanderburg, C. R., Costantino, I. M., Bien, E. A., Rycyna, L. G., Klunk, W. E., Mathis, C. A., Ikonovic, M. D., Debnath, M. L., Vasdev, N., Dickerson, B. C., Gomperts, S. N., Growdon, J. H., Johnson, K. A., Frosch, M. P., Hyman, B. T., & Gómez-Isla, T. (2015). Validating novel tau positron emission tomography tracer [F-18]-AV-1451 (T807) on postmortem brain tissue: Validation of PET Tracer. *Annals of Neurology*, 78(5), 787–800.
<https://doi.org/10.1002/ana.24517>

Mattsson, N., Palmqvist, S., Stomrud, E., Vogel, J., & Hansson, O. (2019). Staging β -Amyloid Pathology with Amyloid Positron Emission Tomography. *JAMA Neurology*, 76(11), 1319–1329. <https://doi.org/10.1001/jamaneurol.2019.2214>

Mattsson-Carlgen, N., Grinberg, L. T., Boxer, A., Ossenkoppele, R., Jonsson, M., Seeley, W., Ehrenberg, A., Spina, S., Janelidze, S., Rojas-Martinez, J., Rosen, H., La Joie, R., Lesman-Segev, O., Iaccarino, L., Kollmorgen, G., Ljubenkova, P., Eichenlaub, U., Gorno-Tempini, M. L., Miller, B., ... Rabinovici, G. D. (2022). Cerebrospinal Fluid Biomarkers in Autopsy-Confirmed Alzheimer Disease and Frontotemporal Lobar Degeneration. *Neurology*, 98(11), e1137–e1150.
<https://doi.org/10.1212/WNL.0000000000200040>

McKhann, G. M., Knopman, D. S., Chertkow, H., Hyman, B. T., Jack, C. R., Kawas, C. H., Klunk, W. E., Koroshetz, W. J., Manly, J. J., Mayeux, R., Mohs, R. C., Morris, J. C., Rossor, M. N., Scheltens, P., Carrillo, M. C., Thies, B., Weintraub, S., & Phelps, C. H. (2011). The diagnosis of dementia due to Alzheimer's disease:

- Recommendations from the National Institute on Aging-Alzheimer's Association workgroups on diagnostic guidelines for Alzheimer's disease. *Alzheimer's & Dementia*, 7(3), 263–269. <https://doi.org/10.1016/j.jalz.2011.03.005>
- Mehta, R. I., & Schneider, J. A. (2021). What is “Alzheimer's disease”? The neuropathological heterogeneity of clinically defined Alzheimer's dementia. *Current Opinion in Neurology*, 34(2), 237–245. <https://doi.org/10.1097/WCO.0000000000000912>
- Menon, S. S., & Krishnamurthy, K. (2019). A Comparison of Static and Dynamic Functional Connectivities for Identifying Subjects and Biological Sex Using Intrinsic Individual Brain Connectivity. *Scientific Reports*, 9(1), 1–11. <https://doi.org/10.1038/s41598-019-42090-4>
- Miranda-Dominguez, O., Feczko, E., Grayson, D. S., Walum, H., Nigg, J. T., & Fair, D. A. (2017). Heritability of the human connectome: A connectotyping study. *Network Neuroscience*, 2(2), 175–199. <https://doi.org/10.1162/NETN>
- Montine, T. J., Phelps, C. H., Beach, T. G., Bigio, E. H., Cairns, N. J., Dickson, D. W., Duyckaerts, C., Frosch, M. P., Masliah, E., Mirra, S. S., Nelson, P. T., Schneider, J. A., Thal, D. R., Trojanowski, J. Q., Vinters, H. V., & Hyman, B. T. (2012). National institute on aging-Alzheimer's association guidelines for the neuropathologic assessment of Alzheimer's disease: A practical approach. *Acta Neuropathologica*, 123(1), 1–11. <https://doi.org/10.1007/s00401-011-0910-3>
- Morris, J. C., Schindler, S. E., McCue, L. M., Moulder, K. L., Benzinger, T. L. S., Cruchaga, C., Fagan, A. M., Grant, E., Gordon, B. A., Holtzman, D. M., & Xiong, C. (2019). Assessment of Racial Disparities in Biomarkers for Alzheimer

Disease. *JAMA Neurology*, 76(3), 264–273.

<https://doi.org/10.1001/jamaneurol.2018.4249>

Mueller, S., Wang, D., Fox, M. D., Yeo, B. T. T., Sepulcre, J., Sabuncu, M. R., Shafee, R., Lu, J., & Liu, H. (2013). Individual Variability in Functional Connectivity Architecture of the Human Brain. *Neuron*, 77(3), 586–595.

<https://doi.org/10.1016/j.neuron.2012.12.028>

Nadig, A., Seidlitz, J., McDermott, C. L., Liu, S., Bethlehem, R., Moore, T. M., Mallard, T. T., Clasen, L. S., Blumenthal, J. D., Lalonde, F., Gur, R. E. R. C. R. E., Gur, R. E. R. C. R. E., Bullmore, E. T., Satterthwaite, T. D., & Raznahan, A. (2021). Morphological integration of the human brain across adolescence and adulthood. *Proceedings of the National Academy of Sciences of the United States of America*, 118(14), 1–10. <https://doi.org/10.1073/pnas.2023860118>

Nichols, E., Szeoke, C. E. I., Vollset, S. E., Abbasi, N., Abd-Allah, F., Abdela, J., Aichour, M. T. E., Akinyemi, R. O., Alahdab, F., Asgedom, S. W., Awasthi, A., Barker-Collo, S. L., Baune, B. T., Béjot, Y., Belachew, A. B., Bennett, D. A., Biadgo, B., Bijani, A., Bin Sayeed, M. S., ... Murray, C. J. L. (2019). Global, regional, and national burden of Alzheimer's disease and other dementias, 1990–2016: A systematic analysis for the Global Burden of Disease Study 2016. *The Lancet Neurology*, 18(1), 88–106. [https://doi.org/10.1016/S1474-4422\(18\)30403-4](https://doi.org/10.1016/S1474-4422(18)30403-4)

Ossenkoppele, R., Cohn-Sheehy, B. I., La Joie, R., Vogel, J. W., Möller, C., Lehmann, M., Van Berckel, B. N. M., Seeley, W. W., Pijnenburg, Y. A., Gorno-Tempini, M. L., Kramer, J. H., Barkhof, F., Rosen, H. J., Van Der Flier, W. M., Jagust, W. J.,

Miller, B. L., Scheltens, P., & Rabinovici, G. D. (2015). Atrophy patterns in early clinical stages across distinct phenotypes of Alzheimer's disease: Origin and Spread of Atrophy in AD Variants. *Human Brain Mapping, 36*(11), 4421–4437. <https://doi.org/10.1002/hbm.22927>

Ossenkoppele, R., Iaccarino, L., Schonhaut, D. R., Brown, J. A., La Joie, R., O'Neil, J. P., Janabi, M., Baker, S. L., Kramer, J. H., Gorno-Tempini, M. L., Miller, B. L., Rosen, H. J., Seeley, W. W., Jagust, W. J., & Rabinovici, G. D. (2019). Tau covariance patterns in Alzheimer's disease patients match intrinsic connectivity networks in the healthy brain. *NeuroImage: Clinical, 23*(May), 101848. <https://doi.org/10.1016/j.nicl.2019.101848>

Ossenkoppele, R., Lyoo, C. H., Sudre, C. H., van Westen, D., Cho, H., Ryu, Y. H., Choi, J. Y., Smith, R., Strandberg, O., Palmqvist, S., Westman, E., Tsai, R., Kramer, J., Boxer, A. L., Gorno-Tempini, M. L., La Joie, R., Miller, B. L., Rabinovici, G. D., & Hansson, O. (2020). Distinct tau PET patterns in atrophy-defined subtypes of Alzheimer's disease. *Alzheimer's and Dementia, 16*(2), 335–344. <https://doi.org/10.1016/j.jalz.2019.08.201>

Ossenkoppele, R., Pichet Binette, A., Groot, C., Smith, R., Strandberg, O., Palmqvist, S., Stomrud, E., Tideman, P., Ohlsson, T., Jögi, J., Johnson, K., Sperling, R., Dore, V., Masters, C. L., Rowe, C., Visser, D., van Berckel, B. N. M., van der Flier, W. M., Baker, S., ... Hansson, O. (2022). Amyloid and tau PET-positive cognitively unimpaired individuals are at high risk for future cognitive decline. *Nature Medicine, 28*(11), 2381–2387. <https://doi.org/10.1038/s41591-022-02049-x>

x

- Ossenkoppele, R., Rabinovici, G. D., Smith, R., Cho, H., Scholl, M., Strandberg, O., Palmqvist, S., Mattsson, N., Janelidze, S., Santillo, A., Ohlsson, T., Jogi, J., Tsai, R., La Joie, R., Kramer, J., Boxer, A. L., Gorno-Tempini, M. L., Miller, B. L., Choi, J. Y., ... Hansson, O. (2018). Discriminative accuracy of [18F]flortaucipir positron emission tomography for Alzheimer disease vs other neurodegenerative disorders. *JAMA - Journal of the American Medical Association*, 320(11), 1151–1162. <https://doi.org/10.1001/jama.2018.12917>
- Ossenkoppele, R., Singleton, E. H., Groot, C., Dijkstra, A. A., Eikelboom, W. S., Seeley, W. W., Miller, B., Laforce, R., Scheltens, P., Papma, J. M., Rabinovici, G. D., & Pijnenburg, Y. A. L. (2021). Provisional research criteria for the behavioral variant of Alzheimer's disease A systematic review and meta-analysis. *JAMA Neurology*, 1–13. <https://doi.org/10.1001/jamaneurol.2021.4417>
- Ourry, V., Binette, A. P., St-Onge, F., Strikwerda-Brown, C., Chagnot, A., Poirier, J., Breitner, J., Arenaza-Urquijo, E. M., Rabin, J. S., Buckley, R., Gonneaud, J., Marchant, N. L., & Villeneuve, S. (2023). How do modifiable risk factors affect Alzheimer's disease pathology or mitigate its effect on clinical symptom expression? *Biological Psychiatry*, S0006322323015627. <https://doi.org/10.1016/j.biopsych.2023.09.003>
- Ousdal, O. T., Kaufmann, T., Kolskår, K., Vik, A., Wehling, E., Lundervold, A. J., Lundervold, A., & Westlye, L. T. (2020). Longitudinal stability of the brain functional connectome is associated with episodic memory performance in aging. *Human Brain Mapping*, 41(3), 697–709. <https://doi.org/10.1002/hbm.24833>

Ozlen, H., Pichet Binette, A., Köbe, T., Meyer, P.-F., Gonneaud, J., St-Onge, F., Provost, K., Soucy, J.-P., Rosa-Neto, P., Breitner, J., Poirier, J., Villeneuve, S., Tam, A., Labonte, A., Pichet Binette, A., Faubert, A.-M., Mathieu, A., Madjar, C., Carrier, C. E., ... Yang, H.-S. (2022). Spatial Extent of Amyloid- β Levels and Associations With Tau-PET and Cognition. *JAMA Neurology*.
<https://doi.org/10.1001/jamaneurol.2022.2442>

Parent, C., Rousseau, L.-S., Predovan, D., Duchesne, S., & Hudon, C. (2023). Longitudinal association between β -amyloid accumulation and cognitive decline in cognitively healthy older adults: A systematic review. *Aging Brain*, 3, 100074.
<https://doi.org/10.1016/j.nbas.2023.100074>

Peña-Gómez, C., Avena-Koenigsberger, A., Sepulcre, J., & Sporns, O. (2018). Spatiotemporal network markers of individual variability in the human functional connectome. *Cerebral Cortex*, 28(8), 2922–2934.
<https://doi.org/10.1093/cercor/bhx170>

Poldrack, R. A., Fletcher, P. C., Henson, R. N., Worsley, K. J., Brett, M., & Nichols, T. E. (2008). Guidelines for reporting an fMRI study. *NeuroImage*, 40(2), 409–414.
<https://doi.org/10.1016/j.neuroimage.2007.11.048>

Poldrack, R. A., Mumford, J. A., & Nichols, T. E. (2011). *Handbook of functional MRI data analysis* (Cambridge). New-York.

Qiu, Y., Jacobs, D. M., Messer, K., Salmon, D. P., & Feldman, H. H. (2019). Cognitive heterogeneity in probable Alzheimer disease: Clinical and neuropathologic features. *Neurology*, 93(8), e778–e790.
<https://doi.org/10.1212/WNL.0000000000007967>

- Rabinovici, G. D., Gatsonis, C., Apgar, C., Chaudhary, K., Gareen, I., Hanna, L., Hendrix, J., Hillner, B. E., Olson, C., Lesman-Segev, O. H., Romanoff, J., Siegel, B. A., Whitmer, R. A., & Carrillo, M. C. (2019). Association of Amyloid Positron Emission Tomography With Subsequent Change in Clinical Management Among Medicare Beneficiaries With Mild Cognitive Impairment or Dementia. *JAMA*, 321(13), 1286. <https://doi.org/10.1001/jama.2019.2000>
- Rascovsky, K., Hodges, J. R., Knopman, D., Mendez, M. F., Kramer, J. H., Neuhaus, J., Van Swieten, J. C., Seelaar, H., Dopper, E. G. P., Onyike, C. U., Hillis, A. E., Josephs, K. A., Boeve, B. F., Kertesz, A., Seeley, W. W., Rankin, K. P., Johnson, J. K., Gorno-Tempini, M.-L., Rosen, H., ... Miller, B. L. (2011). Sensitivity of revised diagnostic criteria for the behavioural variant of frontotemporal dementia. *Brain*, 134(9), 2456–2477. <https://doi.org/10.1093/brain/awr179>
- Raznahan, A., Lerch, J. P., Lee, N., Greenstein, D., Wallace, G. L., Stockman, M., Clasen, L., Shaw, P. W., & Giedd, J. N. (2011). Patterns of coordinated anatomical change in human cortical development: A longitudinal neuroimaging study of maturational coupling. *Neuron*, 72(5), 873–884. <https://doi.org/10.1016/j.neuron.2011.09.028>
- Robinson, J. L., Lee, E. B., Xie, S. X., Rennert, L., Suh, E., Bredenberg, C., Caswell, C., Van Deerlin, V. M., Yan, N., Yousef, A., Hurtig, H. I., Siderowf, A., Grossman, M., McMillan, C. T., Miller, B., Duda, J. E., Irwin, D. J., Wolk, D., Elman, L., ... Trojanowski, J. Q. (2018). Neurodegenerative disease concomitant proteinopathies are prevalent, age-related and APOE4-associated. *Brain*, 141(7), 2181–2193. <https://doi.org/10.1093/brain/awy146>

- Salvadó, G., Larsson, V., Cody, K. A., Cullen, N. C., Jonaitis, E. M., Stomrud, E., Kollmorgen, G., Wild, N., Palmqvist, S., Janelidze, S., Mattsson-Carlgen, N., Zetterberg, H., Blennow, K., Johnson, S. C., Ossenkoppele, R., & Hansson, O. (2023). Optimal combinations of CSF biomarkers for predicting cognitive decline and clinical conversion in cognitively unimpaired participants and mild cognitive impairment patients: A multi-cohort study. *Alzheimer's & Dementia*, *19*(7), 2943–2955. <https://doi.org/10.1002/alz.12907>
- Schaefer, A., Kong, R., Gordon, E. M., Laumann, T. O., Zuo, X.-N., Holmes, A. J., Eickhoff, S. B., & Yeo, B. T. T. (2018). Local-Global Parcellation of the Human Cerebral Cortex from Intrinsic Functional Connectivity MRI. *Cerebral Cortex*, *28*(9), 3095–3114. <https://doi.org/10.1093/cercor/bhx179>
- Scheltens, P., De Strooper, B., Kivipelto, M., Holstege, H., Chételat, G., Teunissen, C. E., Cummings, J., & van der Flier, W. M. (2021). Alzheimer's disease. *Lancet (London, England)*, *6736*(20). [https://doi.org/10.1016/S0140-6736\(20\)32205-4](https://doi.org/10.1016/S0140-6736(20)32205-4)
- Schöll, M., Lockhart, S. N., Schonhaut, D. R., O'Neil, J. P., Janabi, M., Ossenkoppele, R., Baker, S. L., Vogel, J. W., Faria, J., Schwimmer, H. D., Rabinovici, G. D., & Jagust, W. J. (2016). PET Imaging of Tau Deposition in the Aging Human Brain. *Neuron*, *89*(5), 971–982. <https://doi.org/10.1016/j.neuron.2016.01.028>
- Schork, N. J. (2015). Personalized medicine: Time for one-person trials. *Nature*.
- Setton, R., Mwilambwe-Tshilobo, L., Girn, M., Lockrow, A. W., Baracchini, G., Hughes, C., Lowe, A. J., Cassidy, B. N., Li, J., Luh, W.-M., Bzdok, D., Leahy, R. M., Ge, T., Margulies, D. S., Misic, B., Bernhardt, B. C., Stevens, W. D., De Brigard, F., Kundu, P., ... Spreng, R. N. (2022). Age differences in the functional architecture

of the human brain. *Cerebral Cortex*, bhac056.

<https://doi.org/10.1093/cercor/bhac056>

- Shaw, A. R., Perales-Puchalt, J., Johnson, E., Espinoza-Kissell, P., Acosta-Rullan, M., Frederick, S., Lewis, A., Chang, H., Mahnken, J., & Vidoni, E. D. (2021). Representation of Racial and Ethnic Minority Populations in Dementia Prevention Trials: A Systematic Review. *The Journal Of Prevention of Alzheimer's Disease*, 1–6. <https://doi.org/10.14283/jpad.2021.49>
- Sims, J. R., Zimmer, J. A., Evans, C. D., Lu, M., Ardayfio, P., Sparks, J., Wessels, A. M., Shcherbinin, S., Wang, H., Monkul Nery, E. S., Collins, E. C., Solomon, P., Salloway, S., Apostolova, L. G., Hansson, O., Ritchie, C., Brooks, D. A., Mintun, M., Skovronsky, D. M., ... Zboch, M. (2023). Donanemab in Early Symptomatic Alzheimer Disease: The TRAILBLAZER-ALZ 2 Randomized Clinical Trial. *JAMA*, 330(6), 512. <https://doi.org/10.1001/jama.2023.13239>
- Singleton, E. H., Hansson, O., Pijnenburg, Y. A. M., Joie, R. L., Mantyh, W. G., Tideman, P., Stomrud, E., Leuzy, A., Johansson, M., Strandberg, O., Smith, R., Berendrecht, E., Miller, B., Iaccarino, L., Edwards, L., Storm, A., Wolters, E., Coomans, E. M., Visser, D., ... Ossenkoppele, R. (2021). Heterogeneous distribution of tau pathology in the behavioral variant of Alzheimer's disease. *Journal of Neurology, Neurosurgery and Psychiatry*, 0, 1–9. <https://doi.org/10.1136/jnnp-2020-325497>
- Sintini, I., Martin, P. R., Graff-Radford, J., Senjem, M. L., Schwarz, C. G., Machulda, M. M., Spychalla, A. J., Drubach, D. A., Knopman, D. S., Petersen, R. C., Lowe, V. J., Jack, C. R., Josephs, K. A., & Whitwell, J. L. (2019). Longitudinal tau-PET

- uptake and atrophy in atypical Alzheimer's disease. *NeuroImage: Clinical*, 23(April), 1–12. <https://doi.org/10.1016/j.nicl.2019.101823>
- Sorrentino, P., Rucco, R., Lardone, A., Liparoti, M., Lopez, E. T., Cavaliere, C., Soricelli, A., Jirsa, V., Troisi Lopez, E., Cavaliere, C., Soricelli, A., Jirsa, V., Sorrentino, G., & Amico, E. (2020). Clinical connectome fingerprints of cognitive decline. *NeuroImage*, 238(February), 118253. <https://doi.org/10.1016/j.neuroimage.2021.118253>
- Sporns, O., & Betzel, R. F. (2016). Modular brain networks. *Annual Review of Psychology*, 67(September 2015), 613–640. <https://doi.org/10.1146/annurev-psych-122414-033634>
- Sterling, E., Pearl, H., Liu, Z., Allen, J. W., & Fleischer, C. C. (2022). Demographic reporting across a decade of neuroimaging: A systematic review. *Brain Imaging and Behavior*, 16(6), 2785–2796. <https://doi.org/10.1007/s11682-022-00724-8>
- Stimson, J. A., Carmines, E. G., & Zeller, R. A. (1978). Interpreting Polynomial Regression. *Sociological Methods & Research*, 6(4), 515–524.
- St-Onge, F., Chapleau, M., Breitner, J. C., Villeneuve, S., Binette, A. P., & the Alzheimer's Disease Neuroimaging Initiative. (2023). Tau accumulation and its spatial progression across the Alzheimer's disease spectrum. *Medrxiv*. <https://doi.org/10.1101/2023.06.02.23290880>
- Strikwerda-Brown, C., Hobbs, D. A., Gonneaud, J., St-Onge, F., Binette, A. P., Ozlen, H., Provost, K., Soucy, J.-P., Buckley, R. F., Benzinger, T. L. S., Morris, J. C., Villemagne, V. L., Doré, V., Sperling, R. A., Johnson, K. A., Rowe, C. C., Gordon, B. A., Poirier, J., Breitner, J. C. S., ... Bourgeat, P. (2022). Association of

Elevated Amyloid and Tau Positron Emission Tomography Signal With Near-Term Development of Alzheimer Disease Symptoms in Older Adults Without Cognitive Impairment. *JAMA Neurology*, 79(10), 975.

<https://doi.org/10.1001/jamaneurol.2022.2379>

Sun, N., Mormino, E. C., Chen, J., Sabuncu, M. R., & Yeo, B. T. T. (2019). Multi-modal latent factor exploration of atrophy, cognitive and tau heterogeneity in Alzheimer's disease. *NeuroImage*, 201(June).

<https://doi.org/10.1016/j.neuroimage.2019.116043>

Sun, Y., Zhao, Y., Hu, K., Wang, M., Liu, Y., Liu, B., & for the Alzheimer's Disease Neuroimaging Initiative. (2023). Distinct spatiotemporal subtypes of amyloid deposition are associated with diverging disease profiles in cognitively normal and mild cognitive impairment individuals. *Translational Psychiatry*, 13(1), 35.

<https://doi.org/10.1038/s41398-023-02328-2>

Svaldi, D. O., Goñi, J., Abbas, K., Amico, E., Clark, D. G., Muralidharan, C., Dziedzic, M., West, J. D., Risacher, S. L., Saykin, A. J., & Apostolova, L. G. (2021). Optimizing differential identifiability improves connectome predictive modeling of cognitive deficits from functional connectivity in Alzheimer's disease. *Human Brain Mapping*, 42(11), 3500–3516.

<https://doi.org/10.1002/hbm.25448>

Tavor, I., Parker Jones, O., Mars, R. B., Smith, S. M., Behrens, T. E., & Jbabdi, S. (2016). Task-free MRI predicts individual differences in brain activity during task performance. *Science*, 352(6282), 216–220.

<https://doi.org/10.1126/science.aad8127>

- Taylor, J. R., Williams, N., Cusack, R., Auer, T., Shafto, M. A., Dixon, M., Tyler, L. K., Cam-CAN, & Henson, R. N. (2017). The Cambridge Centre for Ageing and Neuroscience (Cam-CAN) data repository: Structural and functional MRI, MEG, and cognitive data from a cross-sectional adult lifespan sample. *NeuroImage*, *144*, 262–269. <https://doi.org/10.1016/j.neuroimage.2015.09.018>
- Thal, D. R., Beach, T. G., Zhanette, M., Lilja, J., Heurling, K., Chakrabarty, A., Ismail, A., Farrar, G., Buckley, C., & Smith, A. P. L. (2018). Estimation of amyloid distribution by [18F]flutemetamol PET predicts the neuropathological phase of amyloid β -protein deposition. *Acta Neuropathologica*, *136*(4), 557–567. <https://doi.org/10.1007/s00401-018-1897-9>
- Thal, D. R., Rüb, U., Orantes, M., & Braak, H. (2002). Phases of A β -deposition in the human brain and its relevance for the development of AD. *Neurology*, *58*(12), 1791–1800. <https://doi.org/10.1212/WNL.58.12.1791>
- Therriault, J., Pascoal, T. A., Lussier, F. Z., Tissot, C., Chamoun, M., Bezgin, G., Servaes, S., Benedet, A. L., Ashton, N. J., Karikari, T. K., Lantero-Rodriguez, J., Kunach, P., Wang, Y.-T., Fernandez-Arias, J., Massarweh, G., Vitali, P., Soucy, J.-P., Saha-Chaudhuri, P., Blennow, K., ... Rosa-Neto, P. (2022). Biomarker modeling of Alzheimer's disease using PET-based Braak staging. *Nature Aging*, *2*(6), 526–535. <https://doi.org/10.1038/s43587-022-00204-0>
- Therriault, J., Pascoal, T. A., Savard, M., Mathotaarachchi, S., Benedet, A. L., Chamoun, M., Tissot, C., Lussier, F. Z., Rahmouni, N., Stevenson, J., Qureshi, M. N. I., Kang, M. S., Thomas, É., Vitali, P., Soucy, J. P., Massarweh, G., Saha-Chaudhuri, P., Gauthier, S., & Rosa-Neto, P. (2022). Intrinsic connectivity of the

human brain provides scaffold for tau aggregation in clinical variants of Alzheimer's disease. *Science Translational Medicine*, 14(659), eabc8693.

<https://doi.org/10.1126/scitranslmed.abc8693>

Tijms, B. M., Möller, C., Vrenken, H., Wink, A. M., de Haan, W., van der Flier, W. M., Stam, C. J., Scheltens, P., & Barkhof, F. (2013). Single-Subject Grey Matter Graphs in Alzheimer's Disease. *PLoS ONE*, 8(3), 1–9.

<https://doi.org/10.1371/journal.pone.0058921>

Tijms, B. M., Seris, P., Willshaw, D. J., & Lawrie, S. M. (2012). Similarity-based extraction of individual networks from gray matter MRI scans. *Cerebral Cortex*, 22(7), 1530–1541. <https://doi.org/10.1093/cercor/bhr221>

Tremblay-Mercier, J., Madjar, C., Das, S., Pichet Binette, A., Dyke, S. O. M., Étienne, P., Lafaille-Magnan, M. E., Remz, J., Bellec, P., Louis Collins, D., Natasha Rajah, M., Bohbot, V., Leoutsakos, J. M., Iturria-Medina, Y., Kat, J., Hoge, R. D., Gauthier, S., Tardif, C. L., Mallar Chakravarty, M., ... Breitner, J. C. S. (2021). Open science datasets from PREVENT-AD, a longitudinal cohort of pre-symptomatic Alzheimer's disease. *NeuroImage: Clinical*, 31(June).

<https://doi.org/10.1016/j.nicl.2021.102733>

Tsvetkova, D. Z., Bergquist, S. H., Parker, M. W., Jarrett, T. L., Howell, J. C., Watts, K. D., Kollhoff, A., Roberts, D. L., & Hu, W. T. (2017). Fear and Uncertainty Do Not Influence Reported Willingness to Undergo Lumbar Punctures in a U.S. Multi-Cultural Cohort. *Frontiers in Aging Neuroscience*, 9.

<https://doi.org/10.3389/fnagi.2017.00022>

- Valizadeh, S. A., Liem, F., Mérillat, S., Hänggi, J., & Jäncke, L. (2018). Identification of individual subjects on the basis of their brain anatomical features. *Scientific Reports*, 8(1), 1–9. <https://doi.org/10.1038/s41598-018-23696-6>
- Van De Ville, D., Farouj, Y., Preti, M. G., Liégeois, R., & Amico, E. (2021). When makes you unique: Temporality of the human brain fingerprint. *Science Advances*, 7(42), 1–11. <https://doi.org/10.1126/sciadv.abj0751>
- Van Dyck, C. H., Swanson, C. J., Aisen, P., Bateman, R. J., Chen, C., Gee, M., Kanekiyo, M., Li, D., Reyderman, L., Cohen, S., Froelich, L., Katayama, S., Sabbagh, M., Vellas, B., Watson, D., Dhadda, S., Irizarry, M., Kramer, L. D., & Iwatsubo, T. (2023). Lecanemab in Early Alzheimer's Disease. *New England Journal of Medicine*, 388(1), 9–21. <https://doi.org/10.1056/NEJMoa2212948>
- Van Essen, D. C., Smith, S. M., Barch, D. M., Behrens, T. E. J., Yacoub, E., & Ugurbil, K. (2013). The WU-Minn Human Connectome Project: An overview. *NeuroImage*, 80, 62–79. <https://doi.org/10.1016/j.neuroimage.2013.05.041>
- Van Essen, D. C., Ugurbil, K., Auerbach, E., Barch, D., Behrens, T. E. J., Bucholz, R., Chang, A., Chen, L., Corbetta, M., Curtiss, S. W., Della Penna, S., Feinberg, D., Glasser, M. F., Harel, N., Heath, A. C., Larson-Prior, L., Marcus, D., Michalareas, G., Moeller, S., ... Yacoub, E. (2012). The Human Connectome Project: A data acquisition perspective. *NeuroImage*, 62(4), 2222–2231. <https://doi.org/10.1016/j.neuroimage.2012.02.018>
- Vanderwal, T., Eilbott, J., Finn, E. S., Craddock, R. C., Turnbull, A., & Castellanos, F. X. (2017). Individual differences in functional connectivity during naturalistic viewing

conditions. *NeuroImage*, 157(April), 521–530.

<https://doi.org/10.1016/j.neuroimage.2017.06.027>

Vanderwal, T., Eilbott, J., Kelly, C., Frew, S. R., Woodward, T. S., Milham, M. P., & Castellanos, F. X. (2021). Stability and similarity of the pediatric connectome as developmental measures. *NeuroImage*, 226(November 2019), 117537.

<https://doi.org/10.1016/j.neuroimage.2020.117537>

Váša, F., Seidlitz, J., Romero-Garcia, R., Whitaker, K. J., Rosenthal, G., Vértes, P. E., Shinn, M., Alexander-Bloch, A., Fonagy, P., Dolan, R. J., Jones, P. B., Goodyer, I. M., Sporns, O., & Bullmore, E. T. (2018). Adolescent tuning of association cortex in human structural brain networks. *Cerebral Cortex*, 28(1), 281–294.

<https://doi.org/10.1093/cercor/bhx249>

Verdi, S., Kia, S. M., Yong, K. X. X., Tosun, D., Schott, J. M., Marquand, A. F., & Cole, J. H. (2023). Revealing Individual Neuroanatomical Heterogeneity in Alzheimer Disease Using Neuroanatomical Normative Modeling. *Neurology*, 100(24), e2442–e2453.

<https://doi.org/10.1212/WNL.0000000000207298>

Villemagne, V. L., Leuzy, A., Bohorquez, S. S., Bullich, S., Shimada, H., Rowe, C. C., Bourgeat, P., Lopresti, B., Huang, K., Krishnadas, N., Fripp, J., Takado, Y., Gogola, A., Minhas, D., Weimer, R., Higuchi, M., Stephens, A., Hansson, O., Doré, V., ... the AIBL research group. (2023). *CenTauR: Towards a Universal Scale and Masks for Standardizing Tau Imaging Studies* [Preprint]. *Neurology*.

<https://doi.org/10.1101/2023.03.22.23287009>

Villeneuve, S., Rabinovici, G. D., Cohn-Sheehy, B. I., Madison, C., Ayakta, N., Ghosh, P. M., La Joie, R., Arthur-Bentil, S. K., Vogel, J. W., Marks, S. M., Lehmann, M.,

- Rosen, H. J., Reed, B., Olichney, J., Boxer, A. L., Miller, B. L., Borys, E., Jin, L., W., Huang, E. J., ... Jagust, W. (2015). Existing Pittsburgh Compound-B positron emission tomography thresholds are too high: Statistical and pathological evaluation. *Brain*, *138*(7), 2020–2033. <https://doi.org/10.1093/brain/awv112>
- Vogel, J. W., Iturria-Medina, Y., Strandberg, O. T., Smith, R., Levitis, E., Evans, A. C., Hansson, O., Alzheimer's Disease Neuroimaging Initiative, Weiner, M., Aisen, P., Petersen, R., Jack, C. R., Jagust, W., Trojanowki, J. Q., Toga, A. W., Beckett, L., Green, R. C., Saykin, A. J., Morris, J., ... Wollmer, P. (2020). Spread of pathological tau proteins through communicating neurons in human Alzheimer's disease. *Nature Communications*, *11*(1), 2612. <https://doi.org/10.1038/s41467-020-15701-2>
- Vogel, J. W., Young, A. L., Oxtoby, N. P., Smith, R., Ossenkoppele, R., Strandberg, O. T., Joie, R. L., Aksman, L. M., Grothe, M. J., Devous, M. D., Rabinovici, G. D., Alexander, D. C., Lyoo, C. H., Evans, A. C., & Hansson, O. (2021). Four distinct trajectories of tau deposition identified in Alzheimer's disease. *Nature Medicine*. <https://doi.org/10.1038/s41591-021-01309-6>
- Waller, L., Walter, H., Kruschwitz, J. D., Reuter, L., Müller, S., Erk, S., & Veer, I. M. (2017). Evaluating the replicability, specificity, and generalizability of connectome fingerprints. *NeuroImage*, *158*, 371–377. <https://doi.org/10.1016/j.neuroimage.2017.07.016>
- Weintraub, S., Wicklund, A. H., & Salmon, D. P. (2012). The neuropsychological profile of Alzheimer disease. *Cold Spring Harbor Perspectives in Medicine*, *2*(4). <https://doi.org/10.1101/cshperspect.a006171>

- Whitcomb, D. C. (2012). What is personalized medicine and what should it replace? *Nature Reviews Gastroenterology & Hepatology*, 9(7), 418–424.
<https://doi.org/10.1038/nrgastro.2012.100>
- Xifra-porxas, A., Kassinopoulos, M., & Mitsis, G. D. (2020). Physiological and head motion signatures in static and time-varying functional connectivity and their subject discriminability. *bioRxiv*, 1–55.
- Xu, T., Opitz, A., Craddock, R. C., Wright, M. J., Zuo, X. N., & Milham, M. P. (2016). Assessing Variations in Areal Organization for the Intrinsic Brain: From Fingerprints to Reliability. *Cerebral Cortex*, 26(11), 4192–4211.
<https://doi.org/10.1093/cercor/bhw241>
- Yakoub, Y., Ashton, N. J., Strikwerda-Brown, C., Montoliu-Gaya, L., Karikari, T. K., Kac, P. R., Gonzalez-Ortiz, F., Gallego-Rudolf, J., Meyer, P., St-Onge, F., Schöll, M., Soucy, J., Breitner, J. C. S., Zetterberg, H., Blennow, K., Poirier, J., Villeneuve, S., & PREVENT-AD Research Group. (2023). Longitudinal blood biomarker trajectories in preclinical Alzheimer's disease. *Alzheimer's & Dementia*, alz.13318. <https://doi.org/10.1002/alz.13318>
- Young, A. L., Marinescu, R. V., Oxtoby, N. P., Bocchetta, M., Yong, K., Firth, N. C., Cash, D. M., Thomas, D. L., Dick, K. M., Cardoso, J., van Swieten, J., Borroni, B., Galimberti, D., Masellis, M., Tartaglia, M. C., Rowe, J. B., Graff, C., Tagliavini, F., Frisoni, G. B., ... Furst, A. J. (2018). Uncovering the heterogeneity and temporal complexity of neurodegenerative diseases with Subtype and Stage Inference. *Nature Communications*, 9(1), 1–16. <https://doi.org/10.1038/s41467-018-05892-0>

Zonneveld, H. I., Pruijm, R. H., Bos, D., Vrooman, H. A., Muetzel, R. L., Hofman, A., Rombouts, S. A., van der Lugt, A., Niessen, W. J., Ikram, M. A., & Vernooij, M. W. (2019). Patterns of functional connectivity in an aging population: The Rotterdam Study. *NeuroImage*, 189(September 2018), 432–444.
<https://doi.org/10.1016/j.neuroimage.2019.01.041>

X – Annex: *sihnpy* documentation

This annex presents *sihnpy*, a Python-based package developed to bundle and offer openly available tools to study interindividual differences in brain data. *sihnpy* adapts four tools: fingerprinting originally developed in MATLAB (Finn et al., 2015), spatial extent originally developed in Python in Chapter 3 of this thesis (St-Onge et al., 2023), sliding-window originally developed in R (Váša et al., 2018) and the imbalance mapping originally developed in R (Nadig et al., 2021). *sihnpy* also includes data from the PREVENT-AD Open Dataset (Tremblay-Mercier et al., 2021), a repository of data collected from cognitively unimpaired participants at risk of developing Alzheimer’s disease, to allow users to test the functionalities of the package. This annex will present each of the module by describing their rationale, their definitions and methods, their use cases, limitations and strengths and briefly demonstrating their application on PREVENT-AD data. Detailed information on data preprocessing for the datasets module is also included. Finally, this annex will discuss potential applications and future directions. Full-fledged tutorials, examples, and explanations are available on the original web-based documentation at <https://sihnpy.readthedocs.io/en/latest>.

X.I – Introduction to *sihnpy*

Variability between individuals is usually ignored in brain imaging research. Most statistical methods derive an average signal across individuals and attribute deviation from the norm to random, statistical noise (Brett et al., 2011; Poldrack et al., 2011). Yet emergent research suggests that interindividual variability is instead a core, genetically determined (Demeter et al., 2020) feature of the brain. Variability in functional organization (Mansour et al., 2020; Mueller et al., 2013), brain anatomy, (Mansour et al., 2020) and electrophysiological (da Silva Castanheira et al., 2021) patterns have all been reliably shown across cognitively healthy individuals.

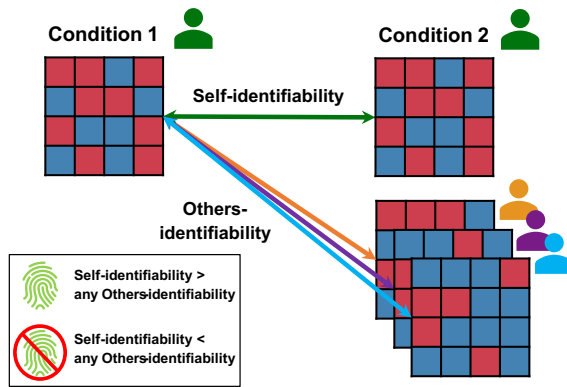
Despite this evidence of interindividual differences, much of the research in brain disorders, such as on Alzheimer’s disease (AD) dementia, still heavily relies on the “group-average” assumption. In AD, clinical symptoms—mainly episodic memory (Scheltens et al., 2021; Weintraub et al., 2012)—are thought to be caused by the accumulation of two pathological hallmarks, amyloid (Thal et al., 2002) and tau (Braak & Braak, 1991) misfolded protein, in a similar spatial pattern across individuals. Originally studied using histopathology, advancements in recent years with positron emission tomography (PET) now allow for in-vivo measurements (Grothe et al., 2017; Therriault, Pascoal, Lussier, et al., 2022).

Research in the past decade shed doubt on the vision that patients all share the same pathological patterns. Evidence is emerging that patterns of amyloid (Collij et al., 2022), tau (Vogel et al., 2021), atrophy (Ferreira et al., 2020), and consequently, clinical presentations (La Joie et al., 2020) differ significantly between participants. This, in conjunction with evidence that patient-centred methods offer a significant improvement in

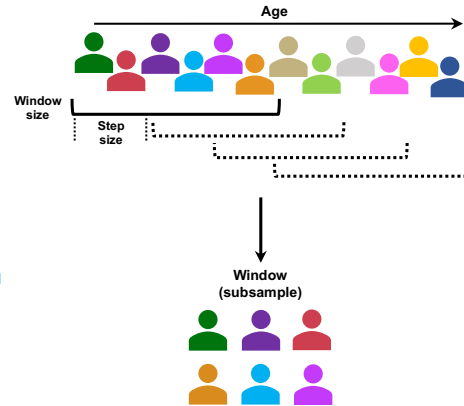
predicting the spread of pathology over time (Franzmeier et al., 2020; Leuzy et al., 2023), suggests that integrating interindividual differences in tools used in AD research is likely to yield better accuracy and outcomes for patient research, in line with the concept of precision medicine (Iturria-Medina et al., 2018).

Yet, scientists are still faced with important methodological challenges: few tools exist to measure interindividual differences, and existing tools are often not shared openly (Franzmeier et al., 2020; Leuzy et al., 2023; Tijms et al., 2012), lack thorough explanations to use for scientists with less computing experience (Nadig et al., 2021) or require massive amounts of data to work (Iturria-Medina et al., 2018). This prompted us to create *sihnpy*, a Python-based package that provides the scientific community with open, easy-to-use tools to investigate interindividual differences in brain data. *sihnpy* integrates these tools (fingerprinting, spatial extent, sliding window and imbalance mapping) with reproducible and detailed tutorials as well as open-access and simulated data from the PREVENT-AD cohort for scientists to test out the functions of the package before using them on other datasets (Tremblay-Mercier et al., 2021). In this shortened documentation, we present the modules of *sihnpy* and its application to brain imaging data from the PREVENT-AD cohorts.

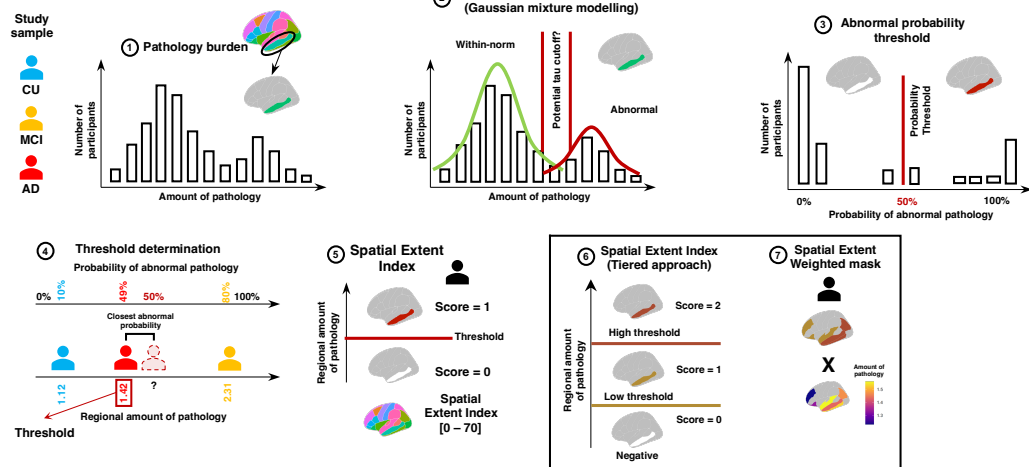
A. Fingerprinting methodology



B. Sliding-window approach



C. Spatial extent methodology



D. Imbalance mapping methodology

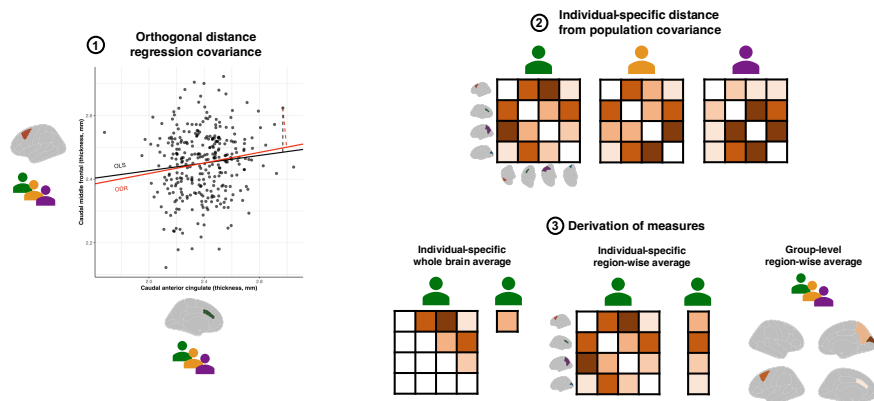


Figure X.1 – Illustration of sihnpy’s modules. A) In the fingerprinting module, the data from each participant—here illustrated with functional connectivity matrices—is correlated to their own data at a different timepoint (self-identifiability) and to the data from all other participants (others-identifiability). A stronger self-identifiability indicates an accurate fingerprint. Panel adapted from

St-Onge et al. 2023a. **B)** In the sliding-window module, subgroups of overlapping participants are selected based on a continuous variable (e.g., age), by varying the size of the subgroups (window size) and the size of the overlap (step size). Panel adapted from St-Onge et al. 2023a. **C)** In the spatial extent module, the data from each brain region (1) is used to determine a threshold over which the data should be considered abnormal. The default method in *sihnpy* is to use Gaussian Mixture modelling (2) to derive a threshold based on the probability of belonging to the cluster with highest pathology (3). Then, the value of the participant with the probability closest to the probability threshold is used as the actual threshold to determine if a participant has normal or abnormal value in a given region (4). The sum of all regions above threshold is the spatial extent index (5). *sihnpy* provides additional measures of tiered spatial extent (6) and weighted masks (7) further described in the method section. Panel adapted from St-Onge et al. 2023b. **D)** In the imbalance mapping module, the values in each pair of brain feature is correlated using orthogonal distance regression (1). The figure illustrates this correlation using PREVENT-AD Open Dataset volumetric data: the red line represents the correlation from the orthogonal distance regression and the black line represents the correlation from a classical ordinal least square regression. For each pair of region, the perpendicular distance between an individual's values and the regression line is calculated (2). This represents the imbalance that the individual has for a given pair of region. Then, different measures are calculated, such as a global average by person, an average for each brain region for each person and an average for each region at the group-level (3). Panel adapted from Nadig et al. 2021.

X.II – Description of *sihnpy*'s modules

X.II.I – Software development and general philosophy

sihnpy was developed using Python v.3.9 and Poetry v.1.4.1 in a Conda environment v.23.1.0. Package development followed the principles outlined in Beuzen & Timbers (Beuzen & Timbers, 2022). This includes continuous integration and testing, and a continuous deployment workflow set-up on GitHub (<https://github.com/stong3/sihnpy>), allowing for automatic testing of package modification, automatic deployment of the package to PyPi (<https://pypi.org/project/sihnpy/>) and automatic update of the documentation hosted on ReadTheDocs (<https://sihnpy.readthedocs.io/>).

The package was developed with three principles in mind: open tools accessible to all, ease of use and thorough explanations. To this end, extensive step-by-step documentation was developed for all modules. We also focused on using similar code architecture between modules to facilitate their use. Nearly all functions in *sihnpy* work with two simple Python objects: numpy-based n-dimensional arrays and pandas-based dataframes. Numpy arrays are objects containing many data of the same type (e.g., floats) structured alongside one or multiple dimensions (Harris et al., 2020). Pandas-based dataframes are tabular objects with columns and rows where each column represents a variable and each row an observation (The pandas development team, 2020). This choice was made as both types of Python objects are relatively easy to understand, they both work well with one another and they can usually be exported relatively easily to spreadsheets. Finally, while a basic understanding of both object types

is recommended, the package instructions usually allow users to run the functions regardless.

X.II.II – Datasets module

sihnpy is shipped with a small subset of data from the PREVENT-AD Open Dataset (Tremblay-Mercier et al., 2021), with access from the Canadian Open Neuroscience Platform (Poline et al., 2023). The goal is to provide users with data to familiarize themselves with the different modules and what the results from these modules should look like, but at the same time to not make the package too memory-heavy for users. Instead, we invite users to visit the documentation online which describes in further details how to download data from the PREVENT-AD. Here, we describe the data available in the package and how it was derived.

Data on 308 participants from the PREVENT-AD Open Dataset were available for download. First, we downloaded a random subset of 15 participants with baseline resting-state functional MRI (fMRI) available. A smaller subset of participants also had fMRI data available during memory encoding and memory retrieval tasks, and a smaller subset still also had fMRI data available at the 12-month follow-up. We used fMRIPrep v.20.2.0 to preprocess all fMRI scans available for the 15 participants. Then, we used Nilearn v.0.9.2 for Python 3.9 with partial correlations to calculate pair-wise functional connectivity in the Schaefer 400 atlas (Schaefer et al., 2018). Partial correlation was chosen specifically because the fMRI data is used to test the fingerprinting package, and we found that partial correlation tends to yield much more accurate fingerprint measures than product-moment correlations (St-Onge, Javanray, et al., 2023). We chose only 15 participants as including functional connectivity data for all 308 participants would have made the package

particularly memory-heavy and 15 participants is sufficient to test the module. Specific details on the preprocessing of fMRI scans can be found in the Data Preprocessing section.

We preprocessed structural T1-weighted MRI for 308 participants who had at least one baseline MRI scan available using FreeSurfer v6.0.0. A total of 306 baseline scans were successfully preprocessed without error. From these participants, a subset of 234 participants had 12-month follow-up scan that we also pre-processed. We extracted grey matter volume and thickness data for all baseline and follow-up scans available for all regions of the Desikan atlas (Desikan et al., 2006). We additionally extracted the grey matter volume in subcortical regions. All of the resulting data was made available within `sihnp.py`.

To allow users to test the spatial extent module, we simulated tau positron emission tomography (PET) data to replicate the use of the tool in the original publication on this method (St-Onge, Chapleau, et al., 2023). While PREVENT-AD participants do have tau-PET data available, they are not yet made openly available to the research community. As such, we generated simulated tau-PET data based on the regional average of tau-PET data within the ADNI. Specifically, to ensure we would have two Gaussian distributions for the Gaussian Mixture models, we generated random data for our 308 participants from the PREVENT-AD for each region from two distributions based on a normal distribution around the average tau-PET SUVR of CU amyloid-negative participants and on the average tau-PET SUVR of participants with AD dementia who were amyloid-positive. We then split our sample of 308 participants into two unequal parts: 100 participants with data taken from the high tau-PET distribution and 208

participants with data taken from the low tau-PET distribution. For two regions (right precentral and right postcentral gyri), we purposefully took random data from a single distribution or inverted the number of participants from the low and high tau-PET distribution to introduce errors in the test data. This was done so users can see these issues arise and understand potential solutions to apply should these errors occur in their own data.

Finally, we wanted to give users a continuous demographic variable to test the sliding window analysis. This is usually done using the age of participants. However, due to confidentiality issues, age of PREVENT-AD participants is not disclosed in the Open dataset. Instead, we once again simulated the age of our participants using a Gaussian distribution centred on the average and standard deviation of the age of participants in the PREVENT-AD ($65 \text{ years} \pm 5$), with the additional requirement that age could not be lower than 55 years. This was to match the inclusion criteria of the cohort (Tremblay-Mercier et al., 2021).

X.II.III. – Fingerprinting module

Rationale

Fingerprinting is a methodology aiming to derive unique individual-level signatures of brain patterns (Finn et al., 2015). Originally studied using functional connectivity patterns (Amico & Goñi, 2018; Finn et al., 2015), the method was successfully used in many different data types, including structural (Mansour et al., 2020) and electrophysiological (da Silva Castanheira et al., 2021) imaging. In a fingerprinting analysis, as illustrated in Figure X.IA, the brain features of an individual (e.g., regional brain volume) are first correlated to the brain features of the same participant scanned

during a different scan and/or at a different time point (self-identifiability) (Amico & Goñi, 2018). Then, the brain features of the first individual are correlated to the brain features of all other participants in the dataset (others-identifiability) (Amico & Goñi, 2018). Accurate identification of a unique signature of brain features for an individual occurs when the self-identifiability of that individual is higher than any others-identifiability across all the other participants. This is referred to as fingerprint accuracy (Amico & Goñi, 2018; Finn et al., 2015).

Fingerprints were previously associated with different health outcomes (Bijsterbosch et al., 2018; Mansour et al., 2020) and cognitive measures (Finn et al., 2015). This suggests that fingerprints could have potential clinical utility outside of personal identification.

Definitions and methods

sihnpy computes fingerprints as the correlation between two vectors of brain features (e.g., volume/functional connectivity in a set of brain regions). Fingerprinting can be performed with two different types of input. First, *sihnpy* accepts local paths to two folders containing functional connectivity matrices from two different scanning sessions or timepoints. In that case, *sihnpy* will first import the functional connectivity matrices and remove the diagonal and lower half of the matrix (as a functional connectivity matrix is symmetric). Then, the rest of the connectivity values will be vectorized. The user also has the option to normalize the values at this stage using a Fisher r-to-z transformation. Finally, the script will correlate the connectivity values of each participant in the first modality or timepoint to all participants in the second modality or timepoint. This is done by default using a product-moment correlation but can be adjusted to Spearman or

Kandall correlation. Second, *sihnpy* also accepts two pandas dataframes (i.e., two tables) with columns as brain regions and rows as individual participants. This second option will be the case most of the time when a single measure (e.g., volume) is available in each brain region. The software performs exactly the same steps as with the connectivity matrices, but with the additional restriction that at least some participant IDs must match between the two dataframes.

sihnpy outputs a single dataframe following the calculations containing, for each participant, the self-identifiability (i.e., correlation within the same individual across scans) the average other-identifiability (i.e., the average correlation between a given individual and all other individuals in the cohort), the differential identifiability (i.e., the difference between the self- and average other-identifiability) and the fingerprint identifiability accuracy (i.e., whether the participant was accurately identified). *sihnpy* also outputs a similarity matrix with the individual correlations between each participant, which can be useful to study the similarity between a specific set of participants.

Several options are available for users such as normalizing—or not—the data with the Fisher transformation before executing the fingerprinting, the type of correlation and which brain regions are selected in the analysis.

Use cases, strengths and limitations

The fingerprinting methodology can usually be applied when the data is highly dimensional for each participant, i.e., a lot of brain regions being measured. Each participant must also have two brain scans to be able to do the correlation. In terms of strengths, the fingerprinting module is easy to apply, and the software's options are flexible even with minimal Python knowledge. In terms of limitations, fingerprinting

measures can be hard to interpret (i.e., is an accurate identification positive or negative regarding other outcomes?), they are highly dependent on the resolution of the data as less data per participant will produce poor identification and the implementation in *sihnpy* is computationally expensive due to its operations being done in sequence rather than in parallel, which can result in high computational time.

Demonstration

In the documentation, a step-by-step tutorial is given with code to follow along to obtain the fingerprinting measures for the PREVENT-AD data. For brevity, interested parties are directed to the documentation. Users can derive fingerprinting measures using either functional connectivity or structural—thickness or volume—data available from the datasets module.

Functional connectivity is available on 15 participants and was measured during a resting-state, a memory encoding or memory retrieval task. A subset of these participants has longitudinal data available 12 months later. Tutorial demonstrations are done with the resting-state data available at baseline and at the 12-month follow-up. Using these data, all 15 participants are correctly identified at 12 months. Users are invited to try different combinations of the data as they see fit.

Regional thickness and volume are available on 306 participants and was available at baseline and at 12-months for a subset of participants. Tutorial demonstrations are done use brain volume in the left and right hemispheres for fingerprinting. Using these data, 98.29% of participants were accurately identified.

X.II.IV. – Spatial extent module

Rationale

The goal of the spatial extent module is to calculate the spatial extent index, i.e., the number of regions, that a given pathology is present throughout the brain of individuals (St-Onge et al., 2023). This is done by determining a threshold at which each region has an abnormal level of pathology. In *sihnpy*, this is implemented using a Gaussian mixture framework, where a threshold is established based on the probability that the data from a participant belongs in the abnormal distribution of the data. This method was originally developed using PET data (Ozlen et al., 2022; St-Onge et al., 2023; Vogel et al., 2020) as both amyloid and tau naturally presents a bimodal distribution when pathology accumulates.

Definitions and methods

The spatial extent is a simple framework in which the spatial distribution of a specific pathology in the brain is regionally binarized by applying a threshold to each region of the brain to determine which regions are abnormal at the individual level. In *sihnpy*, this is coded in two major steps. In the first step, *sihnpy* derives thresholds for each region of interest. This is done by applying a two-component Gaussian Mixture model to the values in each brain region. More details on the specific steps of the Gaussian Mixture approach can be found in Figure 1C. *sihnpy* users using this approach can choose multiple probability thresholds. *sihnpy* also provides several checkpoints to ensure that the data provided is adequate for the Gaussian Mixture approach such as ensuring that a two-component solution is appropriate and making sure that the final thresholds are not too high or too low in the original scale of the data. The file provided

by *sihnpy* for thresholds is made of columns representing the different probability thresholds chosen by the user and the rows represent the different brain regions where the thresholds were applied. In the second step, *sihnpy* applies the thresholds to the data. By default, *sihnpy* accepts thresholds derived from its “apply” step, but it will also accept any thresholds derived by users if the format of the file matches what is normally output by *sihnpy*. In this second and last step, *sihnpy* will output a spatial extent index for each participant (i.e., the number of regions above thresholds), a binary mask for each participant indicating which regions are above threshold and a weighted mask where the binary mask is multiplied by the original data, such that regions below threshold have a value of 0 and regions above threshold have the original value.

Use cases, strengths and limitations

In terms of conditions and limitations, the spatial extent module needs data on more than one brain region. The module can still be used to derive thresholds in individual regions or markers, but won't provide an index in the second step. Finally, the data fed to the module should be able to be binarized: the module will not provide accurate thresholds in the case of only 1 normal distribution being found nor will it be able to find more than two clusters in each region. In terms of strengths, the module is easy to apply to data. It is also an easy-to-interpret individual-specific measure as the spatial extent index simply counts the number of regions above regional thresholds. It also provides users with good flexibility as it allows for multiple thresholds to be derived at once and it provides a variety of different measures (global number of regions, binary mask of regions and weighted mask of regions). However, this method can lose information as it forces binarization of the data. Furthermore, if different teams use different methods to derive thresholds or use

different number of brain regions, results may not be comparable. Deriving thresholds with Gaussian Mixture also comes with some limitations, including the arbitrary choice of probability thresholds and the possibility that the data will not conform to Gaussian distributions.

Demonstration

At the time *sihnpy* was created, there was no PET data openly available from the PREVENT-AD. To allow users to test the package, simulated data was instead created. We selected 14 bilateral brain regions: entorhinal, amygdala, fusiform, parahippocampal, inferior temporal, middle temporal, precentral and postcentral. All of these, with the exception of the precentral and postcentral gyri, are regions where tau pathology tends to accumulate in priority in patients with Alzheimer's disease. Tau pathology data tends to present in a bimodal distribution: a large proportion of individuals with little to no tau, tightly distributed, and a small proportion of individuals with high amounts of tau loosely distributed. To simulate this distribution, we used Gaussian randomizers. To start the randomizers, we extracted the average and standard deviation of tau standardized uptake value ratio (SUVR; i.e., amount of tau) from the data we used in Chapter 3 in each of the brain regions of interest. We used the values of cognitively unimpaired amyloid-negative participants to simulate "low tau" data and the values of patients with Alzheimer's disease and amyloid-positive to simulate "high tau" data. Ten thousand numbers were generated for "high tau" and "low tau" distributions. We then randomly selected 200 values from the "low tau" values and 108 values from the "high tau" values and assigned them to PREVENT-AD participants.

While this yields cleanly separated distributions, this is not always the case when dealing with actual PET data. Gaussian Mixture Models can identify a single distribution of the data rather than two, and it can also misidentify the “high tau” distribution as being the “low tau” distribution. To simulate these issues for users, two regions (precentral and postcentral gyri) were modified. In the first case, a single Gaussian randomizer was used to create simulated data for all 308 participants. In the second, 108 random data from the “low tau” distribution were taken, while 200 random data from the “high tau” distribution were taken. The full tutorial addresses how to handle these scenarios for users.

X.II.V. – Sliding-window module

Rationale

Contrary to other modules in sihnp, which provide individual-level measures of heterogeneity, the sliding window instead targets group-level heterogeneity. Specifically, in the sliding-window analysis, the sample of interest is sorted and divided into overlapping subgroups based on ascending or descending values on a specific variable (St-Onge, Javanray, et al., 2023; Váša et al., 2018). The size of each subset and the degree of overlap are determined by the user when creating the groups. This method allows to verify whether a variable, or association, of interest changes based on a third variable.

Definitions and methods

In the sliding-window analysis, groups of overlapping participants are created along a continuous variable of interest (Váša et al., 2018). The goal of this procedure is to test whether an outcome remains the same across slight variations in the variable of

interest. It starts with the user determining the size of the group of interest (window size) and the size of the overlap between groups (step size). Then, the user must input a dataframe to `sihnpy` with the one variable to use to split the groups. The variable must be continuous, and ideally, different enough between participants so they can be accurately sorted. The dataframe is then sorted in ascending order and `sihnpy` computes the number of windows (i.e., subgroups) it should build based on the sample size. `sihnpy` will select the first N participants for the first window where N is the window size, skip S participants where S is the step size and select the next N participants for the second window. Finally, `sihnpy` will output a spreadsheet for each window created which will contain the IDs of the participants included as well as their value on the splitting variable. It will also output a single spreadsheet with the average value of the splitting variable in each window, which can be useful when plotting results from this analysis.

Use cases, strengths and limitations

The only requirement for this module to function is that the splitting variable must be continuous and, ideally, should vary enough between individuals so that no or few participants share the same value. This method has the advantage of being easy to use and creates more data-driven group divisions rather than splitting on an arbitrary number. However, it still requires the users to choose arbitrary values such as the size of the groups and their overlap. Consequently, users should test multiple window and step sizes when using this method to ensure that results are congruent. Furthermore, as window and step sizes will rarely result in an exact division of participants, the last window created will always have an unequal number of participants. While you can somewhat control this behaviour in `sihnpy` by adjusting whether the last window has more or fewer participants

than other windows, any projects using this method will need to acknowledge this limitation.

Demonstration

Demographic information on the PREVENT-AD participants is limited due to ethical reasons. Normally, age is used in the sliding window analysis, but this information is not available in the open dataset. Instead, similarly to the tau-PET data, we simulated the age of participants with a Gaussian randomizer based on the inclusion criteria in the PREVENT-AD. We used an average age of 65 years and a standard deviation of 5 years. Additionally, we capped the minimum age at 55 years (i.e., minimum age criteria to be included in the PREVENT-AD).

X.II.VI. – Imbalance mapping module

Rationale

Imbalance mapping is an analysis that calculates the distance between an individual's brain feature and the average of their sample, with the idea that the further a person is from their population average, the more imbalance they present (Nadig et al., 2021). This is calculated using a covariance analysis, where the values of each brain feature are correlated to the values of each other brain feature across the group. The population average (i.e., regression line) and the individual distances (i.e., individuals' residuals from the regression line) are computed using an orthogonal distance regression method based on principal component analysis (Jolliffe & Cadima, 2016; Nadig et al., 2021). Contrary to other regression methods, such as ordinal least squares, orthogonal distance regression assumes that values in each brain feature both present errors that need to be accounted for, deriving distances with less bias between regions. In this

analysis, a greater distance means more difference from the population for a given individual.

Definitions and methods

In a traditional covariance analysis, values in each region of the brain are correlated to values in all other regions across a group of participants using a linear model. The deviation (i.e., imbalance) for a single participant is then determined as the distance between the predicted covariance and the actual covariance. In a regular linear model with an ordinal least square estimator, the distance from the predicted value is assumed to stem only from an error or difference in the outcome variable. However, in the case of a covariance analysis involving brain regions, the degree of error cannot be reliably attributed only to the outcome or predictor. Instead, we can use an orthogonal distance regression to compute the individual distance between the predicted and actual covariance and assume that the distance is a mixture of error from the outcome and predictor variable. Several methods exist to estimate an orthogonal distance regression (Carr, 2012), but the original imbalance mapping methodology leverages a principal component analysis to find a regression line that minimizes the orthogonal distance between the observed covariance and the predicted covariance (Nadig et al., 2021). The method was initially developed in R but was translated to Python and integrated into *sihnp*. As input, *sihnp* requires a single dataframe where each row is a unique observation, and each column is a brain region. *sihnp* will then compute the orthogonal distance regression between each pair of brain regions and will calculate the individual-level imbalance for each pair of regions. Finally, *sihnp* will output a global imbalance

average across the whole brain for each participant, an average imbalance by region for the group and an average imbalance by region for each individual.

Use cases, strengths and limitations

As a basic condition of use, you must have values for at least two brain regions to launch the imbalance mapping analysis. In terms of strengths, the method is easy to use and provides rich data for each participant and at the group level. It is also relatively computationally inexpensive to run. However, interpreting the data is more difficult as it is unclear whether having more imbalance is detrimental in the long term. Structural covariance, which imbalance mapping is based on, is also subject to multiple limitations that should be accounted for by users (Carmon et al., 2020), such as poor estimation in small sample sizes, with low-resolution images and in smaller parcellations. Furthermore, users should also check that orthogonal distance assumptions are respected before launching the method.

Demonstration

Thickness and volume data is available for 306 participants within the dataset to test the imbalance mapping functions. In the tutorial, this is demonstrated with volume data from participants with baseline data available.

X.II.VII. – Data preprocessing

This section contains additional information on how the data in sihnpys datasets module was preprocessed. This includes specifically the functional connectivity matrices and the volume and thickness measures. Most preprocessing information below comes from the boilerplate citations recommended by fMRIPrep and FreeSurfer.

Functional connectivity

fMRI data from a resting-state task, an encoding and a retrieval task was preprocessed using fMRIPrep for 15 participants. We used fMRIPrep v20.2.0 (Esteban, Markiewicz, et al. (2018); Esteban, Blair, et al. (2018), which is based on Nipype 1.5.1 (Gorgolewski et al. (2011); Gorgolewski et al. (2018).

First, all available T1-weighted (T1w) images for each participant across visits were used. They were corrected for intensity non-uniformity (INU) with N4BiasFieldCorrection (Tustison et al. 2010), distributed with ANTs 2.3.3 (Avants et al. 2008). The T1w-reference was then skull-stripped with a Nipype implementation of the antsBrainExtraction.sh workflow (from ANTs), using OASIS30ANTs as the target template. Brain tissue segmentation of cerebrospinal fluid (CSF), white matter (WM) and gray matter (GM) was performed on the brain-extracted T1w using fast (FSL 5.0.9, Zhang, Brady, and Smith 2001). A T1w-reference map was computed after registration of all T1w images (after INU-correction) using mri_robust_template (FreeSurfer 6.0.1, Reuter, Rosas, and Fischl 2010). Brain surfaces were reconstructed using recon-all (FreeSurfer 6.0.1, Dale, Fischl, and Sereno 1999), and the brain mask estimated previously was refined with a custom variation of the method to reconcile ANTs-derived and FreeSurfer-derived segmentations of the cortical gray-matter of Mindboggle (Klein et al. 2017). Volume-based spatial normalization to one standard space (MNI152NLin2009cAsym) was performed through nonlinear registration with antsRegistration (ANTs 2.3.3), using brain-extracted versions of both T1w reference and the T1w template. The following template was selected for spatial normalization: ICBM 152 Nonlinear Asymmetrical template version 2009c [Fonov et al. (2009); TemplateFlow ID: MNI152NLin2009cAsym] Note that while the Prevent-AD Open Dataset BIDS does contain other brain imaging

modalities that can be leveraged by fMRIPrep (e.g., FLAIR), it is not consistent across participants. As such, preprocessing was restricted to T1w and EPI images only.

The following preprocessing was performed for each BOLD run found per subject (across all tasks and sessions). First, a reference volume and its skull-stripped version were generated using a custom methodology of fMRIPrep. A B0-nonuniformity map (or fieldmap) was estimated based on a phase-difference map calculated with a dual-echo GRE (gradient-recall echo) sequence, processed with a custom workflow of SDCFlows inspired by the epidewarp. The full script and further improvements in HCP Pipelines (Glasser et al. 2013). The fieldmap was then co-registered to the target EPI (echo-planar imaging) reference run and converted to a displacements field map (amenable to registration tools such as ANTs) with FSL's fugue and other SDCflows tools. Based on the estimated susceptibility distortion, a corrected EPI (echo-planar imaging) reference was calculated for a more accurate co-registration with the anatomical reference. The BOLD reference was then co-registered to the T1w reference using `bbregister` (FreeSurfer), which implements boundary-based registration (Greve and Fischl 2009). Co-registration was configured with six degrees of freedom. Head-motion parameters for the BOLD reference (transformation matrices and six corresponding rotation and translation parameters) are estimated before spatiotemporal filtering using `mcfliirt` (FSL 5.0.9, Jenkinson et al. 2002). BOLD runs were slice-time corrected using `3dTshift` from AFNI 20160207 (Cox and Hyde 1997). The BOLD time series (including slice-timing correction when applied) were resampled onto their original, native space by applying a single composite transform to correct for head motion and susceptibility distortions. These resampled BOLD time series will be called preprocessed BOLD in the original space or

just preprocessed BOLD. The BOLD time series were resampled into standard space, generating a preprocessed BOLD run in MNI152NLin2009cAsym space. First, a reference volume and its skull-stripped version were generated using a custom methodology of fMRIPrep. Several confounding time series were calculated based on the preprocessed BOLD: framewise displacement (FD), DVARS and three region-wise global signals. FD was computed using two formulations following Power (absolute sum of relative motions, Power et al. (2014)) and Jenkinson (relative root mean square displacement between affines, Jenkinson et al. (2002)). FD and DVARS are calculated for each functional run, both using their implementations in Nipype (following the definitions by Power et al. 2014). The three global signals are extracted within the CSF, the WM, and the whole-brain masks. Additionally, physiological regressors were extracted for component-based noise correction (CompCor, Behzadi et al. 2007). Principal components are estimated after high-pass filtering the preprocessed BOLD time series (using a discrete cosine filter with 128s cut-off) for the two CompCor variants: temporal (tCompCor) and anatomical (aCompCor). tCompCor components are calculated from the brain mask's top 2% variable voxels. For aCompCor, three probabilistic masks (CSF, WM and combined CSF+WM) are generated in anatomical space. The implementation differs from that of Behzadi et al. in that instead of eroding the masks by 2 pixels on BOLD space; the aCompCor masks are subtracted a mask of pixels that likely contain a volume fraction of GM. This mask is obtained by dilating a GM mask extracted from the FreeSurfer's aseg segmentation, and it ensures components are not extracted from voxels containing a minimal fraction of GM. Finally, these masks are resampled into BOLD space and binarized by thresholding at 0.99 (as in the original

implementation). Components are also calculated separately within the WM and CSF masks. For each CompCor decomposition, the k components with the largest singular values are retained, such that the retained components' time series are sufficient to explain 50 percent of variance across the nuisance mask (CSF, WM, combined, or temporal). The remaining components are dropped from consideration. The head-motion estimates calculated in the correction step were also placed within the corresponding confounds file. The confound time series derived from head motion estimates and global signals was expanded by including temporal derivatives and quadratic terms for each (Satterthwaite et al. 2013). Frames that exceeded a threshold of 0.5 mm FD or 1.5 standardized DVARS were annotated as motion outliers. All resamplings can be performed with a single interpolation step by composing all the pertinent transformations (i.e. head-motion transform matrices, susceptibility distortion correction when available, and co-registrations to anatomical and output spaces). Gridded (volumetric) resamplings were performed using `antsApplyTransforms` (ANTs), configured with Lanczos interpolation to minimize the smoothing effects of other kernels (Lanczos 1964). Non-gridded (surface) resamplings were performed using `mri_vol2surf` (FreeSurfer). Many internal operations of fMRIPrep use Nilearn 0.6.2 (Abraham et al. 2014), mostly within the functional processing workflow. For more pipeline details, see the workflow section in fMRIPrep's documentation.

Finally, we extracted the functional connectivity using Nilearn v.0.6.2. Once preprocessed by fMRIPrep; confounds were removed from the images and frames with excessive motion were scrubbed using Nilearn. Time series were extracted in 400 brain parcels from the Schaefer atlas (Schaefer et al. 2018). The time series in each region

were correlated with every other region using partial correlations to generate the functional connectivity matrices. This process yielded 400x400 matrices representing the functional links between each brain region of the atlas.

Volume and thickness

Longitudinal structural MRI data is available for most participants within the PREVENT-AD Open Dataset. In our case, we preprocessed baseline and follow-up at 12-month structural MRI of all 308 cohort participants. This yielded 543 structural MRIs available for preprocessing. Two scans failed preprocessing, producing a final number of 541 scans. Preprocessing was done using FreeSurfer 7.1.0., described below.

Cortical reconstruction and volumetric segmentation were performed with the FreeSurfer image analysis suite, which is documented and freely available for download online (<http://surfer.nmr.mgh.harvard.edu/>). The technical details of these procedures are described in prior publications (Dale et al., 1999; Dale and Sereno, 1993; Fischl and Dale, 2000; Fischl et al., 2001; Fischl et al., 2002; Fischl et al., 2004a; Fischl et al., 1999a; Fischl et al., 1999b; Fischl et al., 2004b; Han et al., 2006; Jovicich et al., 2006; Segonne et al., 2004, Reuter et al. 2010, Reuter et al. 2012). Briefly, this processing includes motion correction and averaging (Reuter et al. 2010) of multiple volumetric T1 weighted images (when more than one is available), removal of non-brain tissue using a hybrid watershed/surface deformation procedure (Segonne et al., 2004), automated Talairach transformation, segmentation of the subcortical white matter and deep gray matter volumetric structures (including hippocampus, amygdala, caudate, putamen, ventricles) (Fischl et al., 2002; Fischl et al., 2004a) intensity normalization (Sled et al., 1998), tessellation of the gray matter white matter boundary, automated topology correction

(Fischl et al., 2001; Segonne et al., 2007), and surface deformation following intensity gradients to optimally place the gray/white and gray/cerebrospinal fluid borders at the location where the most significant shift in intensity defines the transition to the other tissue class (Dale et al., 1999; Dale and Sereno, 1993; Fischl and Dale, 2000). Once the cortical models are complete, several deformable procedures can be performed for further data processing and analysis, including surface inflation (Fischl et al., 1999a), registration to a spherical atlas which is based on individual cortical folding patterns to match cortical geometry across subjects (Fischl et al., 1999b), parcellation of the cerebral cortex into units for gyral and sulcal structure (Desikan et al., 2006; Fischl et al., 2004b), and creation of a variety of surface-based data including maps of curvature and sulcal depth. This method uses both intensity and continuity information from the entire three-dimensional MR volume in segmentation and deformation procedures to produce representations of cortical thickness, calculated as the closest distance from the gray/white boundary to the gray/CSF boundary at each vertex on the tessellated surface (Fischl and Dale, 2000). The maps are created using spatial intensity gradients across tissue classes and are therefore not simply reliant on absolute signal intensity. The maps produced are not restricted to the original data's voxel resolution and thus can detect submillimeter differences between groups. Procedures for measuring cortical thickness have been validated against histological analysis (Rosas et al., 2002) and manual measurements (Kuperberg et al., 2003; Salat et al., 2004). Freesurfer morphometric procedures have shown good test-retest reliability across scanner manufacturers and field strengths (Han et al., 2006; Reuter et al., 2012). While longitudinal data was available and used in this package, each session was processed individually.

The aseg atlas is built from 40 subjects acquired using the same mp-rage sequence (by people at Wash U ages ago in collaboration with Randy Buckner). The subjects that make up the atlas are distributed in 4 groups of 10 subjects each: (1) young, (2) middle-aged, (3) healthy older adults, and (4) older adults with AD.

Following preprocessing, volume and thickness were extracted from the 68 bilateral parcels comprising the Desikan atlas (Desikan et al., 2006). The volume in the Aseg atlas was also extracted. Volume and thickness in the Desikan and Aseg atlas are shipped with *sihnpy*.

X.III. – Discussion

This annex presented *sihnpy*, an openly available Python package comprising analytical methods from Chapters 2 and 3. The goal was to adapt and provide these tools openly for the scientific community in a user-friendly manner. More broadly, through the use of open access data, this project promotes open access to advance science forward. *sihnpy*, contrary to traditional scientific publications, is a living tool. New modules will continue to be developed with the aim of providing scientists with more tools to investigate interindividual differences, based on user feedbacks, scientific discoveries and research in the field of interindividual differences.

XI – Annex: Optina Diagnostics – Data science report

During my thesis work, I was recruited for an internship at Optina Diagnostics Inc. financed by Mitacs in May 2020. Optina Diagnostics is a biomedical company working on an artificial intelligence algorithm to classify individuals with low or high levels of amyloid pathology based on a retinal scan. I worked on multiple projects for the company between May 2020 and September 2023 where I recruited participants for a study, preprocessed positron emission tomography and structural magnetic resonance imaging, and analyzed quantitative SUVR measurements. This culminated in the report presented in this Annex, where the goal of the study was to compare positivity from visual readings of expert neuroradiologists to quantitative SUVR measurements in participants recruited within the PREVENT-AD. While not central to this project, I also utilized *sihnpy* to apply the spatial extent methodology which revealed insights on the spread of amyloid in the brain of participants at the individual level. Overall, the report found that neurologist visual reads will only identify scans as positive when amyloid is widespread throughout the brain, likely missing early regional-only amyloid cases. I also revealed significant discrepancies between visual readers, suggesting that some readers are more sensitive to regional amyloid. As the consensus visual reading is the variable used to train their algorithm, I made recommendations to either 1) include only participants where the scans were declared positive or negative by all readers, which will effectively strengthen the training of the model on more clearly labelled data, or 2) use a tiered approach to capture regional amyloid should they want their algorithm to identify early accumulation of amyloid.

Optina and PREVENT-AD:

Comparison of majority voting visual read and standardized uptake value ratio methods in cognitively unimpaired individuals

Frédéric St-Onge

Data science intern

McGill University

October 3rd 2023

Montreal, Canada

Section 1 – Summary and recommendations

Optina Diagnostics is developing an artificial-intelligence-based retinal imaging biomarker to detect amyloid positivity in patients with Alzheimer's disease based on majority voting from a panel of three neuroradiologist experts. After recruiting 128 participants from the PREVENT-AD cohort, the company asked me to describe the data, and particularly, to compare amyloid positivity derived from majority visual reading from experts to quantitative standardized uptake value ratio (SUVR)-based methods.

Overall, the report found that SUVR-based methods are usually as accurate as the majority voting neuroradiological readings in identifying amyloid positive cases. However, SUVR thresholds identified by this report matching the accuracy of the visual reads were much higher than based on data-driven methods. Diving in this discrepancy revealed that neuroradiologists were more conservative than data-driven methods, only classifying participants as positive once amyloid was widespread across the entire brain, despite evidence of regional accumulation. We found discrepancies between neuroradiologists, with one specifically identifying regional accumulation of amyloid not identified by others. Majority voting visual reads also missed significant longitudinal accumulation of amyloid.

In the future, if the objective is to capture early accumulation, the company is likely to miss it when using majority voting of visual read as an indicator of amyloid positivity in cognitively unimpaired participants at risk of AD. The company could use instead categorical unanimous voting (positive, ambiguous, negative) or weighting visual reads by the SUVR amount when training the algorithm. Another solution could be to train a different algorithm specifically for participants without cognitive impairments based on their SUVR values.

Section 2 – Introduction and objectives

Optina Diagnostic Inc. is currently developing an artificial intelligence-based retinal imaging marker that uses features of hyperspectral imaging in the retina to predict amyloid positivity status in the brain of participants based on amyloid positron emission tomography (PET) scans. The company currently uses a majority vote of neuroradiologists to establish whether a participant has a positive amyloid PET scan.

Between July 2021 and December 2022, the VilleneuveLab collected amyloid positron emission tomography (PET) with the NAV tracer for Optina Diagnostics Inc. My project aimed at describing and comparing amyloid positivity status of participants included in the study measured with the qualitative gold-standard visual read method the company is currently using to quantitative standardized uptake value ratio (SUVR) methods used in academic settings to quantify amyloid accumulation in the brain. A subset of participant also had longitudinal data available.

The overall goal of this project is to describe the preliminary data and to give recommendations on the development of the algorithm designed by Optina to detect amyloid positivity in the retina in this population.

This report will:

- 1) Describe demographics, neuroradiological visual reads, and quantitative PET SUVR positivity.
- 2) Compare visual reads to PET SUVR information.
- 3) Explore discordant cases between visual read and PET SUVR.
- 4) Describe preliminary longitudinal data.

Section 3 – Methodology

Section 3.1 – Participants

After exclusions, 128 participants from the PREVENT-AD cohort underwent a PET scan with the amyloid-specific tracer [18F]NAV4694 and a retinal scan for Optina. Inclusion criteria for the PREVENT-AD cohort are described elsewhere (Tremblay-Mercier et al., 2021). For this specific study, participants were recruited if they had no counter-indications to undergo the PET and the retinal imaging. We made no restriction on the cognitive status of participants, so participants recruited were cognitively unimpaired or had mild cognitive impairment at the time of the scans.

Optina Diagnostics initially recruited a subtotal of 20 participants in 2018 for a pilot study during which they underwent a retinal and PET scan, and then came back for the study in 2022-2023. These participants have longitudinal data available.

Section 3.2 – Data gathering and preprocessing

Participants included are all participants within the larger PREVENT-AD study. We pooled demographic and genetic information from these participants from the data dump of the PREVENT-AD on August 30th 2023. Optina attributed participants a unique identifier, starting with PAM for the study in 2018 and PAD for the study in 2022. We matched visual reads back to the Optina IDs using an identifying list kept by the PREVENT-AD team.

The VilleneuveLab received and preprocessed scans from the Montreal Neurological Institute scanning site. We preprocessed them using an in-house pipeline, described elsewhere (Ozlen et al., 2022; McSweeney et al., 2020). Briefly, each PET scan is first realigned, averaged and coregistered to the closest magnetic resonance

imaging scan that the participant has available. These images were transferred to Optima for the visual readings. Then, each PET scan was segmented in the cortical regions defined by Desikan et al. (2006) and the PET uptake in each brain region is calculated as a ratio to the reference region (i.e., cerebellum cortex) which yields standardized uptake value ratios (SUVR).

Section 3.3 – Variables

The primary goal of the analyses is to compare SUVR-based measures to visual reads. Three neuroradiologists experts in PET and dementia executed the visual reads. Positivity was determined by blind majority voting.

We computed multiple SUVR based measures as comparators. First, we computed a global SUVR average comprising brain regions spanning the frontal, temporal, and parietal lobes. Second, we calculated a spatial extent index based on a recent method from our group (St-Onge et al. 2023), which calculates how many regions have abnormal levels of SUVR based on region-specific thresholds at the individual level. See Figure 1A for more details. Third, based on other papers from our group (Villeneuve et al., 2015; Ozlen et al., 2022), we know amyloid pathology accumulates early in 7 key bilateral regions of the brain. We derived the average SUVR in these seven bilateral regions. We also used the spatial extent method to derive a categorical variable representing whether participant had: 1) no regions within the 7 that were abnormal ("Negative"), 2) at least 1 of the seven regions that was abnormal ("Regional") or 3) all seven regions were abnormal ("Widespread"). We also derived the SUVR in these 7 bilateral regions for the ROC curve analysis. For all three variables, we established thresholds for abnormality by using the probability of being abnormal as calculated with

Gaussian Mixture Models. Other than traditional data cleaning, no additional transformations were applied to the rest of the variables available for analysis.

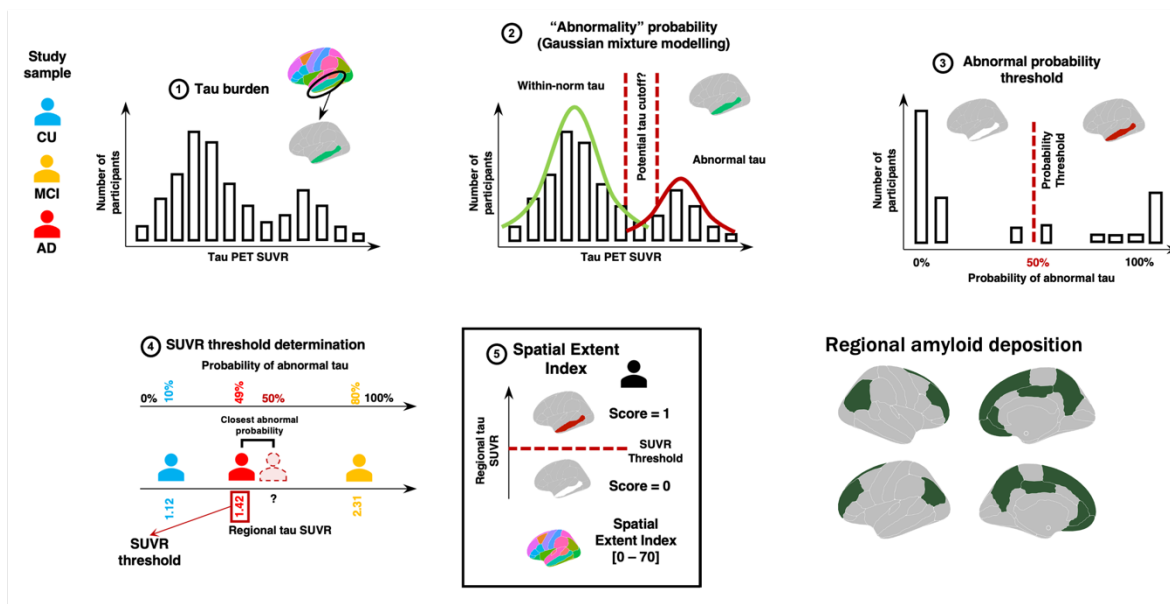


Figure 1 – Presentation of the method used to derive SUVR-based measures. *Other than calculating the average SUVR across regions of the brain, we apply a method known at the spatial extent to derive measures of abnormal amyloid across the brain. For each brain region, we extract the standardized uptake value ratio (SUVR) of our participants (1). Then, a two-component Gaussian mixture modelling technique is applied to the SUVR values in each region (2-3). The second distribution is considered to reflect abnormally high SUVR tau values. We extract the probability that each participant belongs to the “abnormal” distribution and establish a threshold that individuals with over 50% probability are considered positive for the given region (4). Once thresholds are derived across all regions, we derive the spatial extent index for each participant by summing the number of positive regions across the brain. (5). We also apply this methodology to 7 bilateral regions known for early amyloid accumulation (“Regional amyloid deposition”). Note that while the original figure include cognitively unimpaired (CU) participants, participants with mild cognitive impairment (MCI) or participants with Alzheimer’s disease (AD). Figure adapted from sihnp’s documentation (<https://sihnp.readthedocs.io/>) with permission of the first author.*

Section 4 – Results

Section 4.1 – Describe demographics, neuroradiological visual reads and quantitative PET SUVR positivity

Table 1 – Demographic information

Variables	
Sample size	128
N females (%)	90 (70.3)
Education in years (mean (SD))	15.53 (3.10)
Apoe4 (%)	
Homozygote (E4/E4)	4 (3.10)
Heterozygote (E3/E4)	50 (39.1)
No allele (E3/E3)	28 (21.9)
Majority read (% positive)	28 (21.9)
Unanimous read (%)	
Negative	88 (68.8)
Ambiguous	19 (14.8)
Positive	21 (16.4)
Global SUVR positivity at 1.31 (%)	39 (30.5)
Regional SUVR positivity (%)	
Regional negative	74 (57.8)
Regional positive	28 (21.9)
Regional widespread	26 (20.3)
Global SUVR values (mean (SD))	1.33 (0.35)
Spatial extent of amyloid (mean (SD))	12.89 (22.20)

Conclusions:

- Most are women (70%), aged 70 years and highly educated
 - Close to half have an ApoE4 allele; i.e., increased risk of AD
 - 21% are positive by majority vote visual read (2/3 readers); 16% when considering unanimous votes of all three readers
 - 31% are positive with the PREVENT-AD threshold (derived from Gaussian Mixture Modelling in 239 participants from the PREVENT-AD); 42% have at least one early amyloid region with abnormal amyloid levels
-

Section 4.2 – Compare visual reads to PET SUVR information

Next, we explored the different SUVR measures in relation to the visual reads. Visual reads are currently considered the gold-standard to identify whether or not a scan is positive. However, as the majority visual read classification is a binary evaluation, SUVR can bring depth to the analysis by quantifying the amount and the location of pathology.

To compare the different SUVR measures to the visual reads, we first did a ROC curve analysis where we computed the area under the curve for each SUVR measure when compared to the visual read (Figure 2A) to determine how well the SUVR measures performed at identifying amyloid positive cases. Next, we used the Youden Index to find the threshold that would maximize the sensitivity and specificity of the SUVR measures compared to the visual reads (Table 2). Finally, we illustrated the global amyloid SUVR, the most common SUVR measure used in the field, in relation to the visual read using a histogram (Figure 2B) to visually compare the sensitivity of SUVR and visual read measures to detect abnormal amyloid.

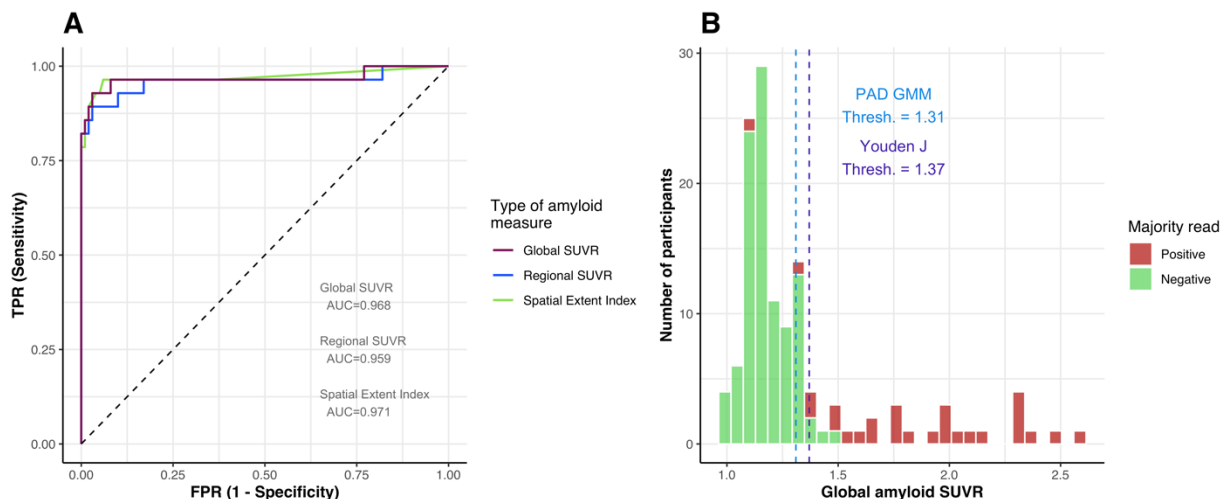


Figure 2 – Comparison of SUVR methods and visual readings. A) ROC curve representing the prediction of amyloid positivity from visual reading by the different SUVR

methods. Area under the curve (AUC) represents the accuracy of the measure (0.5 = no better than luck at predicting the visual reads). B) Distribution of global amyloid SUVR in the 128 participants included in the study, colored by their majority vote visual read. The dashed lines represent the thresholds determined by the PREVENT-AD group and determined by the Youden Index (see Table 2).

Table 2 – Optimal amyloid thresholds

Variable	Threshold	Sensitivity	Specificity	FP (n)	FN (n)
Global SUVR PREVENT-AD	1.31	0.93	0.88	12	1
Global SUVR Youden Index	1.37	0.92	0.97	3	2
Spatial Extent Index	12	0.96	0.94	5	2
Regional SUVR	1.54	0.89	0.97	3	4

Thresholds in the table above were derived on SUVR values, excepted for the Spatial Extent Index which was derived on the number of abnormal regions. The Global SUVR - PREVENT-AD threshold was derived from a Gaussian Mixture Model with 2 components applied to all 239 participants with a baseline amyloid PET scan in the PREVENT-AD.

Conclusions Section 4.2:

- All SUVR measures can accurately predict majority visual reading
- Readers classify participants as positive when amyloid is widespread (> 12 regions in the brain with abnormal amyloid)
- The data-driven threshold in PREVENT-AD is lower than the threshold predicting visual reads, but it is unclear whether the false positives are the result of early detection of amyloid.

Section 4.3 - Exploring discordant cases between visual read and PET SUVR

To understand the mismatch between the SUVR and visual reads, we need to study who are the individuals who mismatch between the SUVR and visual reads. We hypothesize that the SUVR threshold on global amyloid in the PREVENT-AD captures earlier accumulation of amyloid. Using that threshold, let's take a look at false negative and false positive participants.

Table 3 – False positive and false negative participants' characteristics

False Negative (n = 1)	False positive (n = 12)
<ul style="list-style-type: none">- Unanimously positive with visual read- Negative on all SUVR measures<ul style="list-style-type: none">o Global SUVR = 1.11o No positive region- ApoE4 carrier- Male- 10 years of education	<ul style="list-style-type: none">- All participants had abnormal regional amyloid- 10/12 cases are ambiguous (1 or 2 readers classified them as positive)

Upon exploration of the scans, the false negative participant incurred a co-registration error during the creation of the SUVR image. The new data release of this participant is being prepared, but a preliminary check of their SUVR image indicates a SUVR of 1.80, which is clearly positive.

Meanwhile, false positive cases seem to have a meaningful accumulation of regional amyloid, with some disagreements between readers on positivity. We can explore this disagreement further, in Figure 3.

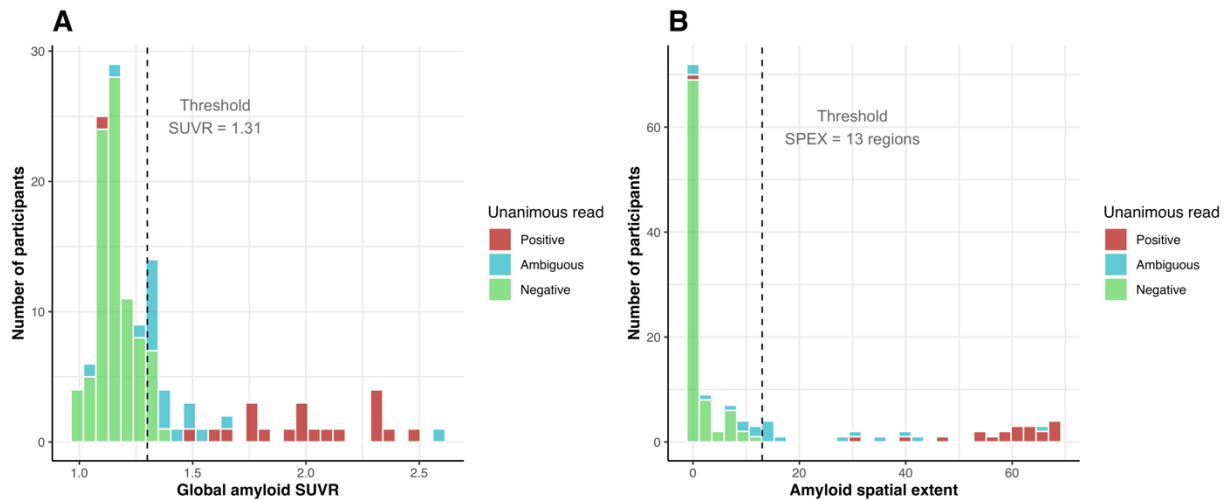


Figure 3 – Reader agreement by the amount of amyloid. A) Amount of global amyloid in the participants included, colored by the reader agreement on the positivity of the scan. B) Spatial extent index of participants colored by reader agreement. Positive shows all readers marked the scan as positive, negative shows all readers marked the scan as negative, ambiguous shows one or two readers dissented from the rest.

Conclusions:

- False positive cases likely are participants with regional amounts of participants. They are also ambiguous cases for readers
 - What leads to the ambiguity between readers? What can explain the discrepancies between SUVR and visual reads?
-

Section 4.3.1 – Demographic differences in ambiguous reads

One explanation could be that the ambiguous cases differ systematically based on specific demographic differences. We tested whether age, education, sex or ApoE4 status influenced the ambiguity of the reading. We also tested whether participants with ambiguous reads had higher SUVR values. We used ANOVA and Tukey HSD post-hoc for continuous measures and chi-square test for categorical measures.

Conclusions:

- Age, sex and education were not different between positive, ambiguous and negative cases
 - Ambiguous participants were more likely to be ApoE4 carriers compared to unambiguously negative participants
 - Ambiguous participants had higher amyloid (global SUVR and spatial extent index) compared to negative participants, but lower amyloid than positive participants
-

Section 4.3.2 – Localization differences in ambiguous reads

Another explanation is that amyloid uptake in ambiguous readings is located in regions that are not typically considered for positivity by the visual readers. We can plot the positivity and SUVR in each region in individuals with negative, ambiguous and positive readings to determine if there are specific patterns.

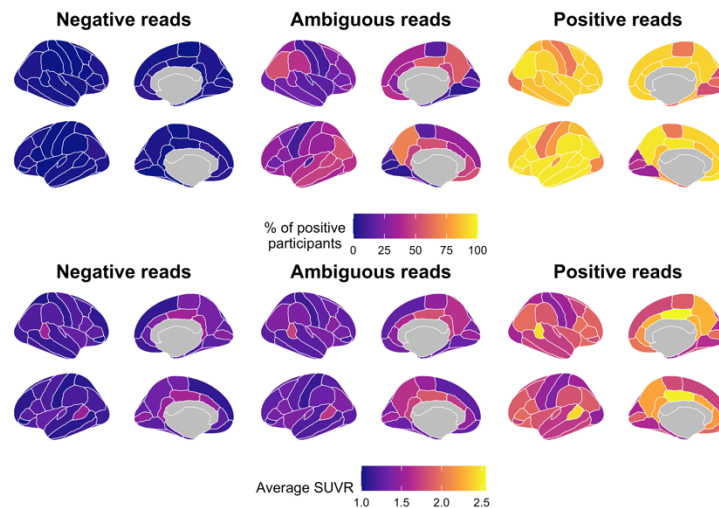


Figure 4 – Localization of amyloid by agreement. *Brain templates illustrating A) the percentage of participants with abnormal amounts of amyloid pathology in each cortical region, divided by groups based on their overall visual read, and B) the average SUVR in each brain region by their overall visual read.*

Conclusions:

- Similarly to the previous points, positive reads have positive regions all across the brains, while ambiguous reads have specific region uptake
 - However, regions with abnormal amyloid are regions readers would look for when determining a visual read positivity
 - Perhaps certain readers are more sensitive to regional abnormality?
-

Section 4.3.3 – Reader-specific biases in visual readings

Results thus far are suggesting that participants with ambiguous readings are accumulating more pathology than participants with fully negative readings, indicating that these participants are likely to have abnormal amounts of pathology. If that is the case, why aren't more participants identified by readers? Do they identify participants in the same way?

Overall, reader OPET01 identified 22 cases as positive, OPET03 identified 27 cases, and OPET04 identified 40 cases. We used Cohen's Kappa to measure agreement between ratings of all three readers. Overall, readers presented substantial agreement (> 0.61). Rater "OPET4" had the lowest agreement with the other readers: 0.63 with OPET1 and 0.74 with OPET3. However, these score are still considered as substantial agreement.

To test whether specific readers were more sensitive to regional differences in amyloid, we used logistic regressions. Reader OPET1 and OPET3 identified participants as positive only when amyloid was widespread, however OPET3 sometimes identified participants as positive when amyloid was only regional. OPET4 was more likely to identify participants as positive when participants had regional amounts of amyloid.

Conclusions:

- Readers had clear discrepancies between them, with nearly twice the number of cases being identified by OPET4 compared to OPET1.
 - OPET4, and to some extent OPET3, identified participants as being positive when they had regional amounts of pathology, where as OPET1 did not.
-

Section 4.4 – Longitudinal data

A small subset of 20 participants had longitudinal data available, with both a retinal scan visit in 2018 and a new visit between 2021 and 2022. We investigated whether visual reads for these participants changed over time in relation to their change in SUVR and spatial extent index.

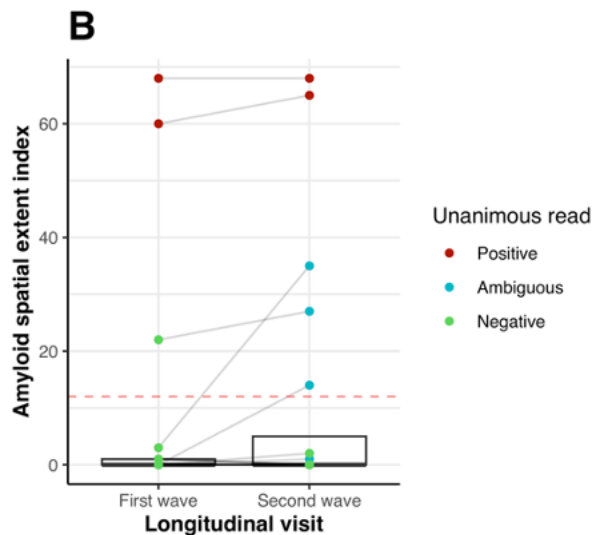
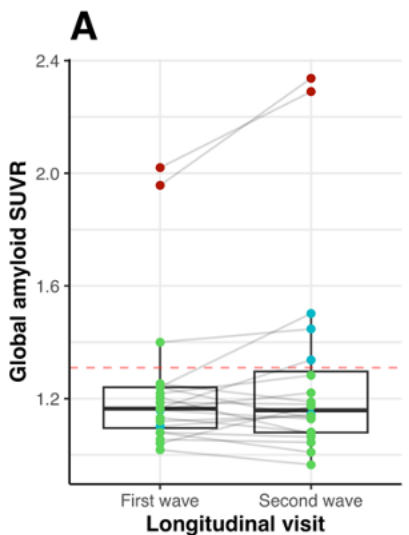
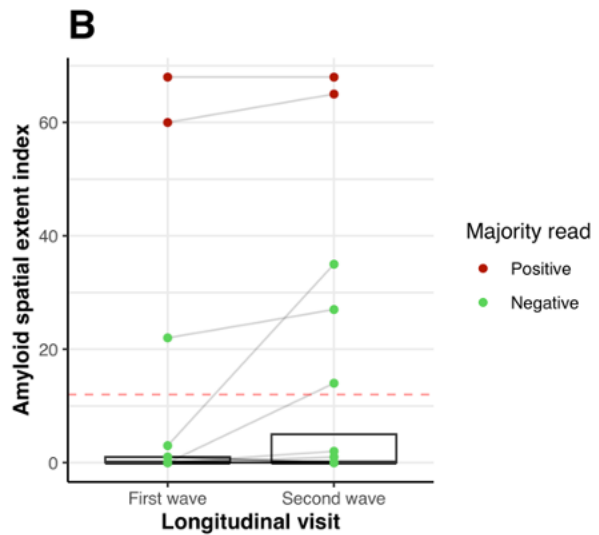
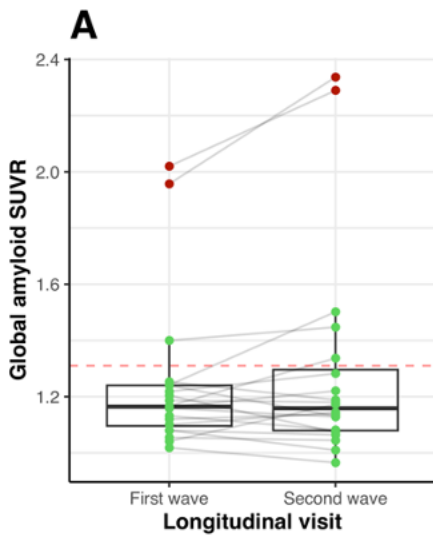


Figure 5 – Longitudinal change in visual reading status. *Both rows present the longitudinal change in SUVR (A) or spatial extent index (B) between the two visits, colored by their visual reading status: in the first row, the status of the majority voting reads are used, while in the second row, we use the unanimous reading status. In all panels, the dashed red lines represent the thresholds derived in Section 4.2: 1.31 SUVR (PREVENT-AD threshold) for panels A and 12 spatial extent index (visual reads-based threshold).*

Conclusions:

- Participants accumulating amyloid did not accumulate enough in 4.5 years to be positive by a majority of reader
 - Some participants who were negative became positive using SUVR-based measures, but not on majority visual reading
 - Participants who became positive on SUVR-based measures were ambiguous when considering unanimous visual readings
-

Section 5 – Conclusions and recommendations

In summary, this report finds that, while SUVR measures can identify amyloid positive cases with a similar accuracy to blind majority voting visual reads, these thresholds are higher than data-driven thresholds within the PREVENT-AD. Exploring the discrepant cases between the two methods revealed that readers typically only identify cases as positive once abnormal SUVR is present across the whole brain. Yet, participants identified as positive by the SUVR methods are at risk of progression (i.e., higher likelihood of ApoE4, higher amount of amyloid and more positive regions) and have more regional amounts of amyloid. Importantly, there were discrepancies between readers, cases with regional amyloid being flagged as positive by one reader but not by others.

Overall, the results suggest that if Optina trains their algorithm using majority voting visual reading, their algorithm will probably miss participants with significant amounts of regional amyloid at risk of progressing.

Recommendations:

- Use a categorical variable rather than a binary variable for majority visual reads (i.e., unanimously positive, ambiguous, unanimously negative)
 - If possible, the visual reads could be weighed by the amount of SUVR or the number of regions with abnormal amyloid in the brain of participants
 - Consider training a different algorithm to identify amyloid positivity in cognitively unimpaired participants
-

Future directions:

- Visual reading on the whole PREVENT-AD cohort to increase sample size
 - Comparison to other cohorts collected by Optina (CQDM and Ottawa site sub-studies had higher agreement between readers)
 - Prediction of other markers (tau, cognition, clinical progression to MCI) from baseline visual read or SUVR
-

XII – Copyright

Chapter 2 was previously published in the journal Network Neuroscience. All figures, text and information contained in the article is full reproducible because of its CC-BY Open License. Chapter 3 was posted as a pre-print on medrxiv. It is also fully reproducible because of a CC-BY Open License. *sihnpy*, presented in Annex X, is a fully downloadable package through the PyPi repository, with an MIT license. Annex XI is fully reproducible because of a CC-BY Open License.